

**Astrophysical signatures of neutron stars in compact
binaries and experimental improvements on
gravitational-wave detectors**

by

Hang Yu

B.S., Physics, Johns Hopkins University (2014)

Submitted to the Department of Physics
in partial fulfillment of the requirements for the degree of

Doctor of Philosophy

at the

MASSACHUSETTS INSTITUTE OF TECHNOLOGY

June 2019

© Massachusetts Institute of Technology 2019. All rights reserved.

Author
Department of Physics
April 13, 2019

Certified by
Nevin N. Weinberg
Associate Professor
Thesis Supervisor

Certified by
Matthew J. Evans
Associate Professor
Thesis Supervisor

Accepted by
Nergis Mavalvala
Chairman, Associate Department Head

Astrophysical signatures of neutron stars in compact binaries and experimental improvements on gravitational-wave detectors

by

Hang Yu

Submitted to the Department of Physics
on April 13, 2019, in partial fulfillment of the
requirements for the degree of
Doctor of Philosophy

Abstract

Neutron stars (NSs) are astrophysical laboratories that allow us to probe physics at extreme conditions. The first half of this Thesis is devoted to exploring how we can connect theoretical models of NS to observational signatures whose detections are made possible by state-of-the-art instruments. We start by exploring the dynamics of super-Eddington winds launched in type-I X-ray bursts at the surface of a NS. We show that freshly synthesized heavy elements can be exposed by the wind and will dominate the composition at the photosphere after ~ 1 s. This may create detectable absorption edges in burst spectra and explain the observed transitions from superexpansions to moderate expansions.

Gravitational-wave (GW) observatories such as Advanced LIGO (aLIGO) opens up a new possibility to probe deep inside the NS by examining the tidal signatures in the GW waveforms. In this Thesis we study the tidal excitations of g-modes in a cold, superfluid NS during the inspiral driven by gravitational radiation and their consequent phase shifts in the GW waveform. We consider both the g-modes supported by the muon-to-electron gradient in the outer core and the g-modes supported by the hyperon-to-proton gradient in the inner core. We further show that the former might be detectable by event stacking when the third generation of GW detectors are available.

The second half of this Thesis is devoted to the experimental upgrades to aLIGO interferometers. The focus will be on the angular sensing and control system. We will cover the design considerations on the system based on both stability and noise requirements. This is followed by a thorough discussion on the radiation-pressure torques, including both the Sidles-Sigg and the $dP/d\theta$ effects. More importantly, we show that such optical torques can be compensated for with newly developed techniques, which is a critical step for aLIGO to reach high-power operations. Lastly, we discuss the prospects of detecting GW at 5 Hz with ground-based detectors, and demonstrate that the low-frequency sensitivity is crucial for both increasing the de-

tection range of black-hole binaries and enabling timely localization of binary NS systems.

Thesis Supervisor: Nevin N. Weinberg

Title: Associate Professor

Thesis Supervisor: Matthew J. Evans

Title: Associate Professor

Acknowledgments

This is the acknowledgements section. You should replace this with your own acknowledgements.

Contents

1	Introduction	13
2	Super-Eddington winds from type-I X-ray bursts	19
2.1	INTRODUCTION ¹	19
2.2	HYDROSTATIC BURST RISE	23
2.2.1	Evolution of the thermal profile	25
2.2.2	Pre-wind composition profile	27
2.3	HYDRODYNAMIC WIND	28
2.3.1	Time-dependent wind profiles	29
2.3.2	Comparison with steady-state models	32
2.3.3	Dependence of wind structure on ignition depth	35
2.3.4	Ejection of heavy elements	37
2.4	OBSERVATIONAL SIGNATURES	39
2.4.1	Burst spectroscopy and light curve	39
2.4.2	Comparison to observed PRE bursts	42
2.5	SUMMARY AND CONCLUSIONS	45
3	Resonant tidal excitation of superfluid neutron stars in coalescing binaries	47
3.1	INTRODUCTION ²	47
3.2	SUPERFLUID NEUTRON STAR MODEL	49

¹This Chapter is based-on [Yu & Weinberg \(2018\)](#).

²This Chapter is based on [Yu & Weinberg \(2017a\)](#)

3.2.1	Buoyancy in cold neutron stars	53
3.3	TIDAL DRIVING	56
3.3.1	Eigenmodes of a superfluid neutron star	57
3.3.2	Tidal driving of modes	62
3.4	RESULTS	65
3.4.1	Tidal energy transfer	66
3.4.2	Phase shift of the gravitational waveform	70
3.5	CONCLUSIONS	73
4	Dynamical tides in coalescing superfluid neutron star binaries with hyperon cores and their detectability with third generation gravitational- wave detectors	75
4.1	INTRODUCTION ³	75
4.2	SUPERFLUID MODELS WITH HYPERONS	77
4.3	EIGENMODES OF A SUPERFLUID HYPERON STAR	81
4.4	TIDAL DRIVING AND PHASE SHIFT OF THE GRAVITATIONAL WAVEFORM	86
4.5	DETECTABILITY OF THE MODE RESONANCES	89
4.5.1	Modeling the detectability	89
4.5.2	Detectability with second and third generation detectors . . .	93
4.6	CONCLUSIONS	96
5	Overview of the aLIGO detectors	99
5.1	OPTICAL TOPOLOGY	100
5.2	PROPAGATION OF THE DC FIELDS	103
5.2.1	The carrier field	103
5.2.2	The RF sidebands	108
5.3	PROPAGATION OF THE AC FIELDS	111
5.3.1	From mirror motion to optical field	111
5.3.2	DARM signal	112

³This Chapter is based on Yu & Weinberg (2017b).

5.3.3	Quantum fluctuations	118
6	Overview of alignment sensing and control in aLIGO	121
6.1	OPTICAL CAVITIES AND GAUSSIAN BEAMS	122
6.2	DEGREES OF FREEDOM	126
6.3	DETECTION SCHEMES	130
6.3.1	Interferometric DOFs	130
6.3.2	Pointing DOFs	133
6.4	ALIGNMENT SENSING AND CONTROL IN aLIGO	135
6.5	TOLERANCE ON THE RESIDUAL ANGULAR MOTION	139
7	Alignment control of the arm cavities	143
7.1	CONTROL LOOP DESIGN CONSIDERATIONS	144
7.2	EFFECTS OF RADIATION PRESSURE	150
7.2.1	Introduction	150
7.2.2	The Sidles-Sigg effect	152
7.2.3	The $dP/d\theta$ effect	168
7.3	NOISE REDUCTION TECHNIQUES	174
7.3.1	Length-to-pitch feedforward	174
7.3.2	Signal blending	177
7.3.3	Optimal control design using the \mathcal{H}_∞ method	179
8	Thermal distortions in aLIGO	185
8.1	ALIGNMENT OF THE SIGNAL-RECYCLING CAVITY	186
8.2	DETUNING OF THE SIGNAL-RECYCLING CAVITY	192
9	Prospects for detecting gravitational waves at 5 Hz with ground-based detectors	197
9.1	INTRODUCTION ⁴	197
9.2	LIGO-LF DESIGN	198
9.3	ASTROPHYSICAL APPLICATIONS	204

⁴This Chapter is based-on Yu et al. (2018).

9.3.1	Binary BHs.	204
9.3.2	Binary NSs	210
9.3.3	The GW memory	216
9.4	CONCLUSIONS	218
A	Details of the MESA setup for the super-Eddington-wind models	219
B	Thermodynamic relations and superfluid Entrainment	225
B.1	BACKGROUND QUANTITIES	225
B.2	ENTRAINMENT FUNCTION	229
B.3	RATE OF DIRECT URCA PROCESS	231
C	Superfluid oscillation equations and hermiticity of the linear operator	235
C.1	OSCILLATION EQUATIONS	235
C.2	BOUNDARY CONDITIONS	239
C.3	HERMITICITY OF THE LINEAR PERTURBATION OPERATOR	240
C.4	NUMERICAL ACCURACY OF TIDAL COUPLING COEFFICIENT CALCUATION	242
D	Phase shift	245
E	More on Gaussian beams	247
F	Supplemental materials for the LIGO-LF design	251
F.1	LIGO-LF SUSPENSION DESIGN	251
F.2	CALCULATION OF THE SCATTERING NOISE	253

List of Figures

2-1	Temperature as a function of column depth at different moments during the burst rise.	23
2-2	Temperature profiles for five burst models at the moment when their convective zones reach maximum extent.	26
2-3	Composition profiles at the moment just before the wind launches for three burst models.	27
2-4	Temperature and luminosity profiles during the wind phase.	29
2-5	Radial profiles of the wind structure at different times for model y2n21.	31
2-6	Optical depth and mass-loss rate at the photosphere as a function of time for four of the burst models.	32
2-7	Bulk properties of the wind as a function of ignition column depth.	34
2-8	Composition of the wind at $t = 10$ s for model y2n21.	36
2-9	Timescale to expose the heavy-element ashes and the duration of the wind as a function of ignition column depth y_b	38
2-10	Ion mean molecular weight at the photosphere as a function of time.	39
2-11	Evolution of properties at the photosphere.	40
2-12	Photon count rate as a function of time assuming a source at a distance of 10 kpc.	41
3-1	Composition profile of the $1.4 M_\odot$ NS model.	53
3-2	Buoyancy frequency for the NS models.	54
3-3	Structure of the g-modes of our superfluid NS model.	60
3-4	Eigenfrequencies of the g-modes.	62

3-5	Tidal coupling coefficient of the g-modes.	63
3-6	Energy evolution of g-modes during a binary NS inspiral.	67
3-7	Phase shift of the gravitational waveform due to the resonant excitation of g-modes.	71
4-1	Composition profiles of the HS models.	79
4-2	Comparing the Brunt-Väisälä frequency for the HS and NS models.	79
4-3	Comparing mode structures for the HS and NS models.	84
4-4	Eigenfrequencies of the g-modes in the HS and NS models.	85
5-1	The optical layout of the aLIGO interferometer.	101
5-2	Schematic plots for deriving the DC fields in aLIGO.	104
5-3	Schematic plots for deriving the AC fields in aLIGO.	113
6-1	Carton illustrating the alignment DOFs.	127
6-2	The generic principle of detecting an alignment signal with WFSs.	131
6-3	Angle-to-length coupling due to spot miscentering.	134
6-4	Alignment sensing and control of the interferometric DOFs in aLIGO.	136
6-5	Fractional power build-up inside the power-recycling cavity as a func- tion of the recycling mirrors' misalignment.	139
6-6	The DARM cavity frequency f_d as a function of the misalignment of the signal recycling mirrors.	140
6-7	Requirements on the alignment of the Michelson DOF.	141
7-1	Model for the alignment feedback control.	144
7-2	Typical pitch noise input to the aLIGO arm cavities.	145
7-3	Fractional power build-up in the arm cavities as a function of arm misalignments.	146
7-4	CARM to DARM cross-coupling at different levels of misalignment.	147
7-5	Control filters currently used for stabilizing the differential-hard mode's alignment in pitch.	148
7-6	The closed-loop residual pitch motion of the differential-hard mode.	149

7-7	The signal flow diagram illustrating the Sidles-Sigg effect.	153
7-8	The resonant frequency of the radiation-pressure-modified pendulum as a function of input power.	156
7-9	The radiation-torque-modified pendulum transfer functions at different levels of input power.	157
7-10	The signal flow diagram in the presence of both radiation-torque and digital control.	159
7-11	The diagram illustrating the compensation scheme for the Sidles-Sigg radiation torque.	161
7-12	The implementation of the compensation scheme for the Sidles-Sigg effect in aLIGO.	163
7-13	Comparing the modeled and measured open-loop transfer functions of the hard loops.	164
7-14	Sensing noise from the radiation-pressure-compensation path.	166
7-15	Applying the basic perturbation model to the radiation-compensation system.	166
7-16	Error tolerance of the radiation-torque-compensation system.	169
7-17	The diagram illustrating the $dP/d\theta$ radiation pressure feedback. . . .	170
7-18	Two scenarios that the $dP/d\theta$ effect may lead to the observed instabil- ities in the $0.4 - 0.6$ Hz band.	171
7-19	The open-loop transfer function of the soft mode and its error tolerance.	173
7-20	The performance of the length-to-angle feedforward subtraction mea- sured locally with the optical levers.	176
7-21	The performance of the length-to-angle feedforward subtraction mea- sured with global alignment signals.	177
7-22	Sensing noise level of alignment loops.	178
7-23	The generic form of the mixed sensitivity problem.	179
7-24	Weighting functions used for the \mathcal{H}_∞ design.	182
7-25	The open-loop transfer function SK of the hard modes in pitch. . . .	183

7-26	The residual motion of the hard loop using the controller designed with the \mathcal{H}_∞ method.	184
8-1	The response of the AS_RF36 signal to SRM misalignments.	187
8-2	Decomposition of the AS_RF36_I signal.	188
8-3	The response of the AS_RF72 signal to SRM misalignments.	191
8-4	Decomposition of the AS_RF72_I signal.	191
8-5	The optical response of DARM at different SRM tunings.	193
8-6	The SRCL error signal as a function of the inverse of extra ITMX thermal lens.	194
8-7	The optical response of DARM at different interferometer configurations.	195
9-1	Proposed sensitivity for LIGO-LF and its noise budget.	199
9-2	Inertial sensor noise for aLIGO and the requirement for LIGO-LF.	200
9-3	The residual pitch motion of aLIGO and LIGO-LF.	202
9-4	The detection range and the expected detection rate for LIGO-LF.	205
9-5	Comparing the parameter-estimation posteriors obtained with LIGO-LF and aLIGO.	208
9-6	Posterior distribution of the redshift.	209
9-7	Posterior distribution of the source-frame masses.	210
9-8	The cumulative uncertainty in localization as a function of frequency.	213
9-9	The uncertainty in measuring the phase shift due to resonant excitation of the NS r-mode as a function of the NS spin frequency.	216
9-10	SNR from the GW memory effect as a function of the source-frame total mass.	218
C-1	Fractional difference between different methods of calculating the tidal coupling coefficient.	243
F-1	LIGO-LF's suspension thermal noise from different stages.	252
F-2	The noises due to scattering in the arm tubes and in the vertex.	254

List of Tables

3.1	Parameters of the background NS models.	53
4.1	Parameters of the background NS and HS models.	78
4.2	Eigenfrequencies and gravitational waveform phase shift for the lowest order g-modes.	89
4.3	Threshold distance out to which dynamical tide resonances are de- tectable assuming a single merger event.	93
4.4	Measurement errors found by stacking events for different detectors and values of f_a and $\delta\phi_a$	97
5.1	Parameters of the aLIGO optics in the third observing run.	103
5.2	Lengths in aLIGO's central cavities.	109
6.1	Spot sizes on the aLIGO mirrors in [mm].	125
6.2	One-way Gouy phases of aLIGO cavities.	126
F.1	Summary of the LIGO-LF suspension parameters	251

Chapter 1

Introduction

The study of compact objects – white dwarfs, neutron stars (NSs), and black holes (BHs) – is a major area of research in modern astrophysics. The extreme conditions in the vicinity and interior of these objects extend far beyond anything achievable in terrestrial laboratories, and consequently pose a rich opportunity to confront cutting-edge theories with observations.

Of particular interest to this Thesis is the physics of NSs. NSs are created in the aftermath of the gravitational collapse of the core of a massive star ($> 8 M_{\odot}$; [Lattimer & Prakash 2004](#)). With a typical mass of $1.4 M_{\odot}$ and a radius of ~ 10 km, the central density of a NS can be as high as $\sim 10^{15} \text{ g cm}^{-3}$, 5 times the nuclear saturation density. The equation of state (i.e., the relation between pressure and density) at such supranuclear densities is one of the major unknown in fundamental physics (for reviews, see, e.g., [Lattimer 2012](#); [Özel & Freire 2016](#)). The many-body interactions that govern matter at extreme densities remain poorly constrained by first principle calculations ([Drischler et al., 2016](#)). Meanwhile, our understanding on laboratory nuclei is largely based on matters with nearly equal number of neutrons and protons, whereas a NS has only a few percent of protons. Consequently, large uncertainties exist in extrapolating the properties of laboratory nuclei to NS matter.

Nevertheless, breakthroughs in modern astrophysical theories and observations have begun to shed light onto our understanding of the physics of cold, ultradense matter. By combining the equation of state with the general relativistic structural

equations (the Tolman-Oppenheimer-Volkov equations [Tolman 1934](#); [Oppenheimer & Volkoff 1939](#)), we can predict the a NS mass-radius relation. This, in turn, allows us to use the observed NS masses and radii to place constraints on the equation of state at supranuclear densities. While the mass of a NS can be accurately measured by tracking its orbital motion through the arrival times of the observed pulsations ([Özel & Freire, 2016](#)), the precise measurement of a NS’s radius is challenging. One approach of measuring NS radii is to utilize the thermonuclear (type-I) X-ray bursts in low-mass X-ray binaries. Due to the binary’s close proximity and the strong gravity of the NS, mass is transferred from the companion to the NS. As the accreted layer reaches a critical mass, it ignites explosively, heating the entire surface of the NS and release a sudden burst of X-rays ([Fujimoto et al., 1981](#); [Bildsten, 1998](#); [Strohmayer & Bildsten, 2003](#)). The spectrum of an X-ray burst is dominated by a thermal component, which allows us to infer the effective temperature during the burst and thus the flux at the NS’s surface. Then, by combining the observed flux and the distance to the source we can deduce the radius of the NS. This approach has been predominantly used to study the cooling tails of bursts ([van Paradijs, 1979](#)).

For a subset of the bursts, the luminosity reaches the Eddington limit where the radiation force exceeds the gravitational force and consequently lifts the photosphere off of the NS surface. The study of such photospheric radius expansion bursts has its unique significance. In part, this is because one can relate the flux at the moment when the photosphere touches back down to the stellar surface to the Eddington limit, which helps to break the degeneracies between mass and radius introduced by general relativistic effects ([Özel & Psaltis, 2009](#)). Moreover, [Weinberg et al. \(2006\)](#) suggested that during strong bursts, freshly synthesized heavy elements may be dredged up to close to the photosphere by convection and eventually exposed by the subsequent super-Eddington wind. If an atomic transition line can be identified, we can further infer the surface gravity of the NS by comparing the observed transition wavelength to the one measured in terrestrial laboratories. Detection of heavy elements also provides constraints on the nucleosynthesis which is of interests to its own right ([Parikh et al., 2014](#)). On the observation side, the recent launch of the *Neutron Star Inte-*

rior Composition Explorer (*NICER*, [Gendreau & Arzoumanian 2017](#)) is expected to deliver unprecedentedly high quality of data on photospheric radius expansion X-ray bursts as *NICER* has its sensitivity band extends to as low as 0.2 keV.

Consequently, I will devote Chapter 2 to a theoretical modeling of type-I X-ray bursts with photospheric radius expansions. We will use MESA [Paxton et al. \(2011, 2013, 2015\)](#) to study the time-dependent burning, the convective and radiative heating of the atmosphere during the burst rise, and the launch and evolution of the optically thick radiation-driven wind as the photosphere expands outward to radii $r_{\text{ph}} \gtrsim 100$ km. We show that ashes of nuclear burning are ejected in the wind and dominate the wind composition for bursts that ignite at column depths $\gtrsim 10^9$ g cm $^{-2}$. Moreover, we find that after ≈ 1 s the wind composition transitions from mostly light elements (^4He and ^{12}C), which sit at the top of the atmosphere, to mostly heavy elements ($A > 40$), which sit deeper down. This may explain why the photospheric radii of all superexpansion bursts show a transition after ≈ 1 s from a superexpansion ($r_{\text{ph}} > 10^3$ km) to a moderate expansion ($r_{\text{ph}} \sim 50$ km).

Beyond the traditional observations using electromagnetic radiations, the operation of Advanced LIGO (aLIGO, [Aasi et al. 2015](#)) opens up an entirely new window for us to study the physics of compact objects via gravitational waves (GWs). During the inspiral of a binary NS (or a NS-BH) system, the NS is deformed by its companion’s gravitational field. This allows the energy to be transferred from the orbit to the star and thus enhances the orbital decay rate. As a result, the tidal interaction induces a phase shift in the GW waveform relative to the point-particle one. By measuring such a phase shift, one can in turn infer the NS’s radius and consequently the underlying equation of state ([Flanagan & Hinderer, 2008](#)). Indeed, for the first GW detection of the merger of a NS binary ([Abbott et al., 2017c](#)), an analysis on the tidal interaction has been performed and it has led to valuable estimations on the radii of the two NSs in the system ([Abbott et al., 2018b](#)).

The study above focused on the equilibrium tide which accounts for the large-scale distortion of the NS and has a relatively large phase shift in the GW waveform of ~ 1 rad. While it provides powerful constraints on the bulk properties of the NS such

as the pressure-density relation, it probes the NS composition only indirectly and is insensitive to the state of matter in the core. On the other hand, the superfluidity expected at the core of a cold NS exhibits a rich array of science (Graber et al., 2017) and determining the composition at the supranuclear densities remains an open question to be answered. It thus renders the dynamical tide, especially the resonant excitation of NS g-modes, a particularly appealing topic to consider (Andersson & Ho, 2018). The g-modes are NS oscillation modes supported by the star’s internal buoyancy due to composition gradients (Reisenegger & Goldreich, 1992). Furthermore, in a normal-fluid NS, the buoyancy is due to gradients in the proton-to-neutron fraction, whereas in a superfluid NS it is due to gradients in the muon-to-electron fraction (Kantor & Gusakov, 2014). The latter yields a significantly stronger stratification and leads to a denser spectrum of g-modes with frequencies above 10 Hz. Consequently, the g-modes probes directly both the interior composition and the state of matter in the core of a NS.

In Chapter 3 we carry out the first study combining the NS superfluidity with dynamical tidal interactions in the context of coalescing NS binaries. We show that as a consequence of the stronger stratification in the superfluid NS than in a normal-fluid one, there will be three to four times more g-modes undergo resonant tidal excitation as a NS binary sweeps through the bandwidth of GW detectors such as aLIGO. We find that $\simeq 10$ times more orbital energy is transferred into g-mode oscillations if the NS has a superfluid core rather than a normal-fluid core. However, because this energy is transferred later in the inspiral when the orbital decay is faster, the accumulated phase shift in the gravitational waveform is comparable for a superfluid and a normal fluid NS ($\sim 10^{-3} - 10^{-2}$ rad).

We further extend the study of g-modes in Chapter 4 by allowing for hyperons in the core. While the discovery of $2 M_{\odot}$ NSs (Demorest et al., 2010; Antoniadis et al., 2013) ruled out many NS models involving hyperons, new hyperonic equations of state have been proposed in recent years that are compatible with observations (see, e.g., Gusakov et al. 2014). Hyperon gradients give rise to a new type of composition g-mode. Compared to g-modes due to muon-to-electron gradients, those due to hyperon

gradients are concentrated much deeper in the core and therefore probe higher density regions. We find that the phase shifts due to resonantly excited hyperonic modes are $\sim 10^{-3}$ rad, an order of magnitude smaller than those due to muonic modes. We further show in the Chapter that by stacking events, third-generation GW detectors should be able to detect the phase shifts due to muonic modes. Such a detection will further provide direct constraints on the NS superfluidity¹ and the abundance of charged particles.

As the study of NS physics, as well as other high-energy phenomena involving compact objects with short orbital periods, depends critically on the performance of current and future GW detectors, we will devote the rest of the Thesis to discuss topics on improving the sensitivity and robustness of aLIGO and its potential upgrades. In Chapter 5 we provide an overview of aLIGO and derive how different optical fields propagate in the interferometer. This Chapter is intended to be pedagogical so that future researchers can learn techniques for analyzing the responses of complex optical systems such as aLIGO.

To keep aLIGO at its proper operational point, all the optical elements need to be properly controlled not only in length but also in alignment. Therefore, in Chapter 6 we will discuss how one can sense and control the angular motions both in a generic resonant cavity and in the specific case of aLIGO. The alignment control in aLIGO's 4-km-long arm cavities is particularly challenging. This is because to increase the shot-noise-limited sensitivity, we need to increase the amount of optical power circulating in the arm cavities (Buonanno & Chen, 2001). The designed circulating power for aLIGO reaches nearly 1 MW. Such a high power creates a radiation torque on the mirrors surpassing the restoring torque from the suspension pendulum, which, without carefully designed control system, can lead to various kind of instabilities and keep the instrument from operating. Consequently, we devote Chapter 7 to provide a comprehensive study on the alignment control of aLIGO's arm cavities. The

¹Page et al. (2011) and Shternin et al. (2011) have suggested observational evidences for the core superfluidity based on the rapid cooling of the NS in Cassiopeia A supernova remnant. However, systematic issues regarding the observation remain unsettled (Posselt et al., 2013). Therefore constraint based on tidal interactions would be of great interest as it has a completely different set of systematic uncertainties from X-ray observations.

discussion will be focused on the effects of radiation torques and the corresponding solutions, including both a newly implemented compensation system to cancel out the well-studied Sidles-Sigg effect (Sidles & Sigg, 2006), and a control design to suppress the $dP/d\theta$ effect realized only recently. In addition to the radiation torques, the power may also be absorbed by the mirrors, leading to thermal wavefront distortions. Some consequences of this effect is discussed in Chapter 8.

We introduce the LIGO-LF design in Chapter 9. It discusses the prospects on improving the sensitivity in the 5-30 Hz low-frequency band as well as the upgrade’s astrophysical applications. We show that with technologies currently under development, such as interferometrically sensed seismometers and balanced-homodyne read-out, LIGO-LF can reach the fundamental limits set by quantum and thermal noises down to 5 Hz. These technologies are also directly applicable to the future generation of detectors. We go on to consider this upgrade’s implications for the astrophysical output of an aLIGO-like detector. A single LIGO-LF can detect mergers of stellar-mass BHs out to a redshift of $z = 6$ and would be sensitive to intermediate-mass BHs up to $2000 M_{\odot}$. The detection rate of merging BHs will increase by a factor of 18 compared to aLIGO. Additionally, for a given source the chirp mass and total mass can be constrained 2 times better than aLIGO and the effective spin 3-5 times better than aLIGO. Furthermore, LIGO-LF enables the localization of coalescing binary NSs with an uncertainty solid angle 10 times smaller than that of aLIGO at 30 Hz and 4 times smaller when the entire signal is used. LIGO-LF also significantly enhances the probability of detecting other astrophysical phenomena including the tidal excitation of NS r-modes and the gravitational memory effects.

Chapter 2

Super-Eddington winds from type-I X-ray bursts

2.1 INTRODUCTION¹

Type I X-ray bursts are powered by unstable thermonuclear burning of accreted material on the surface of a NS in a low-mass X-ray binary (for reviews, see [Bildsten 1998](#); [Strohmayer & Bildsten 2006](#); [Galloway & Keek 2017](#)). The peak luminosity and duration of a burst depends primarily on the accretion rate and composition of the accreted material. In photospheric radius expansion (PRE) bursts, which comprise about 20% of all bursts ([Galloway et al., 2008](#)), the luminosity exceeds the Eddington luminosity and radiation forces drive an optically thick wind that lifts the photosphere off the NS surface. Typically, the photosphere moves out to radii $r_{\text{ph}} \approx \text{few} \times (10 - 100) \text{ km}$, although in a small fraction of PRE bursts, known as superexpansion bursts, $r_{\text{ph}} \gtrsim 10^3 \text{ km}$ ([in't Zand & Weinberg 2010](#); hereafter [iZW10](#)). As the emitting area of the photosphere increases, its temperature decreases below 1 keV, leading to a substantial loss of signal for detectors that lack sensitivity at low X-ray energies. Depending on the ignition depth and hence the total nuclear energy release, the entire PRE can last from seconds to minutes.

In order to reliably interpret observations of PRE bursts, it is important to un-

¹This Chapter is based-on [Yu & Weinberg \(2018\)](#).

derstand the dynamics of the wind. Three recent developments particularly motivate such a study: (i) the renewed effort to use PRE bursts to measure NS radii and thereby constrain the NS equation of state (see, e.g., [van Paradijs 1979](#); [Özel et al. 2010, 2016](#); [Steiner et al. 2010, 2013](#)), (ii) evidence of heavy-element absorption features in burst spectra, which might be imprints of ejected ashes of nuclear burning ([iZW10](#), [Barrière et al. 2015](#); [Iwai et al. 2017](#); [Kajava et al. 2017](#)), and (iii) the sensitivity of the *Neutron Star Interior Composition Explorer* (*NICER*; [Gendreau & Arzoumanian 2017](#)) down to 0.2 keV. This makes *NICER* an ideal instrument to study strong PRE bursts at high time resolution since, unlike the Proportional Counter Array (PCA; [Jahoda et al. 2006](#)) on board the *Rossi X-ray Timing Explorer* (*RXTE*), it does not lose signal when the temperature decreases during the expansion (see [Keek et al. 2018](#), who studied the first strong PRE burst detected with *NICER*).

Constraining NS radii with PRE bursts relies on measuring the flux when the temperature reaches a maximum. This is thought to be the moment when the photosphere “touches down” on the NS surface at the end of the PRE. By knowing the distance to a source and associating the touchdown flux with the Eddington flux, it is possible to constrain the NS radius R . However, the measurements may be subject to considerable systematic errors ([Boutloukos et al., 2010](#); [Steiner et al., 2010](#); [Suleimanov et al., 2011](#); [Miller, 2013](#); [Medin et al., 2016](#); [Miller & Lamb, 2016](#)). This is partly due to spectral modeling uncertainties, such as how the color-correction factor, which enters the fit to R , depends on luminosity and composition. Recently, there has been considerable effort to make progress on this front ([Suleimanov et al., 2011, 2012](#); [Medin et al., 2016](#)), including the study by [Nättilä et al. \(2015\)](#), who showed that the emergent spectra are sensitive to the abundance of heavy elements in the wind. There are also uncertainties associated with the dynamics of the PRE. For example, [Steiner et al. \(2010\)](#) found it necessary to relax the assumption that $r_{\text{ph}} = R$ at touchdown in order to avoid unphysical values of NS mass and radius when fitting to PRE burst data. A better understanding of the dynamics of the PRE and the wind composition could help address these uncertainties.

[Weinberg et al. \(2006; hereafter WBS\)](#) modeled the evolution of the atmosphere

during the rise of a PRE burst. However, they only considered times up to when the luminosity first reaches the Eddington luminosity; they did not study the dynamics of the subsequent PRE. Nonetheless, their calculations suggested that the wind could eject ashes of nuclear burning. This is because during the burst rise, there is an extensive convective region that is well mixed with ashes brought up from the burning layer below. Based on approximate energetic arguments, they estimated that the wind would be launched from a region that contains ashes and thereby expose them during (and after) the PRE. Since the ashes are primarily heavy elements (mass numbers $A \sim 30 - 60$; see, e.g., [WBS](#)), they could imprint absorption edges and lines on the burst spectra. A detection would probe the nuclear burning processes and might enable a measurement of the gravitational redshift of the NS. The latter possibility assumes that the heavy elements do not sink too quickly once the photosphere settles back to the NS surface at the end of the PRE; we will show that for deep ignitions there are very few light elements in the photosphere relative to which the ashes could sink, which suggests that the ashes may indeed linger on the surface.

Two superexpansion bursts detected with *RXTE* from 4U 0614+091 and 4U 1722-30 showed significant deviation from an absorbed blackbody ([iZW10](#)). By including an absorption edge in the spectral model, [iZW10](#) found that they could significantly improve the fits to the data. The energy of the fitted edges was consistent with the H-like photoionization edge of Ni and the optical depth of the edges suggested Ni mass fractions $X \gtrsim 0.1$. [Kajava et al. \(2017\)](#) detected similar features in the spectra of an *RXTE* burst from HETE J1900.1-2455. In *NuSTAR* observations of a burst from GRS 1741.9-2853, [Barrière et al. \(2015\)](#) detected, at a 1.7σ confidence level, a narrow absorption line at 5.46 ± 0.10 keV. They proposed that the line, if real, formed in the wind above the photosphere by a resonant $K\alpha$ transition from H-like Cr.

Although including heavy-element absorption features improved the fits to these bursts, the limited spectral resolution of the PCA on *RXTE* and the weakness of the *NuSTAR* spectral line preclude an unambiguous identification. The only high-spectral-resolution observations of PRE bursts from any source to date are six bursts detected with *Chandra* from 4U 1728-34 [Galloway et al. \(2010\)](#) and one from SAX

J1808.4-3658 observed simultaneously with *Chandra* and *RXTE* (in't Zand et al., 2013). No discrete features were detected in the spectra, although this might be because the radius expansions were all weak ($r_{\text{ph}} \approx 20$ km); the upper limits on the edge equivalent widths were a few hundred eV, comparable with the predictions of WBS.

All previous models of PRE assumed a steady-state wind (i.e., time-independent models). The first models were Newtonian (Ebisuzaki et al., 1983; Kato, 1983; Quinn & Paczynski, 1985; Joss & Melia, 1987) and then fully relativistic (Paczynski & Proszynski, 1986). By developing an improved treatment of radiative transfer, Joss & Melia (1987) constructed models that extended into the optically thin regions above the photosphere, where Compton scattering is important. These models all treated the wind mass-loss rate \dot{M}_{w} as a free parameter. Nobili et al. (1994) removed \dot{M}_{w} as a free parameter by including nuclear energy generation due to helium burning in the innermost regions of their model (their models were also relativistic and improved upon previous treatments of radiative transfer). However, most of the energy released from helium burning occurs within a few milliseconds, well before the wind is launched (WBS). We will show that in order to properly account for the driving of the wind, it is necessary to consider the transport of heat (by convection and radiative diffusion) through the hydrostatic layers between the ignition base and the wind base.

We find that it takes a few seconds for nearly time-independent conditions to be established in the wind (see also Table 1 in Joss & Melia 1987). Since most observed PREs only last for a few seconds, the steady-state assumption is often not well satisfied. This, and the recent developments discussed above, motivate a time-dependent calculation of the wind.

Once He ignites, the calculation can be divided into two time-dependent stages: a hydrostatic heating stage (the burst rise) followed by a hydrodynamic wind stage (the PRE phase). In the first stage, which we study in Section 2.2, the atmosphere above the helium burning layer is heated by convection and radiative diffusion. Initially, the radiative heat flux is sub-Eddington and the atmosphere adjusts hydrostatically.

During this time, freshly synthesized ashes are dredged up by convection and mixed throughout the growing convective region. As the atmosphere heats up, the radiative flux increases and eventually exceeds the local Eddington limit at the top of the atmosphere. This marks the beginning of the second stage, the PRE, which we study in Section 2.3. We show that as the photosphere expands outward, the base of the wind moves downwards to greater depths. First it blows away the top most layers of the atmosphere, which consists mostly of light elements. But gradually it digs into the deeper layers and ejects heavy-element ashes. In Section 2.4 we describe the observational signatures of the wind models and compare them with observed PRE bursts. Although our results are broadly consistent with observations, there are also some notable differences. We consider whether these might be attributed to some of our simplifying assumptions, including our neglect of general relativistic effects and our simplified treatment of radiative transfer, which relies on the diffusion approximation and neglects potential line-driving of the heavy elements. In Section 2.5 we summarize and conclude.

2.2 HYDROSTATIC BURST RISE

We model the hydrostatic portion of the burst rise with MESA (version 9575; Paxton et al. 2011, 2013, 2015). Our approach is similar to that of Paxton et al. (2011), who also used MESA to model the evolution of the hydrostatic layers during type I X-ray bursts. We assume that the NS has a mass $M = 1.4 M_{\odot}$ and radius $R = 10$ km and ignore corrections due to general relativity.

We assume pure He accretion (as in ultracompact X-ray binaries; in’t Zand et al. 2007) since bursts that ignite in a pure He layer have especially high luminosities and strong PREs. Systems that accrete H/He at mass accretion rates below $\approx 1\%$ of Eddington also ignite in a pure He layer and exhibit strong PREs (Bildsten, 1998; Cumming & Bildsten, 2000; Galloway & Keek, 2017). We assume that the atmosphere is always in local thermal equilibrium (LTE) and we model convection using mixing-length theory (MLT). During the hydrostatic phase, we set the top boundary at an

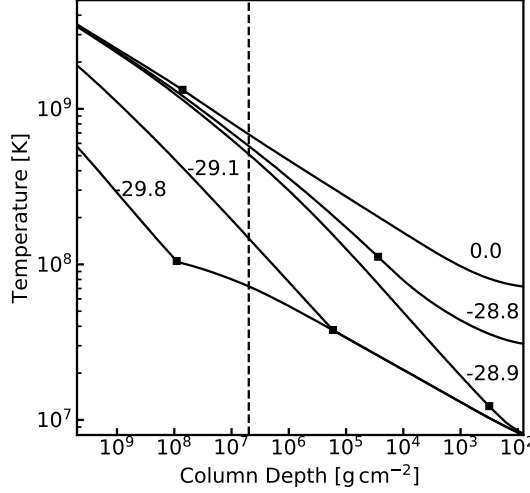


Figure 2-1: Temperature as a function of column depth for model y3n21 at different moments during the burst rise. The numbers label the time in milliseconds, with $t = 0.0$ corresponding to when L_{rad} first exceeds L_{Edd} . The squares indicate the top of the convective zone and the dashed vertical line indicates the maximum depth of the wind base y_{wb} during the PRE phase; material above this line will be ejected by the wind.

optical depth of $\tau = 100$ (during the wind phase we set the top boundary at a much smaller τ in order to capture the regions near the photosphere). By neglecting the shallower layers, we avoid numerical difficulties while still being able to accurately follow the nuclear burning and the atmosphere’s evolution. In the Appendix A, we provide our MESA inlist, which describes the setup we use in more detail.

During the hydrostatic phase, it is convenient to parameterize the vertical coordinate in terms of the column depth y , defined as $y(r) = \int_r^\infty \rho dr$, where ρ is the density and r is the radius. Since the atmosphere is geometrically thin and in hydrostatic equilibrium up until the wind launches, $y \simeq P/g \simeq M_r/4\pi R^2$, where P , g , and M_r are the pressure, gravitational acceleration, and mass above r , respectively. We simulate bursts for column depths at the ignition base ranging from $y_b = 3 \times 10^8 - 5 \times 10^9 \text{ g cm}^{-2}$. The value of y_b is controlled in MESA by varying the core luminosity and the accretion rate (the numerical settings are provided in the Appendix A; see Cumming 2003 and Paxton et al. 2011 for a detailed description of the ignition model). We will primarily show results for three representative values: $y_b = (0.5, 1.5, 5) \times 10^9 \text{ g cm}^{-2}$, which we

will denote as $(y1, y2, y3)$, respectively.

We consider two reaction networks²: a simple 9-isotope network (`basic_plus_fe56.net`) denoted by n9, and a more complete 21-isotope network (`approx21.net`, which is based on the 19-isotope network by [Weaver et al. 1978](#) with the extra inclusion of ^{56}Fe and ^{56}Cr) denoted by n21. We primarily show results for y1n21, y2n21, and y3n21, but will sometimes also show the n9 variants in order to illustrate how the size of the reaction network can impact the simulations.

In Sections 2.2.1 and 2.2.2 we describe, respectively, the thermal and compositional evolutions of the atmosphere during the rise. Since the results are similar to those of [WBS](#), we only describe the key features of the rise and refer the reader to that paper for additional details. It is worth noting, however, that they only consider relatively shallow ignition depths of $y_b = (3 - 5) \times 10^8 \text{ g cm}^{-2}$ compared to our $(3 - 50) \times 10^8 \text{ g cm}^{-2}$.

2.2.1 Evolution of the thermal profile

In Figure 2-1 we show the evolution of the thermal profile of model y3n21 during the burst rise³. As the base temperature T_b rises due to He burning, a convective zone forms and begins to extend outward to lower pressure (smaller y) on a timescale of $\sim 1 \text{ ms}$ (for y1n21 it is about 50 times longer). Initially, T_b rises so quickly that there is not enough time for the radiative layer above the convective zone to thermally adjust. As a result, the thermal profile in the radiative region is unchanged from the pre-ignition profile (see also [WBS](#), [Paxton et al. 2011](#)). This can be seen in Figure 2-1 at times $t < -28.9 \text{ ms}$, where $t = 0$ corresponds to when the wind turns on.

Over most of the convective zone, the convection is highly subsonic and efficient and the temperature profile very nearly follows an adiabat $T \propto y^n$, with $n \simeq 2/5$ (i.e., close to the adiabatic index of an ideal gas). In the overlying radiative region, the temperature profile is shallower and since the opacity varies only slightly with

²http://cococubed.asu.edu/code_pages/burn.shtml

³In the X-ray burst literature, y is usually plotted as increasing to the right. We plot it as increasing to the left in order to match the orientation of the wind structure figures shown later, which are often plotted in terms of the radial coordinate r , rather than y .

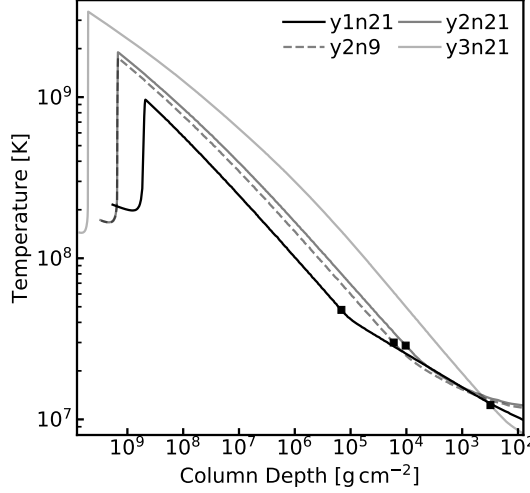


Figure 2-2: Temperature as a function of column depth for five of the burst models at the moment when their convective zones reach maximum extent. The squares indicate the top of the convective zone.

column depth, $T \propto y^{1/4}$.

Eventually, the top of the convective zone reaches low enough y that the local thermal timescale of the overlying radiative layer equals the heating timescale at the base. The radiative flux can then diffuse outward through the radiative region without being overtaken by the growing convective region. This flux begins to heat the radiative region and the convective zone gradually retreats downward to larger y (Figure 2-1 at $t > -28.9$ ms). As the radiative region heats up, the radiative luminosity L_{rad} in the shallower layers begins to approach the local Eddington limit

$$L_{\text{Edd}}(T) = \frac{4\pi cGM}{\kappa(T)}. \quad (2.1)$$

The opacity $\kappa(T)$ is dominated by electron scattering and is temperature-dependent due to Klein-Nishina (i.e., special relativistic) corrections. It varies approximately as (Paczynski 1983; MESA uses a more exact form)

$$\kappa(T) = \kappa_0 \left[1 + \left(\frac{T}{0.45 \text{ GK}} \right)^{0.86} \right]^{-1}, \quad (2.2)$$

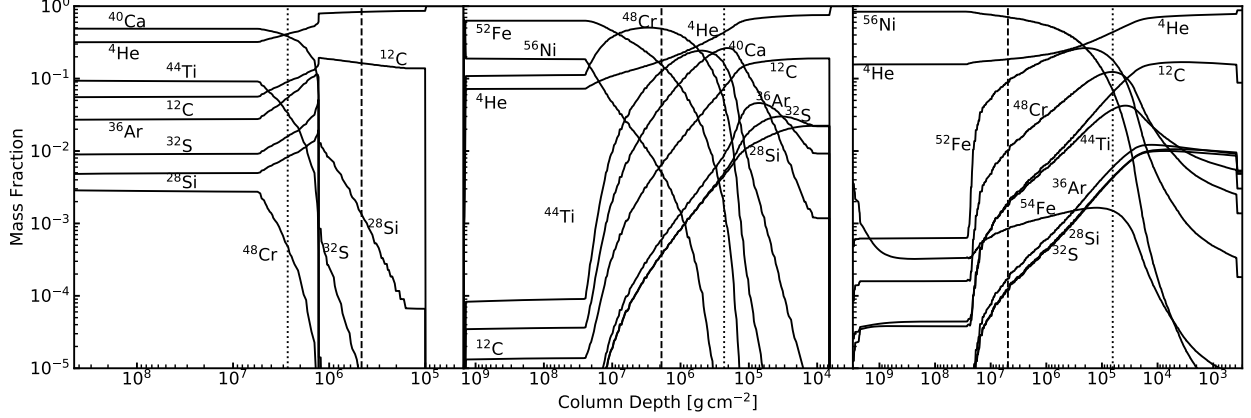


Figure 2-3: Composition as a function of column depth at the moment just before the wind launches for models y1n21 (left), y2n21 (middle), and y3n21 (right). The dashed vertical lines indicate y_{wb} , the maximum column depth of the wind base. The dotted vertical lines indicate y_{ash} , the location where the mass fraction of heavy elements ($A > 40$) equals 50%.

where $\kappa_0 \simeq 0.2(1 + X_H) \text{ cm}^2 \text{ g}^{-1}$ and X_H is the hydrogen mass fraction. Since κ is larger for smaller T , smaller y have smaller L_{Edd} . As a result, a given luminosity L can be sub-Eddington in the deep hotter layers, but becomes super-Eddington as the radiation diffuses upward into the shallow cooler layers (Ebisuzaki et al., 1983). Indeed, as we will show in the hydrodynamic simulations (see Section 2.3.1 and Figure 2-4b), the base of the wind is initially at small y , moves to larger y as the deeper layers heat up, and finally moves back outward to smaller y as the layers begin to cool.

We run the hydrostatic simulations until the moment the luminosity first exceeds the local Eddington limit (defined as $t = 0$). As can be seen in Figure 2-1, at $t = 0$ the convective zone has retreated and the atmosphere is almost fully radiative.

2.2.2 Pre-wind composition profile

As the convective zone extends outward, it efficiently mixes the ashes of burning up to lower column depths. The minimum column depth $y_{c,\text{min}}$ reached by the convective zone, and hence reached by the ashes of burning, is shown by the solid squares in Figure 2-2 for five of the burst models. For model y3n21, which has the deepest

ignition and thus the largest energy release, $y_{c,\min} \approx 10^3 \text{ g cm}^{-2}$, while for the other models, $y_{c,\min} \approx 10^4 - 10^5 \text{ g cm}^{-2}$ (consistent with [WBS](#)). We also see that a more complete reaction network (n21 compared to n9) results in slightly smaller $y_{c,\min}$ due to the increased energy release; comparing the y2 and y3 models, we find that this difference becomes more significant at larger ignition depths.

In [Section 2.3](#) we describe the time-dependent wind and show that the column depth of the wind's base $y_{\text{wb}} \gg y_{c,\min}$. As a result, ashes are ejected by the wind and exposed. In [Figure 2-3](#) we show the composition profiles of models y1n21, y2n21, and y3n21 at the end of the hydrostatic phase, just before the wind is launched. The dashed vertical lines indicate y_{wb} . At a given y , the composition is determined by the burning stage at the moment $y_c(t) = y$, where $y_c(t)$ is the location of the top of the retreating convective zone. For y1n21 ($y_b = 5 \times 10^8 \text{ g cm}^{-2}$), we see that the wind will be dominated by light elements, primarily ^4He with a small amount of ^{12}C . However, for y2n21 ($y_b = 1.5 \times 10^9 \text{ g cm}^{-2}$), the wind will be dominated by heavy elements such as ^{48}Cr and ^{52}Fe , while for models ignited at even deeper depths (y3n21; $y_b = 5 \times 10^9 \text{ g cm}^{-2}$) the wind will be primarily ^{56}Ni .⁴

2.3 HYDRODYNAMIC WIND

When the luminosity first exceeds the local Eddington limit L_{Edd} ([equation 2.1](#)), we stop the hydrostatic calculation. We use the last hydrostatic profile as the initial conditions for the time-dependent spherically symmetric hydrodynamic equations, which we integrate using MESA's implicit hydrodynamics solver. The MESA inlist for our hydrodynamic calculations is given in the [Appendix A](#). Since the atmosphere is almost fully radiative at this stage, we turn off MLT (see [Ro & Matzner 2016](#) and [Quataert et al. 2016](#) for a discussion of convective stability in radiation-driven winds).

⁴[Woosley et al. \(2004\)](#) found that bursts can dredge up the ashes of previous bursts. We do not include such ashes in our simulations and instead focus on newly synthesized elements. We therefore assume that for $y > y_b$, the composition is pure ^{56}Cr , the end product of the 21-isotope network. This ensures that the mass fractions of elements like ^{56}Ni and ^{54}Fe in the wind are not the result of having been dredged up by convection. We find that ^{56}Cr has a mass fraction of $10^{-4} - 10^{-3}$ for $y_b < y < y_{c,\min}$ due to dredge-up (not shown in [Figure 2-3](#)).

We include radiation in the diffusion approximation ($dT^4/dr = -3\kappa\rho L_{\text{rad}}/4\pi a c r^2$) and set the upper boundary at optical depth $\tau = 1$. We define the photospheric radius r_{ph} as the location where $L_{\text{rad}}/4\pi r_{\text{ph}}^2 = \sigma T^4$ (similar to Quinn & Paczynski 1985 and Paczynski & Proszynski 1986). In practice, we find that the optical depth at r_{ph} is $\tau = \int_{r_{\text{ph}}}^{\infty} \kappa \rho dr \approx 3$. Thus, for $r < r_{\text{ph}}$ the diffusion approximation and LTE should be valid. In the region between r_{ph} and the upper boundary of our grid ($\tau = 1$) deviations from LTE may occur, although we expect the photons and gas particles to still be well coupled (Joss & Melia, 1987). Nonetheless, our results should be treated as approximations of the true structure in this region (see the steady-state models of Joss & Melia 1987 and Nobili et al. 1994 for more detailed treatments of this region and the optically thin region above it). Finally, to account for the mass-loss at the top of our grid, we repeatedly remove the top layer of the atmosphere when its density drops below a threshold value of $10^{-14} \text{ g cm}^{-3}$ (by experimenting with different thresholds, we determined that the wind solution is not affected by this procedure).

We describe the evolution of the wind structure in Section 2.3.1. We compare our results with steady-state models in Section 2.3.2 and use these results in Section 2.3.3 to explain why the wind structure is not sensitive to ignition depth. Finally, in Section 2.3.4 we describe the composition of the wind.

2.3.1 Time-dependent wind profiles

In Figures 2-4a and 2-4b we show the temperature and luminosity as a function of both density and column depth at four different times during the hydrodynamic wind phase of model y2n21. The location where L_{rad} first exceeds L_{Edd} corresponds to the wind base. Note that L never exceeds L_{Edd} by more than a few percent, since any excess luminosity is used to expel matter to infinity (Ebisuzaki et al., 1983; Kato, 1983; Paczynski & Proszynski, 1986). At early times ($t = 0.07 \text{ s}$), the column depth of the wind base $y_{\text{wb}} \approx 10^4 \text{ g cm}^{-2}$. As the wind evolves during the next $\approx 10 \text{ s}$, the location where $L_{\text{rad}} > L_{\text{Edd}}$ moves to larger y and ρ and thus higher T , eventually reaching as far down as $y_{\text{wb}} \simeq 10^6 \text{ g cm}^{-2}$. By $t = 29 \text{ s}$, the NS surface layers have

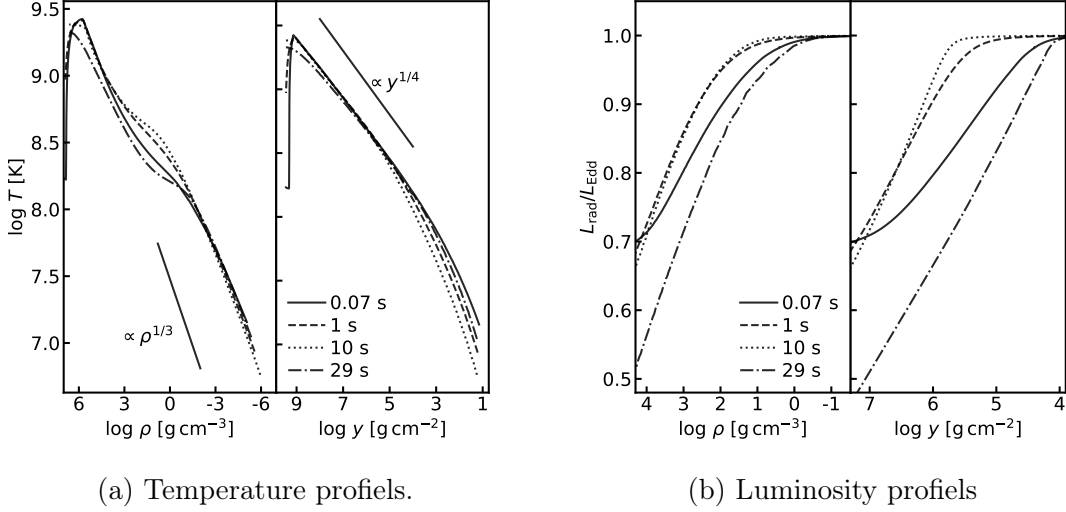


Figure 2-4: Temperature and luminosity $L_{\text{rad}}/L_{\text{Edd}}$ as a function of density and column depth for model y2n21 at different times during the wind phase.

cooled, y_{wb} has moved back to shallower depths, and the wind dies down. As we explain in Section 2.3.2, the profiles at depths greater than that of the wind base approximately follow power-law relations $T \propto \rho^{1/3} \propto y^{1/4}$. The $T \propto \rho^{1/3}$ relation also holds in regions sufficiently above the wind base.

In Figure 2-5 we show the wind structure of model y2n21 in more detail. We plot profiles as a function of r rather than y or ρ in order to more clearly reveal the structure of the tenuous outer regions of the wind out to $r \sim 10^3$ km. The open circles indicate the location of the photosphere r_{ph} . We see that there is a large radius expansion, with the photosphere reaching a maximum of $r_{\text{ph}} \simeq 200$ km (see also Figure 2-11). The pluses indicate the location of the isothermal sonic point, defined as the radius where the velocity satisfies $v^2 = kT/\mu m_p$, where μ is the mean molecular weight and m_p is the proton mass (see, e.g., Quinn & Paczynski 1985; Joss & Melia 1987); the equilibrium sonic point where $v^2 = dP/d\rho$ occurs at $\tau < 1$ and is thus beyond our simulated region.

As the wind gains strength during the first 10 seconds, the mass-loss rate \dot{M}_{w} , temperature, density, and optical depth all increase throughout the wind. The velocity, which never exceeds $\sim 0.01c$, decreases during this time, since $\dot{M}_{\text{w}} \simeq 4\pi r^2 \rho v$ only

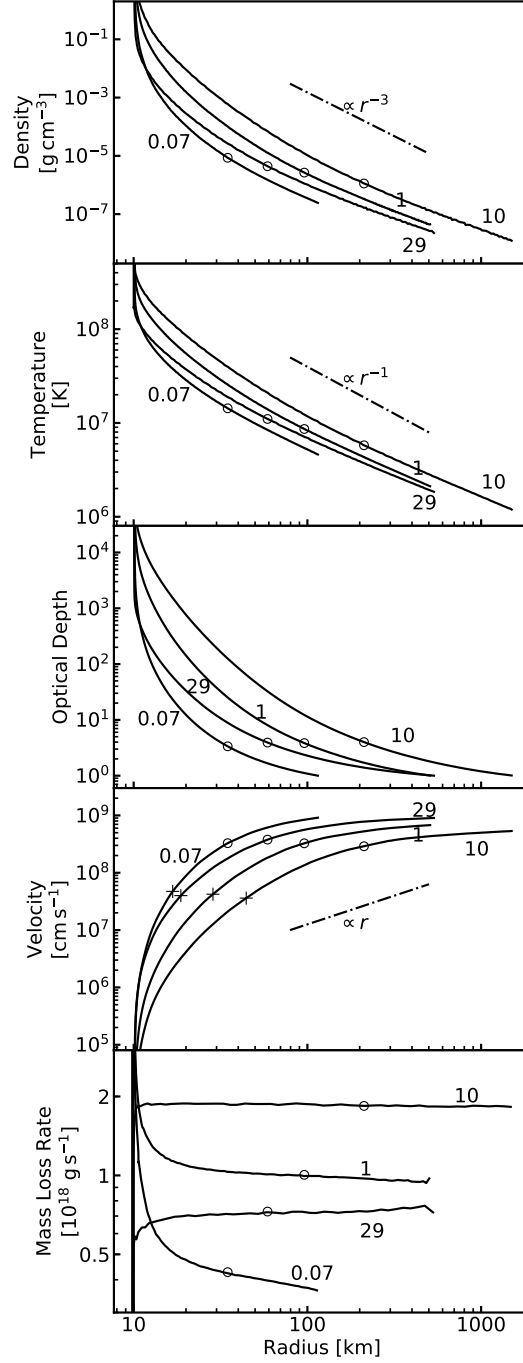


Figure 2-5: Radial profiles of the wind structure at different times for model y2n21. The numbers mark the time (in seconds) since wind onset. Each curve is terminated at the location where the optical depth $\tau = 1$. The circles indicate the location of the photosphere r_{ph} . In the velocity-radius plot (fourth panel), the pluses indicate the location of the isothermal sonic point.

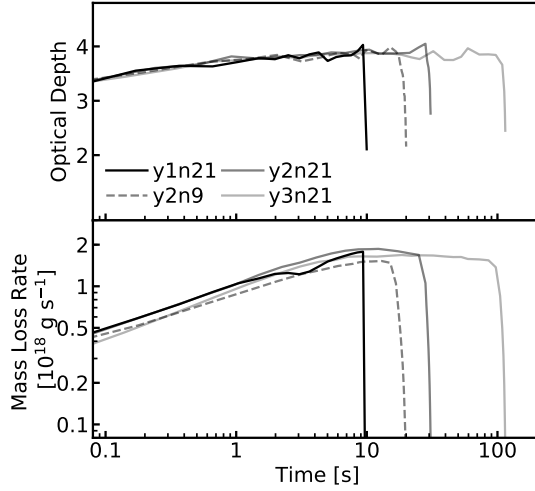


Figure 2-6: Optical depth (top panel) and mass-loss rate (bottom panel) at the photosphere as a function of time for four of the burst models.

changes by order unity whereas ρ increases significantly. At $t \simeq 10$ s the wind settles into a steady state and for the next ≈ 15 s the profiles change very little. For model y2n21, $\dot{M}_w \simeq 2 \times 10^{18} \text{ g s}^{-1}$ at its maximum. By $t = 29$ s, the energy and mass supply have dwindled and \dot{M}_w decreases. As a result, the temperatures and densities drop and the photosphere begins to fall back to the NS surface.

We find that aside from differences in duration, the wind profiles of our other burst models are all similar to that of model y2n21 despite the significant range of ignition depth. This is because the wind structure is largely determined by \dot{M}_w (Kato, 1983; Quinn & Paczynski, 1985; Paczynski & Proszynski, 1986), and the different models all have very similar $\dot{M}_w(t)$ up until the wind terminates. We illustrate this in the bottom panel of Figure 2-6 for four of the models. In Section 2.3.3, we explain why \dot{M}_w is a weak function of y_b .

In the top panel of Figure 2-7 we show the ratio of the total mass ejected by the wind M_{ej} at the end of the PRE to the accreted mass $M_{\text{accr}} \simeq 4\pi R^2 y_b$. We find

$$\eta \equiv \frac{M_{\text{ej}}}{M_{\text{accr}}} \simeq 2.5 \times 10^{-3} \quad (2.3)$$

almost independent of y_b . Burst energetics set an upper bound of $\eta \lesssim 8 \times 10^{-3}$, which

is given by the ratio of the nuclear energy release per nucleon $\simeq 1.6 \text{ MeV nucleon}^{-1}$ (i.e., the difference in binding energy between ^4He and ^{56}Ni) to the gravitational binding energy per nucleon $GM/R \simeq 200 \text{ MeV nucleon}^{-1}$. The value $\eta \simeq 2.5 \times 10^{-3}$ implies that $\approx 30\%$ of the nuclear energy goes to unbinding matter from the NS, independent of ignition depth.

2.3.2 Comparison with steady-state models

Since the flow is subsonic at radii smaller than the equilibrium sonic point (which is located at an optical depth $\tau < 1$), the structure throughout the modeled region is nearly in hydrostatic equilibrium at each instant. Therefore, the evolution approximately follows a sequence of steady-state solutions (i.e., quasi-static profiles) determined by the instantaneous $\dot{M}_w(t)$. Indeed, our profiles are qualitatively similar to those of steady-state wind models in which \dot{M}_w is treated as a free parameter (Ebisuzaki et al., 1983; Kato, 1983; Paczynski & Proszynski, 1986; Joss & Melia, 1987). In steady-state, the time-dependent terms vanish and the mass, momentum, and energy equations are

$$\dot{M}_w = 4\pi r^2 \rho v = \text{constant}, \quad (2.4)$$

$$v \frac{dv}{dr} = -\frac{1}{\rho} \frac{dP}{dr} - g, \quad (2.5)$$

$$\dot{E}_w = \dot{M}_w \left(\frac{v^2}{2} - \frac{GM}{r} + h \right) + L_{\text{rad}} = \text{constant}, \quad (2.6)$$

where \dot{E}_w is the energy-loss rate of the wind, $h = (U + P)/\rho$ is the enthalpy, and U is the energy density. Over a large region between the wind base and the equilibrium sonic point, we find that $dP/dr \simeq -\rho g$, radiation pressure dominates so that $P \propto T^4$ and $h \simeq 4P/\rho$, and $L_{\text{rad}}(r \gg R) \simeq L_{\text{Edd},0} \simeq \dot{E}_w$, where $L_{\text{Edd},0} = 4\pi cGM/\kappa_0$. Together these imply that over this region $P \propto \rho^{4/3}$ and the fluid behaves as if it has an adiabatic index $\gamma = 4/3$, as also noted by Kato (1986).⁵ As a result, $\rho \propto r^{-3}$,

⁵Although the photon diffusion time $t_{\text{diff}} \simeq r^2 \kappa \rho / c$ is much shorter than the advective time $t_{\text{adv}} \simeq r/v$, and thus heat flows in and out of a fluid element, the entropy profile of the wind is nearly constant over a large region (Kato, 1986).

$T \propto r^{-1}$, and $v \propto r$, as shown in Figures 2-4a and 2-5 (see also figure 5 in Paczynski & Proszynski 1986).

Given that $\rho \propto r^{-3}$, the optical depth $\tau \simeq \tau^*/2$, where $\tau^* = \kappa \rho r$ is the effective optical depth used in the steady-state wind calculations of Quinn & Paczynski (1985) and Paczynski & Proszynski (1986). In Figure 2-6 we show that at the photosphere $\tau \simeq 3.5$ nearly independent of time and ignition model, which is comparable to the values found by Quinn & Paczynski (1985) and Paczynski & Proszynski (1986).

Since L_{rad} is much larger than the kinetic power, X-ray burst winds are in the opposite regime from massive star winds, which Quataert et al. (2016) studied. Their analytic steady-state model is therefore not directly applicable here. More recently, Owocki et al. (2017) derived semi-analytic steady-state wind solutions that bridge the two regimes. Although we have not attempted to implement their solutions, they should be applicable to the steady-state regime of PRE bursts.

2.3.3 Dependence of wind structure on ignition depth

The duration of the wind increases with ignition depth y_b , but its structure is nearly independent of y_b . This is because $\dot{M}_w(t)$, which effectively sets the wind structure (see, e.g., Kato 1983; Paczynski & Proszynski 1986), depends only weakly on y_b . We can understand this weak dependence by appealing to energy conservation, assuming a steady-state wind. Just above the base of the wind ($r_{\text{wb}} \simeq R$), the enthalpy and kinetic energy are small compared to the binding energy, and by equation (2.6)

$$\dot{E}_w \simeq -\frac{GM\dot{M}_w}{R} + L_{\text{rad}}(r_{\text{wb}}), \quad (2.7)$$

where $L_{\text{rad}}(r_{\text{wb}}) \simeq 4\pi cGM/\kappa_{\text{wb}}$, i.e., the Eddington luminosity at the wind base, with $\kappa_{\text{wb}} = \kappa [T(r_{\text{wb}})]$. At $r \gg R$, the flow of mechanical energy is small compared to L_{rad} , and

$$\dot{E}_w \simeq L_{\text{rad}}(r \gg R) \simeq \frac{4\pi cGM}{\kappa_0}, \quad (2.8)$$

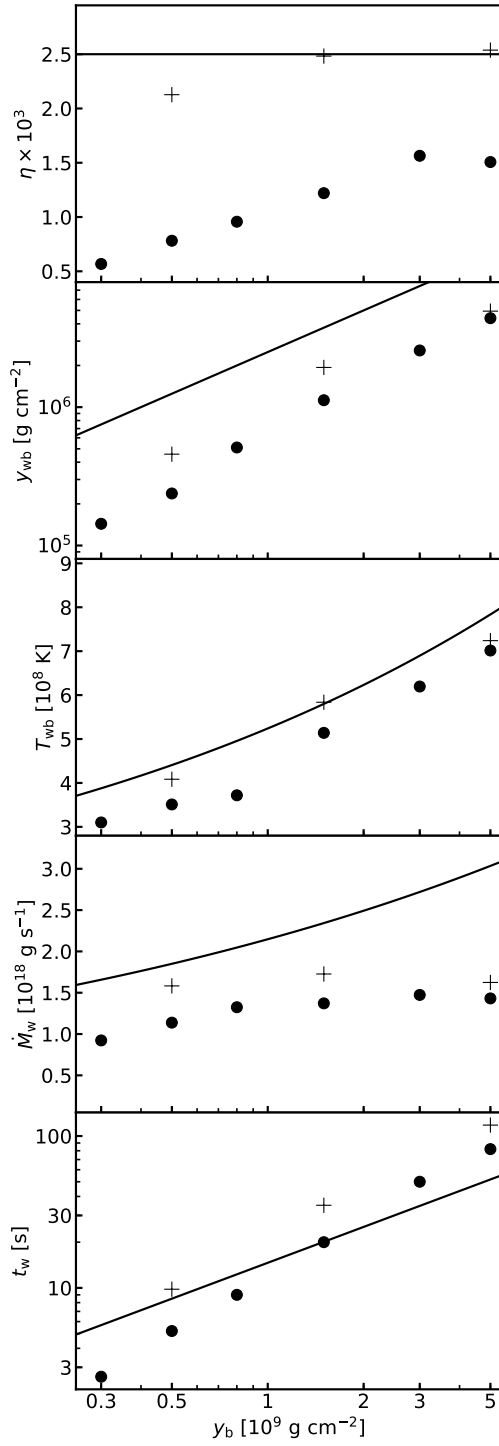


Figure 2-7: Bulk properties of the wind as a function of ignition column depth y_b . The plus (circle) symbols are from numerical simulations using the 21-isotope (9-isotope) network. The y_{wb} , T_{wb} , and \dot{M}_w panels give the values during the approximate steady-state wind phase. The curves are the analytic approximations described in the text.

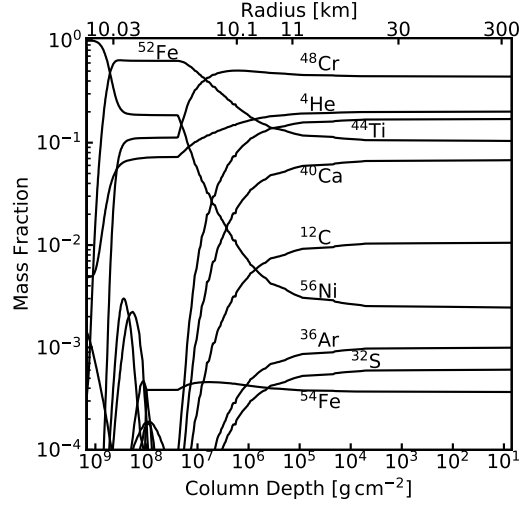


Figure 2-8: Composition of the wind as a function of column depth (bottom axis) and radius (top axis) at $t = 10$ s for model y2n21. The wind is in a near steady state by this time.

where the last equality follows because the luminosity at large r only slightly exceeds the local Eddington limit. During the steady state, \dot{E}_w is constant throughout the wind, and we can equate equations (2.7) and (2.8) to find

$$\dot{M}_w \simeq \frac{4\pi cR}{\kappa_0} \left[\frac{\kappa_0}{\kappa_{wb}} - 1 \right] \simeq \frac{4\pi cR}{\kappa_0} \left(\frac{T_{wb}}{0.45 \text{ GK}} \right)^{0.86} \quad (2.9)$$

(Paczynski & Proszynski 1986 derive a similar expression). We now show that T_{wb} (and hence \dot{M}_w) is a weak function of y_b by first estimating the peak temperature at the ignition base $T_b(y_b)$ and then relating T_b to T_{wb} .

The base temperature T_b rises until it becomes radiation-pressure-dominated, which lifts the degeneracy and stifles the burning (Fujimoto et al., 1981; Bildsten, 1998). At its maximum,

$$T_b \simeq f \left(\frac{3gy_b}{a} \right)^{1/4} \simeq 2.3 y_{b,9}^{1/4} \text{ GK}, \quad (2.10)$$

where $y_{b,9} = y_b/10^9 \text{ g cm}^{-2}$ and at $f = 1$ radiation pressure completely dominates. In the numerical expression here and below we set $f = 0.8$ based on our numerical calculations (see Figure 2-4a and also iZW10). During the wind phase, the bound

layers are fully radiative and satisfy $T \propto y^{1/4}$. When the wind is at its peak strength, $y_{\text{wb}} \simeq \eta y_{\text{b}}$ and $T_{\text{wb}} \simeq \eta^{1/4} T_{\text{b}}$, where η is given by equation (2.3). We thus find

$$y_{\text{wb}} \simeq 2.5 \times 10^6 y_{\text{b},9} \text{ g cm}^{-2}, \quad (2.11)$$

$$T_{\text{wb}} \simeq 0.5 y_{\text{b},9}^{1/4} \text{ GK}, \quad (2.12)$$

where here and below we set $\eta = 2.5 \times 10^{-3}$ (see top panel of Figure 2-7). In practice, this leads to a slight overestimate of y_{wb} since η is determined by the total ejected mass at the end of the burst and therefore $\eta \gtrsim y_{\text{wb}}/y_{\text{b}}$. Plugging equation (2.12) into equation (2.9), we find that during the approximate steady-state phase

$$\dot{M}_{\text{w}} \simeq 2.1 \times 10^{18} y_{\text{b},9}^{0.22} \text{ g s}^{-1}. \quad (2.13)$$

As we show in Figure 2-7, this estimate agrees reasonably well with the wind simulation results (the simulations show a somewhat smaller \dot{M}_{w} and an even weaker y_{b} dependence). We thus see that \dot{M}_{w} and therefore the wind structure is nearly independent of y_{b} .

Given \dot{M}_{w} , we can estimate the wind duration

$$t_{\text{w}} = \frac{M_{\text{ej}}}{\dot{M}} = 15 y_{\text{b},9}^{0.79} \text{ s}. \quad (2.14)$$

This compares well with the numerically calculated value of the total wind duration, shown in the bottom panel of Figure 2-7. The latter is slightly larger because equation (2.13) overestimates \dot{M}_{w} , especially near the beginning and end of the wind.

2.3.4 Ejection of heavy elements

In Figure 2-8 we show the wind composition as a function of radius (top axis) and column depth (bottom axis) for model y2n21 at $t = 10 \text{ s}$; by this time, the wind has settled into a steady state. We find that the wind at that time is dominated by heavy-element ashes, particularly ^{48}Cr , ^{44}Ti , and ^{52}Fe , whose mass fractions are

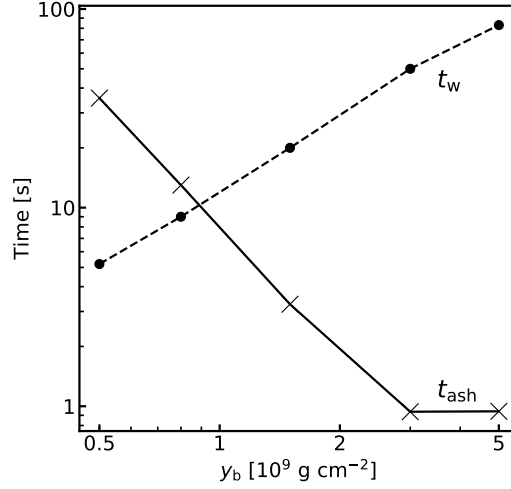


Figure 2-9: Timescale to expose the heavy-element ashes t_{ash} (crosses) and the duration of the wind t_w (circles) as a function of ignition column depth y_b . The t_w points are from the n9 models (see also the bottom panel of Figure 2-7). For clarity, we connect the points with straight lines.

about 0.5, 0.2 and 0.1, respectively. Comparing with the pre-wind profile, we see that this is the material that initially resided at a column depth $y \simeq 10^6 \text{ g cm}^{-2}$ (see dashed vertical line in middle panel of Figure 2-3). This is because $\dot{M}_w \approx 10^{18} \text{ g s}^{-1}$ and thus after $t = 10 \text{ s}$, the wind has ablated the surface layers down to a depth $\dot{M}_w t / 4\pi R^2 \approx 10^6 \text{ g cm}^{-2}$.

An interesting feature of the pre-wind profile is that for deep ignitions ($y_{b,9} = 1-5$) the column depth at which the composition transitions from mostly light to mostly heavy elements is almost a constant value of $y_{\text{ash}} \approx 10^5 \text{ g cm}^{-2}$. In Figure 2-3 we indicate y_{ash} with a vertical dotted line, where we formally define y_{ash} as the location where the total mass fraction of elements with mass number $A > 40$ equals 0.5 (for $y < y_{\text{ash}}$, the elements consist predominantly of ^4He and ^{12}C). We can then define the timescale to expose the heavy ashes

$$\begin{aligned}
 t_{\text{ash}} &= \frac{4\pi R^2 y_{\text{ash}}}{\dot{M}_w} \\
 &\simeq (1.3 \text{ s}) \left(\frac{y_{\text{ash}}}{10^5 \text{ g cm}^{-2}} \right) \left(\frac{10^{18} \text{ g s}^{-1}}{\dot{M}_w} \right).
 \end{aligned} \tag{2.15}$$

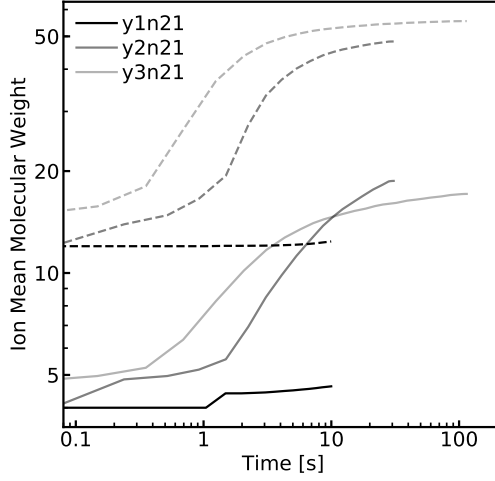


Figure 2-10: Ion mean molecular weight (solid lines) at the photosphere as a function of time. The dashed lines show the result with ${}^4\text{He}$ excluded from the sum over ions.

In Figure 2-9 we plot t_{ash} as a function of y_b . Starting from $y_{b,9} = 0.5$, we find that t_{ash} first decreases sharply as y_b increases, but then for $y_{b,9} \gtrsim 3$ it plateaus at $t_{\text{ash}} \simeq 1$ s. This is because y_{ash} plateaus at $y_{\text{ash}} \approx 10^5 \text{ g cm}^{-2}$, while \dot{M}_w depends very weakly on y_b (see Section 2.3.3). In Section 2.4.2, we describe how this might explain a feature of superexpansion bursts.

In Figure 2-10 we show a related result: the ion mean molecular weight $\mu_{\text{ion}} = (\sum_i X_i/A_i)^{-1}$ at the photosphere as a function of time, where X_i and A_i are the mass fraction and mass number of element i . For reference, a mixture consisting of 50% ${}^4\text{He}$ and 50% ${}^{56}\text{Ni}$ has $\mu_{\text{ion}} = 7.5$. For the y2n21 and y3n21 models, it takes a few seconds for μ_{ion} to increase above 7.5, agreeing well with the t_{ash} estimate. Note that for $t > 10$ s, the y3n21 model has a smaller μ_{ion} than the y2n21 model. This is because a larger amount of ${}^4\text{He}$ is left unburned in y3n21 than in y2n21.⁶ To illustrate this effect, the dashed lines in Figure 2-10 show the ion mean molecular weight excluding ${}^4\text{He}$. The value for the y3n21 model approaches 56 since it is dominated by ${}^{56}\text{Ni}$ while the y2n21 model approaches 48 since it is dominated by ${}^{48}\text{Cr}$.

⁶Hashimoto et al. (1983) showed that for He burning at constant pressure, the mass fraction of unburned ${}^4\text{He}$ increases with increasing pressure for $P \gtrsim 10^{22} \text{ erg cm}^{-3}$ (see their figure 10). The pressure at the base of the burning layer $P_b \simeq g y_b \approx 10^{23} y_{b,9} \text{ erg cm}^{-3}$ is nearly constant during a burst.

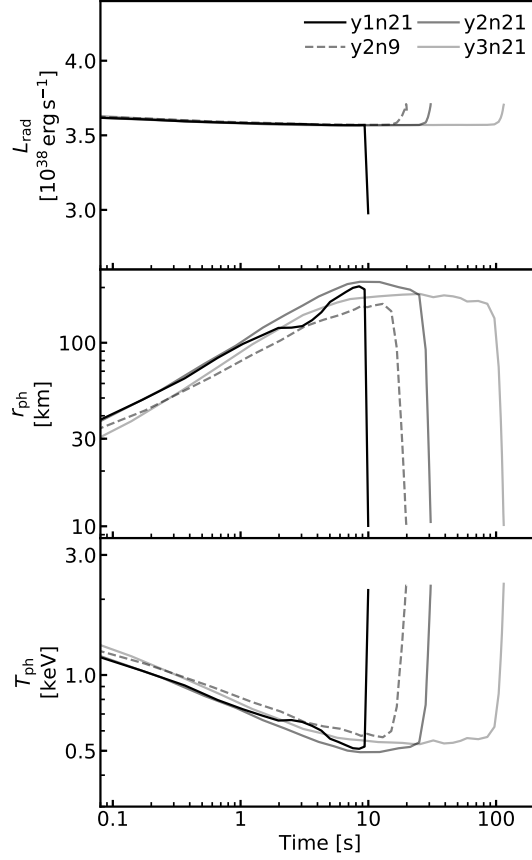


Figure 2-11: Evolution of the bolometric luminosity L_{rad} at the photosphere, the photospheric radius r_{ph} , and the photospheric temperature T_{ph} , for four different models.

2.4 OBSERVATIONAL SIGNATURES

By evaluating quantities at the photosphere of our wind models, we calculate theoretical burst light curves and spectroscopy (Section 2.4.1) and then compare our results to observed PRE bursts (Section 2.4.2).

2.4.1 Burst spectroscopy and light curve

In Figure 2-11 we show the evolution of the bolometric luminosity, photospheric radius r_{ph} , and photospheric temperature T_{ph} , for different ignition models (these are related by $L_{\text{rad}} = 4\pi r_{\text{ph}}^2 \sigma T_{\text{ph}}^4$). Depending on the ignition depth, the PRE phase lasts from $\simeq 5$ s to $\simeq 100$ s (see equation 2.14), during which the bolometric luminosity

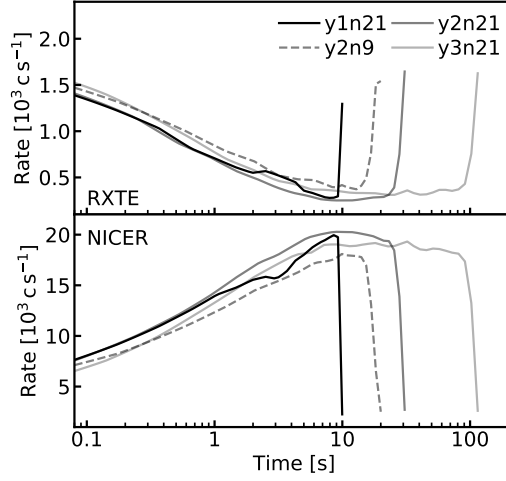


Figure 2-12: Photon count rate as a function of time assuming a source at a distance of 10 kpc. The upper panel assumes a *RXTE*-PCA-like detector, and the lower panel assumes a *NICER*-like detector.

is nearly constant at $L_{\text{rad}} \simeq L_{\text{Edd}}$. Initially, all the models follow similar tracks: from $t = 0$ s to $t \approx 3$ s, the photosphere expands from 10 km to $\gtrsim 100$ km and the temperature $T_{\text{ph}} \propto r_{\text{ph}}^{-1/2}$ drops from about 2 to 0.5 keV. Due to the larger nuclear energy release, the deeper ignition models expand outward for longer and reach slightly larger radii (150 – 200 km). Furthermore, unlike model y1n21, which shows a fairly abrupt contraction after reaching maximum expansion, models y2n21 and y3n21 have a long, approximately steady phase during which r_{ph} remains near its maximum for $\simeq 20$ s and $\simeq 90$ s, respectively. Comparing models y2n9 and y2n21, we see that the latter expands faster and reaches a larger maximum r_{ph} because it has a more complete reaction network and thus a larger energy release.

In Figure 2-12 we show the approximate count rate that *RXTE*-PCA and *NICER* would detect for a source located at a distance of 10 kpc. We assume a blackbody spectrum and use our calculation of $L_{\text{rad}}[r_{\text{ph}}(t)]$ and $T_{\text{ph}}(t)$ to estimate the count rate integrated over the effective area of the detector. For *RXTE*-PCA, we take the effective area from [Jahoda et al. \(2006\)](#) and assume that two out of the five proportional counting units are working, as was typical during its operations ([iZW10](#)).

For *NICER* we adopt the effective area given on the mission website⁷. The effective collecting area of *RXTE*-PCA decreases significantly below 2 keV and therefore its count rate drops during a PRE, as the spectrum shifts to lower T_{ph} . By contrast, the effective collecting area of *NICER* remains large down to 0.3 keV and its count rate actually increases during a PRE. Moreover, since $T_{\text{ph}} \lesssim 1$ keV throughout the PRE, the *NICER* count rate is always significantly larger than *RXTE*'s (note the different scales in Figure 2-12). Both of these effects have been reported in the *NICER* observation of 4U 1820-30 (Keek et al., 2018).

In Section 2.3.4 we showed that the wind ejects heavy elements synthesized during the burst. These ejected ashes include ^{48}Cr , ^{44}Ti , and ^{56}Ni at mass fractions $X \gtrsim 0.1$. WBS showed that the expanded photosphere is sufficiently cool that heavy elements such as these will bind with electrons and imprint significant photoionization edges on the burst spectra. However, they assumed that the wind base is located at $y_{\text{wb}} = 0.01y_{\text{b}}$ whereas our calculations explicitly determine $y_{\text{wb}}(t)$ and show that $y_{\text{wb}} \approx \text{few} \times 10^{-3}y_{\text{b}}$ at its maximum (see Figure 2-7). WBS estimated that during the PRE the edges should have equivalent widths $\text{EW} \sim 0.1$ keV. Using their approach for estimating the edge strengths and the abundances from our wind calculation, we also find $\text{EW} \sim 0.1$ keV during the PRE for bursts with $y_{\text{b}} \gtrsim 5 \times 10^8 \text{ g cm}^{-2}$.

2.4.2 Comparison to observed PRE bursts

Our $r_{\text{ph}}(t)$ results are broadly consistent with observations of PRE bursts, although there are some notable differences. According to iZW10, the vast majority ($\gtrsim 99\%$) of PRE bursts have photospheres that do not expand beyond 10^3 km (the exceptions are superexpansion bursts, which we discuss below). This is consistent with our result that $r_{\text{ph}} \sim 100$ km nearly independent of ignition depth. There are weak PREs with maximum r_{ph} that are only a factor of a few larger than R (Galloway et al., 2008). These PREs may be weaker because they are igniting in mixed H/He layers, and thus by assuming a pure He layer our simulations do not capture this population.

One of the most well sampled measurements of $r_{\text{ph}}(t)$ is from the recent burst

⁷<https://heasarc.gsfc.nasa.gov/docs/nicer/>

detected with *NICER* from 4U 1820-30 (Keek et al., 2018). This source is an ultracompact X-ray binary (UCXB) that is thought to be accreting He-rich material (Cumming, 2003). As Figure 2-12 illustrates, *NICER* is ideally suited to follow the entire PRE phase of bursts due its sub-keV sensitivity. Keek et al. (2018) found that the entire PRE phase lasts $\simeq 3$ s and reaches a maximum expansion radius $r_{\text{ph}} = 190 \pm 10$ km. These are consistent with the duration and expansion radius of our y1n21 model ($y_b = 5 \times 10^8 \text{ g cm}^{-2}$).

On the other hand, the temporal variation of the count rate and r_{ph} of the 4U 1820-30 burst look somewhat different from our y1n21 model (compare Figure 3 in Keek et al. 2018 and our Figures. 2-11 and 2-12). The observed expansion timescale at the start of the PRE is only $\simeq 0.1$ s compared to our $\simeq 1$ s. Also, after reaching maximum expansion, the observed photosphere falls back to the NS surface somewhat more slowly than ours (over $\simeq 3$ s compared to $\simeq 1$ s). A possible explanation for why our expansion is too slow and contraction is too fast is that we ignore general relativistic effects. Paczynski & Proszynski (1986) showed that at small \dot{M}_w , relativistic models predict a larger r_{ph} than Newtonian models (see their figures 10 and 11). For example, at $\dot{M}_w \simeq 4 \times 10^{17} \text{ g s}^{-1}$ we find $r_{\text{ph}} \simeq 35$ km (see Figure 2-5 at $t = 0.07$ s) whereas Paczynski & Proszynski (1986) find $r_{\text{ph}} \simeq 100$ km. (The difference is much smaller at $\dot{M}_w \gtrsim 10^{18} \text{ g s}^{-1}$ and thus our maximum r_{ph} should be reasonably accurate). As a result, our simulations probably underestimate r_{ph} at the small \dot{M}_w that applies near the start and end of the PRE, which would mean we underestimate (overestimate) the rate of expansion (contraction).

Superexpansion bursts ($r_{\text{ph}} > 10^3$ km) provide another interesting point of comparison. According to iZW10, there have been 32 superexpansion bursts detected from 8 sources (of these, 22 were from 4U 1722-30). Of the superexpansion bursts that have been identified with an object (7 out of 8), all are from candidate UCXBs. The neutron star in an UCXB accretes hydrogen-deficient fuel and the bursts tend to be longer (several tens of minutes rather than seconds, i.e., intermediate duration bursts; in't Zand et al. 2005; Cumming et al. 2006). In two superexpansion bursts observed with *RXTE*, iZW10 detected strong absorption edges. The edge energies

and depths are consistent with large abundances of iron-peak elements and support our finding that the wind can eject significant amounts of heavy-element ashes.

Superexpansion bursts always show two distinct phases: a superexpansion phase during which $r_{\text{ph}} \gtrsim 10^3 \text{ km}$, followed by a moderate expansion phase during which $r_{\text{ph}} \sim 30 - 50 \text{ km}$ and $L_{\text{rad}} \simeq L_{\text{Edd}}$ (iZW10). Interestingly, the duration of the superexpansion phase is always a few seconds, independent of the ignition depth y_{b} . By contrast, the duration of the moderate expansion phase ranges from short ($\approx 10 - 100 \text{ s}$) for $y_{\text{b}} \sim 10^9 \text{ g cm}^{-2}$ to intermediate ($\gtrsim 10^3 \text{ s}$) for $y_{\text{b}} \sim 10^{10} \text{ g cm}^{-2}$. iZW10 speculated that the superexpansion phase always lasts a few seconds because it corresponds to a transient stage in the wind’s development. In this stage, they argue, a shell of initially opaque material is ejected to large radii by the sudden onset of super-Eddington flux deep below the photosphere. Within a few seconds the expanding shell reaches such large radii ($> 10^3 \text{ km}$) that it becomes optically thin and the observer suddenly sees the underlying photosphere of the already formed steady-state wind, which is located at $r_{\text{ph}} \sim 30 - 50 \text{ km}$. According to this picture, this marks the onset of the moderate expansion phase, whose duration equals that of the steady-state wind and thus correlates with y_{b} (see Equation 2.14).

We do not, however, see evidence of a shell ejection in our simulations. This might be because our treatment of radiative transfer in the low optical depth regions ($\tau \lesssim 3$) is too simplistic, because we ignore relativistic effects, or because of unaccounted for dynamics during the transition from the hydrostatic rise to the hydrodynamic wind (e.g., in’t Zand et al. 2014 reported two bursts with exceptionally short precursors, which they argue may indicate a detonation initiated by the rapid onset of the $^{12}\text{C}(p, \gamma)^{13}\text{N}(\alpha, p)^{16}\text{O}$ reaction sequence). However, there is a feature in our simulations that suggests an alternative explanation for why the superexpansion phase always lasts a few seconds, regardless of y_{b} . As we described in Section 2.3.4, the timescale t_{ash} to expose heavy elements in the wind is also a few seconds, and plateaus at $t_{\text{ash}} \simeq 1 \text{ s}$ for $y_{\text{b}} \gtrsim 3 \times 10^9 \text{ g cm}^{-2}$. It suggests that the transition from superexpansion to moderate expansion after $\approx 1 \text{ s}$ might be due to the wind’s composition changing from light to heavy elements (and not due to shell ejection). As

discussed in [iZW10](#), the heavy elements will only be partially ionized and the radiative force acting on the bound electrons above the photosphere will be $\gtrsim 100$ times larger than the force acting on the free electrons. Line-driving in the outer parts of the wind may therefore boost the outflow velocity. By mass conservation (equation 2.4), this would decrease the overlying density and bring the photosphere inward to smaller radii. This could explain why the photosphere transitions from very large r_{ph} during the superexpansion (when the ejecta are mostly light elements) to smaller values of $r_{\text{ph}} \sim 30 - 50$ km during the moderate expansion, and why the timescale for such transitions is always a few seconds. Evaluating this in detail likely requires accounting for line-driving in the wind.

2.5 SUMMARY AND CONCLUSIONS

We presented spherically symmetric MESA models of PRE bursts, starting from the hydrostatic burst rise through the hydrodynamic wind phase. We used both a 9-isotope and a 21-isotope reaction network to follow the burning of pure He ignition layers with base column depths $y_b = 3 \times 10^8 - 5 \times 10^9 \text{ g cm}^{-2}$, corresponding to that of short through intermediate duration PRE bursts. Convection during the burst rise mixes the ashes of nuclear burning out to $y \lesssim 10^4 \text{ g cm}^{-2}$ for $y_b \gtrsim 10^9 \text{ g cm}^{-2}$. As the atmosphere heats up, L_{rad} increases and eventually exceeds L_{Edd} , resulting in a radiation-driven wind. Initially, the wind base is located at small column depths but it moves inward to $y_{\text{wb}} \gtrsim 10^6 \text{ g cm}^{-2}$ in a few seconds. As a result, the wind initially ejects mostly light elements (^4He and ^{12}C) but after ≈ 1 s it begins to eject heavy elements, which for $y_b = 1.5(5) \times 10^9 \text{ g cm}^{-2}$ consists mostly of ^{48}Cr (^{56}Ni).

The wind duration t_w increases almost linearly with y_b , lasting from a few seconds to more than 100 s for the considered range of y_b . All y_b show similar wind evolution during the first few seconds: a mass-loss rate that increases to a maximum $\dot{M}_w \simeq 1 - 2 \times 10^{18} \text{ g s}^{-1}$, a photospheric radius that expands out to $r_{\text{ph}} \simeq 100 - 200$ km, and a photospheric temperature that decreases to $\lesssim 0.5$ keV. After the first few seconds, the wind either abruptly dies down (small y_b) or it blows steadily for the next ≈ 100 s

(large y_b). We found that the wind ejects $\approx 0.2\%$ of the total accreted mass, nearly independent of y_b , which corresponds to $\approx 30\%$ of the nuclear energy release being used to unbind matter from the NS surface.

Based on the calculated wind composition, we estimated that the ejected heavy elements should imprint photoionization edges on the burst spectra with equivalent widths of $\sim 0.1\text{ keV}$ for bursts with $y_b \gtrsim 10^9\text{ g cm}^{-2}$. This supports the evidence of heavy-element absorption features detected in some PRE bursts (iZW10, Barrière et al. 2015; Iwai et al. 2017; Kajava et al. 2017) and encourages efforts to catch strong PRE bursts with high-spectral-resolution telescopes such as *Chandra* and *XMM-Newton*.

We showed that our results are broadly consistent with various aspects of observed PRE bursts. In particular, many PRE bursts show maximum photospheric radii $r_{\text{ph}} \sim 100\text{ km}$, photospheric expansion velocities $v_{\text{ph}} \sim 100\text{ km s}^{-1}$ during the start of the PRE, and PRE durations $t_w \sim 1 - 100\text{ s}$. However, we also described some notable differences between our models and observed PRE bursts, which we argued might be because we did not account for general relativistic effects and neglected possible line-driving of heavy elements. Models that solve the relativistic, time-dependent wind equations and adopt a more sophisticated treatment of radiative transfer are needed. This includes relaxing the assumption of LTE and the diffusion approximation in the outer parts of the wind and using composition-dependent opacities that account for bound-free and bound-bound transitions, as well as Compton scattering. Such improvements would allow for a more complete understanding of PRE bursts and might help inform PRE-based measurements of NS radii.

Chapter 3

Resonant tidal excitation of superfluid neutron stars in coalescing binaries

3.1 INTRODUCTION¹

Advanced LIGO’s detection of the merger of binary black holes heralds a new age of gravitational-wave (GW) astronomy ([Abbott et al., 2016c,d](#)). Coalescing binary neutron star (NS) systems ([Abbott et al., 2017c](#)) and NS-black hole systems are another promising source for ground based GW detectors such as Advanced LIGO, Advanced Virgo, and KAGRA (respectively, [Harry 2010](#); [Acernese et al. 2015a](#); [Somiya 2012](#)). The rich array of science that their detection might deliver (for a recent review see [Baiotti & Rezzolla 2017](#)) includes the exciting prospect of constraining the enigmatic supranuclear equation of state from measurements of the tide-induced phase shift of the GW signal ([Read et al., 2009](#); [Hinderer et al., 2010](#); [Damour et al., 2012](#); [Lackey et al., 2012](#); [Lackey & Wade, 2015](#); [Agathos et al., 2015](#)).

The linear tidal response of the NS can be decomposed into an equilibrium tide and a dynamical tide. The equilibrium tide accounts for the quasi-static, large scale

¹This Chapter is based on [Yu & Weinberg \(2017a\)](#)

distortion of the star and the dynamical tide accounts for the internal modes of oscillation that are resonantly excited as the orbit decays and sweeps up in frequency. While most recent studies focus on the impact of the equilibrium tide on the GW signal (including all the references listed at the end of the previous paragraph), there is also an extensive literature studying the impact of the linear dynamical tide. [Lai \(1994\)](#) and [Reisenegger & Goldreich \(1994\)](#) considered non-rotating normal fluid NSs, where the resonant modes are g-modes with frequencies $\lesssim 100$ Hz. They found that the excited g-modes only weakly affect the GW signal (phase shifts of $\lesssim 10^{-2}$ radian; see also [Shibata 1994](#); [Kokkotas & Schafer 1995](#)). Subsequent studies accounted for rotation and found that a rapidly rotating NS could have a much stronger tidal response, resulting in phase shifts of ~ 0.1 to $\gg 1$ radian ([Ho & Lai, 1999](#); [Lai & Wu, 2006](#); [Flanagan & Racine, 2007](#)). However, this requires a spin frequency \gtrsim a few $\times 100$ Hz, which is larger than is thought to be likely for a NS in a coalescing binary ([Brown et al., 2012](#)). Most recently, [Hinderer et al. \(2016\)](#) developed an effective-one-body waveform model that accounts for the resonant response of the high frequency f-modes. They found that in some cases the f-mode contribution to the phase shift might be as much as $\approx 30\%$ of the total tidal effect.

All of these studies assumed a normal fluid NS. However, because the NSs in coalescing binaries are expected to be cold, the core neutrons will be a superfluid ([Yakovlev et al., 1999](#); [Lombardo & Schulze, 2001](#)). The source of buoyancy that provides the restoring force for g-modes is fundamentally different for normal fluid and superfluid NSs. In a normal fluid NS, a perturbed fluid element is buoyant due to gradients in the proton-to-neutron fraction ([Reisenegger & Goldreich, 1992](#)). However, in a superfluid NS the neutrons within the fluid element can flow past the protons and gradients in their relative abundance no longer provides buoyancy. Indeed, studies that assume a zero temperature superfluid NS composed only of neutrons, protons, and electrons (and not muons) find that such stars do not support g-mode oscillations (e.g., [Lee 1995](#); [Andersson & Comer 2001](#); [Prix & Rieutord 2002](#)).²

²The focus here is on g-modes supported by composition gradients. At finite temperatures, thermal gradients are also a source of buoyancy ([Gusakov & Kantor, 2013](#)). However, for the cold NSs in coalescing binaries, thermal gradients make a negligible contribution to the total buoyancy ([Pas-](#)

More recently, [Kantor & Gusakov \(2014\)](#) showed that when the presence of muons is taken into account, there is a new source of buoyancy in the core: the gradient in the muon-to-electron fraction. Thus, a cold superfluid NS does support core g-modes when we extend the model to include a richer chemical composition.

Since the source of buoyancy is different, the g-modes of a superfluid NS are different from the g-modes of a normal fluid NS. In particular, [Kantor & Gusakov \(2014\)](#) showed that the stratification is considerably stronger in a superfluid NS, i.e., the Brunt-Väisälä frequency is larger (see also [Passamonti et al. 2016](#)). As a result, the entire g-mode spectrum is shifted to higher frequencies, including the $l = 2$ g-modes that are resonantly excited by the tide. We will show that a superfluid NS has more than ten $l = 2$ g-modes with frequency > 50 Hz whereas a normal fluid NS has only two or three such modes. This means that there are many more g-modes that undergo resonant excitation as the binary sweeps through the bandwidth of ground-based detectors such as LIGO. Moreover, the nature of the tidal coupling is different in a superfluid NS since the tide forces not one but two fluids (the neutron superfluid and the normal fluid consisting of the charged particles). The purpose of our study is to account for these superfluid effects and thereby extend previous calculations of the dynamical tide in NS binaries.

The plan of the paper is as follows: in Section [3.2](#) we describe our background superfluid NS model and discuss the source of buoyancy in more detail. In Section [3.3](#) we describe tidal driving in superfluid NSs beginning with a calculation of the stellar eigenmodes. In Section [3.4](#) we present the main result of our study, the calculation of the GW phase shift induced by the resonant excitation of g-modes. In Section [3.5](#) we summarize and conclude.

3.2 SUPERFLUID NEUTRON STAR MODEL

We construct our background superfluid NS models using an approach that is similar to that of [Prix & Rieutord \(2002\)](#) except that we account for the existence of muons

samonti et al., [2016](#)).

in the core. This is an important distinction since, as already mentioned in the introduction and described further in Section 3.2.1, the muon-to-electron composition gradient provides the buoyancy that supports g-modes in the core.

We assume an NS composed of neutrons (n), protons (p), electrons (e) and muons (μ), and adopt the SLy4 equation of state for baryons (Rikovska Stone et al., 2003), while treating the leptons as relativistic degenerate Fermi gas. Since an NS in a coalescing binary is expected to be cold ($T \ll 10^8$ K), we neglect thermal effects (we set $T = 0$) and assume that the neutrons in the core are superfluid. In the crust, taken to be the region with baryon density $n_b < 0.1 \text{ fm}^{-3}$, we treat all species of particles as normal fluid matter for simplicity, which is consistent with the treatment in Kantor & Gusakov (2014; see also Dommes & Gusakov 2016). In order to simplify the calculation of the oscillation modes (Section 3.3), we neglect rotation and use Newtonian equations throughout our analysis including, for consistency, in constructing the background hydrostatic models. Corrections to the stellar and mode structure due to general relativistic effects are expected to be at the level of $GM/(Rc^2) \sim 20\%$, where M and R are the mass and radius of the NS. Such corrections are unlikely to change the overall conclusions of our study. We assume all charge densities are strictly balanced and neglect all electrodynamic effects (including proton superconductivity, plasma oscillations, and magnetic fields). We also neglect vortex-tension and vortex pinning of superfluid neutrons, as is appropriate for the macroscopic description of fluid flow that is of interest here. For a more detailed discussion of these effects and the underlying assumptions, we refer the reader to Prix & Rieutord (2002) and references therein.

Given the above simplifications, we can describe the NS as consisting of two fluids: a normal fluid of charged particles (protons, electrons, and muons) and a superfluid of neutrons whose flow drifts through the normal fluid flow. We indicate the fluid variables of the charged (neutron) flow with a subscript c (n). The dynamics of the flow depends on the total internal energy density of the cold superfluid, which is given

by (Prix & Rieutord, 2002).

$$d\varepsilon_{\text{tot}} = \sum_{j=\text{npe}\mu} \mu_j dn_j + \alpha dv_{\text{r}}^2, \quad (3.1)$$

where n_j and μ_j are particle j 's number density and chemical potential, respectively, with j being one of n, p, e, or μ . The quantity \mathbf{v}_{r} is the relative velocity between the normal fluid (charged) flow and the superfluid (neutron) flow,

$$\mathbf{v}_{\text{r}} = \mathbf{v}_{\text{c}} - \mathbf{v}_{\text{n}} \quad (3.2)$$

and α is the entrainment function (see below). The pressure of the fluid is given by

$$\begin{aligned} dP &= \sum_{j=\text{npe}\mu} n_j d\mu_j - \alpha dv_{\text{r}}^2 \\ &= \sum_{j=\text{npe}\mu} \rho_j d\tilde{\mu}_j - \alpha dv_{\text{r}}^2 \\ &= \rho_c d\tilde{\mu}_c + \rho_n d\tilde{\mu}_n - \alpha dv_{\text{r}}^2, \end{aligned} \quad (3.3)$$

where, for each particle species j , we define the mass density $\rho_j = \varepsilon_j/c^2$, the energy density ε_j (rest mass plus interaction/kinetic energy), the specific chemical potential $d\tilde{\mu}_j = d\mu_j/m_j$, and the (relativistic) mass $m_j = \rho_j/n_j$. In the third line we combined the protons, electrons, and muons together to represent our charged flow, with

$$\rho_c = \rho_p + \rho_e + \rho_\mu, \quad (3.4)$$

$$\rho_c d\tilde{\mu}_c = \sum_{j=\text{pe}\mu} \rho_j d\tilde{\mu}_j. \quad (3.5)$$

In Appendix B.1 we discuss these quantities in more detail and provide some additional thermodynamic relations that we use in our study.

The αdv_{r}^2 term characterizes the entrainment effect which, in the zero-temperature limit, is due entirely to the strong interaction between neutrons and protons. The

entrainment function α can be written as (Prix & Rieutord, 2002)

$$2\alpha = \rho_c \left[1 - \frac{m_p^*}{m_N} + O\left(\frac{\rho_c}{\rho}\right) \right], \quad (3.6)$$

where m_p^* is the proton effective mass and $\rho = \rho_n + \rho_c$ is the total mass density. Typical values of m_p^* are in the range $0.3 \leq m_p^*/m_N \leq 0.8$ (Sjöberg, 1976; Chamel, 2008). While in general m_p^* depends on density, for simplicity we consider models that have constant m_p^* throughout the star. As we will see later, tidal coupling depends only weakly on entrainment effects. It will also be useful to describe the entrainment in terms of the dimensionless entrainment functions

$$\epsilon_c = \frac{2\alpha}{\rho_c}, \quad \epsilon_n = \frac{2\alpha}{\rho_n}. \quad (3.7)$$

We discuss the entrainment function in more detail in Appendix B.2.

Using the above relations, we construct spherically symmetric background models by simultaneously solving the equation of hydrostatic equilibrium

$$\frac{dP}{dr} = -(\rho_n + \rho_c) \frac{d\Phi}{dr} \quad (3.8)$$

and chemical (beta) equilibrium

$$\mu_n = \mu_p + \mu_e, \quad (3.9)$$

$$\mu_e = \mu_\mu, \quad (3.10)$$

where $\Phi(r)$ is the gravitational potential and $\mu_e = \mu_\mu$ applies at radii where $\mu_e > m_\mu c^2$ (corresponding to $r < R_\mu$, where R_μ is the critical radius where muons first appear). Equations (3.3) and (3.8)-(3.10) imply

$$\frac{d\tilde{\mu}_n}{dr} = -\frac{d\Phi}{dr}. \quad (3.11)$$

We consider models with masses of $1.4 M_\odot$ and $2.0 M_\odot$ and various levels of entrain-

Table 3.1: Parameters of the background NS models.

$M [M_\odot]$	R [km]	$\rho_0 [10^{14} \text{ g cm}^{-3}]$	R_μ [km]	R_{cc} [km]
1.4	13.0	6.7	11.4	11.7
2.0	13.7	7.85	12.5	12.7

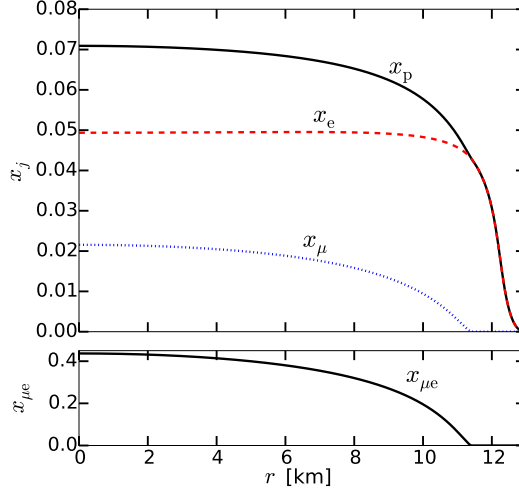


Figure 3-1: Number fraction of protons x_p (solid line), electrons x_e (dashed line), and muons x_μ (dotted line), as a function of radius r for our $1.4 M_\odot$ NS model. In the bottom panel we show the muon-to-electron ratio $x_{\mu e} = x_\mu/x_e$, which determines the buoyancy profile $\mathcal{N}(r)$ of the superfluid NS model.

ment. In Table 3.1 we give the following parameters of the hydrostatic structure: total mass M , radius R , central density ρ_0 , the radius below which muons are present R_μ , and the radius of the core-crust interface R_{cc} . Note that the radii and central density differ from the values in Rikovska Stone et al. (2003) because we solve the Newtonian hydrostatic equations instead of the general-relativistic equations. In Figure 3-1 we show the radial profile of the number fraction $x_j(r) = n_j/(n_p + n_n)$ of protons, electrons, and muons and the muon-to-electron ratio $x_{\mu e}(r) = x_\mu/x_e$ for the $1.4 M_\odot$ model (the profile of the $2.0 M_\odot$ model is very similar). We observe that the composition varies slowly with radius over most of the star but quickly drops to zero when the radius is close to the critical radius (note that at R_μ the muon number density goes to zero with a non-zero derivative).

3.2.1 Buoyancy in cold neutron stars

Because we assume a zero-temperature NS, composition gradients are the only possible source of buoyancy (i.e., the Ledoux convective stability criterion). First consider a normal fluid NS consisting of npe matter. In this case, the buoyancy force that supports the g-modes is due to the proton-to-neutron composition gradient (Reisenegger & Goldreich 1992; see also Lai 1994). To verify this, consider a fluid element in equilibrium with pressure P , proton number fraction x_p ($= x_e$ by charge neutrality), and density $\rho(P, x_p)$. If we adiabatically displace the element upwards against gravity by a distance dr , it will remain in near pressure equilibrium with the surroundings by contracting or expanding on a dynamical timescale (which is much shorter than the buoyancy oscillation timescale). However, its composition will still be x_p because the timescale to reach chemical equilibrium through weak interactions (which are responsible for changes to x_p) is much longer than the buoyancy timescale and because all species of particles within the element move at the same speed (Reisenegger & Goldreich, 1992). The convective stability criterion is therefore

$$\left(\frac{\partial \rho}{\partial x_p} \right)_P \left(\frac{dx_p}{dr} \right) < 0, \quad (3.12)$$

where the subscript P indicates the derivative is taken at constant pressure.

Now consider a superfluid NS consisting of only npe matter (no muons). The above stability criterion is no longer valid because the superfluid neutrons form a separate component that is free to drift through the charged components when the fluid element is displaced. This allows the fraction of superfluid neutrons within the element to always match the background (i.e., x_p is not fixed). As a result, there is no longer a source of buoyancy to support g-mode oscillations, as a number of studies have shown (see, e.g., Lee 1995; Andersson & Comer 2001; Prix & Rieutord 2002).

However, the situation changes again when we consider a superfluid NS consisting of npe μ matter. There are now three independent variables that parametrize the equation of state. As in Kantor & Gusakov (2014), we take these to be P , μ_n , and $x_{\mu e} = x_\mu/x_e$. Now if we displace our fluid element, P and μ_n adjust themselves to

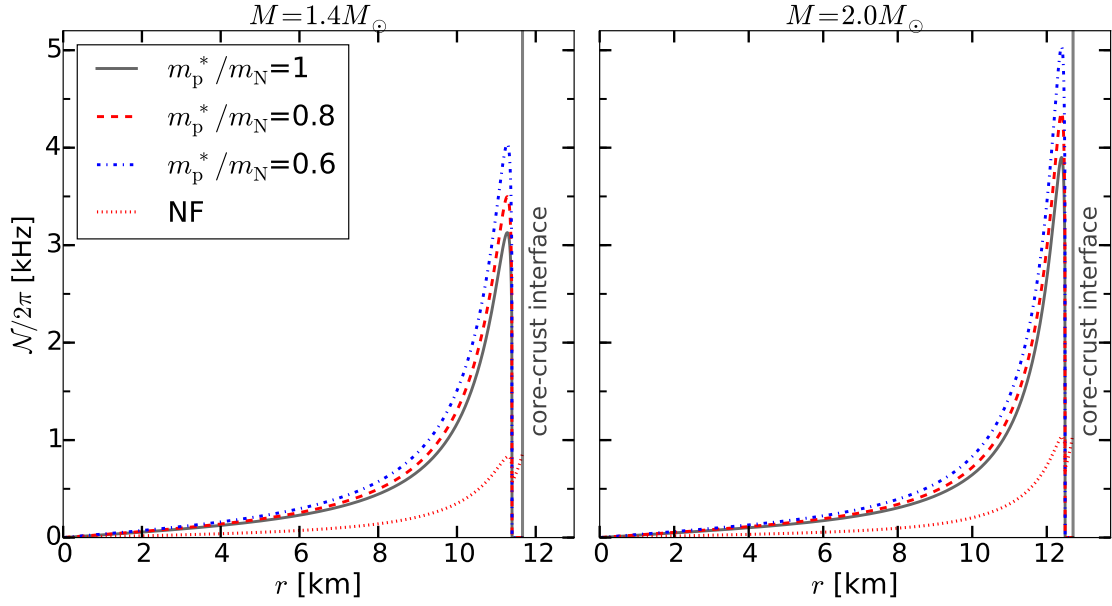


Figure 3-2: Buoyancy frequency $\mathcal{N}/2\pi$ as a function of radius for our $1.4 M_\odot$ (left panel) and $2.0 M_\odot$ (right panel) NS models. We show results for three different entrainment levels, labelled according to their proton effective mass: $m_p^*/m_N = 1, 0.8, 0.6$ (black solid lines, red dashed lines, and blue dash-dotted lines, respectively). We also show $\mathcal{N}/2\pi$ for the normal fluid models (red dotted lines). The vertical lines indicate the core-crust interface.

the new background values (by contracting/expanding and by varying the number of superfluid neutrons, respectively). However, $x_{\mu e}$ remains fixed because the electrons and muons move with the same velocity, that of the charged flow \mathbf{v}_e . The stability criterion is therefore

$$\left(\frac{\partial \rho}{\partial x_{\mu e}}\right)_{P, \mu_n} \left(\frac{dx_{\mu e}}{dr}\right) < 0, \quad (3.13)$$

i.e., gradients in $x_{\mu e}$ provide a buoyancy force that can support g-modes.

The convective stability criteria given above are closely related to the Brunt-Väisälä buoyancy frequency \mathcal{N} . In a npe μ normal fluid, the density can be uniquely parameterized in terms of P , x_e , and x_μ and the buoyancy is given by

$$\mathcal{N}^2 = -\frac{g}{\rho} \sum_{j=e, \mu} \left[\frac{\partial \rho(P, x_e, x_\mu)}{\partial x_j} \right]_{P, x_{i \neq j}} \left(\frac{dx_j}{dr} \right). \quad (3.14)$$

where $g = d\Phi/dr$ is the gravitational acceleration. In a npe μ superfluid, the density can be uniquely parameterized in terms of P , μ_n , and $x_{\mu e}$ and the buoyancy is given by

$$\mathcal{N}^2 = -\frac{1 - \epsilon_n}{x_p - \epsilon_n} \frac{g}{\rho} \left[\frac{\partial \rho(P, \mu_n, x_{\mu e})}{\partial x_{\mu e}} \right]_{P, \mu_n} \left(\frac{dx_{\mu e}}{dr} \right) \quad (3.15)$$

[see, e.g., [Passamonti et al. 2016](#) equations (67), (132), (B29), and (B38); in Appendix B.2 we describe how to relate our notation to that used in [Passamonti et al. 2016](#)]. In Figure 3-2 we show the buoyancy profiles $\mathcal{N}(r)$ of our superfluid and normal fluid models. The curves are for different combinations of NS mass and entrainment levels; specifically, we show results for a superfluid NS with $(M/M_\odot, m_p^*/m_N)=(1.4, 1)$, $(1.4, 0.8)$, $(1.4, 0.6)$, $(2.0, 0.8)$ and for a normal fluid NS with $M = 1.4 M_\odot$.

We find that $\mathcal{N}(r)$ is a factor of approximately $x_p^{-1/2} \simeq 4$ larger in the superfluid models compared to the normal fluid models (with a mild dependence on stellar mass). This is consistent with the results of [Kantor & Gusakov \(2014\)](#) and [Passamonti et al. \(2016\)](#) (see their Figures. 2 and 6, respectively). Physically, this is because the neutron component is nearly decoupled from the charged component and thus the mass of the oscillating fluid element is smaller by a factor of $\simeq x_p$ compared to the normal fluid case [see equations (3.14) and (3.15); note that the differential terms in

these two equations happen to be comparable]. From equations (3.6) and (3.15) we also see that a smaller m_p^* (that is, a larger ϵ_n), yields a larger \mathcal{N} . We will see in Section 3.3.1 that the larger \mathcal{N} of the superfluid models shifts the g-mode spectrum to higher frequencies.

Note that for $r > R_\mu$, there are no muons and $\mathcal{N} = 0$ in the superfluid case. Finally, for simplicity we neglect the buoyancy of the crust and set $\mathcal{N} = 0$ for $r > R_{cc}$ (since only a small fraction of the NS mass is in the crust, this simplification should not significantly affect the core g-modes of interest here).

3.3 TIDAL DRIVING

We now consider small amplitude perturbations to the static background described in Section 3.2. In Section 3.3.1 we describe the homogeneous linear eigenvalue problem in which the perturbations are free to oscillate at their natural frequency (i.e., they are not driven by an external force). In Section 3.3.2 we describe the inhomogeneous tidal problem in which the perturbations are linearly forced by the tidal potential of the NS's companion.

3.3.1 Eigenmodes of a superfluid neutron star

The linearized Newtonian fluid equations describing the free oscillations of the superfluid neutrons and the charged normal fluid are (Prix & Rieutord, 2002)

$$\nabla \cdot (\rho_c \boldsymbol{\xi}_c) + \delta\rho_c = 0, \quad (3.16)$$

$$\nabla \cdot (\rho_n \boldsymbol{\xi}_n) + \delta\rho_n = 0, \quad (3.17)$$

$$\sigma^2 [\boldsymbol{\xi}_c - \epsilon_c (\boldsymbol{\xi}_c - \boldsymbol{\xi}_n)] = \nabla (\delta\tilde{\mu}_c + \delta\Phi), \quad (3.18)$$

$$\sigma^2 [\boldsymbol{\xi}_n + \epsilon_n (\boldsymbol{\xi}_c - \boldsymbol{\xi}_n)] = \nabla (\delta\tilde{\mu}_n + \delta\Phi), \quad (3.19)$$

$$\nabla^2 \delta\Phi = 4\pi G (\delta\rho_c + \delta\rho_n), \quad (3.20)$$

where we assume that the perturbed quantities have a time dependence $e^{i\sigma t}$, $\delta\mathcal{Q}(\mathbf{x})$ denotes the Eulerian perturbation of a quantity \mathcal{Q} at location \mathbf{x} , and $\xi_c(\mathbf{x})$ and $\xi_n(\mathbf{x})$ are the Lagrangian displacement fields of the charged normal fluid and neutron superfluid. These equations express mass continuity [equations (3.16) and (3.17)], momentum conservation [equations (3.18) and (3.19)], and Poisson's equation (3.20) relating the perturbed gravitational potential $\delta\Phi$ to the perturbed total density (we do not make the Cowling approximation).

We solve these equations using standard techniques of stellar oscillation theory. In particular, we consider spheroidal modes in which the perturbed solutions separate into radial and angular functions

$$\delta\mathcal{Q}(r, \theta, \phi) = \delta\mathcal{Q}(r)Y_{lm}(\theta, \phi), \quad (3.21)$$

$$\xi_c(r, \theta, \phi) = \left[\xi_c^r(r), \xi_c^h(r)\frac{\partial}{\partial\theta}, \xi_c^h(r)\frac{1}{\sin\theta}\frac{\partial}{\partial\phi} \right] Y_{lm}(\theta, \phi) \quad (3.22)$$

(and similarly for ξ_n), where $Y_{lm}(\theta, \phi)$ is the spherical harmonic function. The oscillation equations then reduce to a set of linearly coupled ordinary differential equations in radius. In Appendix C.1 we write down the form of these equations that we use in order to obtain numerical solutions. As in Kantor & Gusakov (2014), we assume that the crust is a normal fluid. In Appendix C.2 we give the boundary conditions that we assume at the stellar center, at the core-crust interface (i.e., at the superfluid-normal fluid interface), and at the stellar surface.

In a normal fluid NS we can write the oscillation equations in the form of an eigenvalue problem

$$\mathcal{L}[\xi] = \sigma^2\xi, \quad (3.23)$$

where $\mathcal{L}[\xi]$ is a linear operator representing the internal restoring forces that act on the Lagrangian displacement $\xi(\mathbf{x}, t)$. The eigenmodes $\{(\sigma_a^2, \xi_a)\}$ are those solutions that satisfy the boundary conditions, where $a = \{n_a, l_a, m_a\}$ labels the three quantum numbers of each solution: the radial order n_a , the spherical degree l_a , and the azimuthal order m_a . Since the operator \mathcal{L} is Hermitian with respect to the inner

product

$$\langle \boldsymbol{\xi}, \boldsymbol{\xi}' \rangle = \int d^3x \rho \boldsymbol{\xi}^* \cdot \boldsymbol{\xi}' \quad (3.24)$$

(i.e., $\langle \boldsymbol{\xi}, \mathcal{L}[\boldsymbol{\xi}'] \rangle = \langle \mathcal{L}[\boldsymbol{\xi}], \boldsymbol{\xi}' \rangle$), the eigenmodes form a complete, orthonormal basis (here the asterisk refers to complex conjugation). When considering normal fluid models, we normalize the modes such that

$$\sigma_a^2 \langle \boldsymbol{\xi}_a, \boldsymbol{\xi}_b \rangle = E_0 \delta_{ab}, \quad (3.25)$$

where $E_0 = GM^2/R$ is a characteristic energy scale of the NS.

While a normal fluid NS has a single displacement field $\boldsymbol{\xi}$, a superfluid NS has two distinct displacement fields $\boldsymbol{\xi}_c$ and $\boldsymbol{\xi}_n$ because there are two fluid components, the normal fluid and the superfluid. The oscillation equations of a superfluid NS (eqs. [3.16-3.20](#)) therefore take the form

$$\mathcal{L} \begin{bmatrix} \boldsymbol{\xi}_+ \\ \boldsymbol{\xi}_- \end{bmatrix} = \sigma^2 \begin{bmatrix} \boldsymbol{\xi}_+ \\ \boldsymbol{\xi}_- \end{bmatrix}, \quad (3.26)$$

where this linear operator \mathcal{L} is different from that of the normal fluid case above (see [Appendix C.1](#)) and

$$\boldsymbol{\xi}_+ = \frac{1}{\rho} (\rho_c \boldsymbol{\xi}_c + \rho_n \boldsymbol{\xi}_n), \quad (3.27)$$

$$\boldsymbol{\xi}_- = (1 - \epsilon_n - \epsilon_c)(\boldsymbol{\xi}_c - \boldsymbol{\xi}_n). \quad (3.28)$$

The displacement $\boldsymbol{\xi}_+$ is the mass-averaged flow and the displacement $\boldsymbol{\xi}_-$ is proportional to the difference between the normal fluid flow and the superfluid flow. For the tidal coupling problem, it proves convenient to express displacements in terms of $\boldsymbol{\xi}_+$ and $\boldsymbol{\xi}_-$ rather than $\boldsymbol{\xi}_c$ and $\boldsymbol{\xi}_n$. Note that although there is no direct force between the normal fluid and superfluid, they are nevertheless coupled locally through the equation of state (they are coupled even if entrainment is ignored; see discussion in [Prix & Rieutord 2002](#)). As a result, both components oscillate at the same frequency

σ . The eigenmodes $\{(\sigma_a^2, \xi_{a+}, \xi_{a-})\}$ are those solutions that satisfy the boundary conditions given in Appendix C.2. In Appendix C.3 we show that the linear operator is Hermitian with respect to the inner product

$$\left\langle \begin{bmatrix} \xi_+ \\ \xi_- \end{bmatrix}, \begin{bmatrix} \xi'_+ \\ \xi'_- \end{bmatrix} \right\rangle = \int d^3x \begin{bmatrix} \xi_+^* & \xi_-^* \end{bmatrix} \begin{bmatrix} \rho & 0 \\ 0 & \tilde{\rho} \end{bmatrix} \begin{bmatrix} \xi'_+ \\ \xi'_- \end{bmatrix} \quad (3.29)$$

where

$$\tilde{\rho} = \frac{\rho_c \rho_n}{(1 - \epsilon_n - \epsilon_c)\rho}. \quad (3.30)$$

This result follows directly from the analysis in Lindblom & Mendell (1994) who, using somewhat different notation, showed that the linear operator satisfies a variational principle (see also Andersson & Comer 2001 and, for the case of a rotating NS, Andersson et al. 2004). The above integral reduces to the normal fluid case if we identify $\xi_+ \rightarrow \xi$ and $\xi_- \rightarrow 0$, which allows us to evaluate it not only in the superfluid core but also in the normal fluid crust. We normalize the modes such that

$$\sigma_a^2 \left\langle \begin{bmatrix} \xi_{a+} \\ \xi_{a-} \end{bmatrix}, \begin{bmatrix} \xi_{b+} \\ \xi_{b-} \end{bmatrix} \right\rangle = E_0 \delta_{ab}. \quad (3.31)$$

In Figure 3-3 we show the structure of three $l_a = 2$ g-modes ($n_a = 1, 2, 5$) for the $1.4 M_\odot$ superfluid model with $m_p^* = 0.8 m_N$. In the top panel we plot the radial profile of the total density perturbation $\delta\rho = \delta\rho_c + \delta\rho_n$ and that of the individual fluid components $\delta\rho_c$ and $\delta\rho_n$. In the bottom two panels we plot the radial and horizontal displacements of the two flows.

There exists a discontinuity in the first derivative of $\delta\rho$ at R_μ because the muon gradient is discontinuous at R_μ in our model. There also exists a discontinuity in $\delta\rho$ at R_{cc} where we join the superfluid solution with the normal fluid solution. Nevertheless this discontinuity does not violate any physical principles. In particular, it does not imply a discontinuous mass current since $\mathbf{v}\delta\rho + \rho\delta\mathbf{v}$ is still continuous: the first term is always zero because the background velocity is zero, which suppresses the discontinuity in $\delta\rho$, and the second term is continuous by requiring continuity of the

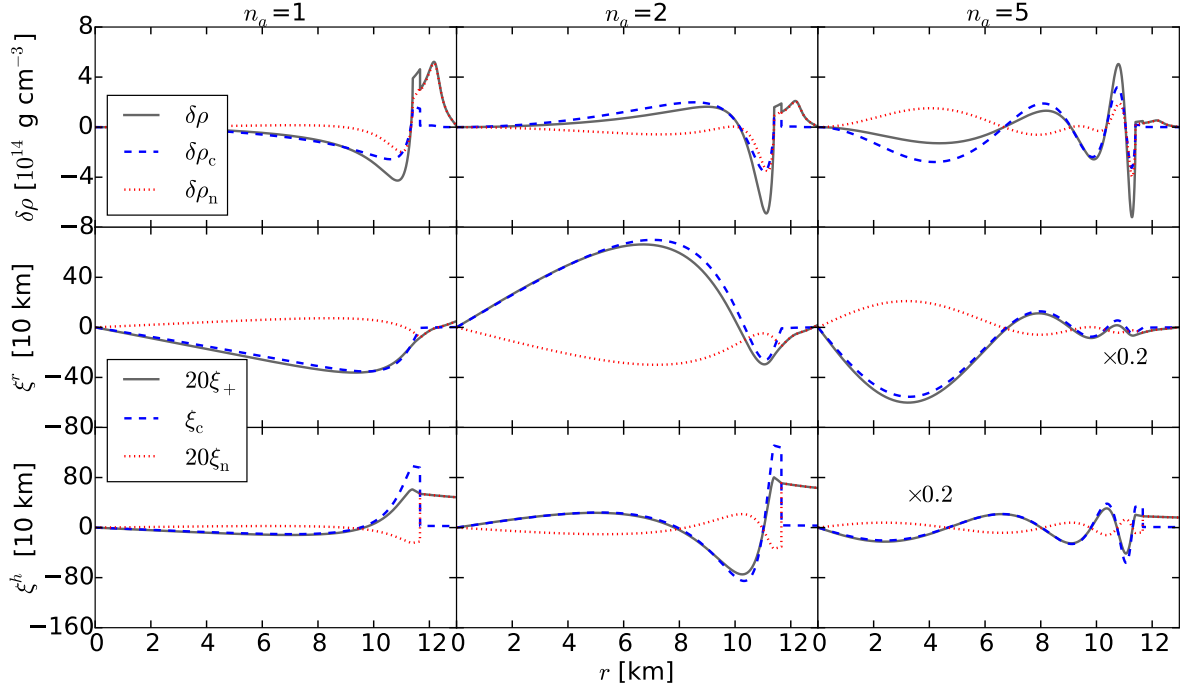


Figure 3-3: Structure of the $l_a = 2$, $n_a = (1, 2, 5)$ g-modes (left, middle, and right panels, respectively) of our $1.4 M_\odot$ superfluid NS model with entrainment $m_p^* = 0.8m_N$. The upper panels show the total Eulerian density perturbation $\delta\rho = \delta\rho_c + \delta\rho_n$ (solid black line), $\delta\rho_c$ (dashed blue line), and $\delta\rho_n$ (dotted red line). The middle and lower panels show, respectively, the radial ξ^r and horizontal ξ^h components of the Lagrangian displacements corresponding to ξ_+ (solid black line), ξ_c (dashed blue line), and ξ_n (dotted red line). In order to plot all the displacements on the same scale, we multiply ξ_+ and ξ_n by a factor of 20 and divide the $n_a = 5$ displacements by a factor of 5.

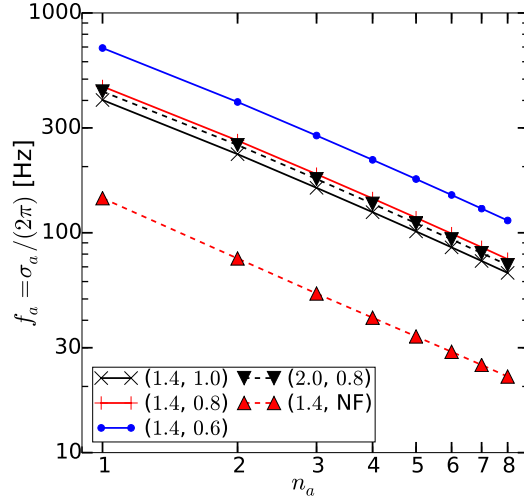


Figure 3-4: Eigenfrequencies $f_a = \sigma_a/2\pi$ as a function of radial order n_a for the first eight $l_a = 2$ g-modes. In the legend, the first number represents the NS mass in units of M_\odot and the second number represents m_p^* in units of m_N (or “NF” for the normal fluid case). We show results for four superfluid models: $(M/M_\odot, m_p^*/m_N) = (1.4, 1.0)$, $(1.4, 0.8)$, $(1.4, 0.6)$, $(2.0, 0.8)$, and a normal fluid model with $M = 1.4 M_\odot$.

Lagrangian displacements (see Appendix C.2).

For a given mode, the amplitude of ξ_c is significantly larger than ξ_n (in Figure 3-3 we multiply ξ_n by a factor of 20 in order to plot it on a similar scale as ξ_c). This is because there is significantly less mass in the charged fluid elements (by a factor of $\simeq x_p$) and thus, for a given mode energy, $|\xi_c|$ must be larger. We also find that ξ_c^r and ξ_n^r cross zero at slightly different locations (e.g., middle panel of Figure 3-3). This effect is due to entrainment and was also observed by [Prix & Rieutord \(2002\)](#) in the case of p-mode oscillations. Finally, we note that in Figure 3-3 the horizontal displacements ξ^h are roughly twice as great as the radial displacements ξ^r , indicating the transverse nature of the g-mode oscillations.

In Figure 3-4 we show the eigenfrequencies $f_a = \sigma_a/2\pi$ of the first eight $l_a = 2$ g-modes for our various NS models. Comparing the superfluid and normal fluid models, we see that the g-mode spectra of the superfluid models are shifted to higher frequencies at a given n_a . This effect was also noted by [Kantor & Gusakov \(2014\)](#) and [Passamonti et al. \(2016\)](#). The spectra shift because the buoyancy frequencies \mathcal{N} are different in different models (see Section 3.2.1); for high-order g-modes ([Aerts](#)

et al., 2010)

$$f_a \simeq \frac{[l_a(l_a + 1)]^{1/2}}{2\pi^2 n_a} \int N d \ln r. \quad (3.32)$$

Indeed, we find that for even relatively low order $l_a = 2$ g-modes of the superfluid and normal fluid models,

$$f_a^{(\text{SF})} \simeq \frac{590}{n_a} \text{ Hz}, \quad \text{and} \quad f_a^{(\text{NF})} \simeq \frac{170}{n_a} \text{ Hz}. \quad (3.33)$$

The relations above are fits to the $1.4 M_\odot$ NS superfluid and normal fluid models, respectively; in the superfluid case we adopt an entrainment level of $m_p^* = 0.8 m_N$. We use these as our default models when providing numerical fits below. Among the superfluid models, increasing m_p^* (that is, decreasing ϵ_n) or increasing the NS mass decreases the eigenfrequencies slightly. Equation (3.33) implies that in the frequency bandwidth of Advanced LIGO at full design sensitivity (10 Hz–3000 Hz; Harry 2010), a superfluid NS has ≈ 3 times more $l_a = 2$ g-modes than a normal fluid NS.

3.3.2 Tidal driving of modes

We can account for tidal driving of the fluid by replacing $\delta\Phi$ in equations (3.16-3.20) with $\delta\Phi + U$, where U is the tidal potential. In a spherical coordinate system (r, θ, ϕ) centered on the primary, the tidal potential due to a companion of mass M' is

$$U(r, \theta, \phi, t) = -GM' \sum_{l \geq 2} \sum_{m=-l}^l \frac{W_{lm} r^l}{D^{l+1}(t)} Y_{lm}(\theta, \phi) e^{-im\psi(t)}. \quad (3.34)$$

The orbit of the companion is oriented in the plane $[D(t), \pi/2, \psi(t)]$, where $D(t)$ is the binary’s orbital separation and $\psi(t)$ is the orbital phase. The general expression for the coefficients W_{lm} can be found in Press & Teukolsky (1977); for the $l = 2$ harmonic, which dominates at small R/D , $W_{20} = -\sqrt{\pi/5}$, $W_{2\pm 2} = \sqrt{3\pi/10}$, and $W_{2\pm 1} = 0$. The superfluid oscillation equations with tidal driving now take the form

$$\left[\frac{\partial^2}{\partial t^2} + \mathcal{L} \right] \begin{bmatrix} \xi_+ \\ \xi_- \end{bmatrix} = - \begin{bmatrix} \nabla U \\ 0 \end{bmatrix}. \quad (3.35)$$

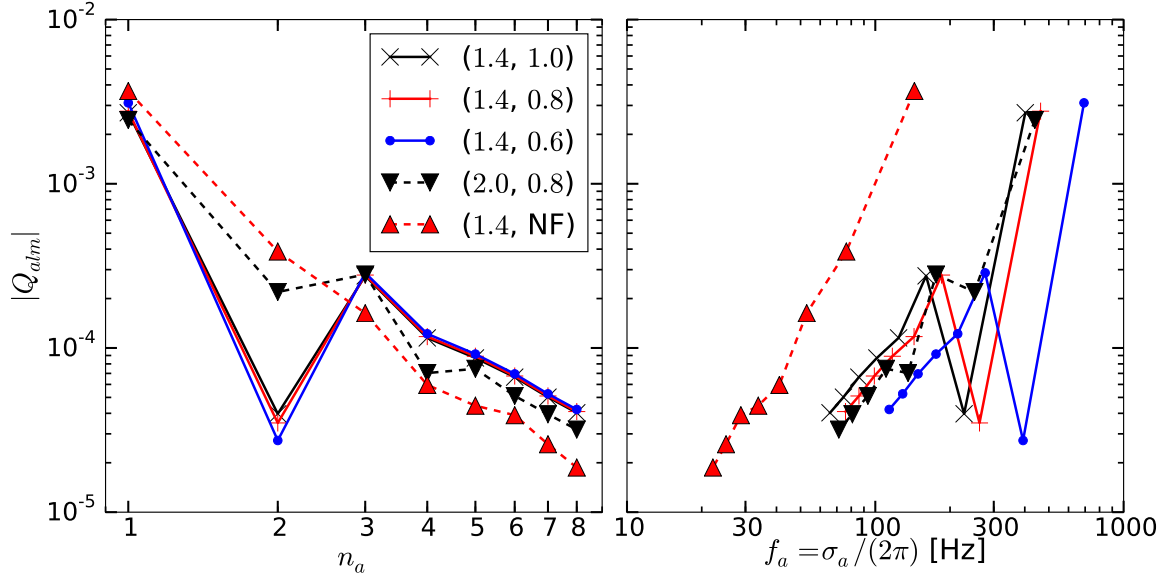


Figure 3-5: Tidal coupling coefficient $|Q_{alm}|$ as a function of the $l_a = 2$ g-mode radial order n_a (left panel) and eigenfrequency $f_a = \sigma_a/2\pi$ (right panel) for the same set of models as in Figure 3-4.

The tidal acceleration ∇U appears explicitly in the equation of the mass-averaged flow ξ_+ but not the difference flow ξ_- . The normal fluid counterpart to equation (3.35) is recovered by identifying $\xi_+ \rightarrow \xi$ and $\xi_- \rightarrow 0$ (see Lai 1994).

Since the linear operator \mathcal{L} is Hermitian (for both the superfluid and normal fluid; Appendix C.3), the star's eigenmodes form an orthonormal basis. This allows us to expand the displacements as

$$\begin{bmatrix} \xi_+(\mathbf{x}, t) \\ \xi_-(\mathbf{x}, t) \end{bmatrix} = \sum_a b_a(t) \begin{bmatrix} \xi_{a+}(\mathbf{x}) \\ \xi_{a-}(\mathbf{x}) \end{bmatrix}, \quad (3.36)$$

where $b_a(t)$ is the time-dependent, dimensionless amplitude of mode a . Given our eigenmode normalization (eq. 3.31), a mode with amplitude $|b_a| = 1$ has energy E_0 . Equation (3.35) can then be written as a set of linear amplitude equations for each mode:

$$\ddot{b}_a + \sigma_a^2 b_a = \sigma_a^2 U_a(t) \quad (3.37)$$

where the tidal driving coefficient (cf. [Weinberg et al. 2012](#))

$$U_a(t) = -\frac{1}{E_0} \int d^3x \rho \boldsymbol{\xi}_{a+}^* \cdot \boldsymbol{\nabla} U \quad (3.38)$$

$$= \frac{M'}{M} \sum_{lm} W_{lm} Q_{alm} \left(\frac{R}{D(t)} \right)^{l+1} e^{-im\psi(t)}. \quad (3.39)$$

The second equality follows from equation (3.34) and defines the time-independent, dimensionless tidal coupling coefficient (sometimes referred to as the tidal overlap integral)

$$Q_{alm} = \frac{1}{MR^l} \int d^3x \rho \boldsymbol{\xi}_{a+}^* \cdot \boldsymbol{\nabla} (r^l Y_{lm}), \quad (3.40)$$

where in the subscripts $a = \{n_a, l_a, m_a\}$ denotes a specific eigenmode of the NS and lm denotes a specific harmonic of the tidal potential. By angular momentum conservation, Q_{alm} is non-zero only if $l_a = l$ and $m_a = m$. Using equations (3.16), (3.17), and (3.20) and integrating by parts we can alternatively express the tidal coupling coefficient as

$$Q_{alm} = \frac{1}{MR^l} \int dr r^{l+2} \delta \rho_a = -\frac{2l+1}{4\pi} \frac{\delta \Phi_a(R)}{GM/R}, \quad (3.41)$$

where $\delta \rho_a = \delta \rho_{c,a} + \delta \rho_{n,a}$ is the total perturbed density due to mode a and $\delta \Phi_a(R)$ is the mode's perturbation to the gravitational potential at the stellar surface.

In Figure 3-5 we show $|Q_{alm}|$ as a function of the radial order n_a and eigenfrequency $f_a = \sigma_a/2\pi$ of the $l_a = 2$ g-modes for our various NS models. The most obvious feature is that smaller n_a tend to have larger $|Q_{alm}|$ (with the exception of the $n_a = 2$ mode of our $1.4 M_\odot$ superfluid models, which has an anomalously small $|Q_{alm}|$). This is because the tide is a long wavelength perturbation and it couples best to modes whose wavelengths are likewise long. For a given n_a , we find that the different models all have similar $|Q_{alm}|$; there is only a weak dependence on whether the NS is superfluid, the level of entrainment m_p^* , and the NS mass. Since the superfluid g-mode spectrum is shifted to higher frequencies (i.e., f_a is larger at a given n_a), at a given f_a the normal fluid models have a significantly larger $|Q_{alm}|$. In particular, based on our numerical

calculations of $|Q_{alm}|$, we find that for the $1.4 M_\odot$ superfluid models (neglecting the anomalous $n_a = 2$ mode) and normal fluid models, respectively,

$$\left|Q_{alm}^{(\text{SF})}\right| \simeq 2.6 \times 10^{-3} n_a^{-2} \simeq 7.6 \times 10^{-5} f_{a,100}^2, \quad (3.42)$$

$$\left|Q_{alm}^{(\text{NF})}\right| \simeq 3.5 \times 10^{-3} n_a^{-5/2} \simeq 9.3 \times 10^{-4} f_{a,100}^{5/2}, \quad (3.43)$$

where $f_{a,100} = f_a/100$ Hz. The oscillatory nature of the g-modes can make calculating Q_{alm} subject to numerical error (Reisenegger & Goldreich, 1994; Reisenegger, 1994; Weinberg et al., 2012). In Appendix C.4 we carry out numerical tests that show that our calculations of Q_{alm} have only a ~ 1 percent error.

3.4 RESULTS

Using the formalism described in the previous Section, we now evaluate the resonant tidal excitation of g-modes in coalescing superfluid NS binaries. Our analysis is similar to that of Lai (1994) and Reisenegger & Goldreich (1994) who studied this problem for normal fluid NSs. In Section 3.4.1 we calculate the energy transferred to the NS from the orbit due to the resonant tidal interactions. In Section 3.4.2 we calculate the resulting GW phase error relative to the point mass estimate.

3.4.1 Tidal energy transfer

As the NS inspirals due to the emission of gravitational radiation, the tidal driving sweeps through resonances with individual g-modes. The dynamics, which are similar to that of a linearly driven oscillator whose driving frequency and forcing strength increase with time, is determined by the amplitude equation (3.37). Focusing on resonant driving by the dominant $l = 2, m = 2$ tidal harmonic, we have

$$\ddot{b}_a + \sigma_a^2 b_a = \sigma_a^2 W_{22} Q_{a22} \left(\frac{M'}{M}\right) \left(\frac{R}{D(t)}\right)^3 e^{-2i\psi(t)}. \quad (3.44)$$

Since linear tidal interactions have a small overall effect on the inspiral, we can use the quadrupole formula for the rate of orbital decay of two point masses, i.e.,

$$\dot{D} = -\frac{64G^3}{5c^5} \frac{MM'(M+M')}{D^3}, \quad (3.45)$$

$$\dot{\psi} = \left[\frac{G(M+M')}{D^3} \right]^{1/2}. \quad (3.46)$$

As $D(t)$ decreases and the orbital frequency $\Omega(t) = \dot{\psi}$ increases, $l_a = 2$ g-modes with $\sigma_a \simeq 2\Omega$ temporarily undergo resonant tidal driving. Post-resonance, the g-modes oscillate at nearly their natural frequency σ_a (Lai, 1994).

We do not include linear damping in equation (3.44) because it has a negligible effect on the peak amplitudes reached by the low order modes we consider. It therefore does not affect the tidal energy transfer or phase error. Damping does heat the neutron star by thermalizing a portion of the mode energy. Nonetheless, as we show later in this section, the core is only heated to $T \sim 10^7$ K, which is too small to significantly modify the g-modes of a superfluid NS (Kantor & Gusakov, 2014; Passamonti et al., 2016).

In order to determine the evolution of the mode amplitudes $b_a(t)$, we solve equations (3.44), (3.45), and (3.46) for the set of g-modes described in Section 3.3. For each mode we initialize the equations following the discussion in Lai (1994), and then numerically integrate them forward in time. In Figure 3-6 we show the mode energy $E_a(t) = 2|b_a|^2 E_0$ as a function of orbital separation $D(t)$ for the low order ($l_a = 2$, $m_a = \pm 2$) g-modes that are resonantly excited during the latter stages of inspiral ($f_{\text{gw}} \gtrsim 30$ Hz). For conciseness, we have used a single letter a in the subscript of mode energy to represent the total contribution of both the $m_a = 2$ and $m_a = -2$ modes, and thus a factor of 2 has been included since each mode contributes equally. We will use this convention in all our results described below. In the left panel we show $E_a(t)$ for our superfluid NS model with $M = M' = 1.4 M_\odot$ and $m_p^* = 0.8 m_N$. In the right panel we show $E_a(t)$ for the normal fluid NS model with $M = M' = 1.4 M_\odot$. Note that the horizontal scale is different in the two panels.

Because the superfluid model has more high-frequency g-modes (see Figure 3-4),

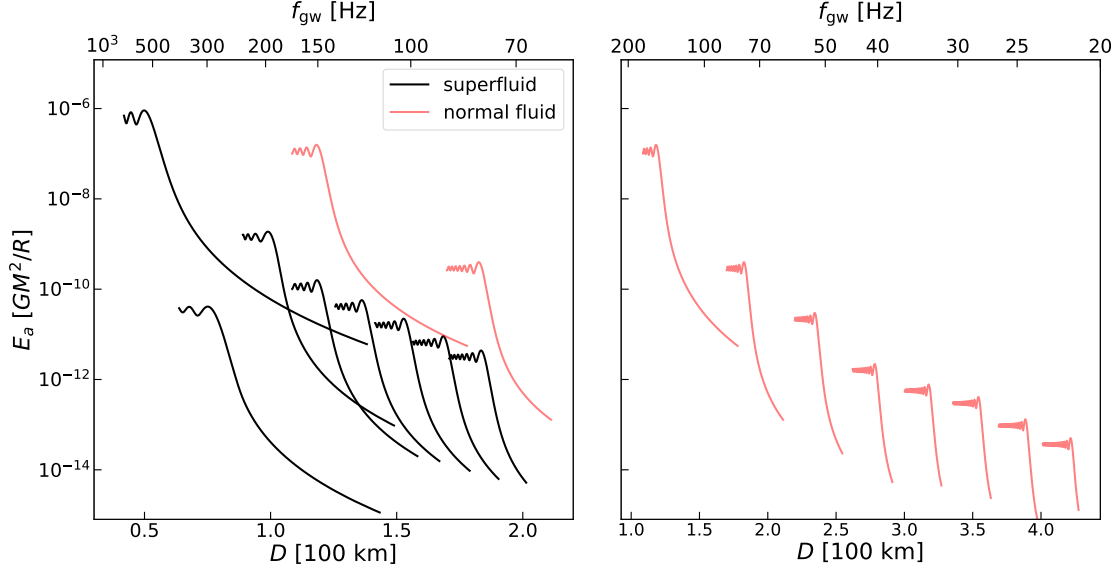


Figure 3-6: Evolution of the mode energy E_a (in units of $E_0 = GM^2/R$) due to the resonant tidal driving of $l_a = 2$ g-modes during an equal mass ($M = M' = 1.4 M_\odot$) binary NS inspiral. The bottom axes give the orbital separation D and the top axes give the gravitational wave frequency f_{gw} . The left panel shows the $n_a = \{1, 2, 3, \dots, 8\}$ g-modes of the superfluid model with $M = 1.4 M_\odot$, $m_p^* = 0.8 m_N$ (black lines) and the $n_a = \{1, 2\}$ g-modes of the normal fluid model with $M = 1.4 M_\odot$ (grey lines). The right panel shows the $n_a = \{1, 2, 3, \dots, 8\}$ g-modes of the normal fluid model (the $n_a = \{1, 2\}$ modes are plotted in both panels). Note the different range of D plotted in the two panels. For clarity, we only show a mode's evolution near its resonant excitation.

it admits eight resonantly excited g-modes for $D(t) < 200\text{km}$ compared to only two for the normal fluid model. The lowest order superfluid g-mode is excited later in the inspiral than the normal fluid one (compare the black and grey curves in the left panel of Figure 3-6). On the other hand, at orbital separations where both models have resonances, the modes of the normal fluid model are excited to a significantly larger maximum energy $E_{a,\text{max}}$. For example, at $D \simeq 120\text{ km}$, the $n_a = 1$ mode of the normal fluid model undergoes resonant driving up to $E_{a,\text{max}} \approx 10^{-7} E_0$ while the $n_a = 4$ mode of the superfluid model undergoes resonant driving up to only $E_{a,\text{max}} \approx 10^{-10} E_0$. This difference is due to the superfluid model's smaller tidal coupling coefficient $|Q_{a22}|$ at a given f_a (see Section 3.3.2).

While the numerical calculations provide the full mode amplitude evolution, we can estimate the post-resonance mode energy $E_{a,\text{max}}$ by solving equation (3.44) using the stationary-phase approximation. Following the approach described in Lai (1994; see also Reisenegger & Goldreich 1994), this gives

$$E_{a,\text{max}} \simeq \frac{\pi^2}{1024} k \left(\frac{GM}{Rc^2} \right)^{-5/2} \left(\frac{\sigma_a}{\omega_0} \right)^{7/3} \sum_{m=\pm 2} Q_{a2m}^2 E_0, \quad (3.47)$$

where $k = q[2/(1+q)]^{5/3}$, $q = M'/M$ is the mass ratio of the binary, and $\omega_0 = (GM/R^3)^{1/2}$ is the NS dynamical frequency. The expression matches equation (6.11) in Lai (1994) except that we use a different convention for normalizing the eigenfunctions. Using our analytic fits to Q_{a22} given by equations (3.42) and (3.43) and the values of M and R given in table 3.1, we find that for the $M = 1.4 M_\odot$ superfluid and normal fluid models, respectively,

$$E_{a,\text{max}}^{(\text{SF})} \simeq 1.0 \times 10^{-6} k n_a^{-19/3} E_0 \simeq 2 \times 10^{-11} k f_{a,100}^{19/3} E_0, \quad (3.48)$$

$$E_{a,\text{max}}^{(\text{NF})} \simeq 1.2 \times 10^{-7} k n_a^{-22/3} E_0 \simeq 3.0 \times 10^{-9} k f_{a,100}^{22/3} E_0, \quad (3.49)$$

where we used equation (3.33) to express the energies in terms of both n_a and f_a . Comparing this with the fully numerical results shown in Figure 3-6, we find that the

stationary-phase approximation gives a good match to the superfluid energy $E_{a,\max}^{(\text{SF})}$ but slightly underestimates the normal fluid case by ≈ 25 percent. At a given frequency, we find that $E_{a,\max}$ of both $M = 2.0 M_\odot$ superfluid and normal fluid models are both about 3 times smaller than $E_{a,\max}$ of the $M = 1.4 M_\odot$ models.

In order to calculate the total energy transfer E_{trans} from the orbit to all the $l = 2$ g-modes, we can sum over n_a using equations (3.48) and (3.49). This gives

$$E_{\text{trans}}^{(\text{SF})} \simeq 1.0 \times 10^{-6} k E_0 \quad \text{and} \quad E_{\text{trans}}^{(\text{NF})} \simeq 1.2 \times 10^{-7} k E_0. \quad (3.50)$$

Thus, a superfluid NS absorbs $\simeq 10$ times more orbital energy by the time the NS merges. The sums over n_a , which formally are given by the Riemann zeta function $\zeta(19/3) \simeq \zeta(22/3) \simeq 1.0$, are strongly dominated by the $n_a = 1$ mode. That is, most of the energy transfer occurs during the excitation of the lowest order g-mode. This result is a consequence of two effects: the tidal coupling coefficient $|Q_{a22}|$ is largest for low-order modes (see Section 3.3.2), and the amplitude of the tide $(M'/M)(R/D)^3$ is largest at small D , which is when the low-order (i.e., high f_a) modes are resonantly excited. The influence of these two effects is only partially mitigated by the shorter decay timescales at small D , which reduces the duration of the resonant driving compared to higher-order modes.

Following Lai (1994), viscous dissipation of the resonant g-modes heats the neutron star by an amount

$$E_{\text{visc}} \simeq -2 \int_{D_a}^{D_{\text{merg}}} \frac{dD}{D} t_D \gamma_a E_a, \quad (3.51)$$

where D_a is the orbital separation at which the mode a becomes resonant, D_{merg} is the separation before the merger (taken to be $3R$), $t_D = |D/\dot{D}|$ is the orbital decay time, and γ_a is the mode's damping rate. We neglect the small amount of viscous dissipation of modes prior to their resonant excitation. Comparing the heating in the superfluid case relative to the normal fluid case, we find

$$\frac{E_{\text{visc}}^{(\text{SF})}}{E_{\text{visc}}^{(\text{NF})}} \simeq 0.3 \frac{\gamma_1^{(\text{SF})}}{\gamma_1^{(\text{NF})}}, \quad (3.52)$$

where γ_1 represents the damping rate of the first g-mode, which we expect to dominate the heating (although higher order modes have larger γ_a and more time to heat the NS prior to the merger, they contribute less to the heating because their $E_{a,\max}$ is much smaller). Following [Lai \(1994\)](#), if we assume that the viscosity is dominated by electron-electron scattering and that the heat content is dominated by the electrons, then the superfluid NS is heated to $T \sim 10^7$ K.³ Such temperatures are too small to significantly modify the g-modes relative to the zero-temperature superfluid model we have adopted in our calculation (see, e.g., figure 4 in [Kantor & Gusakov 2014](#) and [Passamonti et al. 2016](#)).

3.4.2 Phase shift of the gravitational waveform

Given the resonant energy $E_{a,\max}$, the phase shift of the gravitational waveform $\Delta\phi_a$ due to each excited mode is given approximately by ([Lai, 1994](#))

$$\Delta\phi_a \simeq -4\pi \frac{t_D}{t_{\text{orb}}} \frac{E_{a,\max}}{|E_{\text{orb}}|}, \quad (3.53)$$

where $t_{\text{orb}} = 2\pi/\Omega$ is the orbital period and $E_{\text{orb}} = -GMM'/2D$ is the orbital energy (both evaluated at the mode's resonance). Because the modes remove energy from the orbit, the tidal interaction accelerates the rate of orbital decay and thus $\Delta\phi_a < 0$. Using the expression for $E_{a,\max}$ based on the stationary-phase approximation (eq. 3.47; note that the contributions from both $m = \pm 2$ modes are included), we find

$$\Delta\phi_a = -\frac{5\pi^2}{2048} k' \left(\frac{GM}{Rc^2} \right)^{-5} \sum_{m=\pm 2} |Q_{a2m}|^2, \quad (3.54)$$

³Our estimate of the heating differs from that of [Lai \(1994\)](#) in two ways. First, since we are considering a superfluid NS rather than a normal fluid NS, we assume that the main thermal content is due to the electrons rather than the neutrons (see footnote 9 in [Lai 1994](#)). This increases the resulting temperature by a factor of ≈ 2 . Second, we correct a typo in [Lai's](#) expressions for the damping rates which for $l = |m| = 2$ modes decreases the rates by a factor of 24 (see footnote 14 in [Weinberg et al. 2013](#)).

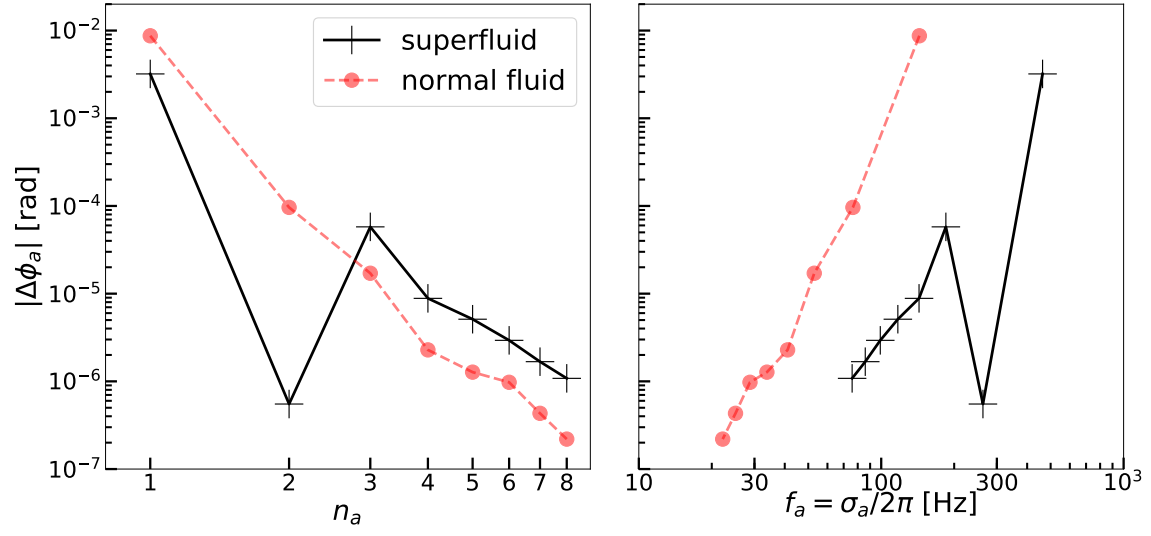


Figure 3-7: Phase shift of the gravitational waveform $\Delta\phi_a$ due to the resonant tidal excitation of individual $l = 2$ g-modes. The left panel shows $\Delta\phi_a$ as a function of the radial order n_a and the right panel as a function of the mode's eigenfrequency f_a . Solid black lines correspond to the $M = 1.4 M_\odot$ superfluid NS model with an entrainment level $m_p^* = 0.8m_N$. For comparison, dashed red lines show the results for the $M = 1.4 M_\odot$ normal fluid NS model.

where $k' = 2/[q(1+q)]$. Note that in our normalization, $\Delta\phi_a$ depends on frequency only through $|Q_{a2m}|$. Using equations (3.48) and (3.49), we find

$$\Delta\phi_a^{(\text{SF})} \simeq -3 \times 10^{-3} k' n_a^{-4} \simeq -3 \times 10^{-7} k' f_{a,100}^4, \quad (3.55)$$

$$\Delta\phi_a^{(\text{NF})} \simeq -7 \times 10^{-3} k' n_a^{-5} \simeq -4 \times 10^{-4} k' f_{a,100}^5. \quad (3.56)$$

These analytic estimates of the phase error are in good agreement (to within $\simeq 25\%$) with the numerical results shown in Figure 3-7.

As in the E_{trans} calculation of Section 3.4.1, we can sum over n_a and m_a to get the total phase error $\Delta\phi$ due to the excitation of all the $l = 2$ g-modes. This gives

$$\Delta\phi^{(\text{SF})} \simeq -4 \times 10^{-3} k', \quad (3.57)$$

$$\Delta\phi^{(\text{NF})} \simeq -7 \times 10^{-3} k'. \quad (3.58)$$

As with E_{trans} , the strong scaling with n_a in equations (3.55) and (3.56) implies that the phase error is almost completely dominated by the resonant excitation of the lowest order modes.

Although each g-mode in a superfluid NS is, compared to a normal fluid NS, excited to a much greater energy [$\simeq 10$ times larger for the lowest order mode; see equations (3.48) and (3.49)], it is excited later in the inspiral when the orbital decay is faster. These two effect cancel and therefore $\Delta\phi_a$ depends only on the tidal coupling strength $|Q_{alm}|$ [equation (3.54)]. For a given n_a , $|Q_{alm}|$ is insensitive to whether the NS is superfluid [equations (3.42) and (3.43)] and, as a result, superfluid and normal fluid NSs have similar dynamical tide-induced GW phase shifts.

3.5 CONCLUSIONS

We studied the dynamical tide in coalescing superfluid NS binaries. We considered NSs with an npe μ composition for different stellar masses ($M = 1.4 M_\odot$ and $2 M_\odot$) and levels of entrainment (as quantified by the proton effective mass m_p^*). Although

we did not account for general relativistic effects in our calculations, this simplification is unlikely to influence the qualitative conclusions of our study. In all of our superfluid NS models, we found that the spectrum of the $l = 2$ g-modes is shifted to higher frequencies compared to a normal fluid NS. As a result, we showed that many more modes undergo resonant excitation during the latter stages of binary inspiral. By calculating the mode coupling strength and integrating the time-dependent mode amplitude equations as the binary sweeps up in frequency, we found that the total energy transfer from the orbit to the oscillations is $\simeq 10$ times larger than the normal fluid case. However, because the energy transfer is dominated by the highest frequency modes, it occurs later in the inspiral when the orbital decay is faster. As a result, the impact of tidal interactions on the GW signal is comparable for a superfluid and normal fluid NS. In particular, the magnitude of the GW phase shift in both cases is \simeq a few $\times 10^{-3}$ radian. Such a phase shift is at least two orders of magnitude too small to be detected by the current generation of GW detectors (see, e.g., [Cutler & Flanagan 1994](#)).

Our analysis did not account for hyperons, which are expected to appear at high core densities ($\sim 7 \times 10^{14}$ g cm $^{-3}$; see, e.g., [Bednarek et al. 2012](#); [Weissenborn et al. 2012](#); [Gusakov et al. 2014](#)). As [Dommes & Gusakov \(2016\)](#) point out, gradients in the hyperon fraction might also be a source of buoyancy in superfluid NSs. While the direct Urca process involving hyperons (see review by [Yakovlev et al. 2001](#)) may be fast enough compared to the g-mode oscillation period to break the assumption of frozen composition, and/or the hyperons may be superfluid themselves ([Takatsuka et al., 2006](#); [Wang & Shen, 2010](#)), the case studied by [Dommes & Gusakov \(2016\)](#) nonetheless shows that there can exist additional g-modes in hyperonic NSs. In particular, hyperons produce an additional peak in the Brunt-Väisälä frequency profile, one that occurs much deeper in the core than the peak due to the muon-to-electron gradient (see Figure 6 in [Dommes & Gusakov 2016](#)). This will modify the properties of the g-modes calculated here and it is not clear to what extent this might alter the conclusions of our analysis. We plan to address this problem in the future.

We also did not account for NS rotation. Studies that have find that rapid rotation

can lead to significantly larger tide-induced phase shifts (Ho & Lai, 1999; Lai & Wu, 2006; Flanagan & Racine, 2007). However, even though these studies all assume normal fluid NSs, the modes that are responsible for the largest phase shifts are f-modes, r-modes, and inertial modes. Such modes are unlikely to be significantly modified by superfluid effects (e.g., Lee 1995; Passamonti et al. 2009).

It has been suggested that the tide in coalescing NS binaries becomes unstable to nonlinear fluid effects at relatively low GW frequencies (≈ 50 Hz; Weinberg et al. 2013; Venumadhav et al. 2014; Weinberg 2016). Although these studies assume a normal fluid NS, the nonlinear effects involve non-resonant, low frequency g-modes and such modes still exist in superfluid NSs. However, it is not clear to what extent superfluidity might alter the growth rate and saturation of the instability. It would therefore be interesting to extend these studies to superfluid NSs.

Chapter 4

Dynamical tides in coalescing superfluid neutron star binaries with hyperon cores and their detectability with third generation gravitational-wave detectors

4.1 INTRODUCTION ¹

Tides in coalescing neutron star (NS) binaries modify the rate of inspiral and generate phase shifts in the gravitational wave (GW) signal that encode information about the the NS interior. The tide is often decomposed into an equilibrium tide and a dynamical tide, where the former represents the fluid's quasi-static response and the latter represents its resonant response (e.g., in the form of resonantly excited g-modes). The GW phase shift due to the equilibrium tide, which should be detectable with Advanced LIGO ([Aasi et al., 2015](#)) by stacking multiple merger events, can constrain the NS tidal deformability and therefore the supranuclear equation of state ([Read](#)

¹This Chapter is based on [Yu & Weinberg \(2017b\)](#).

et al., 2009; Hinderer et al., 2010; Damour et al., 2012; Del Pozzo et al., 2013; Lackey & Wade, 2015; Agathos et al., 2015). However, the equilibrium tide can only indirectly constrain the interior stratification (i.e., the composition profile; Chatziioannou et al. 2015) and is insensitive to superfluid effects (see, e.g., Penner et al. 2011). By contrast, the dynamical tide is directly sensitive to both the stratification (Shibata, 1994; Lai, 1994; Reisenegger & Goldreich, 1994; Kokkotas & Schafer, 1995; Ho & Lai, 1999; Hinderer et al., 2016; Steinhoff et al., 2016) and superfluid effects (Yu & Weinberg, 2017a). GW phase shifts due to the dynamical tide can therefore provide a unique probe of the NS interior, similar to asteroseismology observations which are now providing detailed constraints on the physics of the interiors of white dwarfs, solar-type stars, and red giants (Winget & Kepler, 2008; Chaplin & Miglio, 2013).

Previous studies of the dynamical tide in binary NSs focused on “canonical” $1.4 M_{\odot}$ NSs and assumed that the core does not contain exotic hadronic matter, such as hyperons. Although it is energetically favorable for nuclear matter to transition to hyperonic matter at high densities (Ambartsumyan & Saakyan, 1960), the discovery of $2 M_{\odot}$ NSs (Demorest et al., 2010; Antoniadis et al., 2013) ruled out many hyperonic models since they tend to have softer equations of state. However, the degree of softening is uncertain (Lonardoni et al., 2015) and in the last few years many new hyperonic models compatible with the observations of $2 M_{\odot}$ NSs have been proposed (e.g., Bednarek et al. 2012; Weissenborn et al. 2012; Gusakov et al. 2014; Tolos et al. 2016).

The dynamical tide in hyperonic models is modified by the hyperon composition gradient, which provides a new source of buoyancy that can support g-mode oscillations much deeper within the NS core than the leptonic composition gradient (Dommes & Gusakov, 2016). GW phase shifts induced by the excitation of hyperonic g-modes therefore probe the innermost core, where the density is a few times the nuclear saturation density.

The total phase shift accumulated over the inspiral due to the equilibrium tide is ~ 1 rad while that due to the dynamical tide is only $\lesssim 10^{-2}$ rad. However, their detectability is not as different as these numbers might suggest. In part, this is

because the dynamical tide phase shift accumulates at lower GW frequencies, where ground-based detectors are more sensitive. There is also more time before the merger to build up the signal-to-noise ratio (SNR) and compare the waveform signal before and after resonance. In addition, because the dynamical tide causes small but sudden increases in GW frequency at mode resonances, it has a unique signature that cannot be easily mimicked by varying other parameters of the binary (such as the masses).

In this Chapter we extend our previous study of dynamical tides in superfluid NSs (Yu & Weinberg, 2017a) in order to account for the possible presence of hyperons in the core. We also evaluate the detectability of the phase shifts induced by the dynamical tide with second and third generation GW detectors. We begin in Section 4.2 by describing our background hyperonic NS model and in Section 4.3 we solve for its g-modes. In Section 4.4, we consider the resonant tidal driving of the g-modes and calculate the resulting GW phase shift. In Section 4.5, we evaluate the prospects for detecting the phase shifts with current and future GW detectors.

4.2 SUPERFLUID MODELS WITH HYPERONS

We construct our background superfluid models using an approach similar to that of Yu & Weinberg (2017; hereafter YW17a), but with some key differences described below; we refer the reader to YW17a and references therein for further details, particularly as pertains to our treatment of the thermodynamics. Briefly, we assume that the background star is non-rotating, cold (zero temperature), in chemical equilibrium, and that all charge densities are balanced. We treat the neutrons in the core as superfluid and all other particle species (protons, Λ -hyperons, electrons, and muons) as normal fluid matter.²

The two main differences between the present approach and that of YW17a are that here: (1) we use the GM1'B equation of state (Gusakov et al., 2014) rather than SLy4(Rikovska Stone et al., 2003), and (2) we solve the general relativistic

²The conditions under which Λ -hyperons become superfluid in NS cores are uncertain (Takatsuka et al., 2006; Wang & Shen, 2010). We assume that they are normal fluid in this study, similar to the g-mode calculations in Dommes & Gusakov (2016).

(GR) Tolman-Oppenheimer-Volkhov (TOV) equations of stellar structure rather than the Newtonian equations. We use GM1'B because it allows for the existence of hyperons in the inner core, is consistent with the existence of $2 M_{\odot}$ NSs, and [Gusakov et al. \(2014\)](#) provide enough detail to allow for a calculation of the Brunt-Väisälä frequency, \mathcal{N} , and thus g-modes. Regarding the second point, in [YW17a](#) we solved the Newtonian equations of stellar structure in order to be consistent with our Newtonian treatment of the stellar oscillations and tidal driving (a relativistic treatment of the tides would significantly complicate the analysis and would not lead to substantially different results). However, $\approx 2 M_{\odot}$ Newtonian models do not reach high enough core densities to yield hyperons in GM1'B ($\rho \gtrsim 7 \times 10^{14} \text{ g/cm}^3$). We therefore construct GR background models which are more compact than Newtonian models and contain hyperons if $M \gtrsim 1.4 M_{\odot}$. For simplicity, however, we still solve for the g-modes and tidal driving using the Newtonian equations of stellar oscillation. As we describe in [Section 4.3](#), we carry out a partial check of the robustness of this hybrid approach by calculating some of the g-modes (but not tidal driving) using the GR equations of stellar oscillation.

We consider superfluid NS models with three different masses: $1.4 M_{\odot}$, $1.5 M_{\odot}$, and $1.6 M_{\odot}$. The $1.4 M_{\odot}$ NS does not contain hyperons because its central density is too low whereas the $1.5 M_{\odot}$ and $1.6 M_{\odot}$ hyperon star (HS) models both contain Λ hyperons in the inner core. The $1.6 M_{\odot}$ HS mass is chosen such that the density of the inner core is high enough to contain Λ hyperons but just slightly too low to contain other hyperon species. In particular, a more massive NS in GM1'B would contain Ξ^- and Ξ^0 hyperons which, while potentially interesting for tidal physics, would considerably complicate the analysis. Compared to the $1.6 M_{\odot}$ HS model, the $1.5 M_{\odot}$ HS model has a smaller mass fraction of hyperons in the inner core. By comparing the results for the three models, we study how the presence and abundance of Λ hyperons modify the g-mode oscillation spectrum and the dynamical tide GW phase shifts.

The conditions for chemical equilibrium due to weak interactions are ([Dommes &](#)

Table 4.1: Parameters of the background NS and HS models.

$M [M_\odot]$	R [km]	ρ_0 [g cm $^{-3}$]	R_Λ [km]	R_μ [km]	R_{cc} [km]
1.4	13.7	6.5×10^{14}	—	11.3	12.2
1.5	13.6	7.1×10^{14}	3.3	11.5	12.3
1.6	13.5	8.1×10^{14}	5.3	11.6	12.4

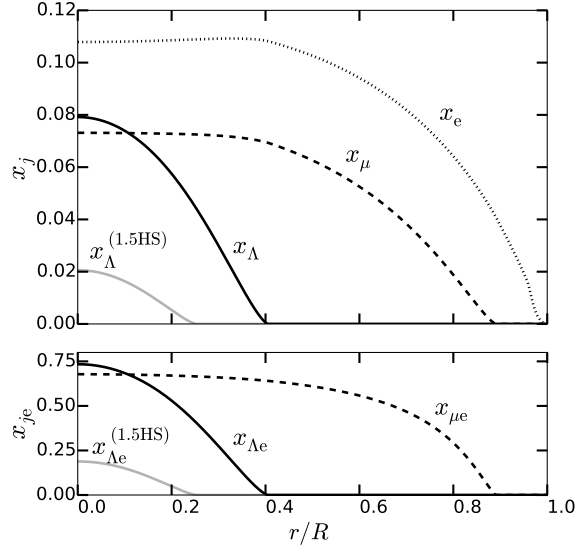


Figure 4-1: Upper panel: number fraction of electrons x_e (dotted line), muons x_μ (dashed line), and Λ hyperons x_Λ (solid black line) as a function of fractional radius r/R for the $1.6 M_\odot$ HS model. For comparison, we also show x_Λ for the $1.5 M_\odot$ HS model (solid grey line). Bottom panel: number of muons per electron $x_{\mu e}$ (dashed line) and Λ hyperons per electron $x_{\Lambda e}$ (solid black line) for the $1.6 M_\odot$ HS model, and $x_{\Lambda e}$ for the $1.5 M_\odot$ HS model (solid grey line).

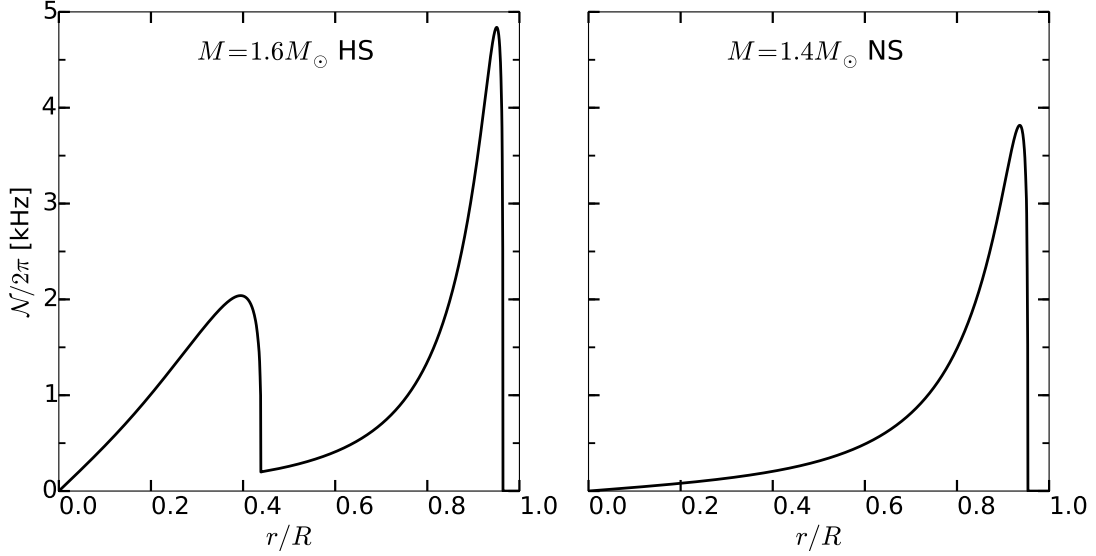


Figure 4-2: Brunt-Väisälä frequency $\mathcal{N}/2\pi$ for the $1.6 M_{\odot}$ HS (left panel) and the $1.4 M_{\odot}$ NS (right panel). Both models have a muonic contribution that peaks in the outer core. The HS has an additional contribution due to hyperons that peaks in the inner core. Note that we evaluate the frequencies in the Newtonian limit [eq. (4.4)].

[Gusakov, 2016](#)),

$$\mu_n = \mu_p + \mu_e, \quad (4.1)$$

$$\mu_n = \mu_{\Lambda}, \quad (4.2)$$

$$\mu_e = \mu_{\mu}, \quad (4.3)$$

where μ_j is the chemical potential of particle species j , with j being either a neutron (n), proton (p), Λ hyperon (Λ), electron (e), or muon (μ). These conditions, along with the equations of stellar structure, determine the composition profile for each star. Because of the presence of hyperons, the equation of state has four degrees of freedom instead of the three in [YW17a](#). In particular, we parametrize the thermodynamic relations in terms of the pressure P , the neutron chemical potential μ_n , the muon-to-electron ratio $x_{\mu e} = x_{\mu}/x_e$, and the Λ -to-electron ratio $x_{\Lambda e} = x_{\Lambda}/x_e$, where $x_j = n_j/n_b$ is the number fraction of species j per baryon and n_j is its number density.

In Table 4.1, we give the values of the following parameters for our three models: total mass M , radius R , central density ρ_0 , radius below which Λ hyperons are present

R_Λ , radius below which muons are present R_μ , and radius of the core-crust interface R_{cc} (defined as where the baryon density $n_{\text{b}} = 0.08 \text{ fm}^{-3}$). In Figure 4-1, we show the composition profile for the $1.6 M_\odot$ HS model and for comparison, $x_\Lambda(r)$ and $x_{\Lambda\text{e}}(r)$ for the $1.5 M_\odot$ HS model.

Based on the discussion in YW17a (see their Section 2.1 and Appendix A), in the Newtonian limit the Brunt-Väisälä (i.e., buoyancy) frequency is given by

$$\mathcal{N}^2 = - \frac{1 - \epsilon_{\text{n}}}{1 - x_{\text{n}} - \epsilon_{\text{n}}} \frac{g}{\rho} \sum_{j=\mu,\Lambda} \left(\frac{\partial \rho}{\partial x_{je}} \right) \frac{dx_{je}}{dr}, \quad (4.4)$$

where the partial derivative is evaluated by holding the three other thermodynamic parameters fixed (P , μ_{n} , and x_{ie} for $i \neq j$), $g(r)$ is the gravitational acceleration at radius r , and ϵ_{n} is the superfluid entrainment function (YW17a, see also Prix & Rieutord 2002). Numerical values for entrainment are provided in Gusakov et al. (2014) but using a different parameterization.

In the core, we evaluate the buoyancy using equation (4.4). In the crust, we follow YW17a and assume for simplicity that the crust is neutrally buoyant ($\mathcal{N} = 0$); this does not significantly affect the core g-modes of interest here since the crust contains only a small fraction of the mass. In Figure 4-2 we show \mathcal{N} for the $1.4 M_\odot$ NS model (right panel) and the $1.6 M_\odot$ HS model (left panel). Whereas the $1.4 M_\odot$ model contains only a single \mathcal{N} peak (due to the muon gradient $dx_{\mu\text{e}}/dr$), the $1.6 M_\odot$ HS model contains two \mathcal{N} peaks (one due to the muon gradient $dx_{\mu\text{e}}/dr$ and one at higher densities due to the Λ hyperon gradient $dx_{\Lambda\text{e}}/dr$). As we show in the next Section, this additional peak leads to a new type of g-mode, i.e., hyperonic g-modes.

We assume that $x_{\mu\text{e}}$ and $x_{\Lambda\text{e}}$ do not vary during oscillations of the normal fluid; i.e., the composition is “frozen” and thus the perturbed fluid element is out of chemical equilibrium. Reisenegger & Goldreich (1992) consider the timescale for the proton fraction x_{p} in a normal fluid NS to relax towards chemical equilibrium due to Urca processes (x_{p} is the source of buoyancy in a normal fluid NS). They show that for even a moderately warm NS, the relaxation timescale is much longer than the oscillation period of low-order g-modes and therefore, to a very good approximation, x_{p} is frozen

within the fluid element. Similarly, to check whether $x_{\Lambda e}$ is frozen, we must consider the direct Urca process $\Lambda \rightarrow p + L + \bar{\nu}_L$, where the lepton in the reaction $L = e$ or μ . In Appendix B.3 we show that the corresponding relaxation timescale is much longer than the oscillation period of low order hyperonic g-modes and therefore the assumption of frozen composition should also hold for these modes.

4.3 EIGENMODES OF A SUPERFLUID HYPERON STAR

The oscillation equations of a superfluid HS are similar to those of a superfluid NS and can be written as (Prix & Rieutord 2002, YW17a)

$$\nabla \cdot (\rho_c \boldsymbol{\xi}_c) + \delta\rho_c = 0, \quad (4.5)$$

$$\nabla \cdot (\rho_n \boldsymbol{\xi}_n) + \delta\rho_n = 0, \quad (4.6)$$

$$\sigma^2 [\boldsymbol{\xi}_c - \epsilon_c (\boldsymbol{\xi}_c - \boldsymbol{\xi}_n)] = \nabla (\delta\tilde{\mu}_c + \delta\Phi), \quad (4.7)$$

$$\sigma^2 [\boldsymbol{\xi}_n + \epsilon_n (\boldsymbol{\xi}_c - \boldsymbol{\xi}_n)] = \nabla (\delta\tilde{\mu}_n + \delta\Phi), \quad (4.8)$$

$$\nabla^2 \delta\Phi = 4\pi G (\delta\rho_c + \delta\rho_n), \quad (4.9)$$

where we assume that the perturbed quantities have a time dependence $e^{i\sigma t}$, $\delta\mathcal{Q}(\mathbf{x})$ denotes the Eulerian perturbation of a quantity \mathcal{Q} at position \mathbf{x} , subscript “n” denotes the neutron superfluid flow, and subscript “c” denotes the normal fluid flow (consisting of the charged particles and the Λ hyperons; we continue to use a subscript c in order to match the notation used in Prix & Rieutord (2002) and YW17a). The other quantities are the mass densities $\rho_{c(n)}$ (the total density $\rho = \rho_c + \rho_n$), the perturbed specific chemical potentials $\delta\tilde{\mu}_{c(n)}$, the Lagrangian displacements $\boldsymbol{\xi}_{c(n)}$, the perturbed gravitational potential $\delta\Phi$, and the entrainment function $\epsilon_c = \epsilon_n \rho_n / \rho_c$ (see YW17a for further details).

Although the oscillation equations take a simple form when written in terms of $\boldsymbol{\xi}_c$ and $\boldsymbol{\xi}_n$, it is more convenient to express the tidal excitation of modes in terms of the

mass-averaged flow $\boldsymbol{\xi}_+$ and the difference flow $\boldsymbol{\xi}_-$, where

$$\boldsymbol{\xi}_+ = \frac{1}{\rho} (\rho_c \boldsymbol{\xi}_c + \rho_n \boldsymbol{\xi}_n), \quad (4.10)$$

$$\boldsymbol{\xi}_- = (1 - \epsilon_n - \epsilon_c) (\boldsymbol{\xi}_c - \boldsymbol{\xi}_n). \quad (4.11)$$

When solving the oscillation equations, we choose $(\boldsymbol{\xi}_+, \boldsymbol{\xi}_n, \delta P, \delta \tilde{\mu}_n, \delta \Phi)$ to be our independent variables. We can then use equations (4.10) and (4.11) to calculate $\boldsymbol{\xi}_c$ and $\boldsymbol{\xi}_-$. Since the Lagrangian perturbations to $x_{\mu e}$ and $x_{\Lambda e}$ vanish for a frozen composition, we can use the chain rule to express the density perturbation as

$$\delta \rho_c = \left(\frac{\partial \rho_c}{\partial P} \right) \delta P + \left(\frac{\partial \rho_c}{\partial \tilde{\mu}_n} \right) \delta \tilde{\mu}_n - \sum_{j=\mu, \Lambda} \left(\frac{\partial \rho_c}{\partial x_{je}} \right) \frac{dx_{je}}{dr} \xi_c^r, \quad (4.12)$$

and similarly for $\delta \rho_n$, where $\xi_c^r(r)$ denotes the radial dependence of the radial component of $\boldsymbol{\xi}_c$ (the angular dependence is given by the spherical harmonic function $Y_{lm}(\theta, \phi)$ of degree l and order m). As we show in YW17a (see also Lindblom & Mendell 1994; Andersson et al. 2004), the operator \mathcal{L} corresponding to equations (4.5)-(4.9) is Hermitian with respect to the inner product

$$\left\langle \begin{bmatrix} \boldsymbol{\xi}_+ \\ \boldsymbol{\xi}_- \end{bmatrix}, \begin{bmatrix} \boldsymbol{\xi}'_+ \\ \boldsymbol{\xi}'_- \end{bmatrix} \right\rangle = \int d^3x \begin{bmatrix} \boldsymbol{\xi}_+^* & \boldsymbol{\xi}_-^* \end{bmatrix} \begin{bmatrix} \rho & 0 \\ 0 & \tilde{\rho} \end{bmatrix} \begin{bmatrix} \boldsymbol{\xi}'_+ \\ \boldsymbol{\xi}'_- \end{bmatrix}, \quad (4.13)$$

where

$$\tilde{\rho} = \frac{\rho_c \rho_n}{(1 - \epsilon_n - \epsilon_c) \rho}. \quad (4.14)$$

The set of eigenmodes thus forms an orthonormal base. We use the same boundary conditions as YW17a and normalize the modes such that

$$\sigma_a^2 \left\langle \begin{bmatrix} \boldsymbol{\xi}_{a+} \\ \boldsymbol{\xi}_{a-} \end{bmatrix}, \begin{bmatrix} \boldsymbol{\xi}_{b+} \\ \boldsymbol{\xi}_{b-} \end{bmatrix} \right\rangle = E_0 \delta_{ab}, \quad (4.15)$$

where σ_a is the eigenvalue of mode a and $E_0 = GM^2/R$.

As Dommes & Gusakov (2016) first showed, the core g-modes of an HS can be

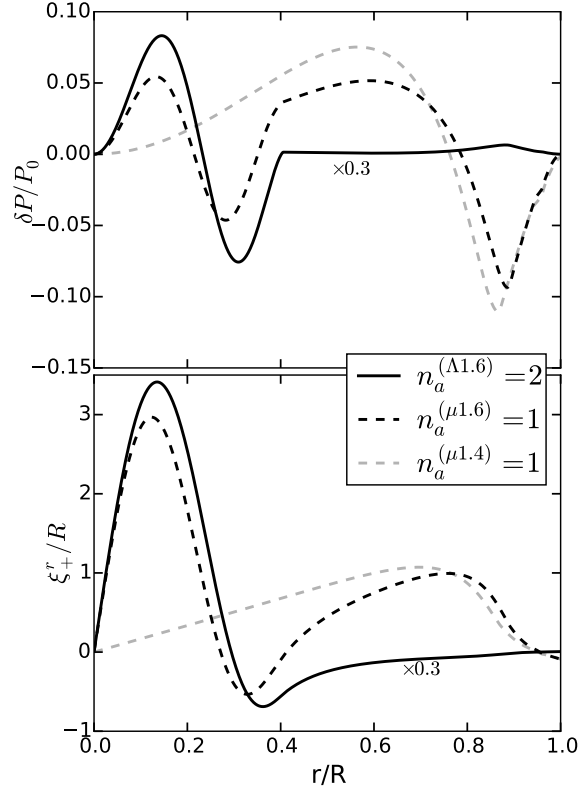


Figure 4-3: Structure of the second hyperonic g-mode $n_a^{(\Lambda 1.6)} = 2$ (solid black lines) and the first muonic g-mode $n_a^{(\mu 1.6)} = 1$ (dashed black lines) of the $1.6M_\odot$ HS and the first g-mode $n_a^{(\mu 1.4)} = 1$ of the $1.4 M_\odot$ NS (dashed grey lines). All three modes have spherical degree $l_a = 2$. The upper panel shows the Eulerian perturbation of the pressure δP in units of the central pressure P_0 . The lower panel shows the radial component of the mass-averaged Lagrangian displacement ξ_+^r in units of R . All quantities are normalized according to Equation (3.31); for display purposes, those corresponding to the $n_a^{(\Lambda 1.6)} = 2$ mode are multiplied by an additional factor of 0.3.

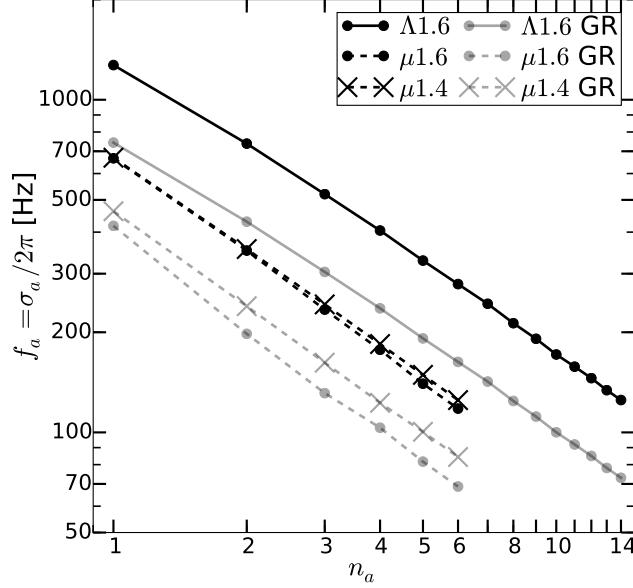


Figure 4-4: Eigenfrequencies $f_a = \sigma_a/2\pi$ of $l_a = 2$ g-modes calculated with the Newtonian oscillation equations (black lines) and the GR oscillation equations (grey lines). For the $1.6 M_\odot$ HS model, we show the hyperonic modes with filled circles connected by solid lines and the muonic modes with filled circles connected by dashed lines. For the $1.4 M_\odot$ NS model, which only have muonic g-modes, we use crosses connected by dashed lines.

classified into two types: “hyperonic” g-modes and “muonic” g-modes. The hyperonic g-modes are primarily supported by the Λ hyperon gradient and are concentrated in the inner core, while the muonic g-modes are supported by a combination of the Λ hyperon and muon gradients and span both the inner and outer core. In Figure 4-3 we show the structure of the second hyperonic g-mode $n_a^{(\Lambda 1.6)} = 2$ and the first muonic g-mode $n_a^{(\mu 1.6)} = 1$ of our $1.6 M_\odot$ HS model.³ In the superscript, $\Lambda 1.6$ ($\mu 1.6$) stands for the hyperonic (muonic) modes of the $1.6 M_\odot$ HS model. We will use this labeling convention throughout the Chapter. For comparison, we also show the first g-mode of our $1.4 M_\odot$ NS model. All three g-modes have angular degree $l_a = 2$ and thus couple to the $l = 2$ harmonic of the tide.

³We use $n_a^{(\Lambda 1.6)}$ and $n_a^{(\mu 1.6)}$ to label the sequential order of each type of g-mode, with $n_a^{(\Lambda 1.6)} = 1$ and $n_a^{(\mu 1.6)} = 1$ corresponding to the highest frequency hyperonic g-mode and muonic g-mode, respectively. They do not necessarily correspond to the mode’s radial order, i.e., the number of radial nodes.

In Figure 4-4 we show the eigenfrequencies $f_a = \sigma_a/2\pi$ of the first several $l_a = 2$ g-modes of our $1.6 M_\odot$ HS and $1.4 M_\odot$ NS models. To guide the eye, we use straight lines to connect each of the hyperonic modes (solid) and, separately, each of the muonic modes (dashed). As we describe in Section 4.2, in order to build HSs without complicating the dynamical tide calculation, we solve the TOV equations to construct the background models but the Newtonian equations to calculate the g-modes and tidal driving. We partially assess the impact of this hybrid approach by redoing the calculation of the g-modes using the GR oscillation equations. For this calculation, we ignore the gravitational perturbations (i.e., we adopt the Cowling approximation) and solve the superfluid GR oscillation equations (see, e.g., Dommes & Gusakov 2016; Passamonti et al. 2016). We find that our hybrid approach overestimates the g-mode eigenfrequencies by $\simeq 70\%$ (see grey lines in Figure 4-4). For example, the highest frequency $l_a = 2$ hyperonic g-mode in the $1.6 M_\odot$ HS has a frequency of $f_a^{(\text{GR})} = 743$ Hz in the fully relativistic calculation (as seen by an observer at infinity) compared to $f_a = 1271$ Hz in the hybrid calculation. Nevertheless, as we show in Section 4.4, the dynamical tide phase shift is independent of the eigenfrequency f_a (in our normalization) and is therefore unaffected by the overestimate of f_a . There is still an error due to our hybrid calculation of the tidal coupling strength, but we argue in Section 4.4 that this should not be too significant.

Consistent with the asymptotic properties of high-order g-modes (Aerts et al., 2010), we find that for modes with $n_a^{(j)} \gtrsim \text{few}$, the GR oscillation equations yield $l_a = 2$ eigenfrequencies that are well approximated by $f_a^{(j,\text{GR})} = f_0^{(j)}/n_a^{(j)}$, where $f_0^{(j)} = \{1020, 410, 460, 500, 510\}$ Hz for $j = \{\Lambda 1.6, \mu 1.6, \Lambda 1.5, \mu 1.5, \mu 1.4\}$, respectively. We find that the characteristic frequency $f_0^{(\Lambda)}$ of the hyperonic modes scales almost linearly with the size of the hyperonic core R_Λ . This is because $f_0^{(\Lambda)} \propto \int_0^{R_\Lambda} \mathcal{N} dr$ and for $r \lesssim R_\Lambda$, the density $\rho \simeq \text{constant}$ and $\mathcal{N} \propto r$.

4.4 TIDAL DRIVING AND PHASE SHIFT OF THE GRAVITATIONAL WAVEFORM

Following YW17a (see also Lai 1994; Weinberg et al. 2012), we solve for the resonant tidal excitation of g-modes by expanding the tidal displacement field as

$$\begin{bmatrix} \xi_+(\mathbf{x}, t) \\ \xi_-(\mathbf{x}, t) \end{bmatrix} = \sum_a b_a(t) \begin{bmatrix} \xi_{a+}(\mathbf{x}) \\ \xi_{a-}(\mathbf{x}) \end{bmatrix}, \quad (4.16)$$

where the subscript $a = \{n_a, l_a, m_a\}$ denotes a specific eigenmode of the NS and $b_a(t)$ is the time-dependent, dimensionless amplitude of mode a (a mode with amplitude $|b_a| = 1$ has energy $E_0 = GM^2/R$). Inserting this expansion into the linear superfluid oscillation equations (4.5)-(4.9) and including the time-dependent tidal potential ($\delta\Phi \rightarrow \delta\Phi + U$) yields the mode amplitude equation

$$\ddot{b}_a + \sigma_a^2 b_a = \sigma_a^2 U_a(t), \quad (4.17)$$

where the tidal driving coefficient

$$U_a(t) = \frac{M'}{M} \sum_{l \geq 2, m} W_{lm} Q_{alm} \left(\frac{R}{D(t)} \right)^{l+1} e^{-im\psi(t)}. \quad (4.18)$$

Here M' is the mass of the companion, lm are harmonics of the tidal potential, the coefficients $W_{lm} = 4\pi(2l+1)^{-1}Y_{lm}(\pi/2, 0)$ are of order unity for the dominant harmonics (Press & Teukolsky, 1977), $D(t)$ is the orbital separation, and $\psi(t)$ is the orbital phase.

The time-independent, dimensionless tidal coupling coefficient (sometimes referred to as the tidal overlap integral)

$$Q_{alm} = \frac{1}{MR^l} \int d^3x \rho \xi_{a+}^* \cdot \nabla (r^l Y_{lm}). \quad (4.19)$$

By angular momentum conservation, Q_{alm} is non-zero only if $l_a = l$ and $m_a = m$.

Based on our numerical calculations, we find that the Q_{alm} of our different models and mode types are approximately given by

$$|Q_{alm}^{(j)}| = Q_0 n_a^{-\alpha}, \quad (4.20)$$

where $\alpha \approx 2.5$ and

$$Q_0^{(j)} = \{1.7, 3.6, 1.6, 3.5, 4.0\} \times 10^{-3}, \quad (4.21)$$

for $j = \{\Lambda 1.6, \mu 1.6, \Lambda 1.5, \mu 1.5, \mu 1.4\}$, respectively.

Although these values are based on the hybrid calculation (GR background and Newtonian oscillations), we expect the error due to this inconsistency to be relatively small. As an approximate measure of the correction, we computed $|Q_{alm}|$ for the $1.4 M_\odot$ NS model but with the background constructed using the Newtonian structure equations rather than the TOV equations (we could not perform such a test for the HS model because a $2.0 M_\odot$ Newtonian model does not contain hyperons). We find that Q_{alm} changes by at most 5%, which suggests that our hybrid model gives a reasonably accurate estimate of the tidal coupling strength. Indeed, given that $GM/Rc^2 \approx 20\%$, we do not expect relativistic corrections to be much bigger than a few tens of percent.

We numerically solve the amplitude equation (4.17) of the resonantly driven g-modes and find that the result is in good agreement with the analytic solution given by the stationary-phase approximation (Lai, 1994; Reisenegger & Goldreich, 1994). The GW phase shift induced by the resonant excitation of each mode is therefore approximately given by (YW17a)

$$\delta\phi_a = -\frac{5\pi^2}{2048} k' \left(\frac{GM}{Rc^2}\right)^{-5} \sum_{m=\pm 2} |Q_{a2m}|^2, \quad (4.22)$$

where $k' = 2/[q(1+q)]$, $q = M'/M$, and here the subscript a already accounts for the contributions from both the $m_a = 2$ and $m_a = -2$ modes. Since $\delta\phi_a$ depends on f_a only through $|Q_{alm}|$, and we expect that our hybrid approach accurately estimates $|Q_{alm}|$ to within a few tens of percent, our estimate of $\delta\phi_a \propto |Q_{alm}|^2$ should be

Table 4.2: Eigenfrequencies $f_a^{(\text{GR})}$ and gravitational waveform phase shift $\delta\phi_a$ for the three-lowest order $l_a = 2$ g-modes for each stellar model. The format is $\{f_a/100 \text{ Hz}, |\delta\phi_a|/\text{rad}\}$.

j	$n_a^{(j)} = 1$	$n_a^{(j)} = 2$	$n_a^{(j)} = 3$
$\Lambda 1.6$	{7.4, 5.5e-4}	{4.3, 3.4e-4}	{3.0, 3.6e-7}
$\mu 1.6$	{4.1, 3.4e-3}	{2.0, 1.6e-5}	{1.3, 1.2e-5}
$\Lambda 1.5$	{4.1, 1.1e-3}	{2.5, 1.6e-7}	{1.4, 6.6e-7}
$\mu 1.5$	{4.5, 5.4e-3}	{2.4, 6.6e-6}	{1.6, 2.1e-5}
$\mu 1.4$	{4.6, 9.8e-3}	{2.4, 3.6e-7}	{1.6, 3.0e-5}

accurate to within a factor of order unity.

In Table 4.2 we list $f_a^{(\text{GR})}$ (see grey lines in Figure 4-4) and $\delta\phi_a$ for the three-lowest order $l_a = 2$ g-modes of each type, for each stellar model. Numerically, we find that summing over all of the resonantly excited modes yields a total cumulative phase shift

$$\delta\phi^{(1.6\text{HS})} = -4.3 \times 10^{-3} k', \quad (4.23)$$

$$\delta\phi^{(1.5\text{HS})} = -6.7 \times 10^{-3} k', \quad (4.24)$$

$$\delta\phi^{(1.4\text{NS})} = -9.9 \times 10^{-3} k', \quad (4.25)$$

where $\delta\phi^{(\text{HS})}$ accounts for both the hyperonic modes and muonic modes.

As can be gleaned from Table 4.2 [also equations (4.20) - (4.22)], the total phase shift is dominated by the contributions of the $n_a = 1$ g-modes (the modes with the highest frequency). The phase shifts due to muonic modes are insensitive to whether hyperons are present in the core and decrease with increasing HS/NS mass. In the HS models, the cumulative phase shift due to the muonic g-modes is about five times larger than that due to the hyperonic g-modes. Moreover, comparing the $1.6 M_\odot$ HS model to the $1.5 M_\odot$ HS model, we find that the phase shift due to the hyperonic modes is relatively insensitive to the size of the hyperon core R_Λ , in contrast to the eigenfrequency spectrum which is shifted to lower frequencies as the mass of the hyperon core decreases (see discussion at end of Section 4.3).

4.5 DETECTABILITY OF THE MODE RESONANCES

In this Section we estimate the detectability of the dynamical tide phase shift using the Fisher matrix formalism (Cutler & Flanagan, 1994). In Section 4.5.1, we describe how we model the GW signal and the detectability of the resonances based on single events and multiple stacked events. In Section 4.5.2, we present our detectability estimates for Advanced LIGO and proposed third generation GW detectors.

4.5.1 Modeling the detectability

Following Cutler & Flanagan (1994), if we assume a strong GW strain signal $h(t)$ and Gaussian detector noise, then the signal parameters θ^i have a probability distribution $p(\theta^i) \propto \exp[-(1/2)\Gamma_{ij}d\theta^i d\theta^j]$, where $d\theta^i = \theta^i - \hat{\theta}^i$ is the difference between the parameters and their best fit values $\hat{\theta}^i$ and

$$\Gamma_{ij} = \left(\frac{\partial h}{\partial \theta^i} \middle| \frac{\partial h}{\partial \theta^j} \right) \quad (4.26)$$

is the Fisher information matrix. The parentheses denote the inner product

$$(h_1|h_2) = 2 \int_0^\infty \frac{\tilde{h}_1^*(f)\tilde{h}_2(f) + \tilde{h}_1(f)\tilde{h}_2^*(f)}{S_n(f)} df, \quad (4.27)$$

where \tilde{h}_1 and \tilde{h}_2 are the Fourier transforms of h_1 and h_2 and $S_n(f)$ is the strain noise power spectral density. The signal-to-noise ratio (SNR) of a signal h is given by $\text{SNR} = (h|h)^{1/2}$ and the root-mean-square (rms) measurement error in θ^i is given by a diagonal element of the inverse Fisher matrix

$$\Delta\theta^i = \sqrt{(\Gamma^{-1})^{ii}}. \quad (4.28)$$

If the rms error in, say, the phase shift due to a particular resonance $\Delta(\delta\phi_a)$ is smaller than $\delta\phi_a$, then that phase shift is detectable.

The above analysis is based on the detection of a single inspiral event. We can roughly estimate how stacking multiple events would affect the measurement accuracy

by using the approach given in [Markakis et al. \(2010\)](#); a more precise estimate would require a fully Bayesian investigation and is beyond the scope of this paper (see, e.g., the recent studies of the detectability of the equilibrium tide phase shift by [Del Pozzo et al. 2013](#); [Lackey & Wade 2015](#); [Agathos et al. 2015](#)). The estimate assumes that the events are homogeneously distributed in a sphere of effective radius $d_{\text{max}}^{\text{eff}}$ and that the error in each parameter $\Delta\theta$ scales linearly with effective distance $d^{\text{eff}} < d_{\text{max}}^{\text{eff}}$.⁴ Then, [Markakis et al. \(2010\)](#) show that the rms error averaged over all of the events is

$$\langle \Delta\theta \rangle \approx \frac{\Delta\theta_{\text{ref}}}{d_{\text{ref}}^{\text{eff}} \sqrt{4\pi \mathcal{R} P_{\text{obs}} d_{\text{max}}^{\text{eff}}}}, \quad (4.29)$$

where $\Delta\theta_{\text{ref}}$ is the rms error of parameter θ from a single reference event at effective distance $d_{\text{ref}}^{\text{eff}}$, \mathcal{R} is the event rate per unit time per unit volume, and P_{obs} is the total observation period. In the above calculation we ignore the cosmological expansion and assume that the event rate is constant.

Similar to [Balachandran & Flanagan \(2007\)](#), who also studied the detectability of mode resonances (see also [Flanagan & Racine 2007](#)), we assume that the frequency-domain GW signal has the form

$$\tilde{h}(f) = \mathcal{A} f^{-7/6} e^{i\Psi(f)}, \quad (4.30)$$

where the amplitude ([Maggiore, 2007](#))

$$\mathcal{A} = \left(\frac{5}{24\pi^{4/3}} \right)^{1/2} \left(\frac{G\mathcal{M}}{c^3} \right)^{-5/6} \frac{\mathcal{K}}{d}. \quad (4.31)$$

Here $\mathcal{M} = [(MM')^3/(M + M')]^{1/5}$ is the chirp mass, d is the distance to the source, and \mathcal{K} is the antenna response (for an optimally oriented source $\mathcal{K} = 1$). Our model of the phase evolution $\Psi(f)$ accounts for the point-particle contribution including post-Newtonian corrections up to the 1.5th order, and for the resonant tidal excitation of

⁴The effective distance d^{eff} is defined as the distance obtained by averaging over a uniform source orientation for an event with a given SNR. It is related to the horizon distance d^{hor} , the distance assuming an optimal source orientation, as $d^{\text{eff}} = d^{\text{hor}}/2.3$ (see, e.g., Appendix D of [Allen et al. 2012](#)).

individual g-modes. We ignore higher order post-Newtonian terms, spin, the equilibrium tide, and nonlinear tidal effects (such as those considered in [Essick et al. 2016](#)), and assume that the signal shuts off at the gravitational wave frequency corresponding to the inner-most stable circular orbit $f = 2f_{\text{isco}} \simeq 1.6 \times 10^3 \text{ Hz}$ [$2.8M_{\odot}/(M + M')$] ([Cutler & Flanagan, 1994](#); [Poisson & Will, 1995](#)). In Appendix D we show that under these assumptions,

$$\Psi(f) = \Psi_{\text{pp}}(f) - \sum_a \left(1 - \frac{f}{f_a}\right) \delta\phi_a \Theta(f - f_a), \quad (4.32)$$

where $\delta\phi_a$ is the phase shift due to the tidal resonance with a mode a with eigenfrequency f_a , and $\Theta(f - f_a)$ is the Heaviside step function. By the stationary-phase approximation, the point-particle phase is ([Cutler & Flanagan, 1994](#))

$$\begin{aligned} \Psi_{\text{pp}}(f) = & 2\pi f t_c - \phi_c - \frac{\pi}{4} + \frac{3}{4} \left(\frac{8\pi G \mathcal{M} f}{c^3} \right)^{-5/3} \\ & \times \left[1 + \frac{20}{9} \left(\frac{743}{336} + \frac{11\mu}{4M_{\text{tot}}} \right) x - 16\pi x^{3/2} \right]. \end{aligned} \quad (4.33)$$

Here t_c and ϕ_c are constants of integration that set a reference time and phase. $M_{\text{tot}} = (M + M')$ and $\mu = MM'/M_{\text{tot}}$ are the total and reduced mass of the system, respectively, and the quantity x is defined as $x = (\pi G M_{\text{tot}} f / c^3)^{2/3}$. The duration of each resonance is, in general, much shorter than the orbital decay timescale due to radiation reaction (their ratio is $\simeq 0.1 \times [(\mathcal{M}/1.2M_{\odot})(f/500 \text{ Hz})]^{5/6}$; see [Lai 1994](#); [Flanagan & Racine 2007](#); [Balachandran & Flanagan 2007](#)). We therefore model the resonance as an instantaneous process, which should be a good approximation since nearly all the g-modes we consider have $f_a^{(\text{GR})} < 500 \text{ Hz}$ (the one exception is the $n_a = 1$ hyperonic g-mode of the $1.6M_{\odot}$ HS model which has $f_a^{(\text{GR})} = 740 \text{ Hz}$).

Since the phase shift is dominated by the resonant excitation of the lowest order mode, for simplicity we do not sum over the modes in our waveform model but instead just consider the phase shift due to a single mode. Our model therefore depends on 7 parameters: \mathcal{A} , \mathcal{M} , μ , t_c , ϕ_c , f_a , and $\delta\phi_a$. [Flanagan & Racine \(2007\)](#) also consider the effect of phase shifts on the GW signal, although their model is written in terms

of the phase of the time-domain waveform $\phi(t)$ [their equation (1.9)] rather than the frequency-domain waveform $\Psi(f)$. In Appendix D we show that the two treatments are consistent.

Before examining the numerical results, note that

$$\frac{\partial \tilde{h}}{\partial (\delta \phi_a)} = -i \left(1 - \frac{f}{f_a}\right) \Theta(f - f_a) \tilde{h}, \quad (4.34)$$

$$\frac{\partial \tilde{h}}{\partial f_a} = -i \delta \phi_a \frac{f}{f_a^2} \Theta(f - f_a) \tilde{h}. \quad (4.35)$$

Note that the $(1 - f/f_a)$ factor eliminates the δ -function at $f = f_a$ stemming from the derivative of Θ . By equation (4.28), we see that $\Delta(\delta \phi_a)$ and Δf_a both vary linearly with distance (and thus inversely with SNR) and that $\Delta(\delta \phi_a)$ is independent of $\delta \phi_a$ whereas $\Delta f_a \propto (\delta \phi_a)^{-1}$. Conceptually, these last two properties reflect the fact that the measurability of phase shifts $\Delta(\delta \phi_a)$ is mostly determined by how much SNR accumulates before and after the resonance (which is independent of $\delta \phi_a$ itself), whereas the larger $\delta \phi_a$ is, the easier it is to localize the frequency of the resonance (and thus the smaller Δf_a is). Lastly, because the dominating g-modes are excited at frequencies higher than the most sensitive band of ground-based GW detectors (≈ 70 Hz), larger f_a have larger $\Delta(\delta \phi_a)$ and $\Delta(f_a)$ and thus worse detectability. This is different from the results in Balachandran & Flanagan (2007) who found that increasing f_a would make the detection easier, as Balachandran & Flanagan (2007) considered modes that were excited at frequencies lower than the most sensitive band.

4.5.2 Detectability with second and third generation detectors

For the numerical results, we take $M = M' = 1.4 M_\odot$ (using $M = M' = 1.5 M_\odot$ or $1.6 M_\odot$ in the Fisher matrix calculation changes the rms errors only by $\lesssim 10\%$). Since the values of t_c and ϕ_c do not affect the evaluation of $\Delta(\delta \phi)$ and Δf_a , we set them equal to zero. We show results for four sets of tidal parameters, $(f_a/\text{Hz}, \phi_a/\text{rad}) = (100, -0.01), (450, -0.01), (450, -0.001),$ and $(750, -0.001)$, corresponding to the lowest order g-mode in the normal-fluid NS model, the lowest order muonic g-mode

Table 4.3: Threshold distance $d_{\text{th}}^{\text{hor}}$ out to which dynamical tide resonances are detectable [$\Delta(\delta\phi_a) = |\delta\phi_a|$] assuming a single merger event.

f_a [Hz]	$\delta\phi_a$ [rad]	Detector	$d_{\text{th}}^{\text{hor}}$ [Mpc]	SNR	Δf_a [Hz]
100	-0.01	aLIGO	1.8	1.7e+3	32
		CE	52	2.9e3	26
		ET-D	25	2.0e+3	28
450	-0.01	aLIGO	1.2	2.5e+3	220
		CE	26	5.9e3	210
		ET-D	16	3.1e3	220
450	-0.001	aLIGO	0.12	3.1e+4	220
		CE	2.6	5.9e+4	210
		ET-D	1.6	3.1e+4	220
750	-0.001	aLIGO	0.06	5.2e+4	280
		CE	0.8	1.8e+5	240
		ET-D	0.5	1.0e+5	240

in the superfluid NS/HS model, the first hyperonic mode in the $1.5 M_\odot$ HS model, and the first hyperonic mode in the $1.6 M_\odot$ HS model, respectively. Higher order g-modes resonate at lower frequencies and have smaller $\Delta(\delta\phi_a)$ because more SNR is accumulated after their resonances [equation (4.34)]. However, because of the steep falloff of $\delta\phi_a$ with decreasing frequency [increasing n_a ; see equation (4.20)], it is much more difficult to detect their phase shifts.

For the detector noise, we consider the noise curves of Advanced LIGO (aLIGO) at design sensitivity (Aasi et al., 2015), and the noise curves of proposed third generation detectors including the Cosmic Explorer (CE; Abbott et al. 2017a) and the Einstein Telescope (specifically, ET-D; Hild et al. 2011). For simplicity we consider here only the detectability of a single detector instead of a network of detectors (Schutz, 2011). We also ignore the tidal phase shift due to the companion NS/HS which should increase $\delta\phi_a$ by a factor of two if $M = M'$.

Our analysis neglects systematic uncertainties due to calibration errors in the instruments. The current calibration uncertainty of aLIGO is somewhat larger than the phase shift due to dynamic tides (the phase uncertainty is $\simeq 0.03$ rad at 450 Hz; Vitale et al. 2012; Abbott et al. 2016a). Regardless, we show that for aLIGO the measurement errors dominate [$\Delta(\delta\phi_a) \gtrsim 0.1$ rad even with event stacking] and pre-

clude detecting the dynamical tide with aLIGO. As for the third generation detectors, currently there is no published estimate of their expected calibration performance. We therefore ignore this effect in our study and work under the assumption that it will be at least a factor of ~ 10 better than aLIGO's.

Single events

In Table 4.3 we show the threshold horizon distance $d_{\text{th}}^{\text{hor}}$ out to which different GW detectors can measure tidal resonances assuming a single merger event. Here $d_{\text{th}}^{\text{hor}}$ is defined to be the distance at which an event has $\Delta(\delta\phi_a) = |\delta\phi_a|$ assuming an optimal antenna response $\mathcal{K} = 1$. We also give the events corresponding SNR and Δf_a . Compared to the normal-fluid g-modes, the superfluid ones are harder to detect because their resonant frequencies are higher and thus less post-excitation SNR is accumulates. For the dominating muonic mode ($f_a = 450$ Hz, $\delta\phi_a = -0.01$ rad), aLIGO can detect such a feature only for an event happening within 1.2 Mpc (i.e., within the Local Group). With the third generation detectors, this horizon distance can be pushed out to $\approx 10 - 30$ Mpc, and thus could include the Virgo Cluster (16 Mpc). If we account for the random source orientation (by dividing $d_{\text{th}}^{\text{hor}}$ by 2.3) and assume the “most-likely” event rate of $\mathcal{R} = 10^3 \text{ Gpc}^{-3} \text{ yr}^{-1}$ (Abadie et al. 2010; Abbott et al. 2016f), we find that such an event should happen only once every ≈ 150 yr at CE sensitivity (here we ignore that the Universe is far from being homogeneous in such a local range and simply assume that the sources are uniformly distributed).

In terms of SNR, the detection of g-modes from a single event typically requires an $\text{SNR} \gtrsim 2000$, with the exact number depending on the detailed shape of the sensitivity curve. As a comparison, for a typical event with $\text{SNR} = 12$, with aLIGO we can only measure $\Delta(\delta\phi_a) = 2.1$ rad, which is more than two orders of magnitude larger than $\delta\phi_a$, and $\Delta f_a = 4.5 \times 10^4$ Hz, which is greater than the entire detector bandwidth.

As for the hyperonic mode, its small phase shift makes its detection possible only from the extremely loud events with $\text{SNR} \gtrsim 10^4$. Even with CE, the most sensitive

detector we consider, the horizon distance can only reach 2.6 (0.8) Mpc for the $1.5 M_\odot$ ($1.6 M_\odot$) HS model. Therefore, unless there is an extremely rare nearby event, the phase shift due to a hyperonic mode is unlikely to be detected from a single event.

Multiple stacked events

In Table 4.4, we give the rms errors $\langle\Delta(\delta\phi_a)\rangle$ and $\langle\Delta(f_a)\rangle$ found by stacking multiple events. We assume a total observation duration $P_{\text{obs}} = 10$ years, an SNR cutoff of 40 to determine $d_{\text{max}}^{\text{eff}}$, and an event rate of $\mathcal{R} = 10^3 \text{ Gpc}^{-3} \text{ yr}^{-1}$ (Abadie et al., 2010; Abbott et al., 2016f). Under these assumptions, the number of expected events is 2, 2×10^5 , and 1×10^4 for aLIGO, CE, and ET-D, respectively (CE has the largest $d_{\text{max}}^{\text{eff}}$, with a cosmological redshift $z = 0.3$).

We find that aLIGO can only measure phase shifts to an accuracy of $\langle\Delta(\delta\phi_a)\rangle \gtrsim 0.3 \text{ rad}$. Since this is at least an order of magnitude larger than the phase shifts induced by resonant mode excitation, the dynamical tide is unlikely to be detectable with aLIGO even with event stacking.

By contrast, with CE the phase shifts can be measured to an accuracy of $\langle\Delta(\delta\phi_a)\rangle \approx 2 \times 10^{-3} \text{ rad}$. CE should therefore be able to detect the phase shift due to the muonic modes ($\delta\phi_a \approx 10^{-2} \text{ rad}$); they might only be marginally detectable with a single ET-D alone, however. CE has rms errors that are ≈ 100 times smaller than aLIGO because its $\Delta\theta_{\text{ref}}$ is 15 times smaller (it accumulates 15 times more SNR post-resonance than aLIGO for the same source) and, for a given SNR cutoff, its $d_{\text{max}}^{\text{eff}}$ is ≈ 40 times larger [cf. eq. (4.29)].

Detecting the phase shift due to the hyperonic modes ($\delta\phi_a \approx 10^{-3} \text{ rad}$) will, however, be difficult even with CE event stacking given that $\langle\Delta(\delta\phi_a)\rangle > |\delta\phi_a|$. Moreover, \mathcal{R} is predicted to be smaller for higher-mass NSs (Kiziltan et al., 2013), i.e., those containing hyperon cores, and therefore there will be fewer such events to stack. It may also be difficult to distinguish the phase shifts of the hyperonic modes from those of the muonic modes, especially if the dominant (i.e., lowest order) muonic and hyperonic modes have similar frequencies, as is the case in our $1.5 M_\odot$ HS model.

Our stacking calculation only accounts for the distance distribution of the sources

Table 4.4: Measurement errors found by stacking events for different detectors and values of f_a and $\delta\phi_a$.

f_a [Hz]	$\delta\phi_a$ [rad]	Detector	$\langle\Delta(f_a)\rangle$ [Hz]	$\langle\Delta(\delta\phi_a)\rangle$ [rad]
100	-0.01	aLIGO	630	0.19
		CE	2.5	0.0010
		ET-D	9.6	0.0034
450	-0.01	aLIGO	6100	0.28
		CE	42	0.0020
		ET-D	120	0.0053
450	-0.001	aLIGO	6.1e+4	0.28
		CE	420	0.0020
		ET-D	1200	0.0053
750	-0.001	aLIGO	1.7e+5	0.60
		CE	1500	0.006
		ET-D	4100	0.017

but otherwise assumes all the events are identical. It therefore neglects variation of the inspiral parameters, including the NS mass distribution. Although this is a coarse approximation that should be relaxed in future studies, we do not expect it to significantly affect our estimates of $\langle\Delta(\delta\phi_a)\rangle$. From equation (4.29), we see that $\langle\Delta\theta\rangle \propto \Delta\theta_{\text{ref}}$, where $\Delta\theta_{\text{ref}}$ is the reference value that is intended to be representative of all the events. Considering the phase shift measurement ($\theta = \delta\phi_a$), we showed in Section 4.5.1 that $\Delta(\delta\phi_a)$ is independent of $\delta\phi_a$ and instead mostly depends on f_a . From Table 4.2 we see that for the muonic modes, f_a is nearly independent of M (it only changes by 10% in going from $1.4 M_\odot$ to $1.6 M_\odot$). Therefore, for each detector there is a reliable reference value for $\Delta(\delta\phi_a)$ and our estimate of $\langle\Delta(\delta\phi_a)\rangle$ should not be strongly affected by our neglect of the mass distribution of the events.

4.6 CONCLUSIONS

We studied the dynamical tide in coalescing NS binaries and investigated how the resonant excitation of g-modes might impact the GW signal. In our previous work (YW17a), we carried out the first study of dynamical tides in a superfluid NS. We showed that the dynamical tide, unlike the equilibrium tide, is directly sensitive to the

composition and superfluid state of the core and thus offers a unique probe of the NS interior. Here, we extended the results of [YW17a](#) by allowing for hyperons in the NS core. [Dommes & Gusakov \(2016\)](#) showed that hyperons modify the buoyancy profile in the star and give rise to a new type of g-mode. We confirmed their results, and calculated the spectrum of hyperonic g-modes in the inner core and muonic g-modes in the outer core for different NS models (with varying hyperon core radii R_Λ). We found that the characteristic frequency of the hyperonic g-modes increases linearly with R_Λ and that the hyperonic g-modes can have considerably higher frequencies than the muonic g-modes. We also showed that the frequency and tidal coupling of the muonic modes is not particularly sensitive to the existence of hyperons in the core.

The resonant tidal excitation of the hyperonic and muonic g-modes remove energy from the orbit and induce phase shifts in the GW signal. We found that the lowest order g-modes induce the largest phase shifts, with magnitudes $|\delta\phi_a| \sim 10^{-3} - 10^{-2}$ rad. The muonic g-modes, which are concentrated in the outer core where the tide is stronger, induce phase shifts that are a few times larger than that of the hyperonic g-modes.

Using the Fisher matrix formalism, we estimated the detectability of the induced phase shifts both from single events and from stacked events. We found that with the next generation GW detectors (CE and/or ET), a single, optimally oriented event within ≈ 20 Mpc (e.g., within the Virgo Cluster) should be loud enough to detect the phase shift due to the muonic modes. The system would need to be about five to ten times closer (e.g., within the Local Group), in order to detect the smaller phase shifts associated with the hyperonic modes. While such nearby events are rare, we found that by stacking multiple events, there is a reasonably good likelihood that next generation detectors can detect the phase shifts induced by the muonic modes. Measuring the frequency and phase shift of the muonic mode resonance can help constrain the stratification and superfluid state of the NS core. The phase shift due to the hyperonic modes will likely be difficult to detect even with event stacking.

By restricting our models to relatively low masses ($M \leq 1.6M_\odot$), we ensured

that the only type of hyperon in the core were Λ hyperons. In the future, it might be interesting to also study higher mass models, which would include Ξ^- and Ξ^0 hyperons. Their composition gradients presumably give rise to yet more types of g-modes in the core. We also assumed that the Λ hyperons were normal fluid in the inner core (consistent with the treatment in [Dommes & Gusakov \(2016\)](#)). Whether the hyperons will be superfluid is uncertain, but if they are then they might either have a modified g-mode spectrum compared to our model or they might not support g-modes at all (similar to the g-modes supported by the proton-to-neutron gradient, which vanish when the neutrons are superfluid; [Lee 1995](#); [Andersson & Comer 2001](#); [Prix & Rieutord 2002](#)). Finally, it would also be interesting to investigate how tidal coupling in a superfluid NS is modified by rotation and nonlinear instabilities, both of which have been shown to be potentially important in the normal fluid case (see, respectively, [Ho & Lai 1999](#); [Lai & Wu 2006](#); [Flanagan & Racine 2007](#) and [Weinberg et al. 2013](#); [Venumadhav et al. 2014](#); [Weinberg 2016](#); [Essick et al. 2016](#)).

Chapter 5

Overview of the aLIGO detectors

In this Chapter we review the optical topology of the aLIGO interferometer and provide analytical derivations of the optical fields at each port of the instrument. Here we focus on a one-dimensional interferometer where all the optical components are perfectly aligned and mode-matched. The effects of higher-order spatial modes will be examined in details in the following Chapters which build upon the results derived here.

Before going into details, it would be helpful to distinguish three different frequency scales. The first one is the laser oscillation frequency, $\nu_0 = \omega_0/2\pi = c/\lambda_0 \simeq 3 \times 10^{14}$ Hz, where $\lambda_0 = 1.064$ nm is the laser wavelength used by aLIGO. This frequency determines the energy carried per photon being $\hbar\omega_0$. The second scale corresponds to the radio frequency (RF) of a few to a few hundred MHz. For aLIGO, it utilizes multiple RF sidebands to keep the resonant condition of the interferometer via the Pound-Drever-Hall (PDH) technique [Drever et al. \(1983\)](#). Lastly, the frequency band we are mostly interested in lies in the audio band ranging from a few Hz to a few kHz. This is the frequency band where the GW signals from merging stellar-mass BH or NS binaries are above aLIGO's noise background.

Through out this Chapter and the following ones, we adopt the following conventions. We denote an optical field as E whose dimension is set so that E^2 has the dimension of power. To model the transmission and reflection at a dielectric boundary, we let the optical field pick up a phase shift of $\pi/2$ for every transmission through

a surface, whereas it experiences no extra phase change upon reflection. Note that with this convention any optical component considered will have two surfaces. As for field propagations, we assume that the free space is always an integer multiple of the laser wavelength λ_0 , while the residual tuning is then assigned to mirrors as one of their parameters. Those are the same conventions used in the numerical simulation tool **FINESSE** [Brown & Freise \(2014\)](#) which we will use frequently to numerically verify our analytical results.

This Chapter is organized as the following. In [Section 5.1](#) we give a brief, qualitative overview of aLIGO’s optical topology. A more quantitative discussion then follows In [Section 5.2](#) where we consider the DC buildups of both the carrier field and the RF sidebands. At the same time we will also introduce the technique of mapping compound optical cavities into a single effective mirror, thereby allowing one to analyze complex systems such as aLIGO in an analytically trackable manner. These DC fields then serve as the seeds from which signal sidebands at AC are generated. This is discussed in [Section 5.3](#). The focus will be on the differential arm motions which can be generated by a passing-by GW. A semi-classical derivation of the instrument’s limitation due to fundamental quantum limit will also be presented.

5.1 OPTICAL TOPOLOGY

We present the optical layout of the aLIGO interferometer in [Figure 5-1](#). It is known as a “dual-recycled Fabry-Perot Michelson interferometer”, which can be understood as the following. The central beamsplitter (BS) and the two end test masses (ETMs; we will further refer the ETM on the transmission of the central BS the ETMX, and the one on the reflection the ETMY) form a Michelson interferometer which allows differential motions between the ETMs (e.g. the motion generated by GWs) to be detected at the output, or the anti-symmetric port. On the other hand, common-mode signals such as the frequency fluctuations of the laser will be reflected to the input, or the symmetric port. To enhance the sensitivity to the displacement, two input test masses (ITMs) are placed in between the BS and the ETMs. The ITM

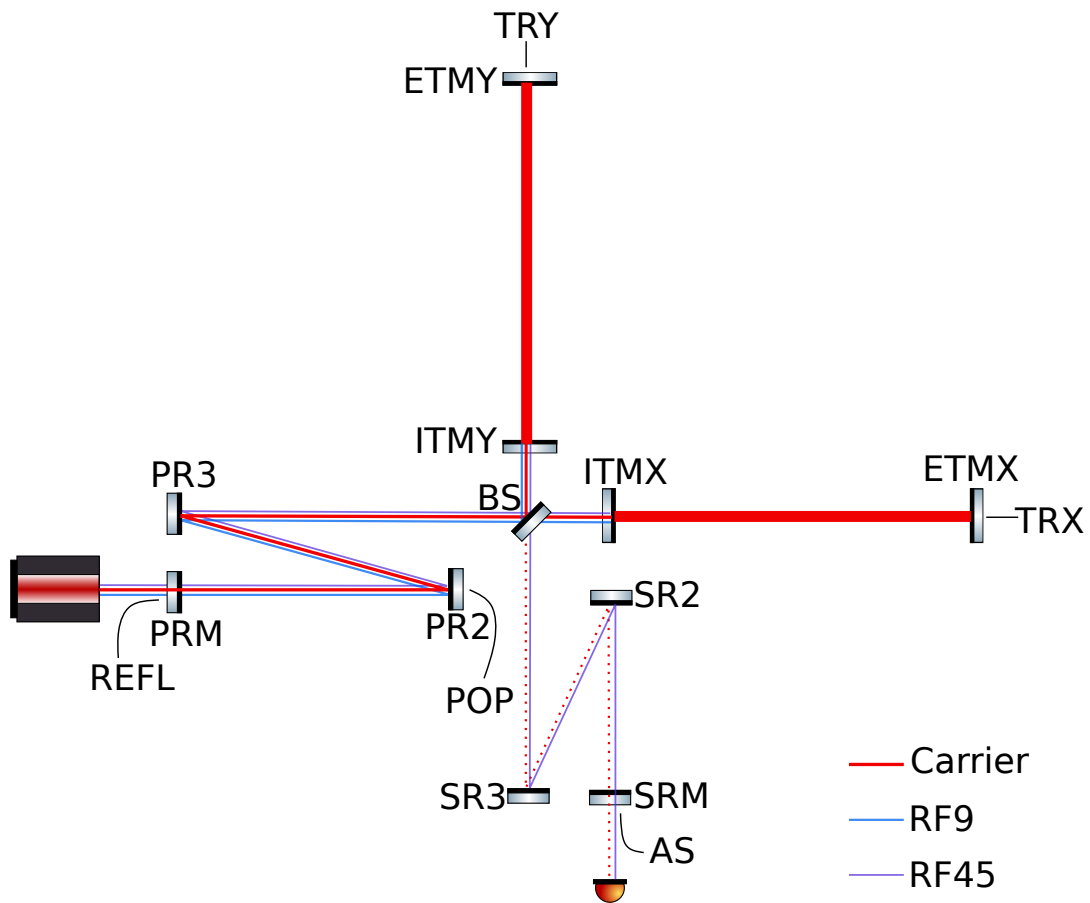


Figure 5-1: The optical layout of the aLIGO interferometer (only core optics are shown). In the drawing we also label the locations of major readout ports.

and the ETM thus forms a Fabry-Perot cavity (also known as the arm cavity) which not only increases the number of photons sampling the test masses' displacement at a given instant, but also traps a given photon inside the cavity to bounce back and forth multiple times and repeatedly performing the displacement measurement. To further enhance the number of photons and consequently reducing the statistical uncertainty, a power-recycling mirror (PRM) is placed at the input port, which sends the beam returning from the BS to the input port back to the arm cavities to further increase the power circulating in the arms. Lastly, a signal-recycling mirror (SRM) is placed at the output (anti-symmetric) port to form a signal recycling cavity¹ with the ITMs. If a photon is trapped inside the arm cavity for a time longer than the oscillation period of a GW harmonic, the sensitivity to such a high-frequency signal will be reduced. The purpose of signal recycling is to modify the effective ITM reflectivity seen by the signal photons and alter its storage time in the arm cavity, thereby allowing the tradeoff between the instrument's peak sensitivity and its bandwidth.

In the following sections we will explore the above descriptions in more quantitative details. For the key optical parameters, they are defined in Table 5.1 with numerical value provided. Throughout this chapter, we will use T (R) to denote the power transmissivity (reflectivity) of a mirror and $t = \sqrt{T}$ ($r = \sqrt{R}$) to denote the amplitude transmissivity (reflectivity). When denoting the properties of a physical mirror (i.e. the ITMs, PRM, and SRM), we keep t and r to be real and positive. However, when considering the effective transmissivity or reflectivity of a cavity, we allow t and r to be complex in general. To keep the analytical expressions trackable, we make the following simplifications. The main BS is assumed to be a perfect 50–50 BS, and we assume the ETMs are perfectly reflecting with power reflectivity of 1. The arm cavity losses are then attributed to the ITMs and denoted by Γ_i . Power conservation thus leads to $T_i + R_i + \Gamma_i = 1$. On the other hand, we ignore the losses in the recycling cavities and therefore $T_{p(s)} + R_{p(s)} = 1$. Note that in our phase convention, each mirror needs to be modeled with two surfaces to preserve energy. Therefore we

¹For our purpose of deriving the fields, we will often treat the recycling cavities as linear cavities. However, in practice they are folded cavities each with three recycling mirrors as shown in Figure 5-1.

Table 5.1: Parameters of the aLIGO optics in the third observing run.

Symbol	Definition	Value
T_i	ITM power transmissivity.	1.5%
Γ_i	Round-trip losses of the arm cavity.	~ 80 ppm
T_p	PRM power transmissivity.	3.1%
T_s	SRM power transmissivity.	32%
ϕ_p	Microscopic phase tuning of the PRM.	0
ϕ_s	Microscopic phase tuning of the SRM.	$\pi/2$

attribute all the reflectivity to the highly reflective (HR) surface of each mirror, while treating all the anti-reflective (AR) surfaces with a transmissivity of 1.

5.2 PROPAGATION OF THE DC FIELDS

In this Section we derive the propagation equations of the “DC” fields. Here by “DC” we mean that the systems is free from perturbations at audio frequencies. In other words, we will consider here how the carrier field and the RF sidebands propagate through the interferometer, with all the optics held perfectly static. To proceed, we will break the “dual-recycled Fabry-Perot Michelson interferometer” into individual components, and gradually compound them together to derive the full interferometer’s response. In the process, we will label the fields that has significant meanings with Roman letters. On the other hand, for fields whose subscripts are numbers, they are only defined for the convenience of the derivation, and we will recycle their labels when we study different components of the interferometer.

5.2.1 The carrier field

To study the carrier field, we start by considering the arm cavity. In the steady state, we have the following input-output relation:

$$E_a = -t_i E_1 + r_i E'_a, \quad (5.1a)$$

$$E'_a = E_a e^{2i\Delta\phi}, \quad (5.1b)$$

$$E'_1 = -r_i E_1 - t_i E'_a, \quad (5.1c)$$

where the fields are defined in Panel 1 of Figure 5-2, $\Delta\phi$ is the detuning of the ETM, and in writing the equation we have assumed the ETM is perfectly reflecting. The above set of equations can be solved in terms of an input field E_1 , leading to

$$\frac{E_a}{E_1} = \frac{-t_i}{1 - r_i e^{2i\Delta\phi}}, \quad (5.2a)$$

$$\frac{E'_1}{E_1} = \frac{-r_i + (r_i^2 + t_i^2)e^{2i\Delta\phi}}{1 - r_i e^{2i\Delta\phi}}. \quad (5.2b)$$

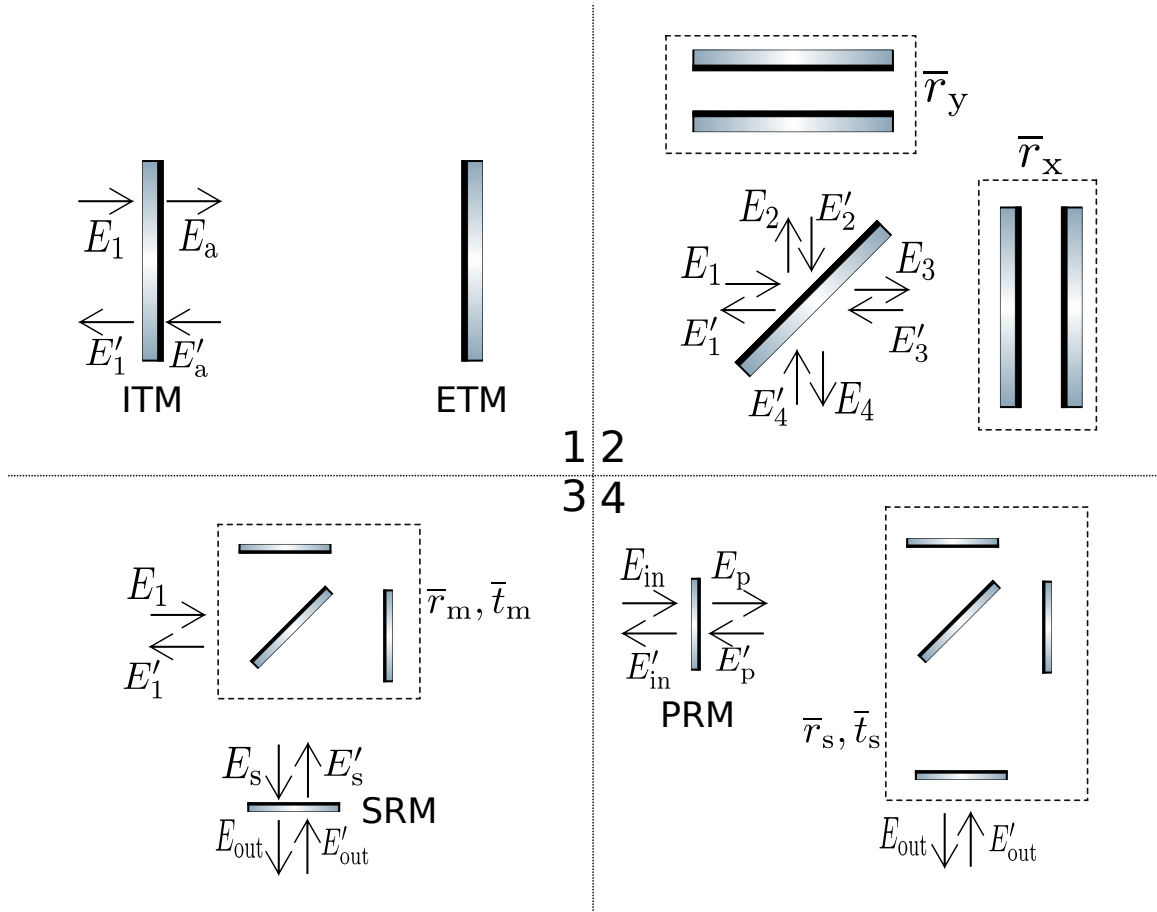


Figure 5-2: Schematic plots for deriving the DC fields in aLIGO.

In the limit where detuning $\Delta\phi \ll 1$ and $\Gamma_i \ll T_i \ll 1$, we can expand $e^{2i\Delta\phi} \simeq 1 + 2i\Delta\phi$ and $1 - r_i \simeq t_i^2/2$. Meanwhile, the detuning of each arm to enable a DC readout of the GW signal (Fricke et al., 2012) is generally small (a few pm), this

further implies that $2\Delta\phi \ll 1 - r_i$. We can further define

$$g_a = \frac{t_i}{1 - r_i} \simeq \frac{2}{t_i} \simeq 16. \quad (5.3)$$

Note that $g_a^2 \simeq 265$ is the power build-up inside the arm cavity,² and $1/(1 - r_i) \simeq g_a^2/2$.

Using these approximations, the input-output relation can be simplified as

$$\frac{E_{\text{arm}}}{E_1} \simeq -g_a (1 + i g_a^2 \Delta\phi), \quad (5.4a)$$

$$\frac{E'_1}{E_1} \equiv \bar{r}_i \simeq 1 - \frac{1}{2} g_a^2 \Gamma_i + 2i g_a^2 \Delta\phi, \quad (5.4b)$$

where we have defined \bar{r}_i as the effective amplitude reflectivity by combining the arm cavity into a single mirror. For future convenience, we will further define $\bar{r}_{x(y)}$ as the effective reflectivity of the X (Y) arm cavity, and similarly for detuning $\Delta\phi_{x(y)}$ and loss $\Gamma_{x(y)}$. For the detuning, we consider it happens only in the differential mode, $\Delta\phi_x = -\Delta\phi_y$, and we define the differential-arm (DARM) detuning³ as $\Delta\phi_d = \Delta\phi_x - \Delta\phi_y$. For the losses, we will keep track of both the common and differential ones, defined as $\Gamma_c = (\Gamma_x + \Gamma_y)/2$ and $\Gamma_d = (\Gamma_x - \Gamma_y)/2$, respectively.

The next step is to consider the Michelson part of the interferometer (Panel 2 in Figure 5-2). The input-output relation for a Michelson that is on the dark fringe can be written as

$$\begin{aligned} \begin{bmatrix} E_2 \\ E_3 \end{bmatrix} &= \frac{\sqrt{2}}{2} \begin{bmatrix} 1 & -1 \\ -1 & -1 \end{bmatrix} \begin{bmatrix} E_1 \\ E'_4 \end{bmatrix}, \quad \begin{bmatrix} E'_2 \\ E'_3 \end{bmatrix} = \begin{bmatrix} \bar{r}_y & 0 \\ 0 & \bar{r}_x \end{bmatrix} \begin{bmatrix} E_2 \\ E_3 \end{bmatrix}, \\ \begin{bmatrix} E'_1 \\ E_4 \end{bmatrix} &= \frac{\sqrt{2}}{2} \begin{bmatrix} 1 & -1 \\ -1 & -1 \end{bmatrix} \begin{bmatrix} E'_2 \\ E'_3 \end{bmatrix}, \end{aligned} \quad (5.5)$$

²Note that for the arm cavity, g_a^2 is related to the cavity finesse by $\mathcal{F}_a \simeq \pi g_a^2/2$.

³In some literatures (e.g., Izumi & Sigg 2017) the DARM detuning is defined as $(\Delta\phi_x - \Delta\phi_y)/2$. Nonetheless, throughout this thesis we define DARM as $\Delta\phi_d = \Delta\phi_x - \Delta\phi_y$ in phase and similarly in displacement, because such a definition simplifies the connection to GW astrophysics. For a piece of GW signal with strain h passing through an aLIGO detector with arm length L , it creates a DARM displacement $\Delta L_d = \Delta L_x - \Delta L_y = hL$ in the long-wavelength approximation.

which leads to

$$\begin{bmatrix} E'_1 \\ E_4 \end{bmatrix} = \frac{1}{2} \begin{bmatrix} \bar{r}_x + \bar{r}_y & \bar{r}_x - \bar{r}_y \\ \bar{r}_x - \bar{r}_y & \bar{r}_x + \bar{r}_y \end{bmatrix} \begin{bmatrix} E_1 \\ E'_4 \end{bmatrix}. \quad (5.6)$$

Using equation 5.4b, we can thus write

$$\bar{r}_m \equiv \frac{1}{2} (\bar{r}_x + \bar{r}_y) \simeq 1 - \frac{1}{2} g_a^2 \Gamma_c, \quad (5.7a)$$

$$\bar{t}_m \equiv \frac{1}{2} (\bar{r}_x - \bar{r}_y) \simeq -\frac{1}{2} g_a^2 \Gamma_d + i g_a^2 \Delta \phi_d, \quad (5.7b)$$

as the effective Michelson amplitude reflectivity and transmissivity.

We are now ready to study the carrier's propagation inside the signal-recycling cavity formed by the the compound Michelson and the SRM (Panel 3 of Figure 5-2). For aLIGO, it operates under the resonant-sideband-extraction configuration (Mizuno et al., 1993), which sets the SRM microscopic tuning to $\phi_s = \pi/2$. As a result, when a field reflects upon the SRM it will pick up a phase of π (note that there is a factor of 2 due to reflection). Similar to the case for the arm cavity, we can solve the fields at each point in terms of an input field E_1 , leading to

$$\frac{E_s}{E_1} = \frac{\bar{t}_m}{1 + \bar{r}_m r_s}, \quad (5.8a)$$

$$\bar{r}_s \equiv \frac{E'_1}{E_1} = \bar{r}_m + \frac{\bar{t}_m^2 r_s}{1 + \bar{r}_m r_s} \simeq \bar{r}_m, \quad (5.8b)$$

$$\bar{t}_s \equiv \frac{E_{\text{out}}}{E_1} = \frac{\bar{t}_m t_s}{1 + \bar{r}_m r_s} = g_s t_m, \quad (5.8c)$$

where we have defined \bar{r}_s and \bar{t}_s as the effective reflectivity and transmissivity of the compound cavity. In deriving \bar{r}_s , we have used the fact that $|\bar{t}_m|$ is already a small quantity, and therefore we can safely neglect the term that is quadratic in this quantity. We have also introduced the amplitude signal-recycling gain g_s , defined as

$$g_s = \frac{t_s}{1 + r_m r_s} \simeq \frac{t_s}{2} \simeq 0.31. \quad (5.9)$$

Lastly, we can bring in the PRM to form the complete interferometer (Panel 4 of

Figure 5-2). The fields can now be written as

$$\frac{E_p}{E_{\text{in}}} = \frac{t_p}{1 - r_p \bar{r}_m} = g_p, \quad (5.10a)$$

$$\frac{E'_{\text{in}}}{E_{\text{in}}} = \frac{\bar{r}_m - r_p}{1 - r_p \bar{r}_m}, \quad (5.10b)$$

$$\frac{E_{\text{out}}}{E_{\text{in}}} = -\frac{t_p \bar{t}_s}{1 - r_p \bar{r}_m} \simeq -\frac{1}{2} g_p g_s g_a^2 \Gamma_d + i g_p g_s g_a^2 \Delta \phi_d. \quad (5.10c)$$

In the process we have introduced the amplitude power-recycling gain $g_p = t_p / (1 - r_p \bar{r}_m)$. For the parameters given in Table 5.1, the numerical values of $g_p \simeq 6.7$, leading to a power-recycling gain of $g_p^2 \simeq 45$ in power. On the other hand, as pointed out in Hall (2017), once the losses in the arm Γ_c is fixed, the optimal choice of the PRM is such that $r_p = \bar{r}_m$. Under this condition the carrier field is critically coupled to the power-recycling cavity with a vanishing field in reflection, $E'_{\text{in}} = 0$. This condition was approximately satisfied in the aLIGO's first and second observing runs when $\Gamma_c \simeq 100$ ppm. However, before the third observing run, new ETMs with better coating qualities are installed, which reduces the round-trip loss in the arm cavity down to about $\Gamma_c \simeq 80$ ppm. If we want to maintain the critical coupling condition with the new arm cavities, the optimal power transmissivity of the PRM should be set to $T_p = 2.1\%$.

To summarize, we can write the fields at different ports in terms of the input field and the different cavities' gain as

$$E_p = -g_p E_{\text{in}}, \quad (5.11)$$

$$E_x = -\frac{\sqrt{2}}{2} g_p g_a (1 + i g_a^2 \Delta \phi_x) E_{\text{in}}, \quad (5.12)$$

$$E_y = \frac{\sqrt{2}}{2} g_p g_a (1 + i g_a^2 \Delta \phi_y) E_{\text{in}}, \quad (5.13)$$

$$E_s \simeq \left(\frac{1}{4} g_p g_a^2 \Gamma_d - \frac{1}{2} i g_p g_a^2 \Delta \phi_d \right) E_{\text{in}}, \quad (5.14)$$

$$E_{\text{out}} = \left(-\frac{1}{2} g_p g_s g_a^2 \Gamma_d + i g_p g_s g_a^2 \Delta \phi_d \right) E_{\text{in}}. \quad (5.15)$$

In the above set of equations, E_{in} is the input field with $P_{\text{in}} = |E_{\text{in}}|^2$ being the input

power, and E_{out} is the output field at the anti-symmetric port of the interferometer. The quantities E_p , E_x , E_y , and E_s correspond to the field inside the power-recycling cavity, the X-arm, the Y-arm, and the signal-recycling cavity, respectively, and $g_p = t_p/(1 - r_p \bar{r}_m) = 6.7$, $g_s = t_s/(1 + r_s \bar{r}_m) = 0.31$, and $g_a = t_i/(1 - r_i) = 16$ are the amplitude gains in the power-recycling cavity, the signal recycling cavity, and the arms. In the expressions of g_p and g_s the effective reflectivity \bar{r}_m of the compound Michelson-arms cavity is given by $\bar{r}_m \simeq 1 - \frac{1}{2}g_a^2\Gamma_c \simeq 0.99$.

In terms of power, we have

$$P_p = g_p^2 P_{\text{in}} \simeq 1.8 \times \left(\frac{P_{\text{in}}}{40 \text{ W}} \right) \text{ kW}, \quad (5.16)$$

$$P_x = P_y = P_a = \frac{1}{2}g_p^2 g_a^2 P_{\text{in}} \simeq 240 \times \left(\frac{P_{\text{in}}}{40 \text{ W}} \right) \text{ kW}, \quad (5.17)$$

$$P_{\text{out}}^{(\Delta\phi_d)} = g_p^2 g_s^2 g_a^4 \Delta\phi_d^2 P_{\text{in}} \simeq 43 \times \left(\frac{\Delta L_d}{10 \text{ pm}} \right)^2 \left(\frac{P_{\text{in}}}{40 \text{ W}} \right) \text{ mW}, \quad (5.18)$$

$$P_{\text{out}}^{(\Gamma_d)} = \frac{1}{4}g_p^2 g_s^2 g_a^4 \Gamma_d^2 P_{\text{in}} \simeq 0.31 \times \left(\frac{\Gamma_d}{10 \text{ ppm}} \right) \left(\frac{P_{\text{in}}}{40 \text{ W}} \right) \text{ mW}, \quad (5.19)$$

where in the last two equations we have separated the contribution to the output power due to DARM detuning (the $\Delta\phi_d$ term) and that due to differential arm losses (the Γ_d term). We have scaled the input power to 40 W which is typical for aLIGO's third observing run.

5.2.2 The RF sidebands

To sense the length of each cavity in a global way, two phase-modulation sidebands are also injected to the interferometer at RF frequencies $f_1 = 9.1 \text{ MHz}$ and $f_2 = 45.5 \text{ MHz}$. The RF sidebands resonate differently from the carrier field in each cavities,⁴ and thus have different responses to the cavity's length fluctuations. By comparing the phases between the carrier and sidebands one can therefore infer the cavity's length. This is the working principle of the PDH technique (Drever et al., 1983). More specifically,

⁴This can be that either a field is on-resonant inside a cavity while the other is off-resonant, or both the carrier and the sideband are resonant inside the cavity yet they experience different cavity gains.

Table 5.2: Lengths in aLIGO’s central cavities.

Symbol	Definition	Value
λ_1	Wavelength of the $f_1 = 9.1$ MHz sideband.	33 m.
λ_2	Wavelength of the $f_2 = 45.5$ MHz sideband.	6.6 m.
l_p	One-way length of the power-recycling cavity.	$8\frac{3}{4}\lambda_2 = 57.7$ m.
l_s	One-way length of the signal-recycling cavity.	$8\frac{1}{2}\lambda_2 = 56$ m.
l_{sch}	Schnupp asymmetry.	8 cm.

the $f_1 = 9.1$ MHz sideband is resonant only in the power recycling cavities while $f_2 = 45.5$ MHz sideband is resonant in both the power- and signal-recycling cavities. On the other hand, neither of the RF sidebands is on-resonance in the arm cavity. In this Section we will describe their “DC” buildups (that is, without perturbations at audio frequencies) in more quantitative details. Some critical lengths are summarized in Table 5.2 and we will use those numbers when calculating numerical quantities.

The steps to study the RF sidebands are essentially the same as the ones we have used for the carrier field in Section 5.2.1. We can start by considering the arm cavity. Since both RF sidebands are off-resonance in the arm cavity, to a good approximation the effective reflectivity of the arm cavity can be written as

$$\bar{r}_{\text{i,rf}} \simeq -r_i - \frac{t_i^2}{1 + r_i} \simeq -1. \quad (5.20)$$

At the Michelson, in order to achieve finite transmissivity of the RF sidebands when the carrier field is on a perfect dark fringe, we deliberately set the distance between BS and ITMX and the one between BS and ITMY to be different by a few centimeters. This is known as the Schnupp asymmetry (Schnupp, 1988). Quantitatively, we can still use the input-output relations for the Michelson given in equation 5.5 but replace $\bar{r}_{\text{x(y)}}$ by

$$\bar{r}_{\text{x(y)}}(f_{\text{rf}}) = \bar{r}_{\text{i,rf}} \exp \left[-4\pi i f_{\text{rf}} \frac{l_{\text{x(y)}}}{c} \right] \simeq -\exp \left[-4\pi i f_{\text{rf}} \frac{l_{\text{x(y)}}}{c} \right], \quad (5.21)$$

where $l_{\text{x(y)}}$ is the distance between BS and ITMX (ITMY), and f_{rf} can be either f_1

or f_2 . This further leads to

$$\bar{r}_m(f_{\text{rf}}) = \frac{1}{2} [\bar{r}_x(f_{\text{rf}}) + \bar{r}_y(f_{\text{rf}})] \simeq -\cos\left(2\pi f_{\text{rf}} \frac{l_{\text{sch}}}{c}\right), \quad (5.22a)$$

$$\bar{t}_m(f_{\text{rf}}) = \frac{1}{2} [\bar{r}_x(f_{\text{rf}}) - \bar{r}_y(f_{\text{rf}})] \simeq i \sin\left(2\pi f_{\text{rf}} \frac{l_{\text{sch}}}{c}\right), \quad (5.22b)$$

where in the above set of equations we have dropped the $\exp[-2\pi f_{\text{rf}}(l_x + l_y)/c]$ term as it will be absorbed in our definition of recycling cavities' lengths. Numerically, we have

$$|\bar{t}_m(f_{\text{rf}})| \simeq 0.015 \times \left(\frac{f_{\text{rf}}}{9.1 \text{ MHz}}\right), \quad (5.23)$$

for a Schnupp asymmetry of $l_{\text{sch}} \equiv l_x - l_y = 8 \text{ cm}$.

Next we add the recycling cavities to the system. The signal-recycling cavity has a one-way length of $l_s = (17/2)\lambda_2 = 56 \text{ m}$. As a result, the f_2 sideband will be on-resonance in this cavity (note that $\bar{r}_m(f_2) < 0$ and $\phi_s = \pi/2$). Furthermore, the 8 cm of Schnupp asymmetry is chosen such that the effective reflectivity of the compound Michelson-signal-recycling cavity as seen by the f_2 sideband matches approximately to the reflectivity of the PRM. Since the f_2 sideband is also resonant in the power-recycling cavity (one-way length $l_p = (8\frac{3}{4})\lambda_2 = 57.7 \text{ m}$), the f_2 sideband is close to being critically-coupled through the interferometer. Numerically we have

$$\frac{P_p(2f_2)}{P_{\text{in}}(2f_2)} = g_p^2(f_2) \simeq 15, \quad (5.24a)$$

$$\frac{P_{\text{out}}(2f_2)}{P_{\text{in}}(2f_2)} = g_p^2(f_2)g_s^2(f_2)\bar{t}_m^2(f_2) \simeq 0.90, \quad (5.24b)$$

where $P_{\text{in}}(2f_2)$, $P_{\text{out}}(2f_2)$, and $P_p(2f_2)$ are respectively the input power, the output power, and the power circulating in the power-recycling cavity for the $f_2 = 45.5 \text{ MHz}$ sideband. Note that there is a factor of 2 in the frequency for power as we look at the interference between $E(+f_2)$ and $E(-f_2) = -E^*(+f_2)$. Similar to our treatment for the carrier field, we have defined $g_{p(s)}(f_2)$ as the power-(signal-)recycling gain in amplitude with appropriate substitution of $\bar{r}_m(f_2)$ and $\bar{r}_s(f_2)$. The values for them are $g_p(f_2) \simeq 3.9$ and $g_s(f_2) \simeq 3.2$.

As for the f_1 sideband, it is nearly anti-resonance in the signal-recycling cavity, making its reflectivity upon the Michelson-signal-recycling cavity almost one. As a result, it is strongly over-coupled in the power-recycling cavity with $g_p(f_1) \simeq 11$. As a result, we have

$$\frac{P_p(2f_1)}{P_{\text{in}}(2f_1)} = g_p^2(f_1) \simeq 127, \quad (5.25a)$$

$$\frac{P_{\text{out}}(2f_1)}{P_{\text{in}}(2f_1)} \simeq 0.0028, \quad (5.25b)$$

for the $f_1 = 9.1$ MHz sideband. Note that nearly all of the input power at f_1 is reflected by the interferometer back to the input port.

5.3 PROPAGATION OF THE AC FIELDS

In this Section we consider how the “AC” fluctuations of the ETMs at audio frequencies are translated to optical fields, and how those fields propagate through the interferometer. Meanwhile, we will also consider the propagation of the quantum fluctuation entering through the anti-symmetric port of the interferometer, and further derive the instrument’s limitation. The derivation follows closely [Martynov et al. \(2017\)](#); for the AC optical response of other mirrors we refer the reader to [Izumi & Sigg \(2017\)](#) for more discussions.

5.3.1 From mirror motion to optical field

To see the connection between a mirror’s motion and the optical field reflecting upon it,⁵ we can consider the following example. Suppose the incident field is $E_1 = E \exp(-2\pi i f_0 t)$ where $f_0 \simeq 3 \times 10^{14}$ Hz is the laser oscillation frequency, and the mirror (with $r = 1$) has a sinusoidal motion $\Delta l \cos(2\pi f t)$ where $f \ll \omega_0/2\pi$ is an audio-frequency on the order of a few Hz to a few kHz. The mirror’s motion modulates the phase of the field in reflection with an amplitude of $\Delta\phi = 2\pi f_0 \Delta L/c$

⁵We focus on the normal incidence case for simplicity here.

and a frequency f , which can be written as

$$\begin{aligned} E'_1 &= E e^{i[2\pi f_0 t + 2\Delta\phi \cos(2\pi f t)]}, \\ &= E e^{i2\pi f_0 t} \left[\sum_{m=-\infty}^{\infty} i^m J_m(2\Delta\phi) e^{2\pi i m f t} \right], \end{aligned} \quad (5.26)$$

where J_m is the Bessel function of the first kind. For small displacements, this expression can be further simplified as

$$E'_1 \simeq E e^{i2\pi f_0 t} [1 + i\Delta\phi e^{2\pi i f t} + i\Delta\phi e^{-2\pi i f t}]. \quad (5.27)$$

Thus the field in reflection upon an oscillatory mirror can be modeled as the sum of an unperturbed DC field and two sidebands that are phase-shifted by $\pi/2$ with respect to the DC field and vary respectively at $\pm f$.

5.3.2 DARM signal

In Section 5.2 we have derived the DC fields at each point of the interferometer, which serve as the ‘seed’ fields from which the AC fields are generated. We now consider the propagation of the AC fields due to differential motions of the ETMs. Similar to the DC field study, we start by considering a single Fabry-Perot cavity correspond to the arm cavity. Since the AC motion is already a small quantity, we can thus ignore other small DC effects such as the DC detuning to the leading order. The steady-state solution satisfies the following set of equations,

$$E'_1(f) = E_1(f) + i\Delta\phi(f)E_1(0), \quad (5.28a)$$

$$E_1(f) = r_1 e^{-4\pi i f L/c} E'_1(f), \quad (5.28b)$$

$$(5.28c)$$

where $L = 3995$ m is the one-way arm length, $\Delta\phi(f) = 2\pi f_0 \Delta L(f)/c$ with $\Delta L(f)$ being the AC motion of the ETM. The point at which each field is evaluated is indicated in Figure 5-3, Panel 1. Again we have assumed the ETM being perfectly

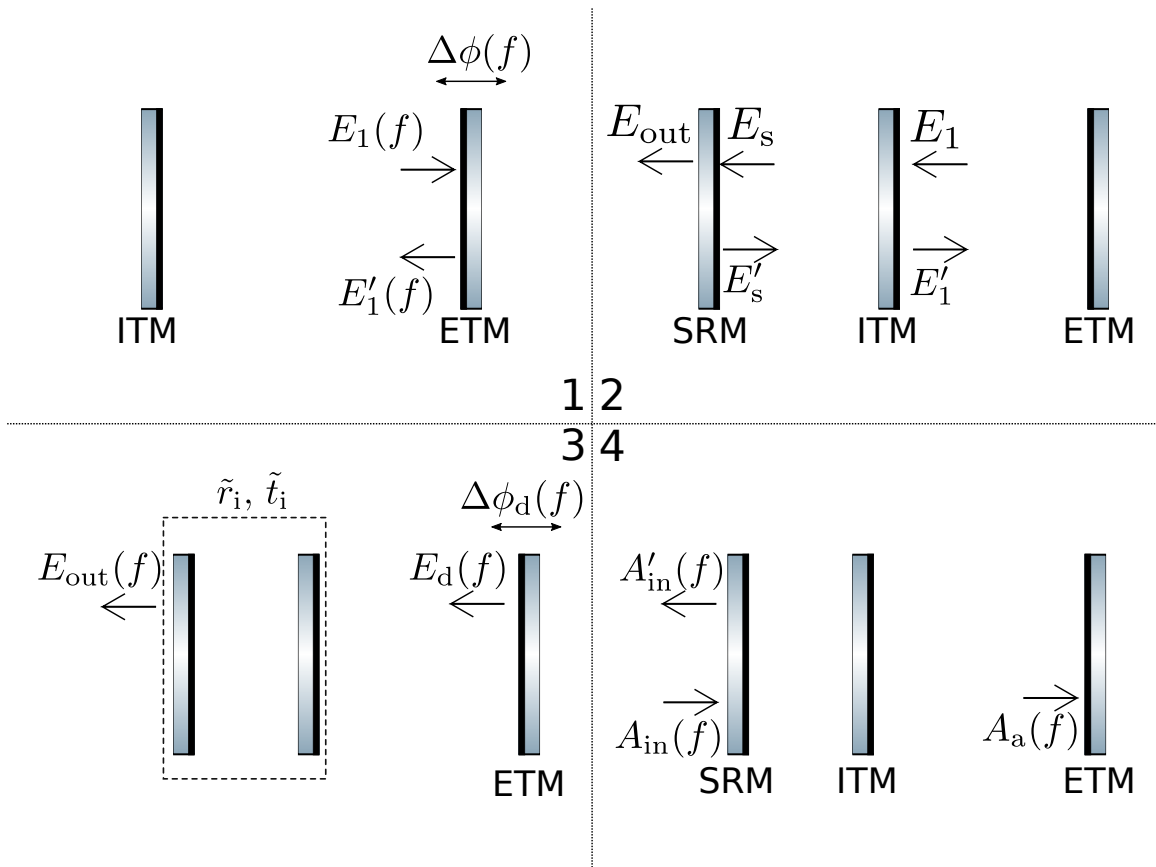


Figure 5-3: Schematic plots for deriving the AC fields in aLIGO.

reflecting for simplicity. In the above equations we have explicitly indicated the frequency at which each quantity is varying (f for the AC quantities and 0 for the DC ones). This time, instead of solving all the fields in terms of an input field, we solve them in terms of the DC field $E_1(0)$ which we have derived in the previous section. This leads to

$$E'_1(f) = \frac{i\Delta\phi(f)}{1 - r_i e^{-i4\pi fL/c}} E_1(0) \simeq \frac{i\Delta\phi(f)}{(1 - r_i) + ir_i 4\pi f \frac{L}{c}} E_1(0). \quad (5.29)$$

Note that due to causality, a field, after propagating a round trip in the cavity, will experience a phase shift of $-4\pi fL/c$ relative to the original one. When the phase lag is sufficiently large, the returning field will be no more in-phase with the original one, thereby decrease the amount of constructive interference. This naturally leads to the pole frequency of the arm cavity f_a , obtained by equating the magnitudes of the denominators real and imaginary part

$$1 - r_i \simeq 4\pi r_i f_a \frac{L}{c}, \text{ or} \\ f_a \simeq \frac{(1 - r_i)}{r_i} \frac{c}{4\pi L} \simeq \frac{1}{g_a^2} \frac{c}{2\pi L} \simeq 45 \text{ Hz}. \quad (5.30)$$

For motions with $f > f_a$, the cavity field will experience an asymptomatic $1/f$ filtering.

Now we consider how the differential-arm motion, or the DARM motion in the LIGO literature, propagates through the interferometer. Defining $\Delta L_{x(y)}(f)$ to be the AC motion of ETMX (ETMY), for DARM we have $\Delta L_d(f) = \Delta L_x(f) - \Delta L_y(f)$ with $\Delta L_x(f) = -\Delta L_y$, and the corresponding phase $\Delta\phi_d(f) = 2\pi f_0 \Delta L_d(f)/c$. Using the Michelson's input-output relation [equation (5.6)] and the fact that the DC field inside the X and Y arm cavities satisfies $E_x(0) = -E_y(0)$ [equations (5.12) and (5.13); ignoring DC detunings], for the DARM motion we can conveniently combine the two arm cavities and the Michelson into a single DARM cavity, with the DC field inside this cavity given by $E_d(0) = -\sqrt{2}/2 E_x(0) \simeq g_p g_a E_{in}/2$, and the corresponding detuning of the combined differential ETM given by $\Delta\phi_d$. The problem now becomes

the derivation of propagations inside the signal-recycled DARM cavity.

To proceed, we first combine the signal-recycling cavity formed by the SRM and ITM into a single effective ITM. The phase delay due to field propagation is ignored in the signal-recycling cavity because it is much shorter than the arms. The input-output relation is given by the following set of equations:

$$E_s = -r_i E'_s - t_i E_1, \quad (5.31a)$$

$$E'_s = -r_s E_s, \quad (5.31b)$$

$$E'_1 = r_i E_1 - t_i E'_s, \quad (5.31c)$$

$$E_{\text{out}} = -t_s E_s, \quad (5.31d)$$

where the fields are defined in Panel 2 of Figure 5-3. All the fields here vary at f and thus we omit it in the notation. Note that while the DC carrier field is anti-resonance in the signal-recycling cavity, the AC signal sidebands are actually resonant in it. The difference is that for the DC fields, its reflectivity off the ITM is determined by the interference between the field resonant in the arm cavity leaking through the ITM and the field directly reflecting off the ITM, whereas for the signal sidebands there is no direct reflection fields.

The above set of equations can be solved to obtain the reflectivity and transmissivity of the effective ITM formed by the signal-recycling cavity, which leads to

$$\tilde{r}_i \equiv \frac{E'_1}{E_1} = \frac{r_i - r_s}{1 - r_i r_s}, \quad (5.32a)$$

$$\tilde{t}_i \equiv \frac{E_{\text{out}}}{E_1} = \frac{t_i t_s}{1 - r_i r_s}. \quad (5.32b)$$

Once the effective ITM is computed, the AC field inside the DARM cavity as well as the one propagate to the anti-symmetric port can be easily obtained by replacing the r_i with \tilde{r}_i in equation (5.29). See also Panel 3 of Figure 5-3. This leads to

$$E_d(f) \simeq \frac{i\Delta\phi(f)}{(1 - \tilde{r}_i) + i\tilde{r}_i 4\pi f \frac{L}{c}} E_d(0), \quad (5.33)$$

for the AC field inside the DARM cavity, and the corresponding signal-recycled DARM cavity pole f_d , given by

$$f_d = (1 - \tilde{r}_i) \frac{c}{4\pi L} \simeq f_a \frac{1 + r_s}{1 - r_s} \simeq 450 \text{Hz}. \quad (5.34)$$

Thus, the signal-recycling cavity increases the single-arm cavity pole by a factor of $(1 + r_s)/(1 - r_s) \simeq 1/g_s^2 \simeq 10$ for $T_s = 0.32$. The AC field at the output port is readily given by

$$\begin{aligned} E_{\text{out}}(f) &= \tilde{t}_i E_d(f) \\ &\simeq i g_p g_s g_a^2 E_{\text{in}}(0) \frac{1}{1 + i f/f_d} \frac{\Delta\phi(f)}{2}, \end{aligned} \quad (5.35)$$

where we have used $E_d(0) = g_p g_a E_{\text{in}}(0)/2$. An overall propagation phase in the numerator has been omitted which does not affect any physical measureables.

Note that while the signal-recycling cavity reduced the DC amplitude of the signal field by a factor of $g_s \simeq 0.3$, it broadens the signal bandwidth by a factor of $1/g_s^2$. Therefore for high-frequency signals with $f > f_d$, the signal field is enhanced by a factor of $1/g_s \simeq 3$. As the merging frequency of coalescing NS or BH binaries is approximately given by the GW frequency at the system's innermost stable circular orbit, $2f_{\text{isco}} \simeq 1.6 \times 10^3 (2.8 M_\odot/M_{\text{tot}}) \text{ Hz} > f_d > f_a$, with M_{tot} being the total mass of the binary, such broadening is significant for increasing the instrument's sensitivity to the signals close to the final merger.

So far we have been focused on the upper side band with frequency $+f$. Propagation of the lower side band with $-f$ can be derived similarly. Without cavity detuning, it is easy to show that

$$E_{\text{out}}(-f) = -E_{\text{out}}^*(f), \quad (5.36)$$

where we have used the “*” symbol to denote complex conjugation.

The detection of the signal fields is accomplished by interfering the signal sidebands $E_{\text{out}}(\pm f)$ with a local oscillator field, E_{lo} , which creates a power fluctuation

varying at $f > 0$ that can be further sensed by a photodiode (PD). Without special quantum manipulations that are beyond the scope of this Thesis, a natural choice of the local oscillator field's phase is such that it maximizes the response to the signal. Without loss of generality we can set the input field to the interferometer E_{in} to be real and positive. Then to maximize the response to signal fields given by equations (5.35) and (5.36), the local oscillator field should then satisfy $E_{\text{lo}}/|E_{\text{lo}}| = \pm i$. We can see from equation (5.15) that a DC detuning of DARM creates such a local oscillator field as long as the differential detuning is greater than the differential arm loss, $\Delta\phi_{\text{d}}(0) \gg \Gamma_{\text{d}}/2$. This is the DC readout technique currently used in aLIGO in which a DC DARM detuning of ~ 10 pm is introduced to sense the DARM displacements. Alternatively, one can pick off a small portion of the laser beam upstream as the local oscillation field and deliver it to the readout port with proper phase control to enable the balanced-homodyne readout scheme (Fritschel et al., 2014).

In either case, the interference between the local oscillator and the signal fields can be written as

$$U(f) = E_{\text{lo}}^*(0)E_{\text{out}}(f) + E_{\text{out}}^*(-f)E_{\text{lo}}(0), \quad (5.37)$$

for the term varying as $\exp(2\pi ift)$. Similarly, we have $U(-f) = U^*(f)$ for the term varying at $\exp(-2\pi ift)$. By choosing the proper demodulation phase one can select which phase to observe at the readout. Conventionally, we define

$$I(f) = \text{Re}[U(f)] + \text{Re}[U(-f)], \quad Q(f) = \text{Im}[U(f)] - \text{Im}[U(-f)], \quad (5.38)$$

for the in-phase (I) signal and the in-quadrature (Q) signal, respectively. We can combine the I- and Q-phase signals into a complex vector as $I + iQ$ to write the final response in power at the readout PD, as

$$P(f) = 2U(f) = 2g_{\text{p}}g_{\text{s}}g_{\text{a}}^2 \frac{1}{1 + if/f_{\text{d}}} \sqrt{P_{\text{in}}P_{\text{lo}}} \Delta\phi_{\text{d}}(f), \quad (5.39)$$

where $P_{\text{in}} = |E_{\text{in}}|^2$ is the input power and $P_{\text{lo}} = |E_{\text{lo}}|^2$ the power in the local oscillator field. By writing $\Delta\phi_{\text{d}}(f) = 2\pi f_0 \Delta L_{\text{d}}(f)/c$, we obtain the optical transfer function

Z_d from DARM displacement to the readout PD as

$$\begin{aligned} Z_d(f) &\equiv \frac{dP_d}{d\Delta L_d} = 4\pi g_p g_s g_a^2 \frac{1}{1 + if/f_d} \frac{\sqrt{P_{\text{in}} P_{\text{lo}}}}{\lambda_0}, \\ &= \frac{8.3 \times 10^9}{1 + if/(450 \text{ Hz})} \left(\frac{P_{\text{in}}}{40 \text{ W}} \right)^{1/2} \left(\frac{P_{\text{lo}}}{0.04 \text{ W}} \right)^{1/2} \frac{\text{W}}{\text{m}}. \end{aligned} \quad (5.40)$$

Note that Z_d scales as g_a^2 . This is because both the DC field building-up inside the arm cavity and the AC field generated from the DC field will experience the arm cavity's amplification. In contrast, the power-recycling cavity affects only the DC seed field and the signal recycling cavity affects only the AC signal field. As a result Z_d scales with g_p and g_s only to the linear order. As for the local oscillator field, it is given by equation (5.18) in the case of DC readout.

5.3.3 Quantum fluctuations

The quantum noise of the interferometer can be modeled as a quantum field $A_{\text{in}}(f)$ entering from the antisymmetric port (Panel 4 of Figure 5-3; Buonanno & Chen 2001; Miao 2012; Martynov et al. 2017). This field reflects off the interferometer and interferences with the local oscillator field at the detection PD to create perturbations in the readout signal. Meanwhile, it also enters the arm cavities and interfere with the DC fields to create power fluctuations there that can displace the test masses via radiation pressure. The former corresponds to the shot noise and the later is known as the quantum radiation pressure noise (QRPN). In this Section we provide a semi-classical derivation of those quantum limits. We will treat $A_{\text{in}}(f)$ as a classical field instead of a quantum operator, and we simply enforce the amplitude spectra density of the beat-note between A_{in} and a classical DC field E (after summing over the signals at $\pm f$) to be $\sqrt{2\hbar\omega_0 P}$ with $P = |E|^2$. Without quantum squeezing, A_{in} has an equal amount of fluctuations in the amplitude and phase quadratures. Despite of our semi-classical simplifications, the input-output relation holds for both classical fields and quantum operators.

The derivation of the propagation of A_{in} is similar to the one presented in the

previous Section. Thus we drop the details but just outline the procedures. Again consider the case of the signal-recycled DARM cavity, we can first map the ITM and ETM into a single effective ITM, and then combine to SRM and the effective ITM to compute the reflectivity of A_{in} by the interferometer. This gives us the shot noise. We can also solve for A_{in} 's propagation into the signal recycling cavity and then the DARM cavity. The important quantities in terms of A_{in} are

$$A'_{\text{in}}(f) = \frac{1 - if/f_d}{1 + if/f_d} A_{\text{in}}(f), \quad (5.41)$$

$$A_a(f) = g_s g_a \frac{1}{1 + if/f_d} A_{\text{in}}(f). \quad (5.42)$$

The shot noise of the system is given by beating $A'_{\text{in}}(f)$ with the local oscillator field E_{lo} at the readout port. The amplitude spectral density of it is given by

$$n_{\text{shot}}(\text{in W}/\sqrt{\text{Hz}}) = \sqrt{2\hbar\omega_0 P_{\text{lo}}}. \quad (5.43)$$

At the PD, such a noise is indistinguishable to the real signal generated by DARM motions. Consequently, dividing it by the DARM optical response [cf. equation (5.40)] leads to the shot-noise-limited DARM sensitivity

$$\begin{aligned} n_{\text{shot}} &= \frac{\lambda_0}{4\pi} \frac{\sqrt{2\hbar\omega_0/\zeta}}{g_p g_s g_a^2 P_{\text{in}}^{1/2}} \left| 1 + i \left(\frac{f}{f_d} \right) \right|, \\ &= 1.8 \times 10^{-20} \left| 1 + i \left(\frac{f}{450 \text{ Hz}} \right) \right| \left(\frac{P_{\text{in}}}{40 \text{ W}} \right)^{-1/2} \frac{\text{m}}{\sqrt{\text{Hz}}}. \end{aligned} \quad (5.44)$$

In the above equation we have included the efficiency of the the PD $\zeta \simeq 0.7$ that takes into account both the loss from SRM to the PD and the PD's intrinsic quantum efficiency.

On the other hand, the power fluctuation inside the arm cavity due to quantum fluctuation is obtained by beating $A_a(f)$ with the DC field inside the DARM cavities. In our mapping, to keep the power fluctuation inside the DARM cavity matches the real differential power fluctuation $\Delta P_d = \Delta P_x - \Delta P_y$, the DC field should be

$-\sqrt{2}E_x(0) = g_p g_a E_{\text{in}}$. Then the amplitude spectral density of the differential power fluctuation is given by

$$n_{\Delta P_d}(\text{in W}/\sqrt{\text{Hz}}) = g_p g_s g_a^2 \frac{\sqrt{2\hbar\omega_0 P_{\text{in}}}}{|1 + \text{i}f/f_d|}. \quad (5.45)$$

Note that the DC field inside the arm and the local oscillator field at the antisymmetric port are $\pi/2$ out of phase [cf. equations (5.12) and (5.15)]. Therefore, while the shot noise is due to the fluctuations of A_{in} in the ‘phase’ quadrature, the power fluctuation inside the arm is due to the fluctuations in the ‘amplitude’ quadrature of A_{in} . This power perturbation can directly cause displacement noise of the test masses which we will model as free masses. For a single mirror its displacement is related to power fluctuations $\Delta P(f)$ as

$$\Delta x(f) = \frac{\Delta P(f)}{2\pi^2 c M} \frac{1}{f^2}, \quad (5.46)$$

with M being the mirror’s mass. For the arm cavity another factor of two needs to be included to account for pushing both the ITM and ETM. Thus the amplitude spectra density of the QRPN is given by

$$\begin{aligned} n_{\text{qrpn}}(f) &= \frac{g_p g_s g_a^2}{\pi^2 c M} \frac{\sqrt{2\hbar\omega_0 P_{\text{in}}}}{|1 + \text{i}f/f_d|} \frac{1}{f^2}, \\ &= \frac{1.8 \times 10^{-19}}{|1 + \text{i}f/(450 \text{ Hz})|} \left(\frac{f}{10 \text{ Hz}} \right)^{-2} \left(\frac{P_{\text{in}}}{40 \text{ W}} \right)^{1/2} \frac{\text{m}}{\sqrt{\text{Hz}}}. \end{aligned} \quad (5.47)$$

Chapter 6

Overview of alignment sensing and control in aLIGO

A realistic interferometer is more complicated than the one-dimensional case we have considered in the previous Chapter. This is because both the seismic motion and the thermal drifts may induce significant amount of angular misalignments. The misalignment both reduces the buildups in the optical cavity and consequently its sensitivity to, e.g., the DARM motion, and increases cross-couplings between different noise terms. Without correcting for the angular motions, the interferometer may not even be able to stay at its nominal resonant condition. Consequently, an active alignment sensing and control system is critical for the proper operation of optical interferometers. We thus devote this Chapter to describe how the angular control is accomplished in aLIGO.

In Section 6.1 we introduce the concepts of transverse electromagnetic modes (specifically, the Hermite-Gaussian modes) which are convenient tools for analyzing cavity misalignments. The angular degrees of freedom (DOFs) needed to be controlled and their corresponding detection schemes are discussed in a generic sense in Sections 6.2 and 6.3, respectively. These components are further integrated together to form the alignment sensing and control system of aLIGO in Section 6.4. Lastly, in Section 6.5 we study the error tolerance of each DOF. Here the discussion will be focused on the corner of the interferometer (that is, the recycling cavities and the

Michelson DOF). A comprehensive study of the arm cavities will be provided in the following Chapter.

6.1 OPTICAL CAVITIES AND GAUSSIAN BEAMS

In this Section we review the basic concepts of Gaussian beams that are essential in our discussions of the alignment of optical cavities. The paraxial approximation is assumed throughout the Chapter and it is generally well-satisfied in aLIGO's case. For a more detailed and complete analysis, we refer the reader to [Siegman \(1986\)](#).

An optical cavity can be formed with an input mirror and an end mirror, separated by a distance L . The cavity is stable if

$$0 < \left(1 - \frac{L}{\text{RoC}_i}\right)\left(1 - \frac{L}{\text{RoC}_e}\right) < 1, \quad (6.1)$$

where $\text{RoC}_{i(e)}$ is the radius of curvature of the input (end) mirror. The quantities $g_{i,e} \equiv (1 - L/\text{RoC}_{i,e})$ are known as the cavity g-factors.¹ The eigenmodes of a cavity define a complete orthonormal basis that allows us to expand an electric field as

$$E(f, x, y, z) = \sum_{mn} a_{mn}(f) u_{mn}(x, y, z), \quad (6.2)$$

where the $u_{mn} \in \mathbb{C}$ are the Hermite-Gauss functions, and the $a_{mn} \in \mathbb{C}$ are the amplitudes of the modes. The spatial coordinate (x, y, z) is chosen to be right-handed with the z -axis pointing along the direction of beam propagation and the y -axis vertically up. In this coordinate system, the mode order m (n) corresponds to number of nodes in the x (y) direction and we can further separate $u_{mn}(x, y, z) = u_m(x, z)u_n(y, z)$. We have omitted the temporal dependence as all the modes vary at the same frequency as E . For future convenience we further write $E_{mn} = a_{mn}u_{mn}$ and drop the (x, y, z) part as the indices m, n carry the spatial information already. Furthermore, to be consistent with FINESSE ([Brown & Freise, 2014](#)), we let the amplitude coefficient a_{mn} to

¹We will use the Roman g for the g-factors to distinguish them from an optical's amplitude gain inside a cavity, which is denoted with an Italic g .

absorb the Gouy phase of the Hermite-Guass modes, while leaving the rest of the spatial dependence in the function u_{mn} normalized such that $\int_{-\infty}^{\infty} u_{m'}^*(x)u_m(x)dx = \delta_{mm'}$ and similarly for $u_n(y)$. In the following, when we refer to a mode E_{mn} alone, unless specified, we will generally refer to its complex amplitude a_{mn} that includes the Gouy phase, whereas when we consider the interference between two fields $\propto E_{m'n'}^*E_{mn}$, we will let them follow the orthogonality dictated by u_{mn} with the integration range specified by the PD type (e.g., the whole-plane for a regular PD, or the upper/lower half-plane for a quadrant PD). A more detailed discussion on the Gaussian beam is presented in Appendix E.

When the input beam is perfectly aligned and mode-matched to a cavity, the mode resonating inside the cavity corresponds to the spherical Gaussian mode with $m = n = 0$. We will also refer such a mode as the 00 mode for conciseness.

Now consider the case where a mirror is misaligned in pitch² with respect to the beam incident onto it. Upon reflection, the beam's wavefront will experience a differential phase delay at different locations in the xy -plane as it no more matches exactly to the curvature of the mirror. As a result, modes with different spatial orders will be generated. To the leading order in misalignment angle $\Delta\theta$, this can be written as (Hefetz et al., 1997)³

$$\begin{bmatrix} E'_{00} \\ E'_{01} \end{bmatrix} = r \begin{bmatrix} 1 & i\frac{2\pi w}{\lambda_0}\Delta\theta \\ i\frac{2\pi w}{\lambda_0}\Delta\theta & 1 \end{bmatrix} \begin{bmatrix} E_{00} \\ E_{01} \end{bmatrix}, \quad (6.3)$$

where the unprimed fields are the incident fields and the primed ones are the ones on reflection, and w is the spot size at the mirror's locations.

On the other hand, if a beam is shifted laterally along the y -axis by Δy , the leading-order scattering matrix connecting the original basis to the shifted beam

²Pitch corresponds to a rotation about the x -axis in our coordinate system. Yaw, or rotation about the y -axis, will be similar and hence our discussion will be focused on the pitch case.

³Note that our sign convention follows the one used in FINESSE which has an overall sign flip relative to the one used in Hefetz et al. (1997). Also here we consider only the case of normal incidence. For the non-normal incident case, e.g., the alignment of the main BS, the pitch misalignment angle is reduced by a factor of $\cos\alpha$ where $\alpha = \pi/4$ is the incident angle whereas yaw is unaffected. See the FINESSE manual (Brown & Freise, 2014) for a more detailed discussion.

reads

$$\begin{bmatrix} E'_{00} \\ E'_{01} \end{bmatrix} = r \begin{bmatrix} 1 & \frac{\Delta y}{w} \\ -\frac{\Delta y}{w} & 1 \end{bmatrix} \begin{bmatrix} E_{00} \\ E_{01} \end{bmatrix}. \quad (6.4)$$

We can thus see that $\text{Re}[E'_{01}/E'_{00}] \propto \Delta y/w$ while $\text{Im}[E'_{01}/E'_{00}] \propto w\Delta\theta$. In other word, if we choose the 00 mode to be real, then a real 01 mode indicates a lateral shift and an imaginary 01 mode corresponds to a tilt with respect to the basis.

Also note that relative to the 00 mode, the 01 mode will experience an extra propagation phase shift η due to the Gouy phase [generically, for mode mn the Gouy phase shift relative to the 00 mode will be $(m+n)\eta$].

Knowing how a field reflects upon a mirror and how it propagates through free spaces allows us to solve for the steady-state solution of an optical system with misalignments. The principles of this calculation (Hefetz et al., 1997) are similar to the ones we have used in, e.g., Section 5.2. As an illustration, we consider the case of a single Fabry-Perot cavity consisting of an ITM and an ETM, and focus on fields that vary temporally as $\exp(2\pi i f_{\text{rf}} t)$. Now instead of a single field E , we will consider a vector $\mathbf{E} = [E_{00}, E_{01}]^T$. Here we focus on pitch and thus include only E_{01} ; including E_{10} as well as modes with higher spatial order to the system is nonetheless straightforward. For the reflection upon the ETM, we can define a matrix

$$\mathbf{M}_e = r_e e^{2\pi i \Delta\phi_e} \begin{bmatrix} 1 & i \frac{2\pi w_e}{\lambda_0} \Delta\theta_e \\ i \frac{2\pi w_e}{\lambda_0} \Delta\theta_e & 1 \end{bmatrix}, \quad (6.5)$$

where r_e , w_e , $\Delta\phi_e$, and $\Delta\theta_e$ are the amplitude reflectivity, spot size, microscopic detuning, and misalignment of the ETM, respectively. And similarly we define \mathbf{M}_i for the ITM. The propagation through free space is given by a propagation matrix

$$\mathbf{P} = e^{-2\pi i f_{\text{rf}} L/c} \begin{bmatrix} 1 & 0 \\ 0 & e^{(0+1)i\eta} \end{bmatrix}, \quad (6.6)$$

where L and η are the one-way length and Gouy phase shift of the cavity. We are

Table 6.1: Spot sizes on the aLIGO mirrors in [mm].

PRM	PR2	PR3	ITM	ETM	SR3	SR2	SRM
2.3	6.2	54	53	62	54	8.2	2.1

now ready to obtain the cavity fields as

$$\mathbf{E}_c = -t_i \mathbf{E}_{in} + \mathbf{M}_i \mathbf{P} \mathbf{M}_e \mathbf{P} \mathbf{E}_c, \quad (6.7)$$

where \mathbf{E}_c is the cavity field evaluated right after the HR surface of the ITM, and \mathbf{E}_{in} is the input field entering the cavity. The above equation can be solved easily to obtain the higher-order mode content inside a cavity. Using the techniques of mapping a cavity into a single mirror as we have done in Section 5.2 then allows us to extend the analysis to complex optical system such as aLIGO.

In Table 6.1 we summarize the spot size on each aLIGO mirror and in Table 6.2 the one-way Gouy phase of each cavity. These are the parameters needed when solving equation (6.7).

Note that in the propagation matrix \mathbf{P} the Gouy phase shift is frequency-independent. The significance of this property is the following. Suppose the carrier field is either propagating in the free space (which by construction is set to an integer number of λ_0 ; see Brown & Freise 2014) or is exactly on-resonance or anti-resonance inside a cavity, the 00 modes of the upper and lower RF sideband will then satisfy the relation that $E_{00}(+f_{rf}) = -E_{00}^*(-f_{rf})$, as their propagation phases satisfy $\phi_{00}(+f_{rf}) = -2\pi f_{rf} L_{prop}/c = -\phi_{00}(-f_{rf})$ where L_{prop} is the propagation distance. Therefore when consider the propagation of the 00 modes we can focus only on the upper sidebands. This is no more the case when the higher-order modes are present because $\phi_{mn}(+f_{rf}) = \phi_{00}(+f_{rf}) + (m+n)\eta \neq -\phi_{mn}(-f_{rf})$! Consequently, the higher-order modes at $+f_{rf}$ will generally experience propagation effects and/or cavity filtering in an asymmetric manner with respect to the higher-order sidebands at $-f_{rf}$. Even if $[\phi_{00}(+f_{rf}) \bmod \pi] = 0$, the symmetry between the higher-order modes is such that $\phi_{mn}(+f) = \phi_{mn}(-f)$, different from the RF propagation effect.

Due to the orthogonality of the Hermite-Gauss function, the interference between

Table 6.2: One-way Gouy phases of aLIGO cavities.

Power-recycling	Signal-recycling	Arm
25°	21°	146°

a 01 mode and a 00 mode will vanish on a whole-plane-integrated PD. Nevertheless, if the integration is performed over only the upper half-plane, the 00 and 01 mode will have a non-zero overlap, $\int_0^\infty u_0^* u_1 dy = 1/\sqrt{2\pi}$. As a result, to have a signal that is linearly dependent on the amplitude of the 01 mode encoding the alignment information, we can interfere the signal 01 mode with a reference 00 mode and detect the signal using a PD split into two halves.⁴ Subtracting the upper and lower signals thus lead to the alignment information of interest. We will discuss the detection schemes in more details in Section 6.3.

Similar to that tilt and shift of a beam will generate 01/10 modes, if an incident beam has a spot size greater or smaller than that of the eigenmode of a cavity, real 02/20 modes will be generated from the 00 mode. On the other hand, if there exists a mismatch in the radius of curvatures between the input beam and the cavity eigenmode, it generates imaginary 02/20 modes. Those effects are closely related to the thermal state of the interferometer as the thermal lenses created by the high-input power will create radius of curvature mismatches between different cavities (Brooks et al., 2016). We will explore some of the consequences due to this effect in Chapter 8.

6.2 DEGREES OF FREEDOM

In this Section we consider the alignment DOFs present in complex interferometers, which serves as a crucial first step in understanding the full alignment control system of aLIGO.

To start, we consider the case of aligning a Fabry-Perot cavity (for example, the arm cavity) to an input beam, as shown in Figure 6-1 Panel 1. We use the red-solid line to represent the input axis and the orange-dash line for the cavity axis. To

⁴In reality we want the PD to be able to detect both pitch and yaw signals simultaneously, and therefor a PD is usually divided into 4 quadrants.

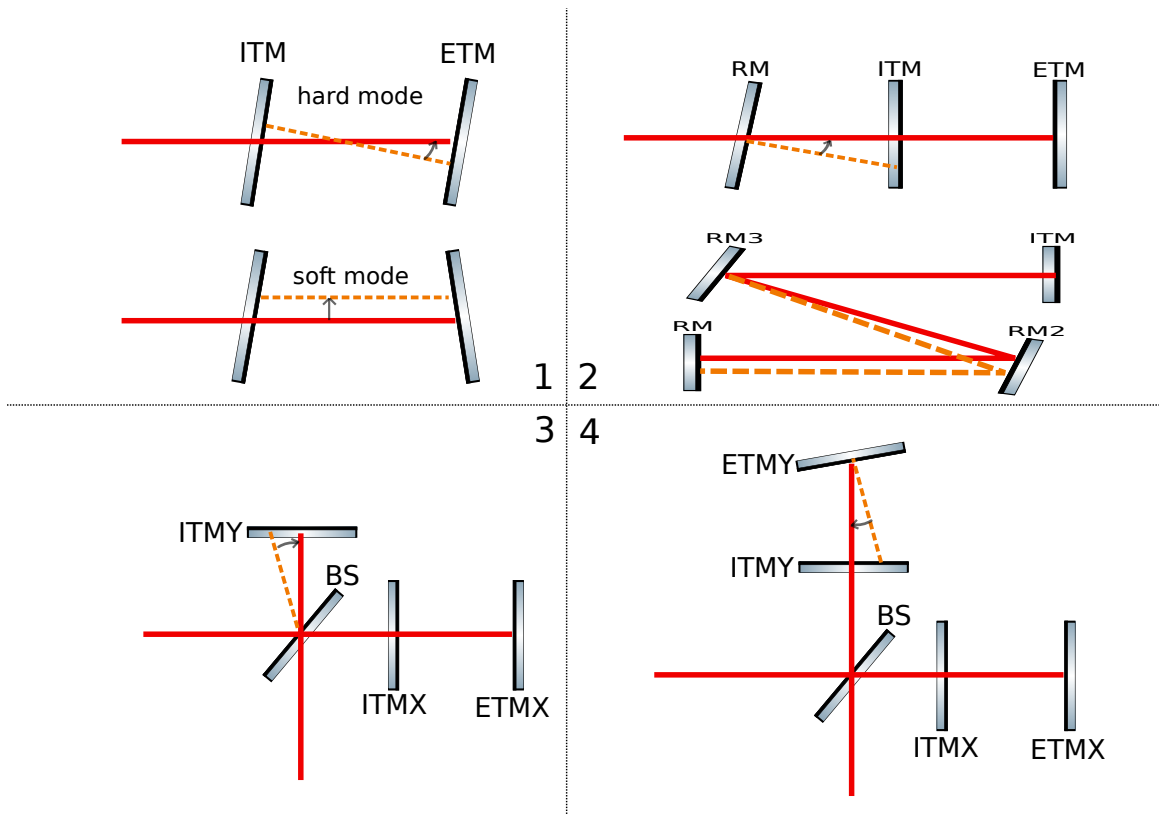


Figure 6-1: Cartoon illustrating the alignment DOFs.

achieve the maximum power buildup inside the cavity, the two axes need to be fully overlapped. This includes two DOFs, corresponding respectively to a tilt and a shift of the cavity axis with respect to the input axis at the cavity’s waist. We will refer to the combined motion of the ITM and the ETM that generates a tilt at the cavity’s waist as the “hard mode”, and the one that generates a shift as the “soft mode”. The reason for these names will become transparent when we discuss the effect of radiation pressure torque in Section 7.2.2. Note that besides aligning the cavity to the input beam, it is also possible to steer the input beam with two mirrors separated by some Gouy phase (ideally $\pi/2$) to align the input axis to the cavity, or to use one steering mirror at the input and one combinations of the test masses.

The two DOFs discussed above involve the overlap between axes of two optical components. We will refer to such a DOF as an “interferometric” DOF. In contrast, another type of freedom exists in the system. Note that we can move the input axis and cavity axis together, which will change the spot position on, e.g., the ETM. The power buildup inside the cavity, however, will not be affected as long as the motion keeps the two optical axes overlapped. We will refer to it as a “pointing” DOF. Despite that a pointing DOF does not directly affect the circulating power inside a cavity, we still need to control it to minimize the scattering losses due to inhomogeneity of the mirror surface. As we will see shortly in Section 6.3.2, a pointing DOF also affects the angle-to-length noise coupling.

Now suppose we have the arm cavity and the input beam aligned both interferometrically and in pointing, and we want to add a recycling mirror (RM) into the system. Consider first the case that the recycling cavity is a linear cavity. Adding the RM will create a new interferometric DOF as shown in the upper part of Panel 2 in Figure 6-1. Consider the beam returning from the arm cavity to the input port, when hitting the RM, it needs to be reflected back to be along the cavity axis to maximize the recycling gain. This condition thus determines the alignment of the RM. In reality, the recycling cavity is a folded cavity formed with three recycling mirrors (RM, RM2, and RM3). Thus, in addition to the interferometric freedom discussed above, there will also be a new pointing DOF as illustrated in the lower part of Panel 2.

For instance, it is possible to change the alignment of RM2 and RM3 to modify the spot position on the RM2, while keeping all the axes aligned as well as the pointing to the arm cavity fixed. Note that we illustrated this new pointing freedom as the spot position on the RM2 only for conceptual simplicity. In reality it can be the spot on a different mirror depending on how we choose the interferometric DOFs to be controlled first. The only critical thing is that the control scheme needs to include the right number of DOFs (both the interferometric and the pointing ones), whereas the detailed implementation is non-unique and depends on other constraints such as the signal-to-noise ratio of sensors.

We then consider the scenario that the input axis and the X-arm cavity axis have been aligned, and we want to add a beamsplitter and an ITMY to the system. This is illustrated in Panel 3. We can let the ITMY's location to be arbitrary and then the beamsplitter needs to be aligned such that it bisects the angle formed by the norms to the two ITMs. This corresponds to a new interferometric DOF due to the Michelson interferometer.

Lastly, we can add the ETMY into the system. As can be seen from Panel 4, this corresponds to a new interferometric DOF, because we need to align the ETMY so that the cavity axis of the Y-arm overlaps with the axis formed by the input beam and the BS in order to maximize the Y-arm's circulating power. Adding the ETMY also leads to a new pointing DOF, as we can shift the entire Y-arm cavity perpendicular to its input while keeping its cavity axis overlapped with the input one.

While in the carton above we separately consider the X-arm and the Y-arm, in practice it is often convenient to combine them into the common ($X+Y$) and differential ($X-Y$) basis. Such a change of basis is fine as long as the total number of DOFs is preserved. Also note that in the carton we have only illustrated the motion in the plane of the page (i.e. the YAW motions). Similar motion can happen in pitch as well and therefore the total DOFs should be doubled.

6.3 DETECTION SCHEMES

Before combining the components above together to form the full aLIGO system, we will discuss here first how we can extract an alignment signal. As we have separated the DOFs into two types, the interferometric ones and the pointing ones, we will consider their detection schemes individually.

6.3.1 Interferometric DOFs

The most commonly used detection scheme for an interferometric DOF is to interfere a carrier field with a pair of RF sidebands at a PD. When the PD is a regular full-plane integrated PD, the same carrier-sidebands pair is used to lock the cavity in length using the PDH technique ([Drever et al., 1983](#)). To detect the misalignment, we further divide the PD into 4 quadrants. A pitch signal can be obtained by subtracting the upper and lower quadrants while a yaw signal by subtracting the right and left quadrants. Such a device is also known as a wave-front sensor (WFS) in LIGO literatures.⁵

The generic working principle of this scheme is illustrated in Figure 6-2. For simplicity we assume the RF sidebands (indicated by the blue trace) are off-resonance in the cavity. They directly reflect off the ITM and propagate to the WFS. The carrier field (illustrated by the red trace) is resonant in the cavity and thus probes its alignment. If the cavity is misaligned (modeled as a misalignment of the ETM), then it creates 01/10 mode from the carrier field. The carrier 01/10 mode also propagates to the WFS and interferes with the RF 00 modes. The interference pattern is detected by the WFSs to yield the alignment signal of interest. In other words, we use the RF sidebands that encode the input beam's alignment as a spatial reference and compare the carrier field that samples the cavity's alignment to the reference. By zeroing the difference in power in the WFS's upper and lower, or right and left quadrants, we ensure the cavity is aligned with respect to the input beam.

⁵Note that a WFS operates at RF frequencies. This is in contrast with a DC quadrant PD, or a DC QPD, which, as indicated by its name, detects signals at DC.

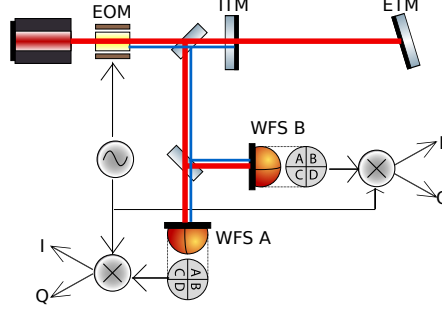


Figure 6-2: The generic principle of detecting an alignment signal with WFSs. The carrier field (represented by the red line) is resonant in the cavity and probes the cavity mode. The RF sidebands (the blue trace; they are generated by the electro-optic modulator, or the EOM) are off-resonance and hence encodes only the information about the input beam. The two wave-fronts are compared at the WFSs. Subtracting the upper and lower (right and left) halves leads to signals for pitch (yaw) misalignment. To account for the Gouy phase shift, two WFSs (A and B) separated by $\pi/2$ in Gouy phase are used. The carrier-sidebands pair is also used for the longitudinal locking via the PDH technique, which ensures the WFS signal to be free from contaminations due to DC spot drifts on the sensor.

Note that since the WFS operates at RF frequencies, to demodulate the signal down to DC a demodulation phase needs to be specified. Often this phase is chosen to be the same as the demodulation phase for the longitudinal PDH signal, and we will use I and Q to refer to the in-phase and in-quadrature signals, respectively. Moreover, since the 01/10 modes experience an extra Gouy phase shift η with respect to the 00 mode during propagation, to fully reconstruct the signal we need to put at least two WFSs separated by $\pi/2$ in Gouy phase per detection port. We will call them WFS A and B in the future.

A nice property of a WFS is that its signal is not contaminated by the spot's motion on the PD. If we again choose the carrier 00 field $E_{00}(0)$ to be real with the spatial basis defined by the cavity's eigenmodes, then the RF 00 modes will satisfy $E_{00}(+f_{\text{rf}}) = -E_{00}^*(-f_{\text{rf}})$ for the upper and lower sidebands when the cavity is PDH locked. Therefore, the power due to the interference between carrier and RF 00 modes vanishes as $P_{\text{spot}}(f_{\text{rf}}) \propto E_{00}^*(0)E_{00}(+f_{\text{rf}}) + E_{00}^*(-f_{\text{rf}})E_{00}(0) = [E_{00}(+f_{\text{rf}}) + E_{00}^*(-f_{\text{rf}})]E_{00}(0) = 0$. In other words, even if the spot position on

a WFS shifts with respect to the cavity basis, this motion will not be picked up by the WFS as the total power vanishes at f_{rf} without cavity misalignment⁶. Consequently, a WFS senses only the true wavefront distortion signal of the form $P_{\text{wfs}}(f_{\text{rf}}) \propto E_{01}^*(0)E_{00}(+f_{\text{rf}}) + E_{00}^*(-f_{\text{rf}})E_{01}(0) \neq 0$ in general, as $E_{01}(0) \in \mathbb{C}$ when we set $E_{00}(0)$ to be real. Also note that when detecting a pitch signal at the WFS, the spatial integration is performed only over half planes and then the difference between the upper and lower halves is used (and similarly for yaw).

Besides using a WFS, an interferometric DOF can also be detected by dithering an optic and then demodulate the fluctuations in the cavity's circulating power at the dithering frequency. This is because the fluctuations in power ΔP depends on the alignment quadratically, as

$$\frac{\Delta P}{P_0} \simeq \frac{1}{2} \left(\frac{\Delta\theta}{\theta_0} \right)^2 + \frac{1}{2} \left(\frac{\Delta y}{w_0} \right)^2, \quad (6.8)$$

where P_0 is the cavity's nominal circulating power (which is also the maximum power), $\Delta\theta$ and Δy are the tilt and shift at the cavity's waist, and θ_0 and w_0 are the cavity's divergence angle and spot size at the waist. Now suppose our dithering excitation creates a tilt signal $\Delta\theta_{\text{exc}}(f_{\text{exc}})$,⁷ then the power fluctuation at the dithering frequency f_{exc} can be written as

$$\frac{\Delta P(f_{\text{exc}})}{P_0} \propto \left[\frac{\Delta\theta_{\text{exc}}(f_{\text{exc}})}{\theta_0} \right] \left[\frac{\Delta\theta(0)}{\theta_0} \right]. \quad (6.9)$$

Therefore, by introducing the dithering, the power fluctuation $\Delta P(f_{\text{exc}})$ becomes a signal linearly proportional to the cavity's misalignment $\Delta\theta(0)$. This technique can be used to probe the cavity's alignment at DC or at frequencies much smaller than the dithering frequency f_{exc} .

In general, the dithering scheme is a much simpler setup than using the WFS,

⁶This is the same reason why a PDH signal is insensitive to amplitude fluctuations.

⁷We will ignore the Δy_{exc} term as the analysis is similar. To fully sample the cavity's alignment we need two excitations respectively for the $\Delta\theta_{\text{exc}}$ and Δy_{exc} terms, or for two different linear combinations of them. This is conceptually equivalent to using two WFSs separated by $\pi/2$ in Gouy phase.

as it only requires a whole-plane PD operating at “DC” (that is, capable to detect signals in the audio-frequency band), whereas a WFS requires RF electronics capable to detect signals up to tens of MHz. Similar to the WFS technique, the dithering scheme is also insensitive to small spot motions on the diode as long as the incident beam is not clipping. The draw back, however, is that due to realistic constraints such as noise performance, the dithering excitation is small in general. As a result, the dithering technique’s sensitivity is usually orders of magnitude worse than that of using the WFS.

6.3.2 Pointing DOFs

To detect a pointing degree of freedom, for example the spot position on the ETM, one can read out the signal at DC quadrant PDs (DC QPDs) on transmission of the ETMs. The signal takes the form of $P_{\text{spot}}(0) \propto \text{Re}[E_{01}^*(0)E_{00}(0)]$. Note that $E_{01}^*(0) \in \mathbb{C}$ due to the Gouy phase. Therefore two DC QPDs separated by $\pi/2$ are used at each detection port. However, one major drawback of the DC QPD is that it cannot distinguish a true cavity signal from that due to the spot drift on the sensor. This is a serious issue in aLIGO as the table where the QPDs are mounted drifts with respect to the arm cavity in the timescale of a few hours because of the seismic motion and thermal variations.

Another approach for sensing a pointing DOF is again using the dithering technique, but this time instead of reading the output signal from power fluctuations, the pointing information is encoded in the length perturbations. The “angle-to-length” coupling process can be easily understood geometrically, as shown in Figure 6-3. If the spot position on a mirror does not correspond to the mirror’s rotational pivot, a length signal is created as

$$\Delta L(f_{\text{exc}}) \simeq \Delta y(0)\Delta\theta_{\text{exc}}(f_{\text{exc}}), \quad (6.10)$$

where $\Delta y(0)$ is the distance between the spot position and the pivot. If we want to lock the spot instead to the pivot but another position, we can feedforward the

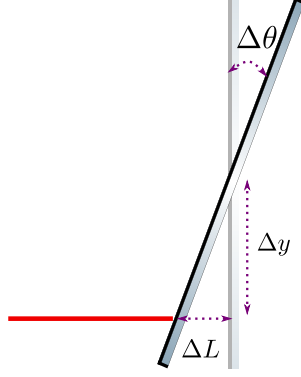


Figure 6-3: Carton illustrating the angle-to-length coupling due to spot miscentering.

angular signal to length as $\Delta L_{\text{ff}}(f) = -\Delta y_{\text{ff}}\Delta\theta(f)$, then the demodulated length signal will give us spot position measured in $[\Delta y(0) - \Delta y_{\text{ff}}]$.

The difference between the angle-to-length (for sensing a pointing DOF) and the angle-to-power (for sensing an interferometric DOF) couplings can also be understood in the modal picture. For convenience, we consider the case that the 00 mode is resonant inside the cavity and set its amplitude to be real and positive. Suppose the DC spot position is off-centered on a mirror. In the modal picture this corresponds to a real 01 mode at DC incident onto the mirror. As we dither the mirror at AC, we scatter the real 01 mode into an imaginary AC 00 mode. This is exactly the same signal created by a longitudinal AC motion of the mirror. This thus corresponds to the angle-to-length coupling due to spot mis-centering (i.e., the existence of a real 01 mode at DC). Note that the scattered AC 00 mode is out-of-phase with the DC cavity field, and therefore it will not modify the power circulating inside the cavity.

In contrast, if a beam is misaligned with respect to the mirror at DC, it means there is an imaginary 01 mode incident onto the mirror. The AC angular motion of the mirror will then scatter this imaginary 01 mode into a real 00 mode, which

will further interfere with the DC cavity field and cause power fluctuations at AC, leading to an angle-to-power coupling. However, due to the finite mass of the mirrors, the power fluctuation will also create a length signal via the radiation pressure force. This angle-to-power-to-length coupling may confuse the geometrical angle-to-length coupling due to spot mis-centering, and consequently contaminate the error signal used for sensing a pointing DOF. This effect can be significant when aLIGO reaches 100 W of input power, and would thus deserve more detailed study in the future.

6.4 ALIGNMENT SENSING AND CONTROL IN aLIGO

We are now ready to consider the alignment sensing and control in aLIGO. Based on our discussion in Section 6.2, for the pitch alignment there are in total 6 interferometric DOFs and 4 pointing DOFs, and for yaw the numbers are the same. To further assist our discussion, we can geometrically divide the interferometer into three parts, the symmetric/input part, the Michelson, and the anti-symmetric/output part, and study the DOFs at each part individually.

Consider first the interferometric DOFs. On the symmetric (or the input) side of the interferometer, which consists of the input beam, the power-recycling cavity, and the common-arm cavity, there are three interferometric DOFs (cf. Panels 1 and 2 in Figure 6-1; note that we have replaced the single X-arm cavity by the common-arm cavity).

The first freedom is the common-hard mode of the arm cavities measured with respect to the input axis coming from the power-recycling cavity. It can be sensed with a combination of WFSs located at the REFL port (which picks up the beam reflected-off the interferometer; see Figure 5-1) and the error signal is fed-back to the combination of test masses that corresponds to the common-hard motion with a bandwidth of 3 Hz.⁸ The second DOF aligns the power-recycling cavity's axis to

⁸The actual alignment sensing and control of the arm cavity is an involved topic and we will devote the next Chapter to present a more detailed discussion

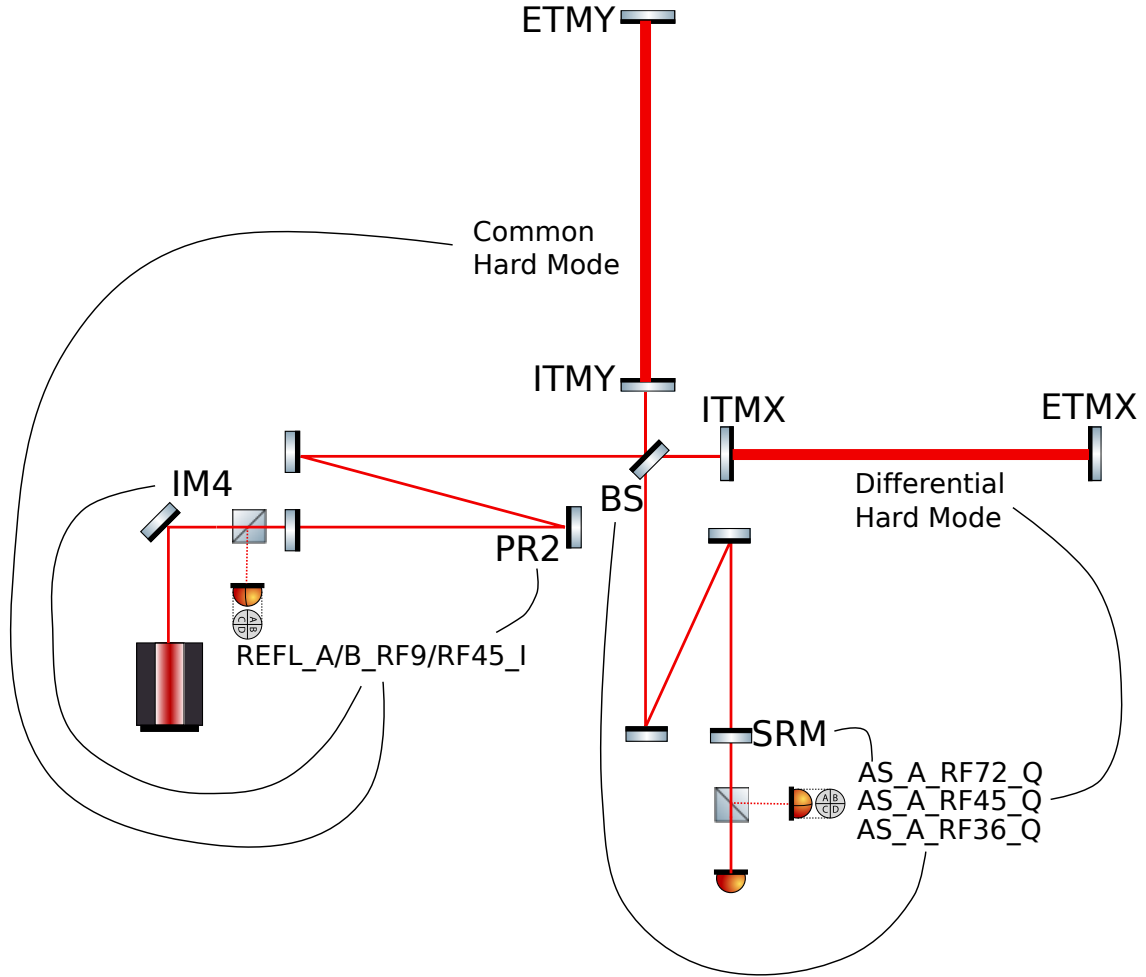


Figure 6-4: Alignment sensing and control of the interferometric DOFs in aLIGO. On the symmetric side, we use three different linear combinations of REFL WFSs to overlap the axes of the input beam, the power-recycling cavity, and the common arm cavity. The Michelson and the differential arm axis are sensed with AS_A_RF36_Q and AS_A_RF45_Q, respectively. Lastly, the signal-recycling cavity's axis is aligned to the differential-arm cavity's axis by using AS_A_RF72_Q as the error signal.

the common-soft mode of the arm cavity (i.e., to minimize the lateral shift between the recycling cavity’s axis and the arm cavity’s axis at the waist of the arm cavity). Instead of controlling it with the test masses, this freedom is controlled with the PR2 mirror with a bandwidth of 0.8 Hz. Lastly, the input axis is aligned to the power-recycling cavity’s axis by actuating on a steering mirror (IM4) with approximately 0.1 Hz bandwidth.

All the three DOFs are sensed with the REFL WFSs. Specifically, we use four error signals which we will refer to as REFL_A/B_RF9/RF45_I. Here “REFL” stands for the detection port from which the signal is derived and different ports are defined in Figure 5-1. The “A” and “B” account for the two Gouy phases separated by $\pi/2$. The “RF9” and “RF45” are the RF frequencies at which a WFS is demodulated. Specifically, the “RF9” signal corresponds to the beat note between the carrier field and the ± 9.1 MHz sidebands, and similarly the “RF45” signal corresponds to the interference between the carrier field and ± 45.5 MHz sidebands. Lastly, the “I” stands for one of the RF demodulation phase that maximizes the whole-plane integrated signal’s response to the common-arm (CARM) motion in length; the other demodulation phase correspond to the “Q” signal which we do not use here. The right combination of sensors can be determined by exciting each DOF individually and measuring the response in each individual sensor. Then such a sensing matrix can be inverted to give the proper linear combinations of sensors to be used as the error signal for each DOF. Note that here we use four sensors (which are treated as linearly-independent) for three DOFs. Such a system can be inverted with the Moore-Penrose pseudo-inverse algorithm (Penrose, 1955).

The Michelson (cf. Panel 3 in Figure 6-1) is sensed with the AS_A_RF36_Q. Note here the “RF36” is from the beat note between the 9.1 MHz and 45.5 MHz sidebands. Unlike the beat note between the carrier and sidebands, the beat note between two sidebands will have a non-vanishing (whole-plane-integrated) power at the beat-note frequency.⁹ Therefore, we define the demodulation phase such that after demodulating the signal at 36.4 MHz, for each quadrant the DC power shows

⁹<https://alog.ligo-wa.caltech.edu/aLOG/index.php?callRep=43574>

up all in the I phase. Then the orthogonal Q-phase signal is used here for sensing the the Michelson alignment. We feedback this error signal to the BS with a bandwidth of 0.8 Hz.

On the anti-symmetric side, there are two more interferometric DOFs. One corresponds to the differential-hard mode of the arm cavities. This DOF is sensed with AS_A_RF45_Q, where the Q phase is defined to maximize the signal's response to the longitudinal DARM motion. The control is accomplished by feeding back the error signal to the four test masses in the linear combination that leads to the differential-hard motion with a bandwidth of 3 Hz.

The last interferometric DOF is to align the signal-recycling cavity's axis to the axis of the differential arm cavity by actuating on the SRM. Originally this signal was sensed using AS_A_RF36_I. However, it turned out that this signal was subject to thermal distortion of the system and could not be used when the input power exceeded 20 W. To overcome this issue, a new RF sideband has been added at 118.3 MHz, and we instead sense the SRM error signal using AS_A_RF72_Q, which is the beat-note between the 118.3 MHz and 45.5 MHz sidebands at 72.8 MHz. The control bandwidth of this loop is set to around 0.1 Hz. We will discuss this sensing scheme in more detail in Section 8.1.

To summarize the discussions above, we show in Figure 6-4 a carton illustrating the sensing and control of all the interferometric DOFs in aLIGO.

As for the four pointing DOFs, two of them correspond to the spot positions on the two ETMs. They are sensed by dithering each ETM in angle individually and then demodulate the longitudinal DARM signal at the excitation frequencies. In other words, they are sensed utilizing the angle-to-length coupling effect [cf., equation (6.10)]. The error signals are then fed back to the combination of test masses corresponding to the soft-mode of each arm with a bandwidth of a few mHz. Similarly, we control the pointing DOF in the power-recycling cavity by locking the PRM alignment to a fixed spot on ITMX using the same angle-to-length coupling effect. Lastly, we point the SR2 alignment to a fixed spot on a DC QPD on the transmission of SRM to fix the pointing freedom of the signal-recycling cavity.

6.5 TOLERANCE ON THE RESIDUAL ANGULAR MOTION

To complete our discussion on aLIGO’s alignment sensing and control, we consider here the requirements set on each control loops. We will focus first on the corner degrees of freedom (i.e., the alignment of the recycling cavities and the Michelson), and defer the discussion of the arm cavities’ requirements to the next Chapter.

In general, the major consideration on the alignment is that the control loop needs to suppress the residual angular motion to a sufficiently small value such that the interferometer can stay at its proper working point. Therefore, the question to ask naturally becomes the following. What is the definition of “sufficiently small” for each DOF?

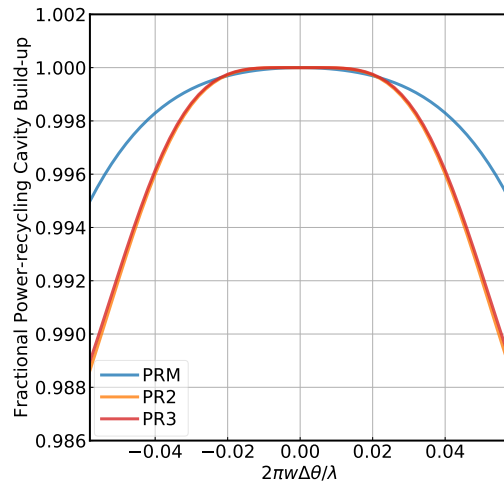


Figure 6-5: Fractional power build-up inside the power-recycling cavity as a function of the recycling mirrors’ misalignment.

First consider the power-recycling cavity. Its purpose is to enhance the DC power input to the arm, so that the shot-noise-limited sensitivity of DARM decreases by a factor of g_p [cf. equation (5.44)], with g_p being the carrier field’s amplitude gain inside the power-recycling cavity. If the power-recycling cavity is misaligned, however, the value of g_p decreases as the carrier 00 mode loses its power to the higher-order modes.

In Figure 6-5 we plot the fractional power build-up inside the power-recycling cavity ($\propto g_p^2$) as a function of the misalignment of recycling mirrors (PRM, PR2, and PR3). The misalignments are plotted in units of the normalized angle $2\pi w\Delta\theta/\lambda_0$ where w is the spot size on the mirror (cf. Table 6.1). For a normalized angle of 0.01, it corresponds to misaligning the PRM, PR2, and PR3 by 0.74, 0.27, and 0.03 μrad , respectively. To reduce the power by 1% (corresponding to 0.5% increase in the shot noise), it requires a misalignment of at least 0.05 normalized angle, or at least 0.15 μrad misalignment of PR3. On the other hand, the input angular perturbation due to the seismic motion has a root-mean-square (rms) on the order of 0.1 μrad for each recycling mirror, already smaller than the value we could tolerant. Consequently, we only need a low-bandwidth (~ 0.1 Hz) control loop to overcome the long-term drift of power-recycling cavity's axis with respect to the input beam.

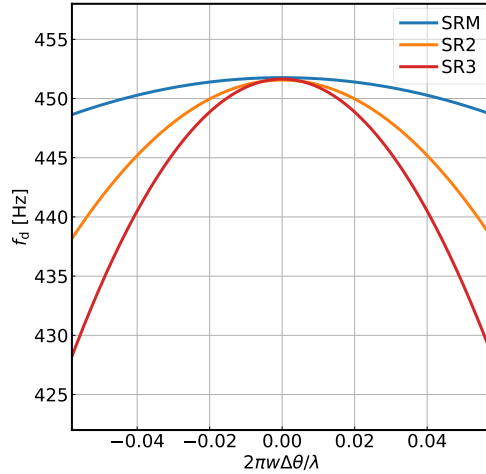
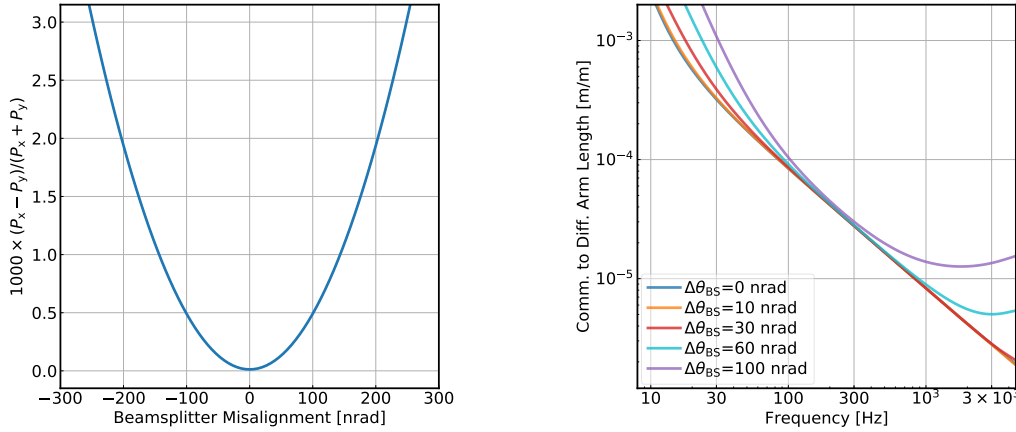


Figure 6-6: The DARM cavity frequency f_d as a function of the misalignment of the signal recycling mirrors.

As for the signal-recycling cavity, the requirement is based on the DARM cavity pole frequency f_d [cf. equation (5.34)]. As misalignment increases the loss inside the signal-recycling cavity, the DARM pole f_d decreases to lower frequency, reducing the instrument's sensitivity to GW signals with $f > f_d$. In Figure 6-6 we plot f_d as a function of the signal recycling mirrors' misalignment. The x -axis is again the

normalized angle. The conversion is that a 0.01 normalized angle corresponds to a misalignment of SRM, SR2, and SR3 by 0.81, 0.21, and $0.03 \mu\text{rad}$, respectively. To control the fluctuation in f_d to be less than 10 Hz, the rms in normalized angle needs to be $\lesssim 0.03$ (or at least $0.1 \mu\text{rad}$ SR3 misalignment). This is once again satisfied by the input motion without extra loop suppression. Therefore, we also control SRM's alignment with a low-bandwidth feedback loop compensating only for the long-term drift.



(a) The difference in the circulating power in the two arm cavities as a function of the beamsplitter's misalignment.

(b) Cross-coupling from CARM to DARM due at different level's of the beamsplitter's misalignment.

Figure 6-7: Requirements on the alignment of the Michelson DOF.

Lastly, we consider the tolerance on the BS's alignment. One apparent consideration is that we need to keep the DC power level in both arms as high as possible. This is considered in Figure 6-7a where we plot the difference in the DC power buildup in the two arm cavities as a function of the BS's misalignment. At a misalignment of 100 nrad, the beamsplitter only induces a difference in the DC power level of 0.05%. As a comparison, the typical difference in the arm losses ($|\Gamma_x - \Gamma_y|/2 \sim 10$ ppm) and the imbalance in ITMs' power transmissivity ($|T_{ix} - T_{iy}|/2 \sim 100$ ppm) will lead to a difference in the two arms' DC power on the order of 1%.

However, a more contingent requirement exists. If the Michelson does not stay on a perfect dark fringe, the common-mode motion such as the input laser's intensity

and frequency noise will not be perfectly reflected back to the symmetric port but will instead leak to the anti-symmetric port, contaminating the DARM signal. In Figure 6-7b we consider the cross-coupling from the CARM motion (which is equivalent to the input laser's frequency noise) to the DARM signal. When the BS is perfectly aligned, the cross-coupling is due to the mismatch in the two arm's cavity pole frequencies caused by the difference in the ITM transmissivity [see, e.g., Izumi et al. 2015; we assume it to be $(T_{ix} - T_{iy})/2 = 100 \text{ ppm}$ here]. When the BS is misaligned, the DC 01 modes it generated will enter the arm cavity and be modulated by the AC CARM motion. As the AC 01 mode propagates back to the misaligned beamsplitter, it will be scattered back to an AC 00 mode that is equivalent to a length fluctuation of the Michelson. This noise further couples to DARM with a coefficient $\frac{|1+if/f_d|}{g_a^2}$. Meanwhile, part of the AC 00 mode will also enter the arm cavities again and interfere with the DC cavity fields. This leads to an excess radiation pressure noise dominating the low-frequency cross coupling with a characteristic $1/f^3$ slope (note that in addition to the $1/f^2$ filtering due to the pendulum, there is another $1/f$ due to the filtering in the power-recycled CARM cavity). Based on the CARM-to-DARM cross-coupling, the residual beamsplitter motion should be controlled to $\lesssim 10 \text{ nrad}$. Nevertheless, this requirement can still be satisfied by the raw input motion, as the vacuum chamber hosting the BS (also known as a BSC) provides 10 times more seismic isolation at the suspension point compared to the chambers hosting the recycling mirrors (Matichard et al., 2015a,b,c). To further increase the safety margin, we also have a relatively high-control bandwidth of 0.8 Hz on the Michelson's alignment control compared to the loops used for the recycling cavities' alignment.

Chapter 7

Alignment control of the arm cavities

In the previous Chapter we provide an overview of aLIGO’s active alignment control system. We find that for DOFs in the corner, the rms of the seismic input generally satisfies the requirement on the residual angular motion, and hence only low-bandwidth controllers are needed for them. This is, however, not the case for the DOFs in the arm cavities. As we will see in Section 7.1, active loop suppression is necessary in order to maintain the interferometer at proper working point. Meanwhile, the controllers bandwidth must be limited to reduce the injection of excess sensing noise, which is one of the dominant noise sources below 30 Hz for aLIGO. Furthermore, hundreds of kW of circulating power in the arm cavities creates a significant amount of optical torque even dwarfing the restoring torque from the pendulum. This can dramatically complicate the control design and we will devote Section 7.2 to discuss it in thorough details. Specifically, we will provide the general mathematical background of radiation torques in Section 7.2.1. A comprehensive study on the Sidles-Sigg radiation torque is provided in Section 7.2.2, including discussions on both its dynamical interactions with the suspension and a newly implemented compensation scheme to remove its effects in aLIGO. Section 7.2.3 is dedicated to the discussion of yet another kind of radiation interaction, known as the $dP/d\theta$ effect. After these discussions on the optical torques, we will return to the noise discussion in Section 7.3 and discussion recently implemented or future upgrades to enhance the controller’s performance.

7.1 CONTROL LOOP DESIGN CONSIDERATIONS

Similar to Section 6.5, we discuss in this Section various requirements we should consider for designing the control feedback of the arm cavity.

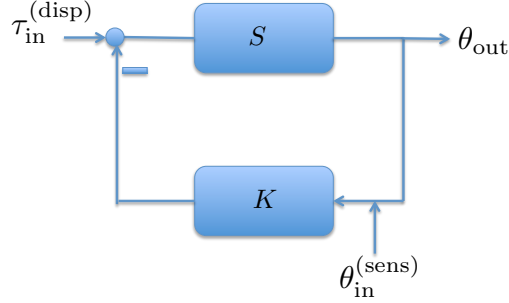


Figure 7-1: Model for the alignment feedback control.

Consider a feedback-loop model as illustrated in Figure 7-1. Here S is the suspension transfer function with in units of $[\text{rad}/\text{N} \cdot \text{m}]$, and K is the control feedback gain in $[\text{N} \cdot \text{m}/\text{rad}]$. We consider two kinds of noise input here. One is the displacement perturbation input to the system $\tau_{in}^{(\text{disp})}$, and the other is the sensing noise $\theta_{out}^{(\text{sens})}$. The closed-loop response to the noises can be respectively written as

$$\theta_{out}^{(\text{disp})} = \frac{S}{1 + KS} \tau_{in}^{(\text{disp})}, \quad (7.1a)$$

$$\theta_{out}^{(\text{sens})} = \frac{-KS}{1 + KS} \theta_{in}^{(\text{sens})}. \quad (7.1b)$$

In Figure 7-2 we show the typical pitch noise input to the aLIGO’s arm cavities. For the displacement noise, the dominant contribution is from the ground’s longitudinal motion coupling to the test mass’ pitch angle due to the suspension length-to-pitch coupling (see, e.g., [Rakhmanov 2000](#); it is labeled with “Seismic” in the Figure). This is a unique coupling to pitch and the seismic noise input to yaw is thus much smaller. Another significant contribution is the local damping noise. This is the noise coming from the shadow sensors ([Carbone et al., 2012](#)) that are used for reducing the quality factors of the suspension resonances. The total rms of the input displacement is $\sim 30 \text{ nrad}$. At the same time, the hard modes of the arm cavities generally has a

sensing noise of $\theta_{\text{in}}^{(\text{sens})} \simeq 10^{14} \text{ rad}/\sqrt{\text{Hz}}$.¹

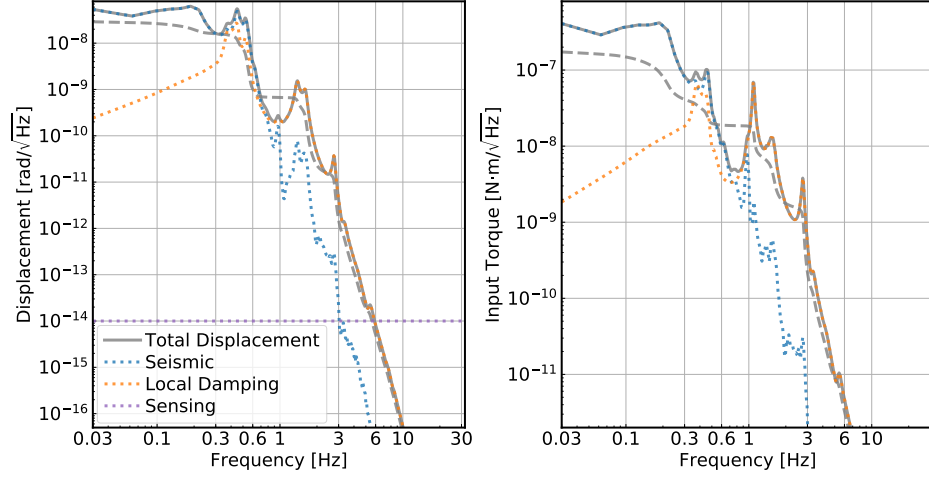


Figure 7-2: Typical pitch noise input to the aLIGO arm cavities. In the left we show noise in $[\text{rad}/\sqrt{\text{Hz}}]$ and in the right we calibrate the displacement noise into the torque exerting on the test masses in $[\text{N} \cdot \text{m}/\sqrt{\text{Hz}}]$. The total displacement (the grey-solid trace) is the quadratic sum of the seismic (blue-dotted) and local damping (orange-dotted) noises. The cumulative rms of the displacement perturbation is shown in the dashed-grey trace. Also shown in the purple-dotted line is the typical sensing noise level.

After knowing the input noise level, we need to consider next the requirements should be set on the closed-loop noises $\theta^{(\text{disp})}$ and $\theta^{(\text{sens})}$. Specifically, there are two requirements related respectively to the low-frequency ($\lesssim 1 \text{ Hz}$; dominated by the displacement noise) and the high-frequency ($\gtrsim 10 \text{ Hz}$; dominated by the sensing noise) portions of the spectrum.

At low frequencies, we need to have sufficient suppression of the residual rms motion. This is similar to our consideration in Section 6.5. In Figure 7-3 we present the fractional power build-up inside the arm cavity as a function of arm misalignment (in the hard/soft basis). Note that the shot-noise-limited DARM sensitivity scales as $1/g_a^2$ [cf. equation (5.44)], and thus a reduction of the power build-up inside the arms by 1% will lead to an increase in the shot noise level by 1%. This is in contrast to the case of the buildup inside the power-recycling cavity where the DARM sensitivity

¹<https://alog.ligo-wa.caltech.edu/aLOG/index.php?callRep=46178>

scales only as $1/g_p$. From Figure 7-3 we can see that to keep the buildup above 99% of its nominal value, we should control the hard modes to within 5 nrad rms. The requirements on the soft modes² is less strict and it can tolerate up to 20 nrad of rms fluctuation.

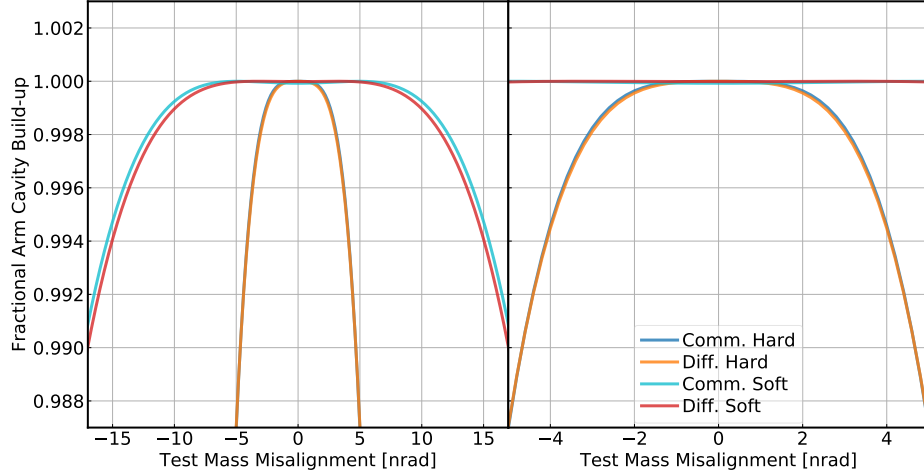


Figure 7-3: Fractional power build-up in the arm cavities as a function of the misalignment in the hard and soft modes. For a 1% reduction in the arm build-up (corresponding to 1% degradation in the shot-noise-limited sensitivity) it corresponds to 5 nrad misalignment in the hard modes and 20 nrad in the soft modes.

Another consideration is the degradation of the common-mode rejection because of misalignment, which we study in Figure 7-4. Here we can see that misalignments in the differential-hard mode (and similarly in the common-hard mode) enhances the CARM-to-DARM coupling at $\lesssim 30$ Hz via the radiation pressure effect. While the CARM/input frequency noise is usually well-suppressed below 100 Hz, other common-mode noise such as the input jitter will couple in a similar manner (Martynov et al., 2016). Consequently, we would like to control the hard-mode motion to a rms of around 1 nrad, which is a more stringent constraint than the one set on power-build up.

²Here we mean specifically the “interferometric” soft mode, which is measured with respect to the power-recycling cavity’s axis. It is actually controlled by actuating on PR2. See Section 6.4. This should be distinguished with the “pointing” soft mode which measures the mirrors motion with respect to the ground. See also Section 7.2.3.

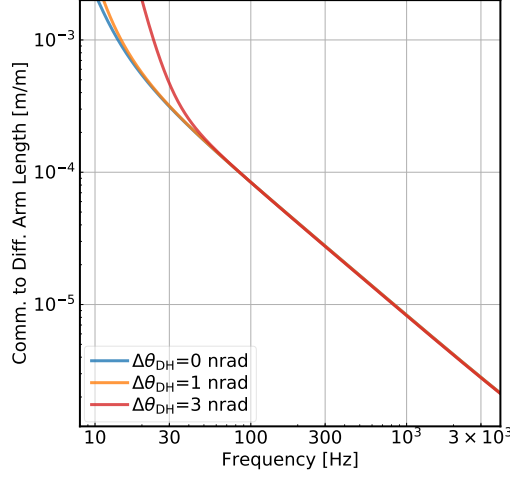


Figure 7-4: CARM to DARM cross-coupling at different levels of misalignment in the differential hard mode $\Delta\theta_{dh}$.

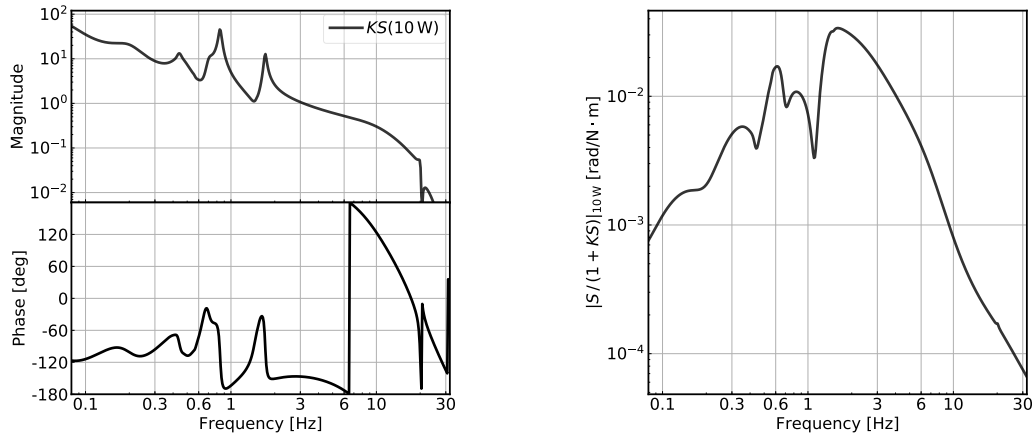
At high frequencies ($\gtrsim 10$ Hz), the control loop feeds back the sensing noise and perturbs the test masses in angle. It can further couple to the DARM readout via the angle-to-length cross-coupling (Section 6.3.2; also also Barsotti et al. 2010). The typically coupling coefficient is (Martynov et al., 2016)

$$Z_{a2l} \simeq 1 \left[\frac{\text{mm}}{\text{rad}} \right]. \quad (7.2)$$

This is greater than the residual spot motion created by the rms fluctuations of the alignment loops (which should be $\lesssim 0.1$ mm), and is likely to be due to the DC offsets in the pointing loops. If we want the angular noise to be below the designed DARM sensitivity at 10 Hz, or $6 \times 10^{-19} \text{ m}/\sqrt{\text{Hz}}$, we need to reduce the closed-loop sensing noise $\theta^{(\text{sens})}(10 \text{ Hz}) < 6 \times 10^{-16} \text{ rad}/\sqrt{\text{Hz}}$. In other words, the open-loop transfer function needs to be reduced to $KS < 0.06$ at 10 Hz.

To summarize, the alignment control of the arm cavity should have a sufficiently large bandwidth to suppress the sub-1 Hz input motion from a rms of about 30 nrad down to 1 nrad. At the same time, it needs to be rolled-off fast enough to be smaller than 0.06 at 10 Hz. These two regions need to be connected in the 1 – 10 Hz band such that it satisfies the stability requirement, $1 + KS \neq 0$. Yet another constraint

is that the control loops need to stabilize the radiation torques and we will discuss it soon in the coming Section.



(a) The open loop transfer function $KS(10W)$.

(b) The closed loop torque-to-angle transfer function $|S/(1 + KS)|_{10W}$.

Figure 7-5: Control filters currently used for stabilizing the differential-hard mode's alignment in pitch. It is evaluated at an input power level of 10 W (or 57 kW of circulating power in each arm).

Currently, the filter used for controlling the pitch motion of the differential-hard mode at the Hanford site is shown in Figure 7-5. Combine it with the input motion shown in Figure 7-2 leads to the closed-loop residual angular motion³ shown in Figure 7-6 .

From Figure 7-6 we can see that our current controller satisfies the low-frequency requirement on the residual rms; it suppresses the input motion to an rms of $0.4 \text{ nrad} < 1 \text{ nrad}$. However, in the $10 - 20 \text{ Hz}$ band our current control loop fails to meet the aLIGO's requirement on the roll-off of the sensing noise (shown in the red curve). One reason we do not use a lower-bandwidth and more-aggressively-rolled-off loop is that the effect of radiation pressure will modify the suspension transfer function S as a function of arm circulating power. It further means that a controller designed at

³Note that multiplying the input noise in $[\text{rad}/\sqrt{\text{Hz}}]$ as shown in the left panel of Figure 7-2 by $[1/(1 + KS)]_{10W}$ does not lead the appropriate closed-loop displacement noise as it does not account for the effect of radiation pressure correctly. See Section 7.2.2. The correct way is to take the noise input in torque (the right panel of Figure 7-2) and then multiply it by $[S/(1 + KS)]_{10W}$.

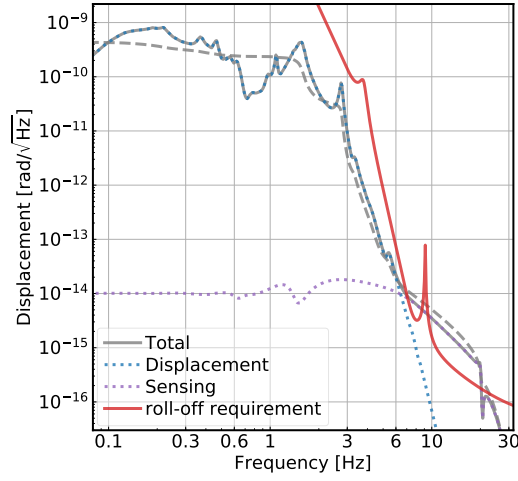


Figure 7-6: The closed-loop residual pitch motion of the differential-hard mode. The grey-solid trace is the total motion by summing the displacement (blue-dotted) and the sensing (purple-dotted) noises in quadrature. The cumulative rms motion is shown in the dashed-grey trace. While the residual rms motion of $\simeq 0.4$ nrad satisfies the requirement, the > 10 Hz roll-off of the sensing noise is not sufficient to meet the aLIGO's design requirement that is shown in the red trace with an assumed angle-to-length coupling of 1 mm/rad.

one power-level may become unstable at another power. Consequently a conservative design is chosen. We will use the next Section to discuss how the effect of radiation pressure modifies the control loop, and more importantly, how we can compensate for such an effect so that in the future we do not need to worry about variations in the plant. This will further open up the possibility of reducing the alignment control noise to a level below the aLIGO's fundamental quantum and thermal limits.

7.2 EFFECTS OF RADIATION PRESSURE

7.2.1 Introduction

In this section we study the interactions between the radiation torques and the suspended test masses, which are the key component of designing the controller for the arm cavities' alignment in aLIGO.

To start, consider first the radiation torque exerted on a test mass in the time domain. The torque exerting on the upper-half plane can be written as

$$\tau^{(\text{up})}(t) = \frac{2}{c} \int_{-\infty}^{\infty} dx \int_0^{\infty} dy [y E_{00}(t, x, y) E_{01}(t, x, y)], \quad (7.3)$$

where we have omitted terms such as $E_{00}E_{00}$ as terms with even parity will be canceled out as we subtract the upper and lower halves and thus not contribute to the total torque. To proceed, we can further write the fields as

$$E_{mn}(t, x, y) = a_{mn}(t) u_{mn}(x, y), \quad (7.4)$$

where $u_{mn} = u_m u_n$ is the normalized Hermite-Gauss function [cf. equation (6.2)]. The spatial integration thus leads to

$$\int_0^{\infty} y u_0(y) u_1(y) dy = \frac{w}{4}, \quad (7.5)$$

where w is the spot size on the mirror. By subtracting the upper and lower halves

and utilizing the spatial symmetry $\tau^{(\text{low})} = -\tau^{(\text{up})}$, we have

$$\tau(t) = 2\tau^{(\text{up})}(t) = \frac{w}{c}a_{00}(t)a_{01}(t). \quad (7.6)$$

Now we can transfer to the Fourier domain⁴ and use the bi-linear approximation to compute the fluctuations in the torque $\delta\tau(f)$ at frequency f , which leads to [without losing generality, we set $a_{00}(0)$ to be real in the equations below],

$$\begin{aligned} \delta\tau(f) &\simeq \frac{w}{c} [a_{01}(f) + a_{01}^*(-f)] a_{00}(0) + \frac{w}{c} a_{01}(0) [a_{00}(f) + a_{00}^*(-f)] \\ &\quad + (\text{terms at } -f) \\ &\simeq \frac{2a_{00}^2(0)}{c} \left(w \text{Re} \left[\frac{2a_{01}(f)}{a_{00}(0)} \right] \right) \\ &\quad + \frac{2a_{00}^2(0)}{c} \left(w \text{Re} \left[\frac{a_{01}(0)}{a_{00}(0)} \right] \right) \text{Re} \left[\frac{a_{00}(f) + a_{00}^*(-f)}{a_{00}(0)} \right]. \end{aligned} \quad (7.7)$$

Or

$$\delta\tau(f) \simeq \frac{2P_{\text{DC}}}{c} \delta y(f) + \frac{2P_{\text{DC}}}{c} y(0) \left[\frac{\delta P(f)}{P_{\text{DC}}} \right], \quad (7.8)$$

where we have used

$$P_{\text{DC}} = a_{00}^2(0), \quad (7.9)$$

$$y(f) = \text{Re} \left[\frac{2a_{01}(f)}{a_{00}(0)} \right], \quad (7.10)$$

$$\frac{\delta P(f)}{P_{\text{DC}}} = \text{Re} \left[\frac{a_{00}(f) + a_{00}^*(-f)}{a_{00}(0)} \right]. \quad (7.11)$$

Note that in the above equations the fields are double-sided with frequency $f \in (-\infty, \infty)$, whereas the direct observables $\delta\tau(f)$, $y(f)$, and $\delta P(f)$ are single-sided with $f \in [0, \infty)$.

Clearly, there are two effects that may cause a radiation torque perturbation on the test mass. One is associated with the fluctuation in the spot position $\delta y(f)$ [i.e.,

⁴Instead of denoting the Fourier transform of a quantity $q(t)$ as \hat{q} , we will omit the “hat” symbol and denote it as $q(f)$.

the first term in equation (7.8)]. As we shall see soon, this term directly leads to the Sidles-Sigg effect (Sidles & Sigg, 2006) that has been a critical concern in LIGO’s commissioning (Hirose et al., 2010; Dooley et al., 2013). We will discuss this effect in detail in Section 7.2.2 and provide there a technique that can compensate for it. The second term illustrates another type of radiation pressure effect, a torque that is due to power fluctuation $\delta P(f)$. Although in the ideal case, if a cavity is perfectly aligned in DC, any small AC misalignment will not generate fluctuations in power in the linear order. Nevertheless, in reality offsets in the alignment loops exist inevitably, which creates linear coupling to power fluctuations, and instabilities due to this effect were observed during aLIGO’s second observing run.⁵ We will talk about this effect in Section 7.2.3.

7.2.2 The Sidles-Sigg effect

Interactions between the radiation torque and the suspension pendulum

In the original work by Sidles & Sigg, the authors described the radiation torque in terms of an effect potential of the optical cavity. Specifically, the authors showed that the potential energy W depends quadratically on the alignments of the two test masses $\boldsymbol{\theta}$, as $W = \boldsymbol{\theta}^T \mathbf{R} \boldsymbol{\theta} / 2$. In other words, the radiation torque couples the two test masses together to form an “optical spring”, with the two eigenvectors of the stiffness matrix⁶ \mathbf{R} corresponding to the hard and soft modes. The geometrical representation of the hard and soft modes has been shown in Panel 1 of Figure 6-1. As illustrated in the carton, if the two test masses are misaligned in the hard mode, the radiation torque will then tend to push them back to the original location. Hence the hard mode “hardens” the optical spring. In contrast, a soft mode misalignment creates an optical torque that pushes the mirrors to be even more misaligned, and consequently “softens” the optical spring.

In this Section, we present an alternative way to study the same effect. Suppose

⁵See <https://alog.ligo-wa.caltech.edu/aLOG/index.php?callRep=26367> and <https://alog.ligo-la.caltech.edu/aLOG/index.php?callRep=37576>.

⁶Note that we have changed the notation of the stiffness matrix to be \mathbf{R} instead of $\boldsymbol{\kappa}$ used in Sidles & Sigg (2006).

that some initial torque perturbation causes the test masses to be misaligned by $\delta\boldsymbol{\theta}$. The misaligned mirrors alter the cavity axis and modify the spot positions on the test masses by $\delta\mathbf{y}$. Then, as we have shown in equation 7.8, the perturbation in the spot positions in turn creates an optical torque on the test masses. The whole process can be modeled as a feedback loop as shown in Figure 7-7. In the plot, S_0 is the free pendulum transfer function, and the torsional stiffness can be further written as

$$\mathbf{R} = \frac{2P_a}{c} \frac{d\mathbf{Y}}{d\boldsymbol{\Theta}}, \quad (7.12)$$

where P_a is the power circulating in the arm cavity [cf. equation (5.17)], and the matrix $d\mathbf{Y}/d\boldsymbol{\Theta}$ connects mirrors' misalignment $\delta\boldsymbol{\theta}$ to the spot position variations on the test masses $\delta\mathbf{y}$.

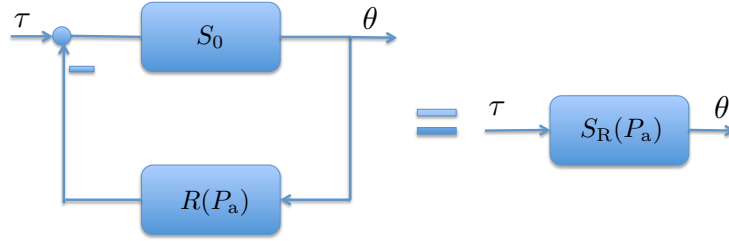


Figure 7-7: The signal flow diagram illustrating the Sidles-Sigg effect.

If we first consider the case of a single Fabry-Perot cavity. We let $\delta\boldsymbol{\theta} = [\delta\theta_e, \delta\theta_i]$ with $\delta\theta_{e(i)}$ being the misalignment of the ETM (ITM), and similarly for $\delta\mathbf{y}$. Then in terms of the cavity g-factors we can write $d\mathbf{Y}/d\boldsymbol{\Theta}$ as

$$\frac{d\mathbf{Y}}{d\boldsymbol{\Theta}} = \frac{L}{1 - g_i g_e} \begin{bmatrix} -g_i & 1 \\ 1 & -g_e \end{bmatrix}. \quad (7.13)$$

Note that it has the same set eigenvectors as \mathbf{R} . The hard and soft modes can be respectively written as

$$\delta\boldsymbol{\theta}_h = \begin{bmatrix} 1 & \bar{g} \end{bmatrix}^T, \quad (7.14a)$$

$$\delta\boldsymbol{\theta}_s = \begin{bmatrix} -\bar{g} & 1 \end{bmatrix}^T, \quad (7.14b)$$

where

$$\bar{g} = \frac{(g_e - g_i) + \sqrt{(g_e - g_i)^2 + 4}}{2} \simeq 0.87. \quad (7.15)$$

When evaluating \bar{g} , we have plugged in the g -factors for aLIGO, which are $g_e = -0.78$ and $g_i = -1.06$. The corresponding eigenvectors are

$$\left. \frac{dy}{d\theta} \right|_h = \frac{L}{2} \frac{(g_e + g_i) - \sqrt{(g_e - g_i)^2 + 4}}{(g_e g_i - 1)} \simeq 4.5 \times 10^4 \frac{\text{m}}{\text{rad}}, \quad (7.16a)$$

$$\left. \frac{dy}{d\theta} \right|_s = \frac{L}{2} \frac{(g_e + g_i) + \sqrt{(g_e - g_i)^2 + 4}}{(g_e g_i - 1)} \simeq -2.1 \times 10^3 \frac{\text{m}}{\text{rad}}. \quad (7.16b)$$

The numerical values are again evaluated with aLIGO g -factors. As pointed out in [Sidles & Sigg \(2006\)](#), for cavities with spot sizes $w_e \simeq w_i \gg \sqrt{L\lambda/\pi}$, the eigenvalues can be further simplified as

$$\left. \frac{dy}{d\theta} \right|_h \simeq \left(\frac{2\pi w_e w_i}{\lambda L} \right)^2 \frac{L}{2}, \quad (7.17a)$$

$$\left. \frac{dy}{d\theta} \right|_s \simeq -\frac{L}{2}. \quad (7.17b)$$

When we consider the full aLIGO interferometer, in addition to the hard/soft modes for each arm cavity, there are also the common/differential modes due to the Michelson nature of the interferometer. As a result, for the full interferometer there are four eigenmodes in total, corresponding respectively to the common/differential-hard/soft modes. For the common-hard mode, the eigenvalue is the same as that of the single-arm's hard mode, while the eigenvector is $\boldsymbol{\theta}_{\text{ch}}^T = [\boldsymbol{\theta}_{\text{xh}}^T, \boldsymbol{\theta}_{\text{yh}}^T]$, where $\boldsymbol{\theta}_{\text{x(y)h}}$ is the eigenvector of the X(Y)-arm's hard mode in the single-arm basis. Similarly, for differential hard the eigenvector is $\boldsymbol{\theta}_{\text{dh}}^T = [\boldsymbol{\theta}_{\text{xh}}^T, -\boldsymbol{\theta}_{\text{yh}}^T]$. The common/differential soft eigenmodes can be obtained in similar manner.

Based on the diagram shown in Figure 7-7, we can define a radiation-pressure-modified suspension transfer function as

$$S_R = \frac{S_0}{1 + RS_0}, \quad (7.18)$$

where S_0 is the free-pendulum transfer function, and R can be either $R_h = (2P_a/c)(dy/d\theta)_h > 0$ for the hard mode, or $R_s = (2P_a/c)(dy/d\theta)_s < 0$ for the soft mode. Note that for the hard mode, it is a negative feedback loop and therefore the radiation torque tends to stabilize the system. On the contrary, for the soft mode it is a positive feedback that tends to amplify the perturbations.

To proceed, we can consider a simple model of S_0 and see how it interacts with the radiation pressure effect. We can write

$$S_0(\omega) = \frac{1/(I\omega_0^2)}{1 - \omega^2/\omega_0^2}, \quad (7.19)$$

where ω_0 is the natural frequency of the pendulum, and I is the moment of inertial. For aLIGO's test mass, the pitch torque-to-angle transfer function has $I = 0.61 \text{ kg m}^2$ and $\omega_0/2\pi = 0.56 \text{ Hz}$. The radiation-pressure-modified pendulum [equation (7.18)] can thus be written as

$$\begin{aligned} S_R(\omega) &= \frac{S_0}{1 + RS_0} \\ &= \frac{1/[I(\omega_0^2 + R/I)]}{1 - \omega^2/(\omega_0^2 + R/I)} \\ &= \frac{1/(I\omega_R^2)}{1 - \omega^2/\omega_R^2}, \end{aligned} \quad (7.20)$$

where we have defined $\omega_R^2 = \omega_0^2 + R/I$ as the effective natural frequency of the pendulum. For future convenience we further define

$$\omega_h^2 = \omega_0^2 + R_h/I, \text{ and} \quad (7.21a)$$

$$\omega_s^2 = \omega_0^2 + R_s/I, \quad (7.21b)$$

for the hard and soft modes, respectively.

Thus the effect of radiation pressure is that it modifies the effective resonant frequency of the pendulum. Note that $R \propto P_a \propto P_{\text{in}}$ [cf. equation (5.17)]. We can thus plot ω_h and ω_s as a function of the input power as shown in Figure 7-8. To get the circulating power in the arms, we have assumed $P_a = 57 \times (P_{\text{in}}/10 \text{ W}) \text{ kW}$.

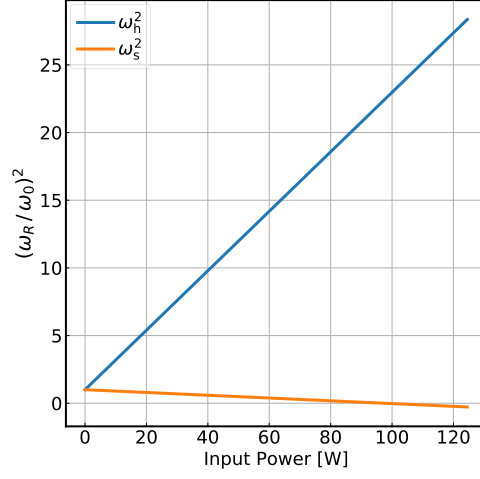


Figure 7-8: The square of the radiation-pressure-modified pendulum's resonant frequency as a function of input power.

First consider the soft mode, a significant feature is that ω_s^2 decreases as $P_a \propto P_{in}$ increases. When P_a reaches a critical value of $P_a = 0.55$ MW, the resonant frequency $\omega_s^2 < 0$, or ω_s becomes imaginary. This means in the time-domain the motion will grow exponentially as $\exp(|\omega_s|t)$. As the targeted power circulating in the arms is $\simeq 0.7$ MW, this instability will eventually happen and will have to be stabilized by external control.

The instability can also be viewed as the following. Note that the radiation pressure forms a feedback loop, and consequently it is subject to the regular loop-stability requirement $1 + RS_0 \neq 0$. However, at DC we have $S_0(0) = 1/(I\omega_0^2) > 0$ and $R_s < 0$. Consequently, for sufficiently large $|R_s|$ the instability threshold $1 + R_s S_0(0) = 0$ will eventually be satisfied at DC. The critical $R_{s,crit}$ is thus given by

$$R_{s,crit} = -I\omega_0^2, \quad (7.22)$$

which is exactly the same as the R_s we would obtain by setting $\omega_s = 0$ in equation (7.21b).

As for the hard mode, the radiation pressure shifts the pendulum resonance to a higher frequency than ω_0 . Therefore it is always stable at DC. Nonetheless, *dy-*

namically even the hard mode will become *nearly* unstable. We can see this effect again by considering the criterion $1 + RS_0 = 0$ for the feedback to become unstable. Note that at $\omega \gg \omega_0$, $S_0(\omega) \simeq -1/(I\omega^2) < 0$ while $R_h > 0$. For sufficiently high radiation torque, the open-loop gain $R_h S_0(\omega)$ will cross the unity gain with a phase of asymptotically approaching $-\pi$. The critical frequency at which $1 + RS_0(\omega) \simeq 0$ happens is given by

$$\omega_{h,\text{crit}}^2 \simeq R/I. \quad (7.23)$$

This is actually the same as the shifted resonant frequency of the hard mode in equation 7.21a (note that we have assumed $\omega_h \gg \omega_0^2$). Thus external control will also be required to damped the hard mode motion at its shifted resonance.

The real aLIGO suspension is more complicated than the simple pendulum we have considered above. Nevertheless, the radiation-pressure-modified suspension transfer function can be straightforwardly obtained from equation (7.18), and the result is shown in Figure 7-9. We can see that the dynamics of the pendulum can be significantly modified due to the radiation pressure effect. Therefore it is critical to take it into account when we design the relevant control loops. In fact, the complicated shape of the current control filters for the hard modes (cf. Figure 7-5) is partially due to that it needs to maintain the system's stability over a range of $\sim 20 - 30$ W of different input powers. The price has to be paid for such a design is that it does not roll-off fast enough to meet the aLIGO noise requirement in the 10 – 30 Hz band.

As an aside, we point out that while our discussion above focuses on the test mass (which is the bottom stage of the quadruple suspension chain [Aston et al. 2012](#)), the radiation pressure will modify the other stages in a similar manner. For example, consider the transfer function from a torque drive at the penultimate stage to an angular response at the test-mass stage. If we define the free-pendulum transfer function to be $S_0^{(\text{pum})}$, then the radiation pressure will modify it as $S_R^{(\text{pum})} = S_0^{(\text{pum})}/(1 + RS_0)$. Note that in the denominator the S_0 is still the torque-to-angle transfer function at the test-mass stage (instead of at the penultimate stage) as the radiation pressure feedback happens there. In general, the transfer function of torque drive at any point

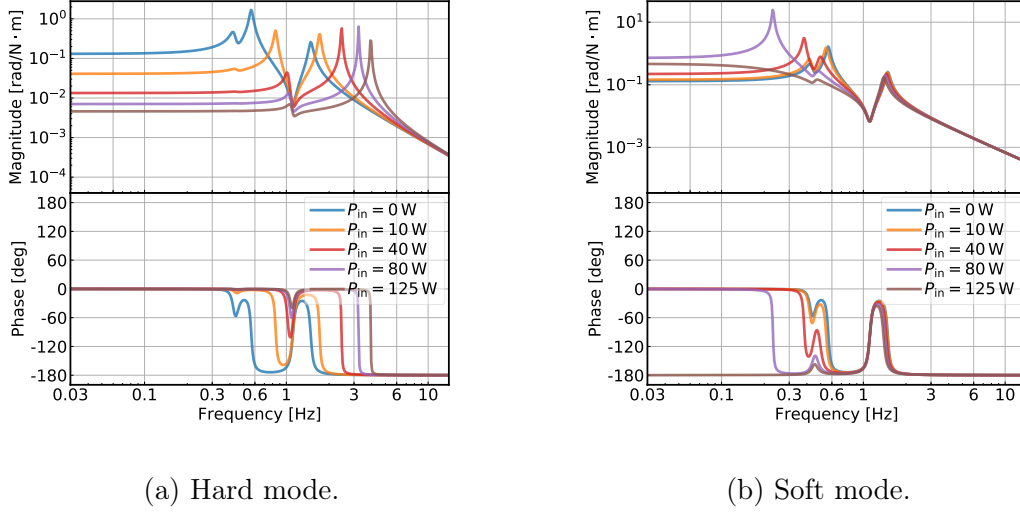


Figure 7-9: The radiation-torque-modified pendulum transfer functions for the pitch DOF at different levels of input power.

of the suspension to the angular response of the test mass will be modified by the factor of $1/(1 + RS_0)$ due to the radiation pressure effect.

Loop dynamics

In this Section, we consider how we can modify the dynamics by adding an external control K to the system⁷. Now the signal flow can be modeled as the loop diagram as shown in Figure 7-10.

First we can consider how the sensing noise $\theta_{\text{in}}^{(\text{sens})}$ propagates in the loop⁸. It is

⁷Note that the spot-position motion causing the radiation torque is measured with respect to the mirror. Therefore they should be sensed as “pointing” DOFs with, e.g., DC QPDs. Nevertheless, up to order unity corrections due to the Gouy phase propagation, the fluctuation in the arm cavity’s axis will cause a spot-position motion on the test masses $\sim 1/(1 - r_i) \simeq g_a^2/2$, or more than 100 times greater than that caused by perturbations in the recycling-cavity’s axis. Therefore in practice we can treat the recycling-cavity’s axis as being static and use a WFS signal to control the radiation-pressure effects. For example, we use a single control loop for the differential-hard mode sensed with the AS_A_RF45_Q WFS signal to simultaneously maximize the interferometric buildup and damp the radiation pressure effects.

⁸Note that the sensing noise happens at the detection PD. It thus enters after the radiation-torque feedback that is inside the cavity. There will be quantum 01/10 entering the arm cavity and create “quantum-radiation-torque noise”, similar to the QRPN. This is nonetheless a small effect because, unlike the quantum 00 mode that is resonant in the arm cavity, the quantum 01/10 modes are off resonance and do not get the amplification due to the cavity buildup. We thus ignore this effect in our discussion.

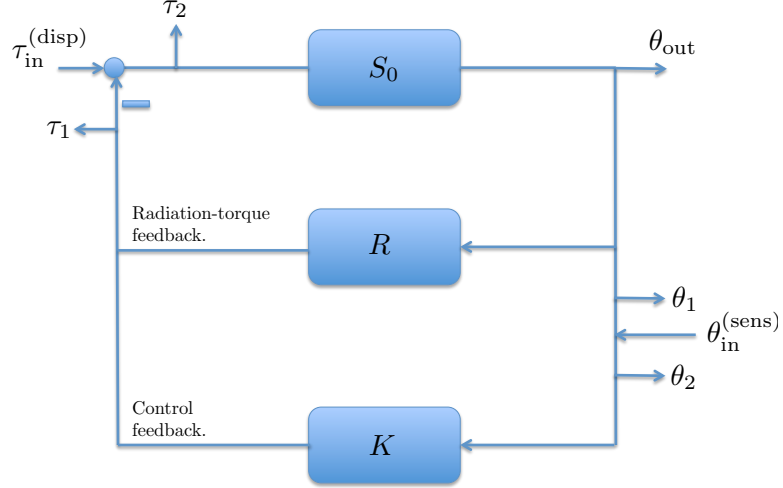


Figure 7-10: The signal flow diagram in the presence of both radiation-torque and digital control.

straightforward to show that the closed-loop output can be written as

$$\theta_{\text{out}}^{(\text{sens})} = \frac{-S_0 K}{1 + S_0 (R + K)} \theta_{\text{in}}^{(\text{sens})}, \quad (7.24)$$

which, by substituting in $S_R = S_0/(1 + S_0 K)$, can be further written as

$$\theta_{\text{out}}^{(\text{sens})} = \frac{-S_R K}{1 + K S_R} \theta_{\text{in}}^{(\text{sens})}. \quad (7.25)$$

Meanwhile, the open-loop transfer function G_{ol} is given by

$$G_{\text{ol}} \equiv \frac{-\theta_1}{\theta_2} = K S_R. \quad (7.26)$$

Note that this is same open-loop transfer function we would measure (e.g., the one shown in Figure 7-5a) by exciting the error point of the control loop and then measure the ratio between the points right before and right after the excitation.

Specifically, equations (7.25) and (7.26) suggest that for the sensing noise we can first combine the free pendulum S_0 and radiation pressure feedback R into a single system S_R , and then directly consider the interaction between the controller K and S_R .

How about the displacement noise then? Similarly, we can show that the closed loop torque-to-angle transfer function satisfies

$$\begin{aligned}\theta_{\text{out}}^{(\text{disp})} &= \frac{S_0}{1 + S_0(R + K)} \tau_{\text{in}}^{(\text{disp})} \\ &= \frac{S_R}{1 + K S_R} \tau_{\text{in}}^{(\text{disp})} = \frac{S_R}{1 + G_{\text{ol}}} \tau_{\text{in}}^{(\text{disp})}.\end{aligned}\tag{7.27}$$

Once again, we see that by using the modified suspension transfer function we obtain the correct closed-loop torque-to-angle response.

However, subtlety comes in when we consider the open-loop gain as seen by the torque disturbance,

$$G'_{\text{ol}} \equiv \frac{\tau_1}{\tau_2} = S_0(R + K) \neq S_R K.\tag{7.28}$$

Therefore, when consider the residual closed-loop displacement noise in angle (cf. Figure 7-6), we should use the input torque noise (cf. the right panel of Figure 7-2) multiplied by equation (7.25), with the free-pendulum transfer function replaced by the radiation-torque-modified one. If instead we want to treat the input displacement noise in angle as a constant as $S_0 \tau_{\text{in}}^{(\text{disp})}$, we have implicitly treated the pendulum as unchanged. As a result we need to separately consider the radiation pressure feedback, and in this picture the proper closed-loop noise is given by $S_0 \tau_{\text{in}}^{(\text{disp})} / [1 + S_0(R + K)] = S_0 \tau_{\text{in}}^{(\text{disp})} / (1 + G'_{\text{ol}})$.

Compensating for the Sidges-Sigg effect

From the discussion above we see that to stabilize the system in the presence of the Sidges-Sigg radiation torque, one can design different control filters such that at each input power level, the transfer function $S_R / (1 + K S_R)$ is stable. This, however, can be both challenging and time-consuming, as S_R depends sensitively on power (Figure 7-9) and will thus require many different filters to be tuned individually. If one instead make a filter that is stable over a relatively large span of input power, then it is hard to keep to filter to be optimal at the same time. For example, the current control filter used at the LIGO Hanford site (cf. Figure 7-5) is stable for

an input power ranging from 0 to ~ 20 W. However, this controller is not optimal as it suppresses the input displacement more than required yet does not have a fast enough high-frequency cutoff.

Nevertheless, a simple solution to tackle the Sidles-Sigg effect exists. Note that $R = (2P_a/c)(dy/d\theta)$ is a frequency-independent quantity that relies only on the cavity geometry (i.e., the g-factors) and the power circulating in the arms. The former was carefully measured with high accuracy prior the installation of aLIGO, and the latter can be measured in real time via, e.g., the PDs on the transmission of the ETMs. Moreover, we also know the suspension transfer function S_0 and can infer the angular motion θ_{out} from the alignment sensing systems. In other words, we know every single component of the radiation pressure torque. Consequently, we can create a new path in the digital control system with a loop gain of $-RS_0$ that exactly cancels out the Sidles-Sigg torque RS_0 . With this scheme, when changing the power circulating in the arms, we only need to change the DC gain of this radiation compensation path accordingly, and the suspension will stay as a power-independent (i.e., a “free”) pendulum. As a result, we only need to design a single controller K that optimally stabilizes the system, and this filter will stay valid over at least a large range of, if not any, input power levels.

The scheme is illustrated in the diagram shown in Figure 7-11. While ideally we would just put a $-R$ in the compensation path, in reality we want to add some gain-adjustment factor F in the path. This is because when we compensate for the hard mode, we need to send to the suspension a digital torque corresponding to the soft mode. If over-compensation accidentally happens, we will destabilize the system with the digital soft mode we create. To avoid such a situation, we deliberately under-compensate for the hard mode by making $F < 1$. Specifically, we can define

$$S'_R = \frac{S_0}{1 + (1 - F)RS_0}. \quad (7.29)$$

When $F = 1$, we have $S'_R = S_0$ the free-pendulum transfer function. This is what we do for the soft modes. On the other hand, we set $F = (P_{\text{in}} - 10 \text{ W})/P_{\text{in}}$, which

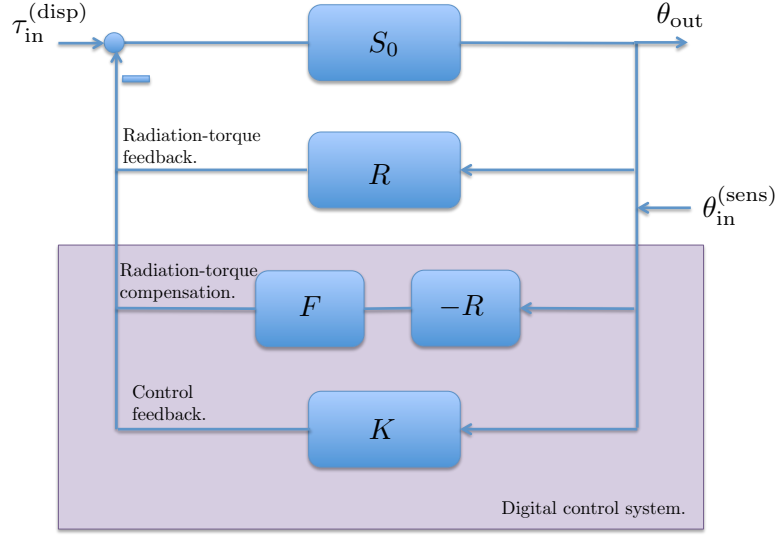


Figure 7-11: The diagram illustrating the compensation scheme for the Sidles-Sigg radiation torque.

makes $S'_h = S_h(10\text{ W})$. In other words, the suspension transfer function will always look like a hard-mode pendulum at an input power of 10 W, and small errors in the compensation path will not turn it into a destabilizing soft mode. Another usage of F is to provide extra cut-off at high frequencies. Since we feedforward the same error signal used in the regular control path to the compensation path, we will inject the same sensing noise as well. Therefore, when $|RS_0| \ll 1$, we will low-pass the digital torque signal to reduce the excess sensing noise.

The conceptual design in Figure 7-11 can be implemented in the diagram shown in Figure 7-12. For aLIGO, the angular control is actuated with the penultimate stage (PUM) instead of the test-mass stage (TST), as it has a larger actuation range. Therefore we need to digitally invert the suspension transfer function to make it looks like the test-mass stage. This is accomplished by the filter $S_0^{(tst)}/S_0^{(pum)}$. Note that this is the only frequency-dependent part in the compensation scheme (except for the high-frequency cut-off filter), and it requires only the free-pendulum transfer functions that can be measured accurately at the observatories.⁹ The other quantities are all DC calibration factors. The mirror's angular motion in radians is converted to the

⁹<https://alog.ligo-la.caltech.edu/aLOG/index.php?callRep=41815>

digital counts by G_{opt} , and the digital counts are further converted into actuation torque by G_{act} . As a result, once $S_0^{(\text{tst})}/S_0^{(\text{pum})}$ is measured, we only need to adjust the DC gain of the compensation path which is $\propto P_a$. This is a much easier way of tackling the Sidges-Sigg effect than designing different frequency-dependent control filters at different power levels.

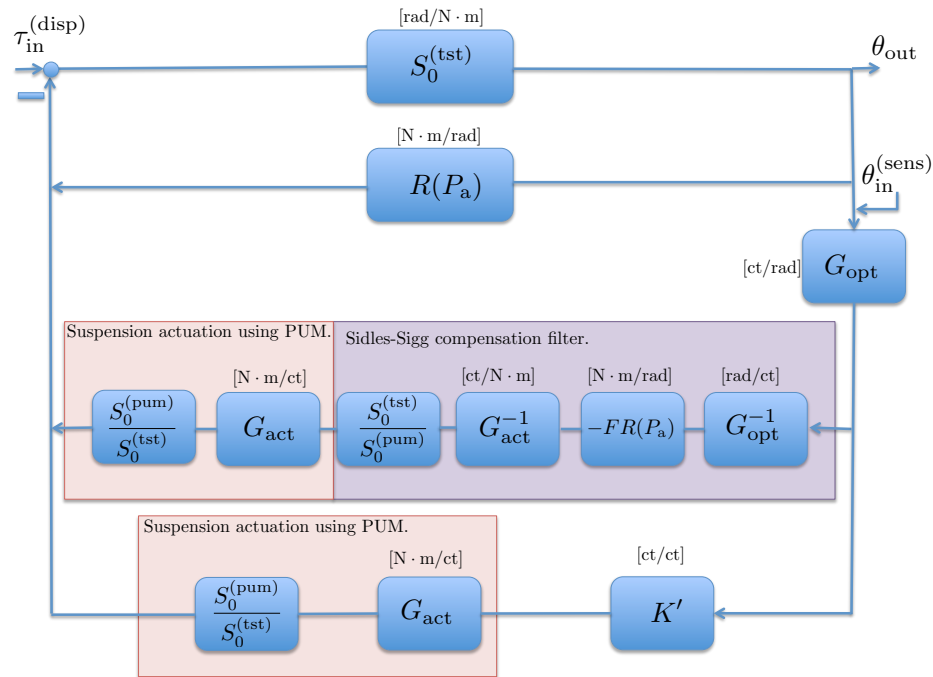


Figure 7-12: The implementation of the compensation scheme for the Sidles-Sigg effect in aLIGO.

This compensation scheme has been tested out at both the Hanford the Livingston observatories,¹⁰ and we summarize the results in Figure 7-13. In the plot we show with red pluses the measured open-loop transfer functions KS'_R at an input power of 10 W, and with brown crosses the transfer functions measured at 20 W and with the radiation-pressure compensation on to keep the suspension plant the same as the 10 W one. We can see that the two measurements match well to each other, and they both show good agreement with the modeled open-loop transfer function at 10 W shown in the blue traces (for the pitch DOF there exists a phase mismatch between

¹⁰See <https://alog.ligo-wa.caltech.edu/aLOG/index.php?callRep=45750> and <https://alog.ligo-la.caltech.edu/aLOG/index.php?callRep=41855>.

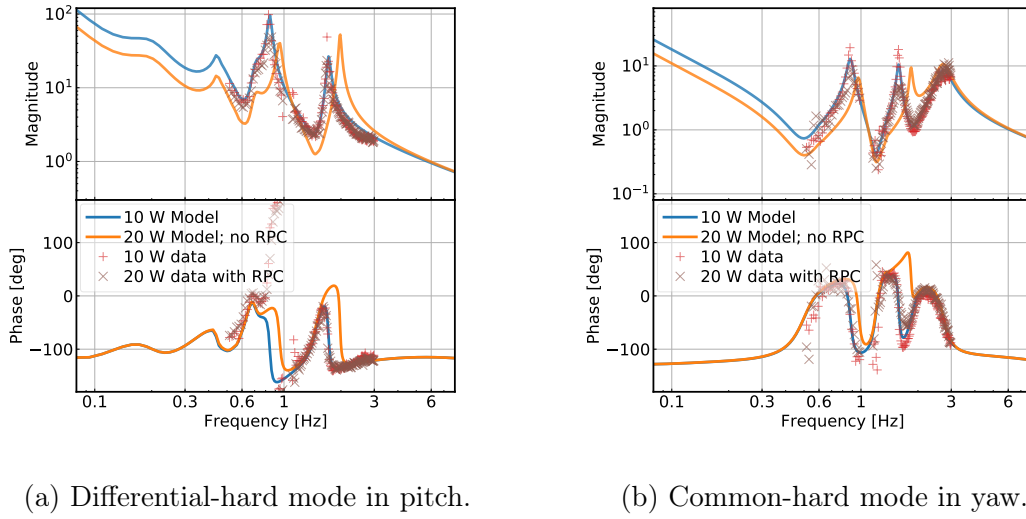


Figure 7-13: The modeled and measured open-loop transfer functions of the hard loops. Using the radiation pressure compensation (RPC) technique, the transfer functions measured at an input power of 20 W (brown-crosses) are essentially identical to the ones measured at 10 W (red-pluses), and match well to the model (blue trace). As a comparison, we also show in the orange trace how the transfer function would look like if we do not compensate for the radiation pressure torque.

the measurement and the model which is likely due to loop cross couplings.¹¹¹² As a comparison, in the orange traces we also present the open-loop transfer function at 20 W without radiation-pressure compensation. As indicated by the plots, our technique works well and it successfully removes the radiation-induced power dependence in the suspension transfer functions. This further implies that in the future we only need to optimize for a single controller K . The variations in the arm power P_a will be taken care of by the compensation path $-FR$ that requires only DC gain adjustments. This will greatly simplify the commissioning of the alignment system at high-power operations.

¹¹<https://alog.ligo-wa.caltech.edu/aLOG/index.php?callRep=46469>

¹²The open-loop transfer functions shown in Figure 7-13 are measured in the “high-bandwidth” configuration, which has about factor of 2 higher DC gain than the one shown Figure 7-5. The high-bandwidth filters also has less aggressive high-frequency cutoffs.

Sensing noise from the compensation path.

As mentioned above, the compensation path will be subject to the same sensing noise as the regular control loop. The total closed-loop sensing noise is

$$\theta_{\text{out}}^{(\text{sens})} = \frac{-KS'_R + FRS'_R}{1 + KS'_R} \theta_{\text{in}}^{(\text{sens})}. \quad (7.30)$$

In the numerator, the KS'_R term is the coupling due to the conventional feedback control, and the FRS'_R term is the contribution from the radiation-compensation path. To avoid this noise contaminating the GW readout, we introduce extra high-frequency cut-off filters in F . We choose the filter to maximize the roll-off above 10 Hz while keeping its phase delay at 3 Hz less than 10° . In Figure 7-14 we show the quantity FRS'_R at different input power levels (the different dotted lines) and compare it with KS'_R (the black trace). We can see that the sensing noise contribution from the radiation-pressure compensation path is always much less than that from the regular control feedback in the 10 – 20 Hz band. Moreover, with the current low-path filters, the compensation path also meets aLIGO's requirement on the noise roll-off (assuming $\theta_{\text{in}}^{(\text{sens})} = 10^{-14} \text{ rad}/\sqrt{\text{Hz}}$ and 1 mm/rad of angular-noise coupling) up to $\simeq 70 \text{ W}$ of input power.

Error tolerance

While we have demonstrated that the radiation-torque compensation technique works in aLIGO with real data in Section 7.2.2, it is also critical to know how much error can be tolerate in this scheme. Thus we investigate its robustness in this Section using the small-gain theorem (See, e.g., [Bosgra et al. 2001](#) and references therein).

Consider a simple model shown in the left panel of Figure 7-15. Here H is the system whose stability robustness is under investigation and Δ_H represents an uncertainty of the dynamics of the system. Such a system is also known as the basic perturbation model. The small-gain theorem states that if both H and Δ_H are stable, then a *sufficient* condition for internal stability of the basic perturbation model

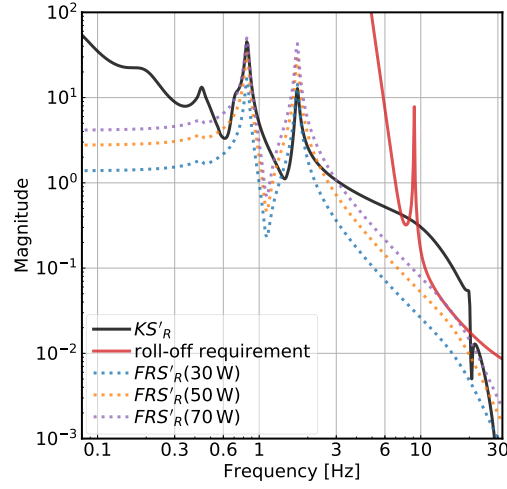


Figure 7-14: Comparison between FRS'_R (the dotted lines) and KS'_R (the black-solid line). At above 3 Hz, these curves represents the rolloff of the sensing noise. The sensing noise contribution from the radiation-pressure-compensation path ($\propto FRS'_R$) is always much less than that from the regular control feedback ($\propto KS'_R$), and it meets aLIGO's requirement on the cut-off of the sensing noise up to an input power of 70 W.

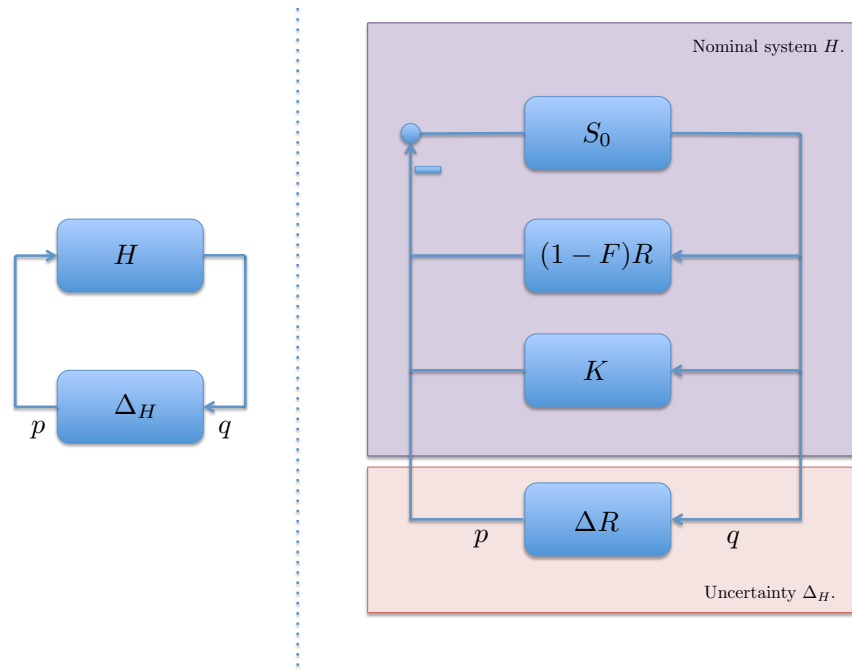


Figure 7-15: Left: the basic perturbation model. Right: Applying the basic perturbation model to the radiation-pressure-compensation system.

is (Bosgra et al., 2001):

$$\|H\Delta_H\|_\infty < 1, \quad (7.31)$$

where the ∞ -norm of a proper and stable system H is given by

$$\|H\|_\infty = \sup_{\omega \in \mathbb{R}} \bar{\sigma}[H(i\omega)]. \quad (7.32)$$

Here $\bar{\sigma}$ denotes the largest singular value. For a single-input-single-output system, the infinity norm is simply the largest value of the frequency response magnitude. More conveniently, equation (7.31) can be reformulated as

$$\bar{\sigma}[\Delta_H(i\omega)] < \frac{1}{\bar{\sigma}[H(i\omega)]}, \quad \forall \omega \in \mathbb{R}. \quad (7.33)$$

The small-gain theorem can be applied to our case as illustrated in the right panel of Figure 7-15. We can combine our nominal system as the function H , leading to

$$H \equiv \frac{q}{p} = -\frac{S'_R}{1 + KS'_R}. \quad (7.34)$$

The sufficient condition for the loop to be stable in the presence of perturbation ΔR can now be written as

$$\left| \frac{\Delta R}{R} \right| < \left| \frac{1 + KS'_R}{RS'_R} \right| \propto \frac{1}{P_a}. \quad (7.35)$$

The bound in equation (7.35) is valid for any perturbation ΔR as long as ΔR is stable by itself. Here we consider two types that are most likely to occur in the system¹³. To proceed, we first write $F = F_0 F_{lp}$, where $F_0 \lesssim 1$ is the overall DC gain and F_{lp} carries the low-pass filter whose DC gain is set to unity. For simplicity we can set our nominal compensation gain such that $F = F_0 = (P_{in} - 10 \text{ W})/P_{in}$. The first type is then the error in the DC gain of the compensation path, which may be caused by fluctuations in the arm power. We can model it as $\Delta R/R = \Delta F$, where

¹³The small-gain theorem is actually more suited to study *unstructured* uncertainties than the structured ones we will consider here, as for a structured uncertainty it provides only the *sufficient* stability condition, which is in general more contingent than the real stability requirement. Nonetheless, as we will see, even such strict conditions can be satisfied with the uncertainty levels typical for aLIGO.

ΔF is a DC constant accounting for the gain mismatch. The second type is due to that we have ignored the extra low-pass F_{lp} in the “nominal” compensation path (this is actually an error that will always happen by our construction and should thus be added with other perturbations). Due to causality constraints the cut-off filter will introduce phase delays in the subtraction band which makes our compensation imperfect. This effect can be modeled by noting $FR = F_0R - (1 - F_{lp})F_0R$, which leads to $\Delta R/R = (1 - F_{lp})F_0 \lesssim (1 - F_{lp})$.

The tolerance to each type of uncertainties is shown in Figure 7-16. Here we evaluate it at an input power of 40 W, or about 0.23 MW of power circulating in each arm. This is the typical power level aLIGO will operate at for the third observing run. Note that while our compensation scheme keeps the suspension independent of power, the error tolerance decreases linearly with power [cf. equation (7.35)]. Nevertheless, the stability margin is sufficiently large. At 40 W of input power, the tolerance on the DC-gain mismatch can be as large as 40%. Even if the power increased by a factor of 3 to reach aLIGO’s designed operation level, the tolerance is still more than 10%. This is still much greater than the typical power fluctuations in the arm cavity due to alignment fluctuations (cf. Figure 7-3). Moreover, the long-term (on timescale of a few hours) drift in power and optical sensing gain can be easily measured in real time and feedback to the DC gain of the compensation path, making it even more robust to this type of perturbations. Meanwhile, the error due to the low-pass filter’s phase delay is also more than a factor of 3 below the error tolerance, and will thus not cause instabilities in the loop.

7.2.3 The $dP/d\theta$ effect

So far we have been focused on the Sidles-Sigg effect: a mirror’s angular motion perturbs the spot position on the mirror, which in turn creates a torque that may lead to either more or less angular motion depending on the phase of the feedback. This process corresponds to the first term in equation (7.8). Meanwhile, the second term in equation (7.8) indicates another potential feedback channel. If a mirror’s angular motion perturbs the circulating power, then the radiation force may couple

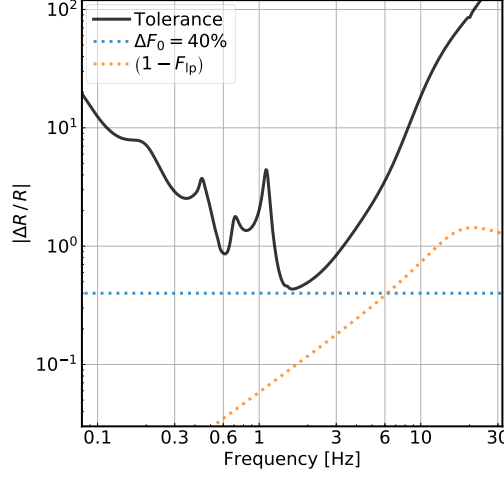


Figure 7-16: The error tolerance on $|\Delta R/R|$ in the radiation-compensation path. If a perturbation is below the black trace (evaluated at $P_{\text{in}} = 40 \text{ W}$), it satisfies the *sufficient* condition for stability. The controller we use currently can tolerate at least 40% error in the DC gain in the compensation path (shown in the blue trace). The phase delay due to the high-frequency cut-off filter is also well-below the error tolerance and thus affect the stability of the loop.

with the DC spot miscentering on the mirror to create a torque feedback as well. Moreover, in addition to the coupling via DC spot miscentering, the radiation force can also push the mirror in length, which may also close the feedback loop via the length-to-pitch cross-coupling in the suspension. In fact, the suspension length-to-pitch coupling is much greater than that due to the spot mis-centering in aLIGO and we will consider only this path. It also means that effect is most relevant for the pitch DOF as there exists no direct length-to-yaw coupling in the suspension. In this Section, we will refer to this feedback channel due to power fluctuations as the $dP/d\theta$ channel whose diagram is shown in Figure 7-17, and discuss its significance. As we will see, this is the main factor determines the design of the soft loops.

In principle, the feedback gain due to the $dP/d\theta$ is much smaller compared to that from the Sidles-Sigg effect. This is because in an ideal cavity small misalignment will only create power fluctuations in the quadratic order. However, during aLIGO's second observing run, both observatories saw growing oscillations at $0.4 - 0.6 \text{ Hz}$ exclusively in pitch in the common-soft mode when the circulating power in the arms

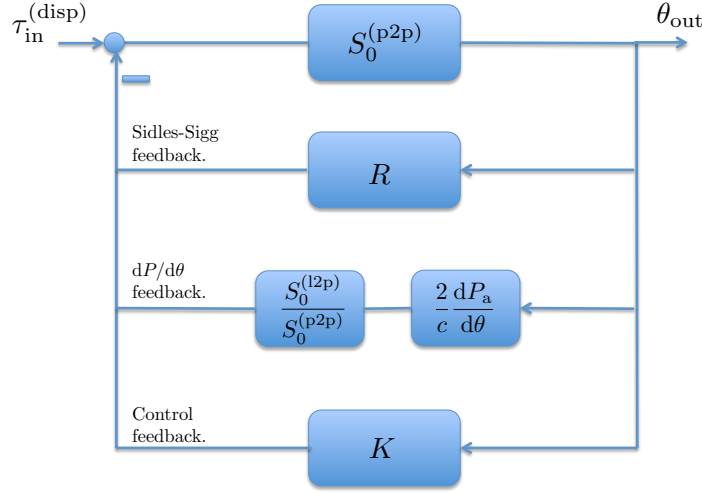


Figure 7-17: The diagram illustrating the $dP/d\theta$ radiation pressure feedback.

reaches $P_a \simeq 160 \text{ kW}$. Here we present a model that may explain this oscillation. We can define

$$G_{\text{spot}}(f) = R_s S_0^{(\text{p2p})}(f) = \frac{2P_a}{c} \frac{dy}{d\theta} \Big|_s S_0^{(\text{p2p})}(f), \quad (7.36)$$

as the feedback gain due to the Sidles-Sigg effect for the soft mode. To distinguish the angular torque-to-angle transfer function from the longitudinal force-to-pitch one, we label the former explicitly with a superscript “p2p” as $S_0 = S_0^{(\text{p2p})}$, while for the latter we define it as $S_0^{(\text{l2p})}$. At the same time, the $dP/d\theta$ effect creates a feedback gain in the soft loop as¹⁴

$$G_{\text{power}}(f) = \frac{2P_a(0)}{c} \frac{d[P_a(f)/P_a(0)]}{d\theta} S_0^{(\text{l2p})}(f). \quad (7.37)$$

To have a non-vanishing $dP/d\theta$ term, we introduce small alignment offset at DC of

¹⁴Strictly speaking, the radiation force will create an angle $\propto [-1, 1]$ in the $[\delta\theta_e, \delta\theta_i]$ basis, which does not correspond exactly to the soft mode $[-\bar{g}, 1]$. Nevertheless, since $\bar{g} \simeq 0.87 \sim 1$, and other uncertainties of similar or greater level exist in the model, we will ignore this effect for simplicity.

$\mathcal{O}(1)$ nrad in the common-soft loop.¹⁵ This leads to

$$\frac{d[P_a/P_a(0)]}{d\theta}(f) \simeq \frac{6 \times 10^3}{1 + if/f_c} \times \left(\frac{\Delta\theta_{cs}}{1 \text{ nrad}} \right), \quad (7.38)$$

for aLIGO in the second observing run with a power-recycling gain of $r_p^2 = 32$ and a CARM-cavity pole of $f_c = 0.7$ Hz. Here $\Delta\theta_{cs}$ is the DC offset in the common-soft loop and it can be either positive or negative. When this effect was first observed, both sites had only low-bandwidth (~ 10 mHz) control on the soft modes to control the DC spot position on the test masses, and therefore we ignore the control filters when considering the loop stability. Consequently, the total open-loop gain can be written as $(G_{\text{spot}} + G_{\text{power}})$, and the system becomes unstable if $(G_{\text{spot}} + G_{\text{power}}) = 1$.

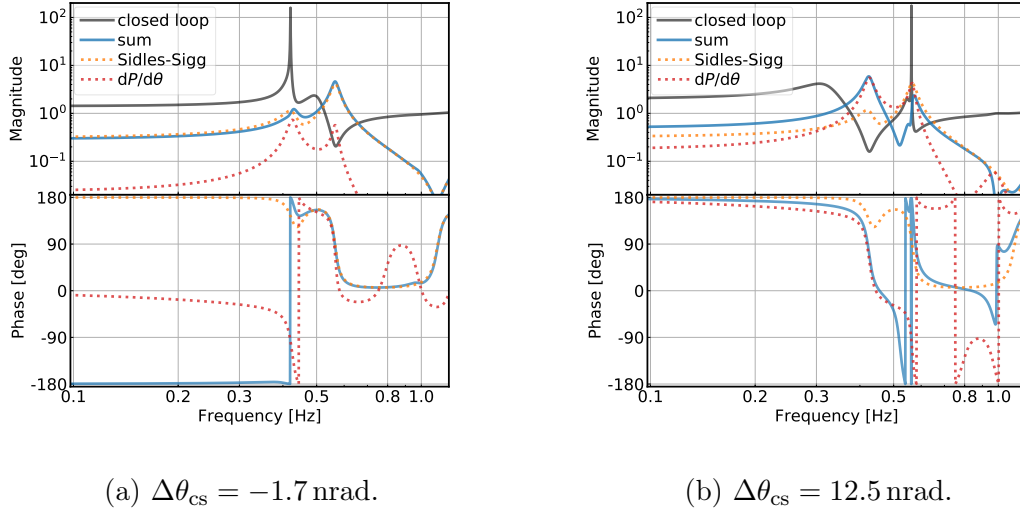


Figure 7-18: Two scenarios that the $dP/d\theta$ effect may lead to the observed instabilities in the $0.4 - 0.6$ Hz band. In each plot we use the blue trace to indicate the open-loop gain and the black trace the closed-loop response. The contributions from the Sidles-Sigg effect and the $dP/d\theta$ effect are represented respectively with the orange- and the red-dotted lines.

In Figure 7-18 we present two possibilities that the $dP/d\theta$ channel could produce the observed instabilities at $0.4 - 0.6$ Hz with a circulating power of $P_a \simeq 160$ kW. In the left panel we let the DC offset in the common-soft loop to be -1.7 nrad. Without

¹⁵This is not the unique mechanism to have linear angle-to-power coupling. For example, if the scattering loss at the test masses varies with spot location, it could also lead to linear coupling.

the $dP/d\theta$ effect, the Sidles-Sigg feedback cross the unity gain at around 0.4 Hz with a small phase margin. This corresponds to the shift in the resonant frequency of the radiation-torque modified plant as shown in the right panel of Figure 7-9, and the resultant gain peaking is $\lesssim 10$, comparable to the quality factor of the original suspension resonance. The $dP/d\theta$ effect, while much smaller effect elsewhere, is comparable to the Sidles-Sigg effect at the suspension resonance ~ 0.5 Hz. This decreases the phase margin and eventually leads to an instability in the loop at 0.4 Hz. Another possibility is illustrated in the right panel of Figure 7-18. In this case we introduce a DC offset of $\Delta\theta_{cs} = 12.5$ nrad. This makes the $dP/d\theta$ effect roughly equals to the Sidles-Sigg effect in amplitude around the suspension resonances. However, the two effects can be out of phase and thus lead to extra unity-gain crossings with fast-evolving phase. As a result, we once again see an instability develops in the system at 0.6 Hz.

Note that the instabilities in the above examples happen at a circulating power of $\simeq 160$ kW, much smaller than the critical power $\simeq 550$ kW for the soft mode to become unstable due to the Sidles-Sigg effect alone (cf. Section 7.2.2). This indicates the necessity of having a relatively high-bandwidth [$\mathcal{O}(1)$ Hz] external control on the soft loop even at an input power of ~ 30 W. However, before realizing this $dP/d\theta$ effect, the soft mode was controlled with the dithering loop that could support only ~ 10 mHz bandwidth because of limited sensitivity (cf. Sections 6.3.2 and 6.4). To circumvent this, we utilize a signal-blending technique. At AC ($\gtrsim 0.01$ Hz) frequencies, we use a combination of DC QPDs on the transmission of ETMs to sense the soft mode motion¹⁶. This error signal is used for both compensating for the Sidles-Sigg effect (Section 7.2.2) and damping of the residual $dP/d\theta$ radiation torque and/or other unmodeled perturbations. To avoid the long-term drift of the QPDs with respect to the arm cavity at timescales of $\gtrsim 1$ hr, the damping loop is flat below 0.1 Hz. On the other hand, the dithering loop that is a simple integrator with $1/f$ slope and it takes

¹⁶Note that the “soft mode” here measures the test masses with respect to the ground and it needs to be sensed as a pointing DOF. There is also an “interferometric soft mode”, which measures the translational shift of the arm cavity’s axis with respect to the power-recycling-cavity’s axis. This is the $\Delta\theta_{cs}$ we need in order to have linear angle-to-power coupling. As discussed in Section 6.4, this interferometric DOF is controlled with PR2 and thus cannot damp the radiation torques.

over the control below about 10 mHz to fix the spot position on the ETM at DC. The control loop is presented in the left panel of Figure 7-19.

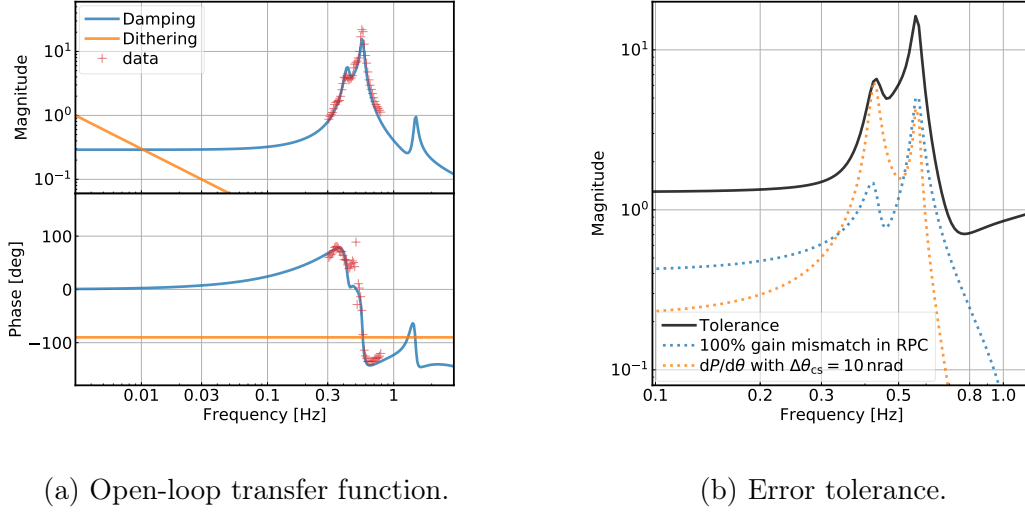


Figure 7-19: Left: the open-loop transfer function for controlling the soft-mode in pitch. The blue trace uses error signal from DC QPDs to damp the $dP/d\theta$ radiation torque. The same error signal is also used to compensate for the Sidles-Sigg effect, which removes the power dependence of the suspension pendulum. The orange trace indicates the dithering control that locks the DC spot position on the ETM to a fixed location. Right: error-tolerance of the soft-mode controller. If a perturbation creates feedback gain whose peak magnitude is below the black trace, it satisfies the *sufficient* condition for the system to maintain internal stability.

Once we specify the controller, we can derive its error tolerance again using the small-gain theorem. This result is shown in the right panel of Figure 7-19. Note that this time we show the tolerance on the total feedback gain instead of that on a certain parameter as we have done in Figure 7-16. For example, we show the feedback gain due to 100% gain mismatch in the radiation pressure compensation path for the soft mode in the blue-dotted line, and the feedback gain due to the $dP/d\theta$ effect with 10 nrad offset in the (“interferometric”) soft loops at DC. All the values are evaluated at an input power of 40 W, or $P_a \simeq 0.23$ MW. With the damping loop engaged, neither of them will cause instabilities any more. The high-bandwidth soft-mode control is thus a crucial step towards aLIGO’s high-power operation.

7.3 NOISE REDUCTION TECHNIQUES

Having discussed the effects of radiation pressure torques extensively in the previous Section, we now return to the noise considerations mentioned at the beginning of this Chapter, and discuss in this Section techniques to further reduce the noise in the alignment systems.

7.3.1 Length-to-pitch feedforward

As shown in Figure 7-2 the displacement noise is dominated by the seismic motion (the blue trace). As the ground move longitudinally, it will also cause the mirror to move in the pitch direction. For a simple pendulum, this transfer function can be written as (we will ignore the damping terms for simplicity; see [Rakhmanov 2000](#))

$$\frac{\theta}{x} \equiv H_\theta(\omega) \simeq \frac{\omega_\theta^2}{l+b} \frac{\omega^2}{(-\omega^2 + \omega_1^2)(-\omega^2 + \omega_2^2)}, \quad (7.39)$$

where x is the longitudinal motion of the ground and θ the mirror's motion in pitch. We use l and b to represent respectively the length of the pendulum suspension, and the distance between the binding point and the mirror's center of mass. We will further write the mirror's mass and moment of inertia as m and I . The frequencies of the resonances $\omega_{1,2}$ are thus given by

$$\omega_{1,2}^2 = \frac{g}{2lI} \left[I_\theta + mb(l+b) \mp \sqrt{[I - mb(l+b)]^2 + 4mb^2I} \right], \quad (7.40a)$$

$$\omega_1 \simeq \omega_\theta \simeq \frac{mgb}{I}, \quad \omega_2 \simeq \omega_x = \frac{g}{l}, \quad (7.40b)$$

where in the second line we have assumed $b \ll l$ and expanded the quantities to first order in b/l . Since the ground's motion x can be readout from seismometers ([Matichard et al., 2015a](#)) and its coupling to pitch is known both theoretically and can be measured in situ. at the observatories, it means that we can *predict* the angular motion of the mirrors and thus feedforward the signal to cancel the mirror's displacement ([Bonila, 2012](#)).

While we can also stabilize the motion using feedback controls, the feedforward subtraction has its unique advantages. This is because the feedback control is subject to loop stability requirements, which limits the high-frequency sensing noise rolloff to be at most $1/f^2$ around the unity-gain frequency. On the other hand, the feedforward subtraction is always stable (as long as the filter itself is stable) and can be cut off much faster. Such a property is especially valuable for the alignment system because currently the sub-30 Hz sensitivity of aLIGO is limited by the residual angular sensing noise from these 3-Hz-bandwidth feedback loops (Martynov et al., 2016). If we instead stabilize the mirror’s motion with feedforward subtraction, the required bandwidth of the feedback loops can thus be reduced,¹⁷ thereby improving the low-frequency sensitivity of ground-based GW detectors.

This effort has been carried out at both observatories.¹⁸ We first excite the suspension point of each test mass in length and measure its angular response with optical levers (Mageswaran & Black, 2010), which allows us to estimate the length-to-angle transfer function $H_\theta(\omega)$.¹⁹ We then send the signal $-H_\theta(\omega)x$ to cancel the seismically induced motion $H_\theta(\omega)x$.

The performance of the feedforward subtraction is shown in Figure 7-20. Here we actively excite the longitudinal motion of suspension point. The blue-solid trace is the pitch motion of the test mass measured locally with optical levers, and the blue-dashed line is its cumulative rms value. As we enable the feedforward cancellation, the displacement is dramatically reduced to the orange trace. In terms of power, we reduced the motion by about 80% with the feedforward cancellation.

More importantly, we can examine the benefits of feedforward with global align-

¹⁷Actually, currently the bandwidth of angular feedback control is limited by the requirement of stabilizing radiation pressure effects instead of suppressing the residual seismic motion. Nonetheless, with the compensation of the Sidles-Sigg effect we have shown that we can remove the variation in the suspension transfer functions. This would make the suppression of seismic motion again the main factor determining the control bandwidth. This will also be the case for future GW detectors with more massive test masses than aLIGO as the significance of radiation torque is naturally mitigated by the increased moment of inertia.

¹⁸See, e.g., <https://alog.ligo-wa.caltech.edu/aLOG/index.php?callRep=42851>, <https://alog.ligo-wa.caltech.edu/aLOG/index.php?callRep=44599>, and <https://alog.ligo-la.caltech.edu/aLOG/index.php?callRep=41810>.

¹⁹The transfer functions are fitted using <https://iirrational.readthedocs.io/en/latest/>.

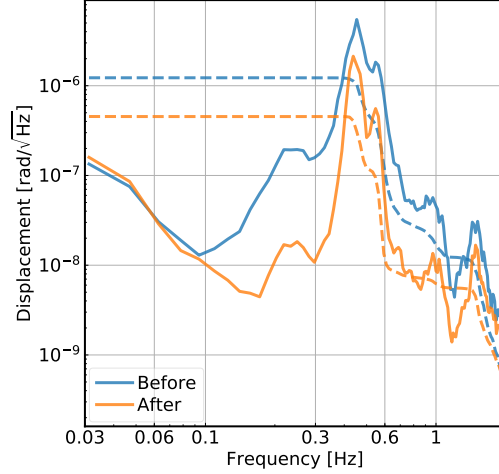


Figure 7-20: The performance of the length-to-angle feedforward subtraction measured locally with the optical levers.

ment signals. This is illustrated in Figure 7-21. In the plots the blue traces are the input displacement noises measured in the differential- and common-hard modes in pitch (corresponding to the left and right panels, respectively) without the feedforward. As a comparison, the input displacement noises when the feedforward cancellation is turned on are represented by the orange traces. We can see that for the differential-hard mode (measured with AS_A_RF45_Q), we achieve a robust subtraction of input motion in the 0.1-0.3 Hz microseismic band with approximately 60% reduction in power. This significantly reduces the rms of the input motion and opens up the possibility of reducing the feedback control's bandwidth in the future. The performance in the common-hard mode, however, is limited. In part, this is due to a non-ideal inversion of the input matrix at the REFL port. At the same time, people have noticed that the common-hard mode signal exhibits large coherence with the motion of the chamber hosting the REFL port sensors. This might be further caused by thermally induced offsets creating a non-vanishing RF spot on the WFS, which cross-couples the local centering loops (which sees the chamber motion) and the interferometric WFS signals. To solve this issue in the future, a better seismic isolation system is planned for the chamber hosting the REFL sensors ([Fritschel](#),

2018). Meanwhile, people are actively researching the possibility of feeding forward the global longitudinal signals (i.e., measured with the interferometric sensors instead of local seismometers) to mirrors' alignment (Adhikari et al., 2018), which, based on the coherence between signals, might remove up to 90% of input motion to the common-hard mode.

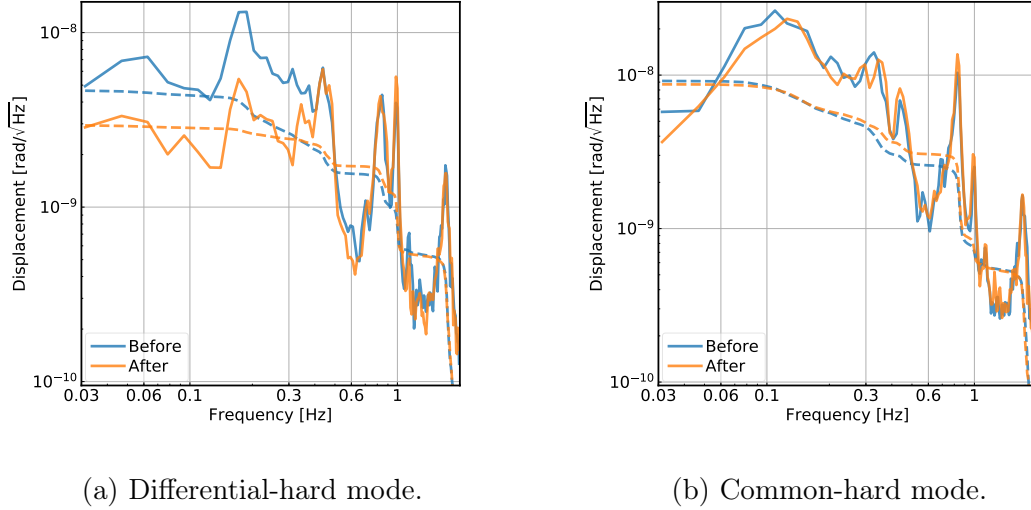


Figure 7-21: The performance of the length-to-angle feedforward subtraction measured with global alignment signals.

7.3.2 Signal blending

At the beginning of this Chapter we said that the typical sensing noise for the alignment control loops is about 10^{-14} rad/ $\sqrt{\text{Hz}}$. This is the case for the differential-hard modes measured with AS_A_RF45_Q as illustrated in Figure 7-22a. For the common-mode signals sensed with a combination of REFL WFSs (the red-dotted curve in Figure 7-22b), however, the sensing noise is significantly worse, at a level of as high as a few $\times 10^{-13}$ rad/ $\sqrt{\text{Hz}}$. This is partially due to an intrinsically higher shot noise level at the REFL port than at the AS port (Barsotti et al., 2010). Moreover, the REFL sensors are subject to the cross-couplings from chamber motions we have just discussed above. This is further suggested by the fact that in the 10-30 Hz band the spectrum of the REFL WFS error signal is not flat (which is characteristic for

shot noise and dark noise). As we have discussed in Section 7.1, with a sensitivity of $10^{-14} \text{ rad}/\sqrt{\text{Hz}}$ the alignment control loop will already inject so much sensing noise that limits aLIGO's sub-30 Hz sensitivity. A higher level of sensing noise will lead to an even worse contamination to the main GW readout.

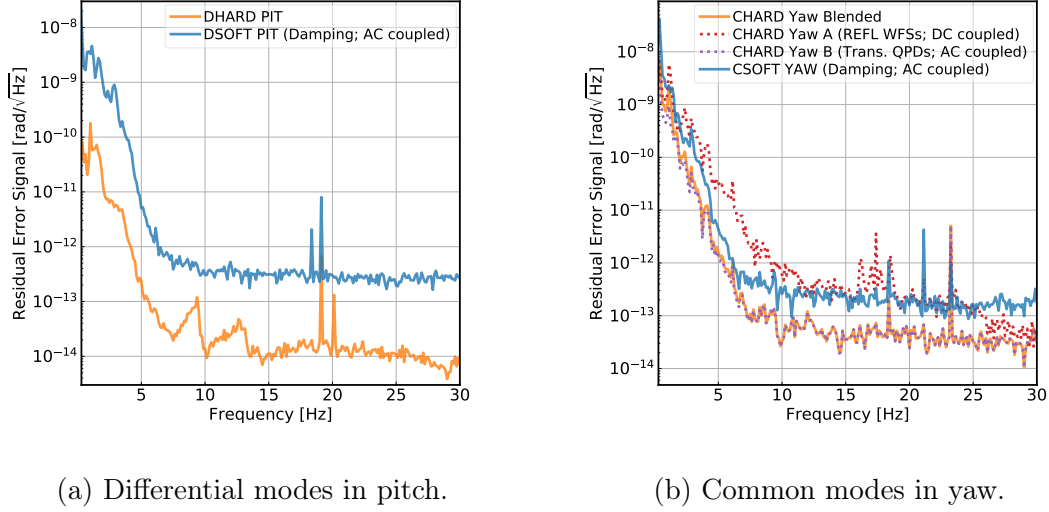


Figure 7-22: Sensing noise level of alignment loops.

To circumvent this, note that we only need an interferometric error signal (cf. Section 6.2) of the common-hard modes at DC. At AC frequencies, the motion of the recycling cavity's axis is much smaller than the motion of the arm cavity's axis [by a factor of $\sim 1/(1 - r_i) \simeq g_a^2/2$] and thus we can treat the recycling cavity's axis as being essentially static at AC. Consequently, we can use non-interferometric sensors such as the QPDs on the transmissions of the ETMs to control the AC hard-mode motion. These QPDs typically have sensing noise of a few $\times 10^{-14} \text{ rad}/\sqrt{\text{Hz}}$, much lower than the REFL WFSs' noise level.

In practice, we blend the REFL WFSs' output and QPDs' output together to form the final error signal of the common-hard modes. The REFL WFSs' signals are DC-coupled and then low-passed with two poles at 0.8 Hz. The complement of this low-pass filter is then multiplied with the QPDs' output to form the AC part of the error signal. As a result, the sensing noise of common-hard mode is reduced from the red-dotted line to the orange-solid line (which is essentially the same as the purple-

dotted line above 10 Hz) in Figure 7-22b. It consequently reduces the common-hard loop's contamination to DARM by about a factor of 10.

Lastly, we also show the sensing noise for the soft modes (for the damping part; see Section 7.2.3) in the solid-blue traces. While their sensing noise is about a factor of 20 higher than that of the hard mode, their bandwidth is also smaller ($\lesssim 1$ Hz) and thus their contribution to the DARM noise is less severe than the hard modes.

7.3.3 Optimal control design using the \mathcal{H}_∞ method

We have discussed in Section 7.1 that our current controller for the alignment loop is suboptimal because it needs to maintain the loop stability as the suspension plant varies significantly over a range of different circulating powers. On the other hand, we have shown in Section 7.2.2 that the newly implemented radiation compensation techniques allows the removal of the Sidles-Sigg effect and thus keep the effective suspension plant unchanged. It thus opens up the possibility of plant inversion in our controller to optimize the overall loop performance. In this Section, we introduce the \mathcal{H}_∞ optimization method (for a nice review of optimal control methods, see [Bosgra et al. 2001](#)) and show that with this approach we can improve our alignment control to simultaneously reach the requirements set on both the suppression of low-frequency rms motion and the cutoff of high-frequency sensing noise (cf. Section 7.1).

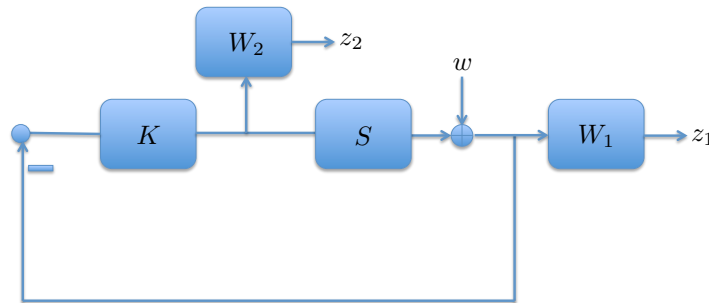


Figure 7-23: The generic form of the mixed sensitivity problem.

The alignment control of aLIGO can be treated as a mixed sensitivity problem ([Kwakernaak, 1983, 1985](#); [Kwakernaak, 2002](#)), which is a special kind of \mathcal{H}_∞ problem.

The generic diagram for this problem is illustrated in Figure 7-23, where, to be consistent with the previous sections, we have labeled the plant as S (which we know) and the controller as K (which we want to find as the solution to the problem). With noise input w and outputs $\mathbf{z} = [z_1, z_2]^T$, the system can be described as

$$\mathbf{z} = \begin{bmatrix} z_1 \\ z_2 \end{bmatrix} = \underbrace{\begin{bmatrix} W_1/(1 + SK) \\ -W_2K/(1 + SK) \end{bmatrix}}_H w, \quad (7.41)$$

where W_1 and W_2 are some custom weighting functions. As we shall see soon that the output z_1 weighted by W_1 corresponds to the residual displacement noise that sets the low-frequency requirements, and the z_2 weighted by W_2 corresponds to the residual sensing noise that determines the high-frequency cutoff. For future convenience, we will also introduce $W_3 = W_2/S$. The objective of the problem can be stated as the following. Given the above system (that is, we know the plant S as well as the weights $W_{1,3}$), we want to find a controller K such that

1. it stabilizes the closed-loop system, and
2. it minimizes the ∞ -norm $\|H\|_\infty$ of the closed-loop transfer matrix H from input w to outputs \mathbf{z} .

In the single-input-single-output case, the second point reduces to finding K such that the quantity

$$\sup_{\omega \in \mathbb{R}} \left[\left| W_1(\omega) \frac{1}{1 + S(\omega)K(\omega)} \right|^2 + \left| W_3(\omega) \frac{S(\omega)K(\omega)}{1 + S(\omega)K(\omega)} \right|^2 \right] \quad (7.42)$$

is minimized.

To proceed, let us first discuss the choice of the frequency-dependent weighting functions W_1 and $W_3 = W_2/S$. Thanks to the equalizing property, it implies that when the optimal solution is obtained, the quantity in (7.42) is often a constant (Kwakernaak, 1985). Let us denote this constant as γ^2 with $\gamma \geq 0$. It then

implies

$$\left| W_1(\omega) \frac{1}{1 + S(\omega)K(\omega)} \right|^2 \leq \gamma^2, \quad (7.43a)$$

$$\left| W_3(\omega) \frac{S(\omega)K(\omega)}{1 + S(\omega)K(\omega)} \right|^2 \leq \gamma^2, \quad (7.43b)$$

for $\omega \in \mathbb{R}$. At low frequencies with $\omega \ll \omega_{\text{bw}}$ where ω_{bw} corresponds to the angular frequency of the control bandwidth, we want the quantity $|SK| \gg 1$ so that we have sufficient loop suppression. Consequently we want $|W_1| \gg |W_3|$ there so that the term (7.43a) dominates, with $|W_1/(1 + SK)| \simeq |W_1/SK| \simeq \gamma$. In other words, the low-frequency loop suppression is given by

$$|SK| \simeq \gamma |W_1| \text{ for } \omega \ll \omega_{\text{bw}}. \quad (7.44)$$

Similarly, at high frequencies with $\omega \gg \omega_{\text{bw}}$, we want $|SK| \ll 1$ to minimize the injection of the sensing noise. Therefore we want the term (7.43b) to be dominant, with $|W_3SK/(1 + SK)| \simeq |W_3SK| \simeq \gamma$. This leads to a high-frequency cutoff

$$|SK| \simeq \frac{\gamma}{|W_3|} \text{ for } \omega \gg \omega_{\text{bw}}. \quad (7.45)$$

Pratically, we usually have some goals $|SK|^{(\text{trgt})}$ that we would like the control loop to achieve. Therefore, we can turn the above equations around to set the weighting functions as

$$|W_1(\omega)| = \gamma |S(\omega)K(\omega)|^{(\text{trgt})} \text{ for } \omega \ll \omega_{\text{bw}}, \quad (7.46a)$$

$$|W_3(\omega)| = \frac{\gamma}{|S(\omega)K(\omega)|^{(\text{trgt})}} \text{ for } \omega \gg \omega_{\text{bw}}. \quad (7.46b)$$

In general, the constant $\gamma \sim 1 - 10$. The problem thus is further reduced to finding K that “optimally” satisfies the goals set by the weights $W_{1,3}$.

Actually, the optimal solution to this problem is generically challenging. Nevertheless, what is easier to find is the *suboptimal* solution. In this suboptimal problem,

one can determine first if there exists a stabilizing K that achieves $\|H\|_\infty < \gamma$ for some given $\gamma > 0$, and if such K exists, it can be obtained explicitly based on Doyle et al. (1989). Then a search in γ can bring us to approach the optimal controller K . This algorithm has been implemented in commercially available softwares. For instance, the results we will show for aLIGO's alignment loop design are calculated with the `hinfscn` function²⁰ in MATLAB's Robust Control Toolbox.²¹

We are now ready to consider how we can use this \mathcal{H}_∞ method to improve our aLIGO's alignment control. Let us focus here on the control of the hard modes in pitch as an example. In our case, the plant is given by $S = S_{R_h}(10\text{ W})$ [cf. equation (7.18)] and is unaffected by the real input power thanks to the radiation pressure compensation system. The weighting functions W_1 and W_3 we use are shown in Figure 7-24. They are determined based on the following considerations.

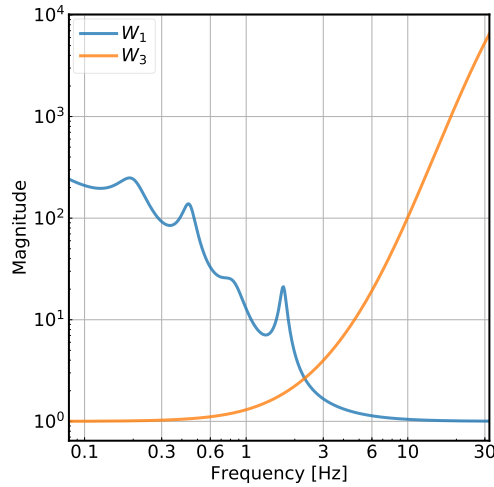


Figure 7-24: Weighting functions used for the \mathcal{H}_∞ design.

The displacement noise input to the system is given by $S_{R_h}(10\text{ W})\tau_{\text{in}}^{(\text{disp})}$ where $\tau_{\text{in}}^{(\text{disp})}$ is given by the right panel of Figure 7-2.²² To suppress such a noise, we would like to have the controller rising as $1/f^2$ between the secondary and primary

²⁰<https://www.mathworks.com/help/robust/controller-synthesis.html>

²¹<https://www.mathworks.com/products/robust.html>

²²Equivalently, it can be obtained by $\theta_{\text{in}}^{(\text{disp})}(10\text{ W}) = \theta_{\text{in}}^{(\text{disp})}(0)/(1 + R_h S_0)$ with $\theta_{\text{in}}^{(\text{disp})}(0)$ given by the left panel of Figure 7-2.

resonances and as $1/f$ below the primary resonance so that the spectral shape of the residual noise is essentially white below 1 Hz. At the 0.1-0.3 Hz microseismic band, we would like a factor of 20 suppression from the control loop. We thus fine tune the zeros of W_1 until it reaches $|W_1(0.2 \text{ Hz})| = 100$ from the smooth part [cf. equation (7.46a); we have assumed $\gamma = 5$ in our design]. We further enhances the loop suppression by adding resonant gains at both the microseismic band and the suspension resonances.

For the sensing noise, as noted in Section 7.1, we need $|SK|^{\text{trgt}} < 0.06$ in order to reach aLIGO's noise requirement at 10 Hz. Therefore we set $|W_3(10 \text{ Hz})| = 100$ according to equation (7.46b). We also let $|W_3|$ rises as f^5 locally at 10 Hz so that the alignment noise decreases faster than the fundamental quantum noise ($\propto f^{-2}$) and the suspension thermal noise ($\propto f^{-5/2}$).

Once the weights are specified, we can solve for the optimal controller K using MATLAB's `hinfsv` function. The open loop transfer function SK is shown in Figure 7-25. In the figure the red trace represents the result obtained with the \mathcal{H}_∞ design, and the black trace is the one we use currently (cf. Figure 7-5). The \mathcal{H}_∞ design has a significantly faster roll-off at 10 Hz compared to the original design. On the hand, the stability of the loop is not compromised by the sharp cutoff, as the red trace has a phase margin of $\simeq 30^\circ$, as large as the original design.

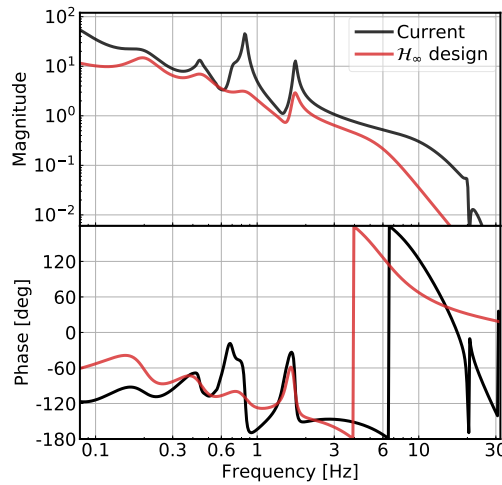


Figure 7-25: The open-loop transfer function SK of the hard modes in pitch.

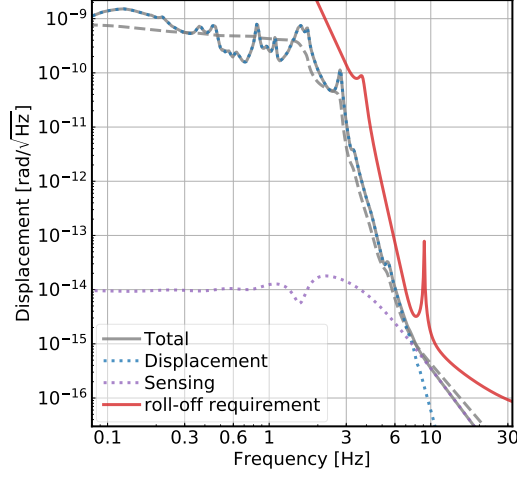


Figure 7-26: The residual motion of the hard loop using the controller designed with the \mathcal{H}_∞ method.

While the low-frequency gain is smaller for the new controller, in Figure 7-26 we show that the residual low-frequency motion is sufficiently low, with a rms of $0.8 \text{ rad}/\sqrt{\text{Hz}}$. Note that here we does not include any length-to-angle feedforward subtractions. With the feedforward on, the low frequency motion can be further reduced. Consequently, the \mathcal{H}_∞ controller meets the requirements on both the cutoff of high-frequency sensing noise, and the suppression of low-frequency input motion. The \mathcal{H}_∞ method is thus a promising way to improve the alignment control for both aLIGO and future generations of GW detectors.

Chapter 8

Thermal distortions in aLIGO

In addition to the radiation pressure effects, the thermal distortion is another challenge posed by aLIGO's high-power operation. The significant amount of circulating power (up to 0.7 MW) in aLIGO's arm cavities may be absorbed by the mirror coatings with a coefficient of about 0.5 ppm. The spatial Gaussian distribution of the laser beam may thus lead to a radial temperature gradient, which subsequently create both thermorefractive substrate lenses and thermoelastic surface deformation. As a result, the beam's wavefront will be distorted by the thermal lenses as the circulating power increases, degrading the mode-matching between different optical cavities. To tackle this challenge, a thermal compensation system has been developed for aLIGO ([Brooks et al., 2016](#)). However, the performance of this system is limited by the presence of point absorbers that are hardly anticipated until the circulating power reaches $\mathcal{O}(0.1)$ MW. Moreover, the current actuators for the thermal compensation system are designed for absorptions whose spatial profiles are given by the cavity's 00 mode, and consequently are not capable to compensate for distortions due to point absorbers involving high spatial orders.

In this Chapter we will explore some phenomena induced by the thermal wavefront distortion. While in reality the residue distortion is caused mainly by point absorbers involving high spatial orders, here we will nonetheless simplify the problem by modeling it as excess thermal lens and truncate the spatial order to second order (i.e., we include only up to 02/20 modes in our calculations). Consequently, we do

not intend to reproduce the exact aLIGO interferometer in our study, but instead focus on capturing the key consequences generated by the thermal distortions.

8.1 ALIGNMENT OF THE SIGNAL-RECYCLING CAVITY

As we have briefly mentioned in Section 6.4, the signal-recycling cavity’s axis was originally controlled by actuating on the SRM using an error signal derived from AS_A_RF36_I. However, at both observatories this ceased to be functional once the input power increased above ~ 20 W. To understand why this situation happened, we discuss here two major drawbacks of this signal.

Note first that here the “RF36” signal (at 36.4 MHz) is the beat note between the two RF sidebands at $f_1 = 9.1$ MHz and $f_2 = 45.5$ MHz. In an ideal interferometer without cavity offsets, the 00 modes of the RF sidebands satisfy $E(-f_i) = -E^*(f_i)$ for $i = 1, 2$ if we set the input carrier field to be real. Thus the whole-plane integrated 36.4 MHz signal can be written as

$$S(36.4 \text{ MHz}) = E^*(-f_2)E(-f_1) + E^*(f_1)E(f_2) = 2E^*(f_1)E(f_2), \quad (8.1)$$

which does not vanish. This is in contrast to the beat note between a RF sideband and the carrier field $E(0) \in \mathbb{R}$, which is given by

$$S(f_i) = E^*(-f_i)E(0) + E(0)E(f_i) = 0. \quad (8.2)$$

Therefore for the RF36 signal we define the I phase to be the phase at which $S(36.4 \text{ MHz})$ shows up. In other words, the RF beam spot shows up in the I phase.

In Figure 8-1 we show the simulated AS_RF36 responses to SRM misalignment as function of the detector’s Gouy phase (and therefore we have dropped the “A” in the sensor’s name) using FINESSE (Brown & Freise, 2014). Here we can first focus on the blue trace that assumes an ideal interferometer with perfect mode matching.

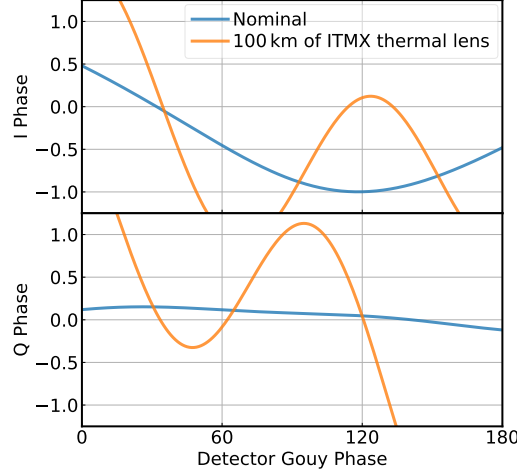


Figure 8-1: The response of the AS_RF36 signal to SRM misalignment as a function of the detector’s Gouy phase. The top and bottom panels show the error signal in the I and Q phases, respectively. The blue trace corresponds to an ideally mode-matched interferometer and the orange trace represents the case with wavefront distortion induced by 100 km of thermal lens. We have normalized the signals by the maximum amplitude of the response in the ideal interferometer.

From the figure, the SRM alignment signal shows up mainly in the I phase, and this is the first issue of the AS_RF36 signal. As we have discussed in Section 6.3, a WFS’s signal derived from a carrier-sideband pair has the nice property that it is insensitive to spot centering thanks to equation (8.2). This is, however, no more true for the 36.4 MHz signal due to equation (8.1) and the fact that the SRM alignment signal is mainly in the I phase. As a result, if the sensors drift in position with respect to the main interferometer, the AS_RF36 signal cannot distinguish such effects from real SRM misalignments. Moreover, as the interferometer powers up, the thermally induced carrier contrast defect may leak to the anti-symmetric port and contaminate the centering loops that steer the DC spot to the PD. The centering loops then drive the spot at 36.4 MHz to be off-centered, and consequently offsets the SRM’s alignment via the alignment feedback (Fulda & Brown, 2015).

The second drawback of the scheme is illustrated by the orange trace in Figure 8-1. Here we introduce an extra thermal lens in the ITMX substrate. The focal length of the lens is set to $f_{ix} = 100$ km, which creates approximately the same amount of

scattering loss in the carrier 00 field as the point absorber developed at the Hanford observatory during the second observing run (Yamamoto, 2017). The thermal lens dramatically changes the error signal's response. While in the nominal case two sensors separated by $\pi/2$ in Gouy phase would be sufficient to reconstruct error signal in the entire Gouy phase space, when 02/20 modes are present, this is no more the case. For instance, if we happen to place the two sensors at Gouy phases of 30° and 120° , the response may essentially vanish in both sensors. Moreover, the signal at Gouy phase of $\simeq 120^\circ$ (which corresponds to the peak sensitivity in the nominal case) changes sign as we include the thermal lens and destabilize the system.

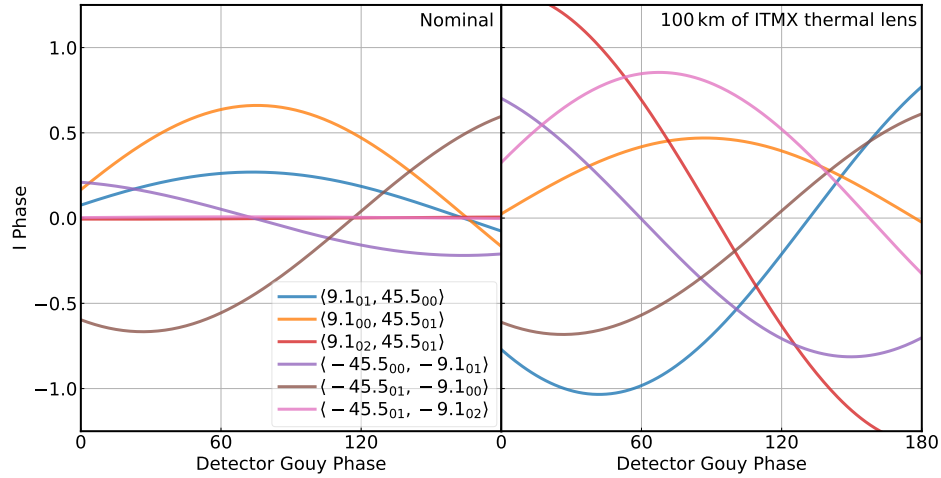


Figure 8-2: Decomposition of the AS_RF36_I signal. On the left is the ideal case with the interferometer perfectly mode-matched. On the right 100 km of extra ITMX thermal lens is introduced.

We further examine the error signal decomposition in Figure 8-2. In the legend we use $\langle f'_{m'n'}, f_{mn} \rangle$ to denote the beat note between the $m'n'$ mode of RF sideband with frequency f' and the mn mode of sideband f . The beat note is detected at a WFS (i.e., we subtract the upper- and lower-half planes to derive the signal). Here we focus on alignment in pitch so $m = m' = 0$, and parity enforces a vanishing signal if $n - n'$ is even. In the ideal interferometer, the error signal is dominated by the 9.1 MHz 00 mode beating 45.5 MHz 01 mode and their complex conjugates (note that the signals are not symmetric because of the Gouy phase; see Section 6.1). When

differential wavefront distortion is taken into account, however, the 02 mode of the 9.1 MHz sideband creates a beat note with the 45.5 MHz 01 mode much greater than the 9.1 MHz 00 mode does. Furthermore, $\langle 9.1_{01}, 45.5_{00} \rangle$ also increases significantly. This is because the 01 mode can be generated not only from the 00 mode but also the 02 mode by reflection upon a misaligned mirror. As the 02 mode of the 9.1 MHz has a greater amplitude than the 00 mode in the signal-recycling cavity, it becomes the main source from which the 01 mode is generated. As a consequence of both effects, the signal content of the AS_RF36 changes dramatically when 02/20 modes are included.

Figure 8-2 indicates that the drastic modification is due to a large $|E_{02}(f_1)|/|E_{00}(f_1)|$ ratio (with $f_1 = 9.1$ MHz) at the anti-symmetric port. The question then becomes the following. What determines this ratio and why is it so large? Since both $E_{00}(f_1)$ and $E_{02}(f_1)$ are off-resonance in the low-finesse signal-recycling cavity, we can ignore the signal-recycling cavity's filtering effects. Then each mode's amplitude is determined by how much it transmits through the Michelson. For the 00 mode, the transmissivity is determined by the Schnupp asymmetry $l_{\text{sch}} = 0.08$ m (cf. Section 5.2.2),

$$|E_{00}(f_1)| \propto \sin\left(\frac{2\pi f_1 l_{\text{sch}}}{c}\right) \simeq \frac{2\pi f_1 l_{\text{sch}}}{c} = 1.5\%. \quad (8.3)$$

For the 02 mode, on the other hand, it is due to the differential wavefront distortion,

$$|E_{02}(f_1)| \sim \frac{1/\Delta f}{1/\text{RoC}_i} \simeq 2\% \times \left(\frac{100 \text{ km}}{\Delta f}\right), \quad (8.4)$$

where Δf is the differential thermal lens and RoC_i is the radius of curvature of the ITM. In the above expression we have ignored order unity corrections. Because of the small transmissivity of $E_{00}(f_1)$ through the Michelson, even a few percent of differential wavefront distortion can lead to a significant amount of high-order mode compared to the main 00 component. Note that the above equations are all for amplitudes. In terms of contrast defect defined in power, it means the $E_{00}(f_1)$ will be greater than the higher-order-mode contaminations only if the contrast defect is better than 100 ppm. Such a condition is hardly satisfied in aLIGO even without

point absorbers.

Consequently, an error signal that is more robust against wavefront distortion is in demand. This leads to the addition of a third RF sideband to the interferometer at $f_3 = 118.3$ MHz and the new AS_RF72_Q detection scheme (Yu & Sigg, 2017). In this scheme, the error signal will be derived from the beat note between the existing 45.5 MHz sideband and the new 118.3 MHz sideband. To see why this signal is more robust, we again consider the ratio $|E_{02}(f_3)|/|E_{00}(f_3)|$. For the 00 mode, note that the transmissivity through the Michelson is proportional to the RF frequency, meaning that the transmissivity of the $E_{02}(f_3)$ is about 13 times greater than that of $E_{00}(f_1)$. The transmissivity of the 02 mode, nonetheless, is independent of frequency and about same fractional amount of $E_{02}(f_3)$ is leaked to the anti-symmetric port as $E_{02}(f_1)$. Overall, this leads to

$$\frac{|E_{02}/E_{00}(f_3)|}{|E_{02}/E_{00}(f_1)|} \simeq \frac{f_1}{f_3} \simeq \frac{1}{13}. \quad (8.5)$$

After taking the signal-recycling cavity's filtering effect into account, a FINESSE simulation leads to a ratio of 1/8.5. Therefore, we should expect the RF72 error signal to be about 10 times more robust than the RF36 signal against thermal distortions.

This is confirmed by the numerical simulation shown in Figure 8-3 where we consider the signal's response to SRM alignment in both the ideal case and the case with thermal distortion. The signal decomposition is shown in Figure 8-4. In the new 72.8 MHz signal, the fractional variations both in the overall response and in each individual beat note pair are significantly reduced compared to the 36.4 MHz signal. Moreover, in this scheme the SRM signal shows up equally in the I and Q phases. This means that we can use the Q phase signal to sense the signal-recycling cavity's alignment, and it is orthogonal to the spot position variation that shows up only in the I phase. Consequently, even if the carrier contrast defect contaminates the DC centering loop, the alignment of the signal-recycling cavity will not be biased with the AS_RF72_Q signal.

The new scheme has been implemented at both LIGO observatories prior the third

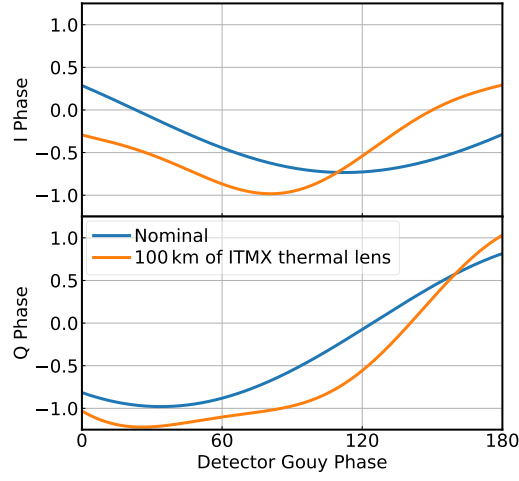


Figure 8-3: Similar to Figure 8-1 but this time it shows the AS_RF72 error signal as a function of the detector Gouy phase. Compared to the AS_RF36 signal, the AS_RF72 signal sees significantly less variations due to differential thermal lenses. Moreover, the response is largely in the Q phase, decoupling the decoupling between spot position drifts and the true signal-recycling cavity's alignment signal.

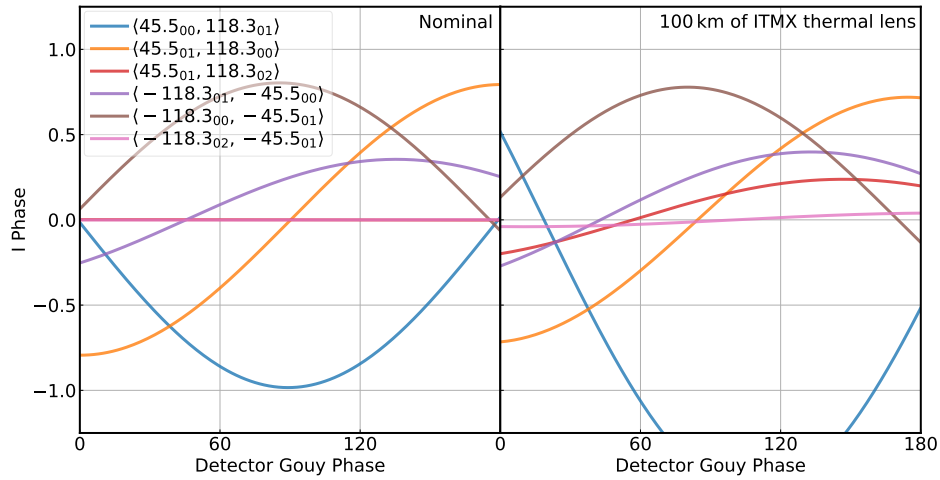


Figure 8-4: Decomposition of the AS_RF72_I signal.

observational run and works properly at an input power of 40 W. In contrast, the original RF36 signal could not be used once the input power increases beyond 20 W.¹

8.2 DETUNING OF THE SIGNAL-RECYCLING CAVITY

In Section 5.3.2 we derived the DARM optical response in the resonant-sideband-extraction configuration, corresponding to a microscopic longitudinal tuning of the SRM of $\phi_s = 90^\circ$. If ϕ_s deviates from an integer number times $\pi/2$, an optical spring will be formed (Buonanno & Chen, 2002). In Figure 8-5 we present the DARM optical responses at $\phi_s = 90^\circ$, 89.5° , and 90.5° , corresponding to the blue, the orange, and the red traces, respectively. We choose these values because in aLIGO’s second observing run, the Hanford observatory experienced an unintentional detuning of the SRM of -0.5° from its nominal position, or $\phi_s = 89.5^\circ$ (Hall, 2017; Cahillane et al., 2017).² The detuning reduces the DARM optical response at $\lesssim 30$ Hz and thus degrades the sensitivity in the same band. In this Section we propose a model to explain this effect (Yu, 2017), and show that the same extra ITMX thermal lens causing SRM alignment issues in the previous Section is also responsible for the detuning of SRM.

The physical process can be summarized as the following. The thermal lens creates a phase shift on the RF sidebands quadratic in the radius of curvature mismatch (for the carrier field this effect is at a higher order as it is resonant in the arm cavity). Such a phase shift breaks the symmetry between the upper and lower sidebands such that $-E(f_{\text{RF}}) \neq E^*(-f_{\text{RF}})$. Consequently, the PDH error signal is not zeroed anymore even there is no real detuning in that DOF (as experienced by the carrier field). However, the control loop cannot distinguish such a higher-order-mode contamination from the real error signal, and as the controller tries to zero the signal, it actually introduces an offset.

¹<https://alog.ligo-la.caltech.edu/aLOG/index.php?callRep=41784>

²Our sign convention follows that defined in FINESSE, which is opposition to the one used by Hall (2017).

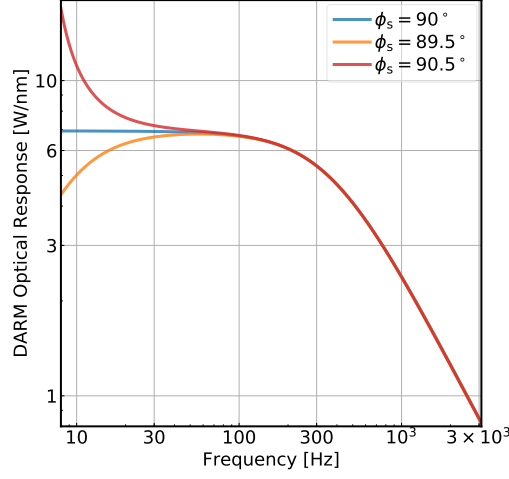


Figure 8-5: The optical response of DARM at different SRM tunings. The orange trace ($\phi_s = 89.5^\circ$) is consistent with the measured optical response of the LIGO Hanford observatory during the second observing run.

In Figure 8-6 we show the error signal,³ S_{srcl} , for the signal-recycling cavity’s length, or SRCL, as a function of the inverse of extra ITMX thermal lens, or $1/f_{\text{ix}}$. In the process, no physical detuning in SRCL (experienced by the carrier field that contains the GW signal) is introduced, and the error signal deviates from zero because of the higher-order-mode contamination in the RF sidebands. As a comparison, the red-dotted line is the error signal caused by a real SRCL detuning of 0.5° , and we have normalized the response such that it corresponds to $S_{\text{srcl}} = 1$. The plot indicates that for an extra ITMX thermal lens of $f_{\text{ix}} \simeq 100$ km, it may induce an error signal equivalent of 0.5° . Then as the negative feedback control is engaged, it will detune the SRM to $\phi_s = 89.5^\circ$ to zero this signal, which further induces the anti-spring in the DARM optical response.

To further confirm the above mechanism, we utilize the `lock` command in FINESSE (Brown & Freise, 2014). Specifically, in our numerical models we construct an error signal for SRCL as it is done in the real aLIGO interferometer, and feed it to the SRM longitudinal tuning ϕ_s iteratively to zero the error signal. Therefore, we are able to simulate

³In aLIGO, it is a linear combination of POP_9_I and POP_45_I that is insensitive to length fluctuations of the power-recycling cavity.

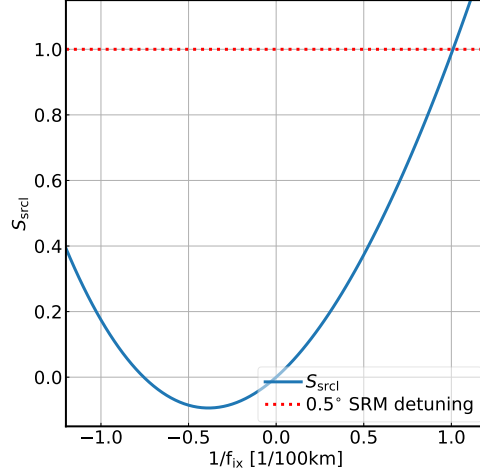


Figure 8-6: The SRCL error signal as a function of the inverse of extra ITMX thermal lens. The differential thermal lens induces an offset that is quadratic in the radius of curvature mismatch (it is not exactly symmetric about $1/f_{ix} = 0$ due to the intrinsic mode-mismatch in our numerical model). When $f_{ix} \simeq 100$ km, the higher-order mode induced offset equals to that from a real 0.5° detuning of SRM (indicated by the red-dotted line).

the real interferometer’s control loops in our numerical models, thereby studying the detuning in a realistic way.

The results are illustrated in Figure 8-7. The blue trace shows the nominal DARM optical response with $\phi_s = 90^\circ$ (i.e., the resonant-side-band extraction configuration). To study the effect of thermal distortion, we introduce an extra ITMX thermal lens of $f_{ix} = 100$ km to mimic the point absorber in the second observing run. Meanwhile, we use the `lock` command to keep the SRM at a position zeroing its PDH error signal. After the lock is completed, we then compute the DARM optical response and the result is shown in the orange trace. Indeed, a loss of response at sub-30 Hz is observed, consistent with the -0.5° detuning of the SRM (cf. the orange trace in Figure 8-5) measured at the Hanford observatory. To verify this is an effect due to the offset in the feedback control, we also present the DARM optical response in the purple-dashed line where we introduce the same amount of thermal lens but do not engage the SRCL feedback. It is inconsistent with the measurement (actually, a small positive optical spring is formed due to effects at higher orders in radius of curvature

mismatch), and thus indicates that the thermal lens by itself is unlikely to explain the observed anti-spring. Lastly, for completeness we also consider the effects due to a common thermal lens. This time we put $f_{ix} = f_{iy} = 100$ km to both the ITMX and ITMY, and then engage the `lock` command for SRCL. The result is illustrated in the red trace, which is essentially consistent with the nominal case.

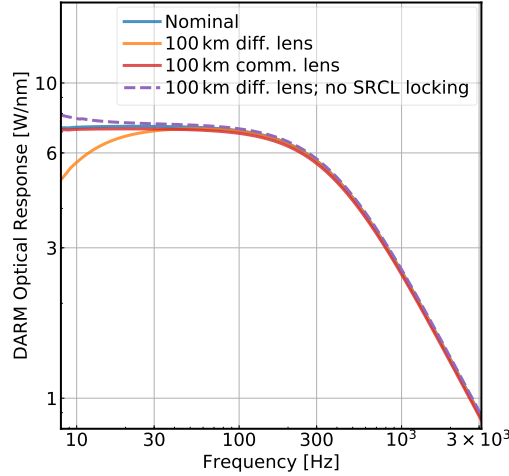


Figure 8-7: The optical response of DARM at different interferometer configurations. The thermal lens induces an offset in SRCL locking point, which detunes the SRM via the control feedback and creates an anti-spring in the DARM response (the orange trace). On the other hand, with only the thermal wavefront distortion but no control feedback it is insufficient to create the anti-spring as indicated by the dashed-purple trace.

To summarize, we have proposed a mechanism to explain the observed loss of low-frequency DARM response. That is, the thermal lens that contaminates mostly the RF sidebands induces an offset in the PDH error signal, and to zero this signal, the control loop detunes the SRM, which affects both the RF sidebands and the carrier field. The net result is thus a detuning on the carrier field that carries the GW signal.

Chapter 9

Prospects for detecting gravitational waves at 5 Hz with ground-based detectors

9.1 INTRODUCTION¹

The detection of GWs from coalescing binary BHs ([Abbott et al., 2016b, 2018a](#)) by aLIGO ([Aasi et al., 2015](#)) and Advanced Virgo (aVirgo) ([Acernese et al., 2015b](#)) heralded the era of GW astrophysics. However, detecting binaries that are more massive and further away than the current BH catalog is challenging. Since the merger frequency decreases as the total mass of the binary increases, systems more massive than a few $\times 100 M_{\odot}$ will no longer lie in the most sensitive band of aLIGO. Intermediate-mass black holes (IMBHs) are an example of systems likely to be missed by aLIGO ([Miller & Colbert, 2004](#); [Mandel et al., 2008](#); [Graff et al., 2015](#); [Veitch et al., 2015b](#); [Haster et al., 2016](#); [Abbott et al., 2017b](#)) . At the same time, a pair of $30 M_{\odot}$ BHs at $z = 2$ will appear to have a total mass of $180 M_{\odot}$ due to the cosmological redshift ([Cutler & Flanagan, 1994](#)), illustrating the difficulties of detecting even the stellar-mass BHs at cosmological distances. Therefore, improving the low-frequency

¹This Chapter is based-on [Yu et al. \(2018\)](#).

sensitivity plays a crucial role in extending both the mass and the spatial range of detectability.

Another scientific goal of GW detectors is to enable multimessenger astronomy, as demonstrated by the detection of a merging neutron star (NS) binary in GW and the follow-ups by electromagnetic telescopes (Abbott et al., 2017c; Abbott et al., 2017d). To help the subsequent observations, GW observatories need to provide the source location not only accurately but also quickly. Since the time to merger scales with frequency f as $f^{-8/3}$, if the error area can shrink small enough at a lower frequency, the location information can be sent out at a much earlier time. Consequently, improving the low-frequency sensitivity allows for more timely follow-up observations.

In this Chapter we propose an upgrade to aLIGO (and its evolution A+ Lazzarini et al. 2016) that enables a significant enhancement in sensitivity in the 5-30 Hz band while maintaining high frequency performance. This new design, dubbed “LIGO-LF”, can be implemented on a timescale of ~ 10 yr and serve as a pathfinder for later upgrades like the Voyager (Adhikari et al., 2017) and next-generation detectors like the Einstein Telescope (Hild et al., 2010; Sathyaprakash et al., 2012) and Cosmic Explorer (Abbott et al., 2017a).

9.2 LIGO-LF DESIGN

The current aLIGO sensitivity below 30 Hz is limited by nonstationary technical noises (Martynov, 2015; Martynov et al., 2016; Hall, 2017). Here we describe the solutions that we propose to reach the LIGO-LF sensitivity shown in Figure 9-1.

The first element of the upgrade reduces the angular control noise. Angular motion of the optics is actively stabilized using wavefront sensors with a typical sensitivity of 5×10^{-15} rad/ $\sqrt{\text{Hz}}$ (Barsotti et al., 2010; Martynov et al., 2016). The bandwidths of the arm cavity angular loops are set to 3 Hz for aLIGO to simultaneously suppress the radiation torque (Sidles & Sigg, 2006; Hirose et al., 2010; Dooley et al., 2013) and reduce the seismically induced motion to a few nrad rms (cf. Chapter 7). However, the control noise disturbs the test masses above 5 Hz and contaminates the GW readout

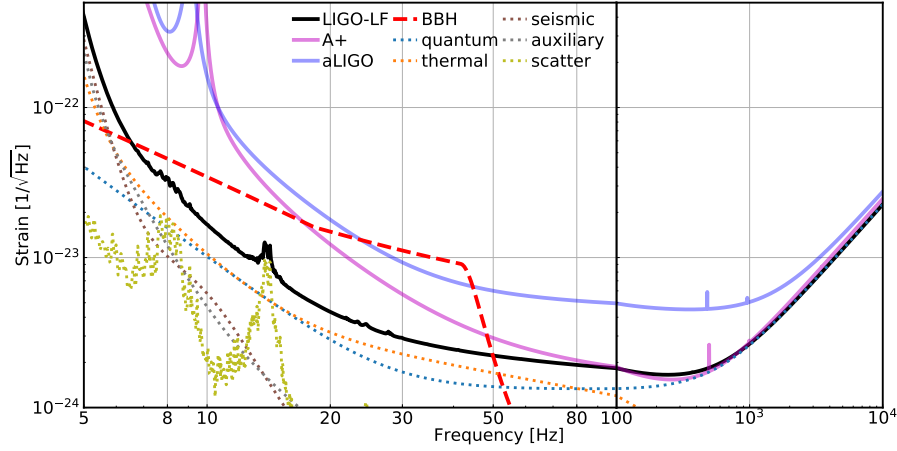


Figure 9-1: Proposed sensitivity for LIGO-LF (solid black line) and its noise budget (dashed lines). Also shown in the dotted red curve is the spectrum of a $200 M_{\odot}$ - $200 M_{\odot}$ binary BH merger (in the detector frame) at 10 Gpc. LIGO-LF’s sensitivity to such systems is greatly enhanced relative to aLIGO (solid blue line) and A+ (solid magenta line). Throughout this Letter, we will adopt the same coloring convention when we compare different sensitivities (i.e., we use black, magenta, and blue for LIGO-LF, A+, and aLIGO, respectively).

via beam mis-centering on the mirrors. To reach the LIGO-LF requirements, we thus need to reduce the control bandwidth to $\lesssim 1$ Hz.

Consider first the effects of radiation pressure. As we have discussed in Section 7.2.2, the shift in the suspension resonant frequency due to the radiation torque is given by

$$\Delta(\omega_{\pm}^2) = \frac{PL}{Ic} \left[\frac{(g_e + g_i) \mp \sqrt{(g_e - g_i)^2 + 4}}{(g_e g_i - 1)} \right], \quad (9.1)$$

where we have used $+$ ($-$) to represent the hard (soft) mode. To mitigate it, we propose to increase LIGO-LF’s test masses from 40 to 200 kg, which also improves the fundamental noises and is a fundamental part of next-generation GW detectors. The moment of inertia of the test masses consequently increased by a factor of $5^{5/3} \simeq 15$ if we assume the mirror geometry stays the same as that of the aLIGO mirror. With further geometrical optimization, a factor of 30 increase in I would be possible. For LIGO-LF, we also slightly reduce the radius of curvature of the ITMs to $g_i = -1.21$ so that the spot size on the ETMs are increased by 50% to reduce the coating thermal

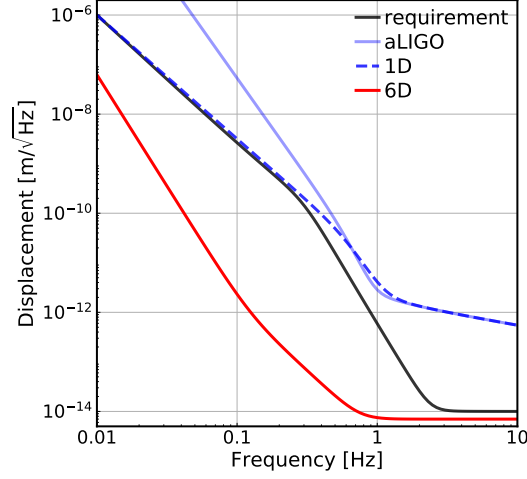


Figure 9-2: Inertial sensor noise for aLIGO (blue line) and the requirement for LIGO-LF (black line). Custom tiltmeters can be used to improve aLIGO sensor noise below 0.5 Hz (blue dashed line). A novel 6D seismometer (red line) can surpass the requirement in the entire band.

noise. As a result, for LIGO-LF we have $\Delta(\omega_+^2) = (2\pi \times 1.0 \text{ Hz})^2$ for the hard mode and $\Delta(\omega_-^2) = -(2\pi \times 0.11 \text{ Hz})^2$ for the soft mode with 0.8 MW of power circulating in each arm. As a comparison, for aLIGO with the same amount of circulating power the numbers are $\Delta(\omega_+^2) = (2\pi \times 3.0 \text{ Hz})^2$ and $\Delta(\omega_-^2) = -(2\pi \times 0.64 \text{ Hz})^2$, respectively. We can further remove the radiation torque with the compensation technique we have discussed in Section 7.2.2 which injects approximately the same amount of sensing noise as the 1-Hz-bandwidth feedback control.

Now the question becomes how can we reduce the residual angular motion to $\lesssim 1 \text{ nrad}$ with a control bandwidth of only 1 Hz. We propose to achieve this by further suppress the motion of the optical benches.

Despite the sophistication of LIGO's seismic isolation (Matichard et al., 2015a,b,c), it does not significantly reduce the microseismic motion at $\sim 0.2 \text{ Hz}$. This is due to tilt-to-horizontal coupling (Lantz et al., 2009; Matichard & Evans, 2015; Matichard et al., 2016), which causes the noise of the aLIGO inertial sensors to grow as $1/f^4$ at low frequencies as shown in Figure 9-2. To reduce the bandwidth of the angular controls to 1 Hz, the tilt motion needs to be suppressed to $10^{-10} \text{ rad}/\sqrt{\text{Hz}}$ in the 0.01-

0.5 Hz band. The corresponding horizontal sensitivity is shown in Figure 9-2. Above 1 Hz we require an improved sensitivity to reduce the direct coupling of the ground motion.

There are two approaches to reach the required sensitivity of the inertial seismic sensors. The first one is to actively stabilize the tilt motion using custom-built tilt-meters (Venkateswara et al., 2014, 2017), which can achieve the requirement below 0.5 Hz. The second approach uses a novel 6D seismometer (Mow-Lowry & Martynov, 2018). In the core of this instrument is a quasimonolithically suspended (Cumming et al., 2012) mass whose position is monitored using an interferometric readout. Figure 9-2 shows that the design performance of the 6D seismometer satisfies the requirement in the entire band.

In Figure 9-3 we compare the residual pitch motion for aLIGO and LIGO-LF after the alignment control is engaged; the yaw motion is similar at high frequencies and is significantly less than pitch below 1 Hz, so the low frequency rms requirement for yaw is less critical. The control bandwidth is set to be 3 Hz and 1 Hz for LIGO-LF². In the calculation for aLIGO, we use the measured ground motion and shadow sensor noise to represent the contributions due to seismic and due to suspension damping, respectively. For LIGO-LF, we adopt the required sensor noise (the black trace in Figure 9-2) for the residual seismic motion, and scale the shadow sensor noise of aLIGO down by a factor of 100 for the damping noise. Therefore our results here should be interpreted as the requirement set for the future seismic and damping sensors. The sensing noise from the wave-front sensors is assumed to be 5×10^{-15} rad/ $\sqrt{\text{Hz}}$ for both aLIGO and LIGO-LF. For LIGO-LF we also include the contribution to the sensing noise from the radiation pressure compensation path. Also shown in the red curve as a comparison is the equivalent quantum noise: with 1 mm of spot mis-centering, an angular fluctuation per test mass given by the red curve will be converted to a length noise equal to the LIGO-LF's quantum limit.

²Here we have assumed a controller with $1/f$ shape around the unity-gain frequency. We then add high-frequency cutoff filters while keeping the phase margin to be at least 30°. The optimal control design is not used here. Therefore Figure 9-3 serve as a conservative estimation of the alignment noise.

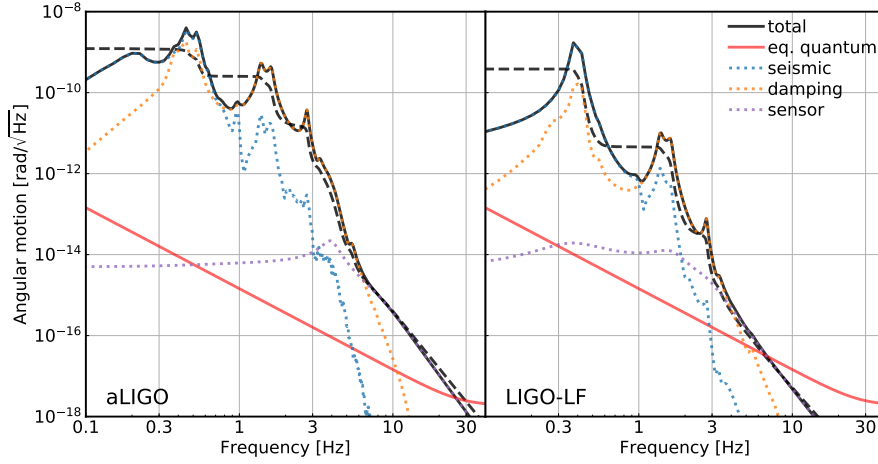


Figure 9-3: The residual pitch motion of aLIGO (left panel) and LIGO-LF (right panel). The black-solid curves are the total angular motion and the black-dashed ones are the corresponding cumulative rms values. The dotted curves are the noise contributions due to seismic (blue), suspension damping (orange), and wave-front sensing (purple), respectively. The red-solid curve is shown for comparison; it corresponds to a noise level equivalent to the LIGO-LF’s quantum noise if the spot mis-centering is 1 mm.

The coupling of the longitudinal motion of the signal recycling cavity contaminates aLIGO’s sensitivity in the 10-50 Hz band (Martynov et al., 2016). This coupling is proportional to the arm detuning (Izumi & Sigg, 2017) introduced to enable the dc readout of the GW signal (Fricke et al., 2012). For LIGO-LF, we assume balanced-homodyne readout (Fritschel et al., 2014) will be implemented instead, which essentially eliminates the coupling.

In aLIGO, high-quality-factor suspension resonances are damped using shadow sensors (Carbone et al., 2012) with a sensitivity of $2 \times 10^{-10} \text{ m}/\sqrt{\text{Hz}}$. A global control scheme has been proposed (Shapiro et al., 2015) to reduce its direct coupling to the GW output. However, this noise still enters the auxiliary loops and couples to the GW output indirectly. This calls for an improvement of the sensor noise by a factor of 100. Interferometric sensors (Aston, 2011) are promising candidates and are used in the LIGO-LF design.

Once technical noises are suppressed, LIGO-LF sensitivity will be limited by quan-

tum and thermal noises. Our strategy to improve the fundamental limits is similar to the Strawman Team Red design (Hild et al., 2012).

Quantum noise (Buonanno & Chen, 2001; Miao, 2012; Martynov et al., 2017) manifests both as sensor shot noise and as displacement noise by exerting quantum radiation pressure (QRP) forces on the test masses. LIGO-LF will operate under “resonant-sideband extraction” (Mizuno et al., 1993) with the same amount of power circulating in the arms as aLIGO. A signal recycling mirror transmissivity of 0.25 is chosen to optimize the broadband sensitivity.

The quantum noise can be further reduced with squeezed light (McClelland et al., 2011; Ligo Scientific Collaboration, 2011; Aasi et al., 2013). Here we assume a frequency-dependent squeezing (Kimble et al., 2001; Harms et al., 2003; Kwee et al., 2014; Oelker et al., 2016) that provides 3 dB reduction of the QRP and 6 dB of the shot noise. Relative to aLIGO, QRP is further suppressed by the heavier test masses mentioned above.

Thermal noise (Saulson, 1990) from the suspension (González, 2000; Cumming et al., 2012) and the optical coatings (Levin, 1998; Hong et al., 2013; Yam et al., 2015; Gras et al., 2017; Martynov et al., 2017) dominates the sensitivity from 5 to 100 Hz. Suspension thermal noise can be lowered by doubling the length of the last suspension stage to 1.2 m (Young & Budynas, 2002; Hammond et al., 2012) and by applying more sophisticated surface treatments (Mitrofanov & Tokmakov, 2003). LIGO-LF’s penultimate masses will also need to be suspended with fused silica fibers to avoid excess noise. Furthermore, the vertical suspension resonance can be shifted down to 4.3 Hz by increasing the fiber tension to 1.7 GPa. Overall, a factor of 5 improvement over aLIGO suspension thermal noise is possible (details of the LIGO-LF suspension are available in Appendix F.1).

The larger test masses and better seismic isolation open up the possibility of increasing spot sizes on the test masses by 50%, with a corresponding reduction in the coating thermal noise. Furthermore, a factor of 2 improvement in the coating loss angle is expected by the time of LIGO-LF (Steinlechner et al., 2016).

Further sensitivity improvement below 30 Hz is limited by gravity gradient noise (Saul-

son, 1984; Hughes & Thorne, 1998; Driggers et al., 2012; Creighton, 2008; Harms, 2015). It can be mitigated with offline regression (Coughlin et al., 2016), and in our calculation we assume a factor of 10 cancellation (Abbott et al., 2017a). The residual is combined with the residual seismic motion in Figure 9-1 under the label “seismic”.

Scattering is another critical noise source below 30 Hz (Flanagan & Thorne, 1994; Ottaway et al., 2012; Martynov, 2015). A small amount of light can scatter off the test masses due to surface imperfections, hit the baffles along the beam tubes, and finally recombine with the main beam. These stray photons induce differential power fluctuations which perturb the test masses via radiation pressure. In Figure 9-1, we present a scattering noise curve estimated from the typical ground motion at the LIGO sites with an anticipated 50% improvement in the mirror surface quality relative to aLIGO. As the relative displacement between the test mass and the tube is comparable to the laser wavelength ($1\ \mu\text{m}$), the coupling can become nonlinear, up-converting the baffle motion below 0.4 Hz up to 5 Hz (Canuel et al., 2013; Martynov et al., 2016). For rare cases where the ground motion is severe, an up-conversion shelf can form (Martynov, 2015) and limit the low-frequency sensitivity. The antireflection surfaces along the optical path also create scattering noise. To suppress it, baffles should be constructed to block 99.9% of the stray light (details available in Appendix F.2).

In summary, the key LIGO-LF advancements consist of low-noise, interferometric sensors for seismic isolation and suspension damping, and heavy test masses with large spot sizes for improving the fundamental limits. The LIGO-LF suspension system is also redesigned. Combined with the squeezed light, balanced-homodyne readout, and low-loss coating that are planned for A+, the upgrades lead to the final LIGO-LF sensitivity.

9.3 ASTROPHYSICAL APPLICATIONS

LIGO-LF can deliver a rich array of science in astrophysics. Here we consider three examples: (i) binary BHs, including the expected range of detectability and detection rate, and parameter estimation of events, (ii) binary NSs, focusing on the source

localization and the detectability of the tidal excitation of NS r-modes, and (iii) the GW memory effect. The searches for the stochastic GW background (Allen, 1997) and the continuous GW (Bejger, 2017) rely mostly on the instrument’s high-frequency performance, and are not enhanced by LIGO-LF.

9.3.1 Binary BHs.

Detectability.

With the LIGO-LF upgrade, both the maximum detectable distance and mass and the number of detections are larger than with aLIGO and A+, as illustrated in Figure 9-4. In the left, we plot the single-detector horizon and range (Chen et al., 2017) (in both redshift z and luminosity distance D_L) for binaries with different total masses M_{tot} . The systems are assumed to be nonspinning and to have equal masses. A single LIGO-LF could detect binary BHs to cosmological distances ($z \simeq 6$), whereas a network of four detectors would observe to $z \sim 10$, potentially accessing the first generation of stellar BHs (Sesana et al., 2009).

The detection range allows us to estimate the detection rate. To proceed, we adopt the standard power-law mass distribution used in LIGO event rate estimation (Abbott et al., 2016b). The probability densities of the primary mass M_1 and the secondary mass M_2 are respectively given by

$$\mathcal{P}_1(M_1) = \mathcal{A}_{M_1} M_1^{-\alpha} \Theta(M_1 - M_{\text{gap}}) \exp\left(-\frac{M_1}{M_{\text{cap}}}\right), \quad (9.2)$$

$$\mathcal{P}_2(M_2) = \mathcal{A}_{M_2} \Theta(M_2 - M_{\text{gap}}) \Theta(M_1 - M_2), \quad (9.3)$$

where \mathcal{A}_{M_1} and \mathcal{A}_{M_2} are overall normalizations, and Θ denotes the Heaviside step function. Following the convention we use a slope of $\alpha = 2.35$ and a lower limit of the mass distribution $M_{\text{gap}} = 5 M_{\odot}$. Consistent with Kovetz (2017), we have an exponential cutoff on M_1 which is set to $M_{\text{cap}} = 60 M_{\odot}$. Additionally we require $M_1 + M_2 \leq 100 M_{\odot}$. We do not consider the IMBHs in our rate calculation because of the large uncertainty in their formation; they are sufficiently rare and are thus

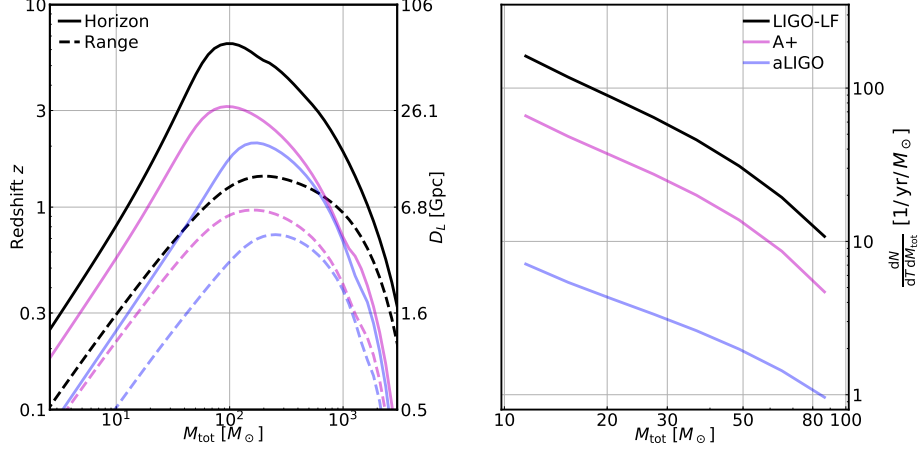


Figure 9-4: Left: The horizon (solid line) and range (dashed line) for binaries with different (source-frame) total masses. A single LIGO-LF may reach a cosmological redshift of $z \simeq 6$. Right: Expected detections rate of coalescing stellar-mass BH binaries as a function of the total mass. We marginalize over the mass ratio in the plot. LIGO-LF can detect ~ 3600 events per year, 18 times more than the expected number for aLIGO. All the numbers are calculated assuming a single detector.

unlikely to affect the total number of detections. For the merging rate, we adopt a simple, mass-independent approximation (Kovetz, 2017)

$$\mathcal{R}(z) = 97(1+z)^2 \text{ Gpc}^{-3} \text{ yr}^{-1}. \quad (9.4)$$

The expected number of detection per unit time dT in the mass interval $[M_{\text{tot}}, M_{\text{tot}} + dM_{\text{tot}}]$ is given by

$$\begin{aligned} \frac{dN(M_{\text{tot}})}{dT dM_{\text{tot}}} &= 4\pi \int_{M_{\text{tot}}/2}^{M_{\text{tot}}} dM_1 \mathcal{P}_1(M_1) \mathcal{P}_2(M_{\text{tot}} - M_1) \\ &\times \int_0^{z_{\text{ran}}(M_1, M_{\text{tot}} - M_1)} \frac{c\chi(z)^2 \mathcal{R}(z)}{(1+z)H(z)} dz, \end{aligned} \quad (9.5)$$

where $z_{\text{ran}}(M_1, M_2)$ is the detection range for a binary system with M_1 and M_2 , $\chi(z)$ the radial comoving distance, and $H(z)$ the Hubble parameter. In the calculation we have assumed a flat universe with Hubble constant $H_0 = 67 \text{ km s}^{-1} \text{ Mpc}^{-1}$ and matter (dark energy) fraction of $\Omega_m = 0.32$ ($\Omega_\Lambda = 0.68$), consistent with the Planck

result (Planck Collaboration, 2016). The $z_{\text{ran}}(M_1, M_2)$ is calculated with a single detector when we do the rate estimation. This is because we would like to focus on the improvements due to better sensitivity, instead of due to more detectors or more optimized network configuration.

The result is shown in the right panel of Figure 9-4. If we integrate over M_{tot} , we find a single LIGO-LF instrument will enable the detection of ~ 3600 stellar mass BH binaries per year. As a comparison, a single aLIGO (A+) can detect only about $\sim 200(1600)$ mergers in the same observational length. Note that the number of detections N yields a Poisson distribution, with a statistical uncertainty of \sqrt{N} . Therefore the statistical SNR grows as \sqrt{N} , illustrating LIGO-LF’s greatly enhanced ability to constrain the population properties of binary BHs relative to aLIGO. Consider a simple case where the merging rate \mathcal{R} is the only unknown, then with LIGO-LF we would be able to constrain it to within $\pm 0.5 \text{ Gpc}^{-3} \text{ yr}^{-1}$ for a total observational period of 10-year, 4 times better than what aLIGO can achieve. As \mathcal{R} is sensitive to, e.g., the metallicity at the time of binary formation (Abbott et al., 2016e), an accurate measurement of \mathcal{R} thus constrains the metal enrichment history of the Universe. Furthermore, the event rate per mass interval can also be used to place constraints on the fraction of dark matter in the Universe that is in the form of primordial BHs (Bird et al., 2016; Kovetz, 2017).

Parameter estimation

Moreover, LIGO-LF enables a more accurate parameter estimation than aLIGO. To emphasize the improved low-frequency sensitivity, we consider binaries with detector-frame total mass $M_{\text{tot}}^{(\text{d})} \geq 100 M_{\odot}$. Since the sensitivity of A+ and aLIGO is similar below 20 Hz, we consider the comparison between LIGO-LF and aLIGO. Qualitatively, the improvements are due to two facts: A more total SNR is accumulated in LIGO-LF than in aLIGO, and the SNR starts to accumulate at lower frequencies. Thus, if aLIGO can measure only the merger-ringdown phase of a coalescence, with LIGO-LF we could access the inspiral phase as well, allowing for a more precise estimation of the component masses and spins.

To quantify these improvements, we simulate GW signals with the `IMRphenomPv2` waveform (Hannam et al., 2014) and inject them to mock detector noise. We consider five total mass bins from $100 M_\odot$ to $2000 M_\odot$, each with three spin configurations: $(\chi_{\text{eff}} = \chi_p = 0)$, $(\chi_{\text{eff}} = 0.5, \chi_p = 0.6)$, and $(\chi_{\text{eff}} = -0.5, \chi_p = 0.6)$. Here χ_{eff} is the mass-weighted sum of component spins along the orbital angular momentum (Ajith et al., 2011; Santamaría et al., 2010), and χ_p captures the precessing components (Schmidt et al., 2015). The effect of the mass ratio has been studied in Veitch et al. (2015b); Haster et al. (2016), so we focus on the equal mass case.

We consider a four-detector network formed by the Hanford (H) and the Livingston (L) sites, LIGO-India (I), and aVirgo (V). For HLI, we consider both the LIGO-LF and aLIGO sensitivities; for V, we fix it at its design sensitivity (Acernese et al., 2015b). KAGRA (Somiya, 2012) is not included as it is less sensitive to IMBHs. For each source, the inclination is fixed to 30° and the distance is chosen such that the network SNR is 16 with aLIGO’s sensitivity. We then use the `LALInference` (Veitch et al., 2015a) to get posterior distributions of source parameters. The parameter estimation results refer to the detector frame and we denote them with a superscript ‘d’.

In Figure 9-5, we plot the 90% credible intervals of the chirp mass $\mathcal{M}_c^{(d)}$, total mass $M_{\text{tot}}^{(d)}$, and χ_{eff} . For the masses, we present the results for the nonspinning case. When spins are included, an aligned (antialigned) spin tends to improve (degrade) the inference accuracy (Ng et al., 2018). Similar effects can also be seen in the posterior distributions of χ_{eff} , as illustrated in the bottom panels. The precession term χ_p cannot be well constrained even with LIGO-LF.

To obtain the source-frame masses, the value of inferred redshift is required (Cutler & Flanagan, 1994). The conversion is

$$\mathcal{M}_c = \frac{\mathcal{M}_c^{(d)}}{1 + z} \quad (9.6)$$

for the chirp mass \mathcal{M}_c , and similarly for the total mass M_{tot} .

In Figure 9-6 we present the 90% credible intervals of the redshift z . To yield a net-

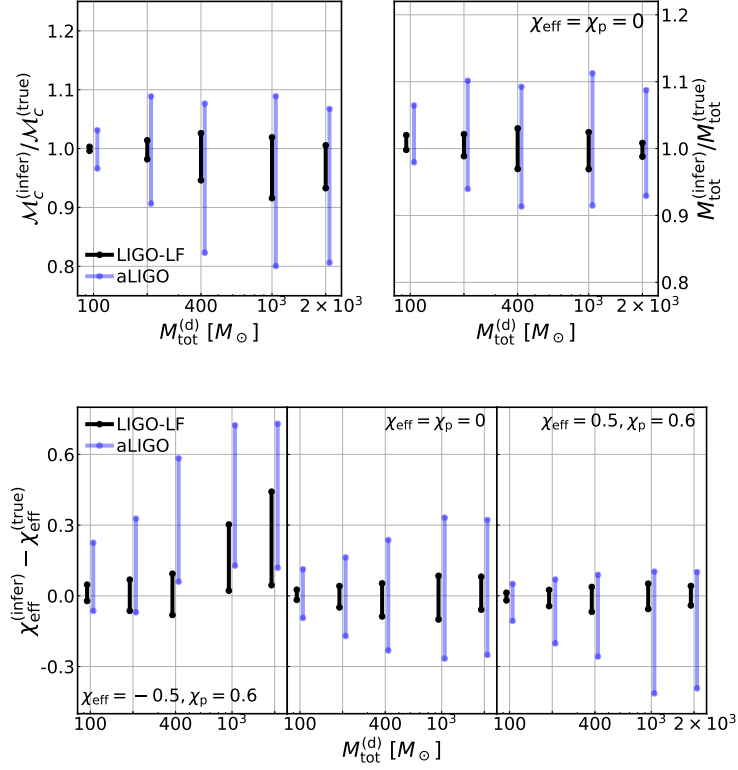


Figure 9-5: The 90% credible intervals of the detector-frame chirp mass $\mathcal{M}_c^{(d)}$ (top left), total mass $M_{\text{tot}}^{(d)}$ (top right), and effective spin χ_{eff} (bottom) are all significantly smaller for LIGO-LF than for aLIGO. LIGO-LF also reduces biases, especially for $\mathcal{M}_c^{(d)}$ and χ_{eff} when the spin is antialigned (bottom left).

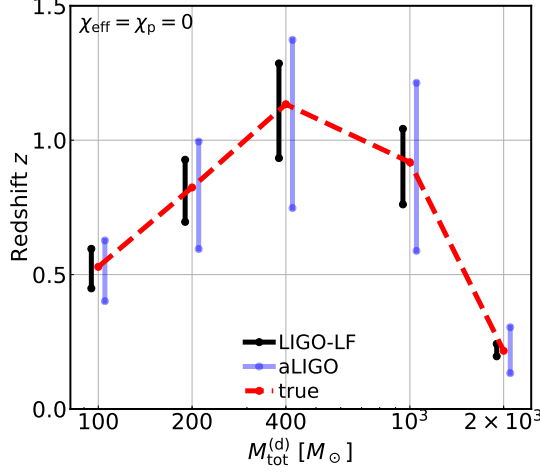


Figure 9-6: Mock sources for each total mass were placed at the redshifts indicated by the red-dashed line. The redshifts were chosen to give a network SNR of 16 in aLIGO. The black (blue) bars indicate the 90% credible interval for the inferred redshift with LIGO-LF (aLIGO) sensitivity. LIGO-LF typically improves the constrain in z by a factor of 2.

work SNR of 16 with aLIGO design sensitivity, the redshifts are $z = (0.53, 0.82, 1.1, 0.92, 0.22)$ for the 5 injections we have with $M_{\text{tot}}^{(d)} = (100, 200, 400, 1000, 2000) M_{\odot}$, respectively. LIGO-LF typically improves the accuracy in the redshift inference by a factor of 2 relative to aLIGO.

We show the 90% credible intervals of the source-frame masses in Figure 9-7. The injected source-frame total masses are $M_{\text{tot}} = (65, 109, 187, 521, 1644) M_{\odot}$, and chirp masses $\mathcal{M}_c = (28, 48, 82, 227, 716) M_{\odot}$. Due to the statistical error in measuring the redshift, LIGO-LF only constrains the source-frame values 2 times better than aLIGO.

The effective spin, nonetheless, is unaffected by the redshift and thus LIGO-LF can achieve 3-5 times better accuracy than aLIGO, which will be essential for discriminating between different formation scenarios that predict different spin configurations (Rodriguez et al., 2016; Farr et al., 2018).

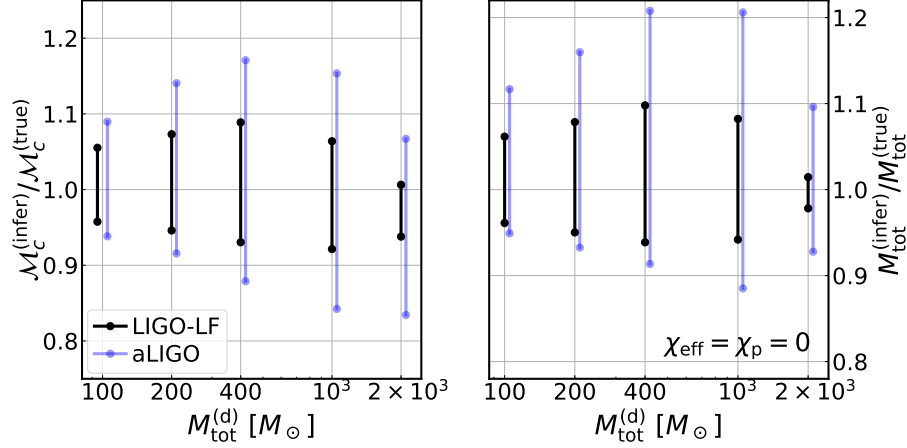


Figure 9-7: The 90% credible interval of the source-frame chirp mass \mathcal{M}_c (left panel) and total mass M_{tot} (right panel). The uncertainty is about a factor of 2 smaller for LIGO-LF compared to aLIGO, and is dominated by the uncertainty in inferring the redshift.

9.3.2 Binary NSs

Localization

We use the Fisher matrix to examine LIGO-LF's ability to localize a binary NS including effects of Earth's rotation. We consider the same HLIV network as in the PE section. The coordinates of HLIV can be found in [Jaranowski et al. \(1998\)](#), and we use the same location for I as in [Vitale & Evans \(2017\)](#).

The data seen in the i th detector in the network can be written as ([Zhao & Wen, 2017](#); [Wen & Chen, 2010](#))

$$d_i(f) = [F_i^+(f)h_+(f) + F_i^\times(f)h_\times(f)] \exp[-i2\pi f\tau_i(f)], \quad (9.7)$$

where $h_{+(\times)}$ is the GW signal in the plus (cross) polarization, $F_{+(\times)}$ the antenna response whose functional form is provided in [Jaranowski et al. \(1998\)](#), and τ_i the traveling time from the coordinate origin to the i th detector. The frequency dependences of $F_{+(\times)}$ and τ_i originate from the rotation of the Earth, and with the

stationary-phase approximation they can be written as,

$$F_{+(\times)}(f) = F_{+(\times)}[t_f(f)], \quad (9.8)$$

$$\tau_i(f) = \tau_i[t_f(f)], \quad (9.9)$$

$$t_f = t_c - \frac{5}{256} \left(\frac{G\mathcal{M}_c}{c^3} \right)^{-5/3} (\pi f)^{-8/3}. \quad (9.10)$$

Here t_c is the time of the coalescence. We compute the signal $h(f)$ using the post-Newtonian (PN) expansion, including phase corrections to the 1.5 PN order.

We parameterize the signal in terms of 9 parameters: $\mathbf{p} = (\mathcal{M}_c, q, t_c, \phi_c, \iota, \theta_s, \phi_s, \psi_s, d_L)$, corresponding to the chirp mass, mass ratio (≤ 1), time and phase at the merger, the source's inclination, declination, right ascension, polarization, and luminosity distance. The spin is not included since the NS is expected to be slow spinning (Abbott et al., 2017c; Burgay et al., 2003). The statistical error of each parameter can be estimated using the Fisher matrix with element

$$\Gamma_{jk} = \left\langle \frac{\partial \mathbf{d}}{\partial p_j}, \frac{\partial \mathbf{d}}{\partial p_k} \right\rangle, \quad (9.11)$$

where the inner product for data from the network, \mathbf{a} and \mathbf{b} , is defined as

$$\langle \mathbf{a}, \mathbf{b} \rangle(f_{\text{up}}) = 2 \sum_i^{\text{HLIV}} \int_0^{f_{\text{up}}} df \left[\frac{a_i^*(f)b_i(f) + a_i(f)b_i^*(f)}{S_i(f)} \right]. \quad (9.12)$$

Here $S_i(f)$ is the noise power spectra density of the i th detector, $f_{\text{up}} \leq 2f_{\text{isco}}$ is the upper limit of the integration, and f_{isco} is the orbital frequency at the system's innermost stable circular orbit (ISCO). We have treated f_{up} as a free parameter so that we can consider the cumulative accuracy using only data with $f < f_{\text{up}}$,

The full covariance matrix Σ can be obtained by inverting Γ ,

$$\Sigma = \Gamma^{-1}, \quad (9.13)$$

and the statistical error for the j th parameter p_j is given by

$$\Delta p_j = \sqrt{\Sigma_{jj}}. \quad (9.14)$$

We are especially interested in the uncertainty solid angle covering the source's location, which is given by

$$\Delta\Omega_s = 2\pi |\sin \theta_s| \sqrt{\langle \Delta\theta_s^2 \rangle \langle \Delta\phi_s^2 \rangle - \langle \Delta\theta_s \Delta\phi_s \rangle^2}. \quad (9.15)$$

In order to demonstrate the improvement made by LIGO-LF over aLIGO and A+, we focus on $1.4 M_\odot$ - $1.4 M_\odot$ NS binaries, and fix the source location to the Coma cluster. We consider two inclination angles, a face-on one with $\iota = 30^\circ$, and a more edge-on one with $\iota = 75^\circ$. The arriving time and polarization of the sources are marginalized over. The result is shown in Figure 9-8. Here we plot the cumulative localization error, $\Delta\Omega_s(f_{\text{up}})$ as a function of f_{up} . In other words, instead of integrating equation (9.12) over the entire signal band, we integrate it only up to f_{up} . We can thus know the localization accuracy at each instant of the inspiral. As shown in the figure, LIGO-LF localize the source 5 (10) times better than A+ (aLIGO) at 30 Hz, and 10 (15) times better at 20 Hz. Note that the time prior the final merger increases sharply as the frequency decreases, as

$$t_c - t_f = 54 \left(\frac{\mathcal{M}_c}{1.2 M_\odot} \right)^{-5/3} \left(\frac{f}{30 \text{ Hz}} \right)^{-8/3} \text{ s}. \quad (9.16)$$

Despite that the final uncertainties are similar for A+ and for LIGO-LF, LIGO-LF would be able to send out the source location minutes before the final merger, while for A+ similar accuracy cannot be achieved until seconds before the merger. This illustrates LIGO-LF's ability to achieve a more timely localization than A+ and aLIGO.

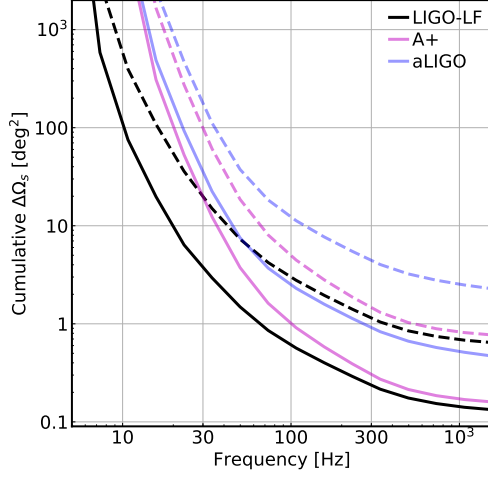


Figure 9-8: The cumulative uncertainty in localization, $\Delta\Omega_s$, for the HLIV network. We consider NS binaries at the Coma cluster with two inclinations, 30° (solid line) and 75° (dashed line), and marginalize over the polarization and time of arrival. LIGO-LF improves the localization accuracy by a factor of 5 over A+ using only the sub-30 Hz data.

NS r-modes

The (linear) tidal response of the NS can be decomposed into an equilibrium tide and a dynamical tide. The equilibrium tide accounts for the quasi-static, large-scale distortion of the star and the dynamical tide (Lai, 1994; Reisenegger & Goldreich, 1994) accounts for the internal modes of oscillation which can be resonantly excited as the orbit decays and sweeps up in frequency. Here we consider the excitation of the NS’s rotational modes (i.e. the r-modes) due to its companion’s gravitomagnetic tidal field (Flanagan & Racine, 2007). We focus on the detectability of the $l = 2$, $m = 1$ r-mode which does not require misalignment between the NS spin and the orbital angular momentum. The GW frequency of mode resonance f_r is related to the NS’s spin frequency f_{spin} as

$$f_r = \frac{4}{3}f_{\text{spin}}. \quad (9.17)$$

Since the NSs in binary NS systems are expected to be slow-spinning (with a rate less than a few $\times 10$ Hz), the r-mode is naturally an interesting science case for the

LIGO-LF upgrade.

The tidal interaction induces a phase shift, $\delta\Phi_r$, relative to the point-particle (pp) GW waveform. As the duration of the mode resonance is typically $\sim 1\%$ of the total GW decay timescale (Flanagan & Racine, 2007), the resonance can thus be treated as an instantaneous process. In this limit, the phase of the frequency-domain waveform $\Psi(f)$ can be written as (Yu & Weinberg, 2017b)

$$\Psi(f) = \Psi_{\text{pp}}(f) - \left(1 - \frac{f}{f_r}\right) \delta\Phi_r \Theta(f_r - f), \quad (9.18)$$

where Ψ_{pp} is the phase of the point particle waveform (calculated to the 1.5 PN order in our study). In the expression above we have aligned the tidal waveform to the pp one at the merger.

While in the case of equilibrium tides the orbital energy is absorbed by the star and thus the inspiral is accelerated, in the case of the r-mode interaction the direction of energy transfer is reversed. The orbit extracts the NS spin energy which decelerates the inspiral. This unique feature of the r-mode corresponds to a *negative* $\delta\Phi_r$ in the expression above. While large theoretical uncertainties exist, previous work suggests that (Flanagan & Racine, 2007)

$$\delta\Phi_r \sim -0.1 \left(\frac{f_{\text{spin}}}{100 \text{ Hz}} \right)^{2/3}. \quad (9.19)$$

To estimate the detectability of this effect, we once again use the Fisher matrix method. A fully Bayesian analysis is deferred to future studies. For simplicity, we focus on the single-detector case and fix the sources at 50 Mpc with optimal orientation. This allows us to write the waveform in terms of 9 parameters, $(\mathcal{M}_c, q, \chi_1, \chi_2, t_c, \phi_c, d_L, f_r, \delta\Phi_r)$, corresponding to the chirp mass, mass ratio, dimensionless spin of mass 1 and 2, time and phase at the coalescence, luminosity distance, and the resonant frequency and the phase shift of the r-mode. The equilibrium tidal deformation is not included here because it is only relevant at $f \gtrsim 600 \text{ Hz}$ (Hinderer et al., 2010). We consider here binaries with $M_1 = 1.4 M_\odot$ and $M_2 = 1.35 M_\odot$.

The mass ratio is slightly off 1 because otherwise χ_1 and χ_2 will be completely degenerate. The relation between the spin frequency f_{spin} and the dimensionless spin parameter χ depends on the NS equation of state. Here we pick the SLy equation of state (Douchin, F. & Haensel, P., 2001) as a typical representation; this equation of state is consistent with the GW170817 event (Abbott et al., 2017c). It leads to

$$\chi \simeq 0.06 \left(\frac{f_{\text{spin}}}{100 \text{ Hz}} \right), \quad (9.20)$$

for a typical $1.4 M_\odot$ NS. A softer equation of state yields a larger χ for a NS with fixed mass. We then vary the spins of the two masses simultaneously (i.e., $f_{\text{spin}1} = f_{\text{spin}2} = f_{\text{spin}}$), and evaluate the Fisher matrix at different values of f_{spin} to obtain the uncertainty on the phase shift, $\Delta(\delta\Phi_r)$.

The results are shown in Figure 9-9. The r-mode is detectable if the statistical error is smaller than the real phase shift calculated from equation (9.19), i.e., we set $\Delta(\delta\Phi_r) \leq |\delta\Phi_r|$ as the detectability threshold³. We find that if the NS spins at a rate greater than 35 Hz (which is approximately the rate of the fastest rotating pulsar in a binary NS system known today (Burgay et al., 2003) when it enters the sensitivity band of a ground-based GW detector), a single LIGO-LF may detect the r-mode resonance up to a distance of 50 Mpc. Since the phase shift of the $l = 2$, $m=1$ r-mode depends on the NS stratification, which is sensitive to the internal composition and the state of matter (Yu & Weinberg, 2017a,b), a detection may thus place constraints on the NS equation of state from physics beyond the star’s bulk properties (Andersson & Ho, 2018). Furthermore, the r-mode resonance provides an independent measurement of the NS spin, which may help break the spin-mass ratio degeneracy (Cutler & Flanagan, 1994) and improve the accuracy in measuring the (equilibrium) tidal deformability (Hinderer et al., 2010; Abbott et al., 2017c).

³Note that we included only a single set of $(f_r, \delta\Phi_r)$ in equation 9.19, whereas in a merging binary NS system each NS should contribute individually a r-mode phase shift. Nevertheless, the typical uncertainty of the resonant frequency is $\Delta f_r \simeq 50 \text{ Hz}$, corresponding to a resolution in the spin frequency of $\Delta f_{\text{spin}} \simeq 40 \text{ Hz} > f_{\text{spin}}$. We are thus unlikely to resolve the individual resonance but only the combined effect of the two NSs. Therefore we included an extra factor of 2 when computing the theoretical prediction (the red-dashed curve in Figure 9-9) according to equation (9.19).

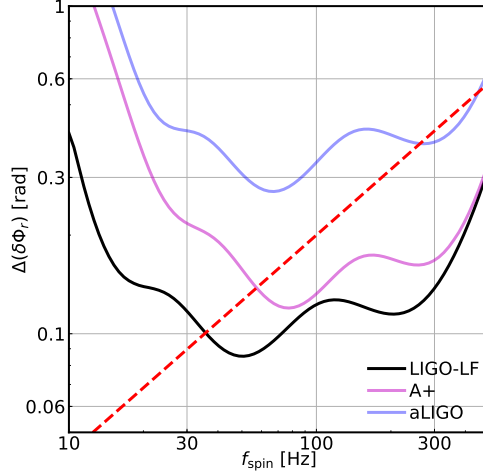


Figure 9-9: The uncertainty (solid lines) in measuring the phase shift due to resonant excitation of the NS r-mode $\delta\Phi_r$ as a function of the NS spin frequency f_{spin} . We consider the single detector case and fix the sources at 50 Mpc with optimal orientation. Also shown in the red dashed line is the expected magnitude of the real r-mode phase shift $|\delta\Phi_r|$. The effect is detectable when the real phase shift is greater than the statistical error.

9.3.3 The GW memory

The GW memory causes a DC displacement of the test masses that persists after the GW has passed ([Christodoulou, 1991](#)). As the effect builds up over a finite amount of time, it can thus be detected by a LIGO-like GW detector which effectively high-passes the signal. The detection of this effect may provide a strong-field test of the general theory of relativity. Therefore we consider it as one of the science cases for LIGO-LF.

Here we adopt the minimal-waveform model proposed in [Favata \(2009\)](#),

$$h_+^{(\text{mem})}(f) = \frac{G\eta M_{\text{tot}}/c^2}{384\pi D_L} \sin^2 \iota (17 + \cos^2 \iota) h^{(\text{mem})}(f), \quad (9.21)$$

where $\eta = M_1 M_2 / M_{\text{tot}}^2$ is the symmetric mass ratio, and $h_{\times}^{(\text{mem})}(f) = 0$. The term

$h^{(\text{mem})}(f)$ is further given by

$$h^{(\text{mem})}(f) = \frac{i}{2\pi f} \left\{ \frac{8\pi G M_{\text{tot}}}{c^2 r_m} [1 - 2\pi i f \tau_{\text{rr}} U(1, 7/4, 2\pi i f \tau_{\text{rr}})] - \frac{c^3}{G \eta M_{\text{tot}}} \sum_{n, n'}^{n_{\text{max}}} \frac{\sigma_{22n} \sigma_{22n'}^* A_{22n} A_{22n'}^*}{2\pi i f - (\sigma_{22n} + \sigma_{22n'}^*)} \right\}. \quad (9.22)$$

The value of $\tau_{\text{rr}} = (5/256) (G M_{\text{tot}} / c^3 \eta) (c^2 r_m / G M_{\text{tot}})^4$ is the characteristic orbital decay time scale at r , and U is Kummer's confluent hypergeometric function of the second kind. The σ_{lmn} are angular frequencies of the final BH's quasi-normal modes, whose value are given in [Berti et al. \(2006\)](#). The coefficients of A_{lmn} can be solved by matching the leading order quadrupole moments in the inspiral phase to the sum of the ringdown normal modes at r_m . Here we choose r_m to correspond to the orbital separation at the ISCO.

In our calculation we consider a simple case where we fix the source distance to $z = 0.1$ ($D_L = 0.48 \text{ Gpc}$) and inclination to $\iota = 30^\circ$. We further assume that the signal is purely in the '+' polarization. We then vary the source-frame total mass (while keeping the mass ratio to 1) and compute the single-detector matched-filter SNR for each source with different detector sensitivities.

The result is shown in Figure 9-10. LIGO-LF increases the peak SNR by a factor of 4 relative to aLIGO. While it may still be challenging to detect the effect from a single event, LIGO-LF nonetheless has a promising future in detecting this event via event-stacking. As suggest in [Lasky et al. \(2016\)](#), aLIGO will need ~ 90 GW150914-like ([Abbott et al., 2016c](#)) events to be able to achieve a SNR of 5 detection of the memory effect. Accumulating these many events will require aLIGO to operate at full sensitivity for ~ 10 years (note that the detection rate calculations in Section 9.3.1 assumes an SNR lower limit of 8 or a range of $z \simeq 0.4$ for a $30 M_\odot$ - $30 M_\odot$ system; restricting to a range of within $z \lesssim 0.1$ will lower the detection rate by a factor of $\simeq 64$). For LIGO-LF, however, only ~ 25 events will be sufficient to reach a similar level of detection. As the detection rate of LIGO-LF also increased by a factor of almost 20 relative to aLIGO, it means within a few months of observation with LIGO-

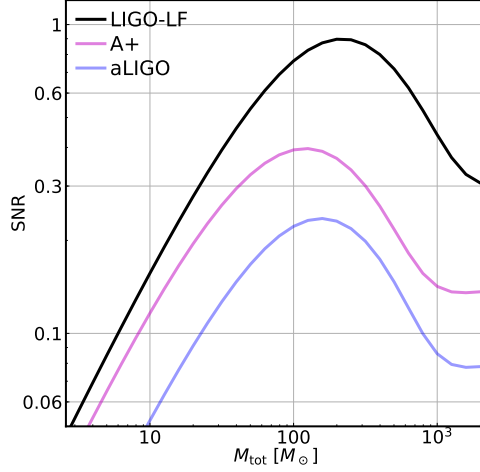


Figure 9-10: SNR from the GW memory effect as a function of the source-frame total mass. The sources are fixed at $z = 0.1$ and an inclination of 30° . The peak SNR seen in LIGO-LF is 4 (2) times greater than that seen in aLIGO (A+).

LF will be sufficient to achieve a high SNR (≥ 5) detection of the memory effect.

9.4 CONCLUSIONS

In this Chapter we proposed LIGO-LF, an upgrade improving aLIGO’s low-frequency performance. With technologies currently under development, such as suspension systems with 200 kg test masses, interferometrically sensed seismometers, and balanced-homodyne readout, LIGO-LF can reach the fundamental limits set by quantum and thermal noises down to 5 Hz. These technologies are also directly applicable to the future generation of detectors. We went on to consider this upgrade’s implications for the astrophysical output of an aLIGO-like detector. Comparing LIGO-LF to aLIGO, we found that the mass and spatial range of binary BHs detectable would be greatly enhanced, and the localization of NS binaries would be achieved at a much earlier time, enabling more timely follow-up.

Appendix A

Details of the MESA setup for the super-Eddington-wind models

Our simulations start from the `NS_envelope` model provided in the MESA test suite. We set $M = 1.4 M_\odot$ and $R = 10$ km at the inner boundary. The module provides a thin NS envelope of pure ^{56}Fe , on top of which we accrete an extra layer of ^{56}Cr with a column depth of 10^9 g cm^{-2} (see footnote 4). We accrete pure ^4He onto this envelope until ^4He ignition using commands similar to the `ns_he` model provided in the MESA test suite.

The column depth of the ignition base, y_b , depends on the pre-burst flux F_{pre} (Bildsten, 1998; Cumming & Bildsten, 2000). For pure helium accretion, $F_{\text{pre}} = Q_{\text{crust}} \dot{M}_{\text{acc}} / 4\pi R^2$, where \dot{M}_{acc} is the accretion rate and Q_{crust} is the energy release per nucleon in the crust (Brown & Bildsten, 1998; Cumming, 2003; Cumming et al., 2006). In MESA, this flux can be controlled by a combination of the mass accretion rate \dot{M}_{acc} and the core luminosity L_c using the commands “`mass_change`” and “`relax_initial_L_center`,” respectively (Paxton et al., 2011). To determine the value of L_c , we adopt the following procedure. First, we perform a side calculation in which we evaluate the ignition condition $d\epsilon_{3\alpha}/dT = d\epsilon_{\text{cool}}/dT$, where $\epsilon_{3\alpha}$ is the triple-alpha energy generation rate and $\epsilon_{\text{cool}} = acT^4/3\kappa y^2$ is the radiative cooling rate. Here we assume that the thermal profile of the pre-burst atmosphere is given by $acT^4 \simeq 3\kappa y F_{\text{pre}}$, with $F_{\text{pre}} = Q_{\text{crust}} \dot{m}_{\text{acc}}$. We determine Q_{crust} by requiring

that ignition occur at $y_b = 5 \times 10^8 \text{ g cm}^{-2}$ when $\dot{M}_{\text{acc}} = 3 \times 10^{-9} M_{\odot} \text{ yr}^{-1}$.¹ With Q_{crust} fixed at this value, we obtain an ignition curve $y_b(\dot{M}_{\text{acc}})$. We then determine the value of L_c by requiring that the MESA model ignite at a depth that matches the ignition curve $y_b(\dot{M}_{\text{acc}})$. For the $\{y1, y2, y3\}$ models, we find $(\dot{M}_{\text{acc}}, L_c)$ equals $\{(3, 2.45), (0.5, 1.36), (0.08, 0.85)\}$, in units of $(10^{-9} M_{\odot} \text{ yr}^{-1}, 10^{34} \text{ erg s}^{-1})$.

Once the base becomes convective, we use the following inlist file to simulate the hydrostatic burst rise.

```
&star_job
  change_initial_net = .true.
  new_net_name = 'approx21.net'
  kappa_file_prefix = 'gs98'
  relax_initial_tau_factor = .true.
  relax_to_this_tau_factor = 100d0
  dlogtau_factor = .1
  change_v_flag = .true.
  change_initial_v_flag = .true.
  new_v_flag = .true.

&controls
  max_timestep = .5d-2
  use_GR_factors = .false.
  varcontrol_target = .75d-4
  which_atm_option = 'grey_and_kap'
  Pextra_factor = 2
  accrete_same_as_surface = .false.
  accrete_given_mass_fractions = .true.
  num_accretion_species = 1
  accretion_species_xa(1) = 1
```

¹ These are typical ignition parameters (see, e.g., Table 1 of [WBS](#)); we find very similar wind simulation results when we instead require $y_b = 3 \times 10^8 \text{ g cm}^{-2}$ at $\dot{M}_{\text{acc}} = 3 \times 10^{-9} M_{\odot} \text{ yr}^{-1}$.

```

accretion_species_id(1) = 'he4'
mass_change = 5d-10
mixing_length_alpha = 1.5
MLT_option = 'Henyey'
okay_to_reduce_gradT_excess = .false.
use_Ledoux_criterion = .false.

```

We use the ‘`approx21.net`’ network for the n21 models and the ‘`basic_plus_fe56.net`’ for the n9 models. For simplicity, we neglect the composition gradient’s contribution to convection (`use_Ledoux_criterion = .false.`), since we assume pure He accretion. Such a simplification would not be appropriate for mixed H/He accretion (WBS). The choice of `mixing_length_alpha` is motivated by the value given in the test suite `ns_he`, although we find that the results are not particularly sensitive to this choice. In order to be consistent with the subsequent hydrodynamic simulations, we turn off the MLT++ option by setting `okay_to_reduce_gradT_excess=.false.`; using it in the hydrodynamics calculation would have suppressed the generation of a wind (Paxton et al., 2013; Quataert et al., 2016).

We edited the `extras_check_model` function in `run_star_extras.f` in order to stop the hydrostatic simulation when L_{rad} first exceeds L_{Edd} at the top boundary. We pass the final profile of the hydrostatic simulation to the hydrodynamic simulation, which uses the following inlist file.

```

&star_job
  relax_initial_tau_factor = .true.
  relax_tau_factor = .true.
  relax_to_this_tau_factor = 1
  dlogtau_factor = .1
  set_initial_dt = .true.
  seconds_for_initial_dt = 1d-4
  remove_surface_by_density = 1d-14
  repeat_remove_surface_for_each_step = .true.

```

&controls

```
varcontrol_target = 2d-5
MLT_option = 'none'
Dutch_scaling_factor = 0.0
Dutch_wind_lowT_scheme = 'de Jager'
Hot_wind_scheme = 'Dutch'
which_atm_option = 'grey_and_kap'
Pextra_factor = 3
use_compression_outer_BC = .true.
use_zero_dLdm_outer_BC = .true.
shock_spread_linear = 0.0
shock_spread_quadratic = 1d-2
use_ODE_var_eqn_pairing = .true.
use_dPrad_dm_form_of_T_gradient_eqn = .true.
use_dvdt_form_of_momentum_eqn = .true.
use_ODE_form_of_density_eqn = .true.
okay_to_remesh = .true.
min_dq = 1d-12
max_center_cell_dq = 5e-6
max_allowed_nz = 14000
max_surface_cell_dq = 1d-12
P_function_weight = 40
log_tau_function_weight = 22
log_kap_function_weight = 20
logQ_min_limit = -18d0
newton_iterations_limit = 7
iter_for_resid_tol2 = 4
tol_residual_norm1 = 1d-8
tol_max_residual1 = 1d-7
```



```
fe_core_infall_limit = 1d99
tiny_corr_coeff_limit = 999999
newton_itermin_until_reduce_min_corr_coeff = 999999
```

The values controlling the numerical mesh and function weights are for the y2n21 model; in order to achieve convergent solutions, some models require slightly different settings (e.g., different values for `varcontrol_target`, `log_tau_function_weight`, `min_dq`, and `max_surface_cell_dq`). Typically, each profile has approximately 1000 zones in our simulations.

Appendix B

Thermodynamic relations and superfluid Entrainment

In this Appendix we present the thermodynamic relations for a superfluid NS. In Section [B.1](#) we give the expressions that we use in order to calculate the background quantities (such as density and pressure). In Section [B.2](#) we describe our implementation of the entrainment effect and provide the connection between our notation and that used in previous studies. Lastly, in Section [B.3](#) we estimate the damping rate due to the direct Urca process.

B.1 BACKGROUND QUANTITIES

We model the superfluid neutron star as a zero-temperature system consisting of two fluids: the superfluid neutrons (denoted by subscript n for “neutrons”) and a normal fluid mixture of protons, electrons, and muons whose abundances are linked through charge neutrality (denoted by subscript c for “charged”). According to the thermodynamic identity, the total energy density ε_{tot} satisfies

$$d\varepsilon_{\text{tot}} = \sum_{j=\text{npe}\mu} \mu_j dn_j + \alpha dv_{\text{r}}^2, \quad (\text{B.1})$$

where n_j and μ_j are the number density and chemical potential of particle species j ($=n, p, e, \mu$), $\mathbf{v}_r = \mathbf{v}_c - \mathbf{v}_n$ is the relative velocity between the charged and neutron flows, and α is a function representing the entrainment effect. Since the relative velocity between the two flows is small (and zero for the background model we consider here), we can separate the entrainment part from the bulk motion and write

$$\varepsilon_{\text{tot}} = \varepsilon + \alpha \mathbf{v}_r^2, \quad (\text{B.2})$$

where the bulk energy density ε can be represented as a sum of the baryonic and leptonic contributions

$$\varepsilon = (n_n + n_p) [m_N c^2 + E_{\text{nuc}}(n_n, n_p)] + T_e + T_\mu. \quad (\text{B.3})$$

Here m_N is the nucleon rest mass, E_{nuc} is the interaction energy per baryon given by the nuclear equation of state, and T_e and T_μ are the total energy of the electrons and muons, respectively. We use the SLy4 nuclear equation of state with E_{nuc} given by equation (3.18) in [Chabanat et al. \(1997\)](#). We assume the leptons are described by a zero-temperature, relativistic free Fermi gas with

$$T_e = \frac{3}{4} \hbar c (3\pi^2)^{1/3} (n_e)^{4/3}, \quad (\text{B.4})$$

$$T_\mu = \frac{m_\mu^4 c^5}{\hbar^3} \frac{1}{8\pi^2} \left\{ x (1 + x^2)^{1/2} (1 + 2x^2) - \ln \left[x + (1 + x^2)^{1/2} \right] \right\}, \quad (\text{B.5})$$

where $x = p_F/m_\mu c = \hbar(3n\pi^2 n_\mu)^{1/3}/m_\mu c$. It is worth noting that to fully parameterize the bulk energy density ε of the npe μ NS under the constraint of charge neutrality, we need three independent variables (for example, n_n , n_e and n_μ , with $n_p = n_e + n_\mu$ by charge neutrality; cf. equation B.1). This is fundamentally different from the npe NS (studied by, e.g., [Lee 1995](#), [Andersson & Comer 2001](#) and [Prix & Rieutord 2002](#)), which requires only two independent variables.

The chemical potential for each species is given by

$$\mu_n = m_N c^2 + E_{\text{nuc}} + (n_n + n_p) \frac{\partial E_{\text{nuc}}}{\partial n_n}, \quad (\text{B.6})$$

$$\mu_p = m_N c^2 + E_{\text{nuc}} + (n_n + n_p) \frac{\partial E_{\text{nuc}}}{\partial n_p}, \quad (\text{B.7})$$

$$\mu_e = \hbar c (3\pi^2 n_e)^{1/3}, \quad (\text{B.8})$$

$$\mu_\mu = \sqrt{(m_\mu c^2)^2 + \hbar^2 c^2 (3\pi^2 n_\mu)^{2/3}}, \quad (\text{B.9})$$

where we have assumed $E_{\text{nuc}} = E_{\text{nuc}}(n_n, n_p)$. Note that because $\partial\mu_n/\partial n_p \neq 0$ and $\partial\mu_p/\partial n_n \neq 0$, even if we neglect entrainment (i.e., terms containing α), neutrons and protons are still coupled through the equation of state (see also [Prix & Rieutord 2002](#)).

Although we use Newtonian equations to describe the stellar structure and oscillations, we write the mass density as $\rho = \varepsilon/c^2$ (and not $\rho = (n_n + n_p)m_N$) in order to capture the composition gradients that arise from the nuclear interaction energy E_{nuc} and lepton fraction gradients. If we write the total mass density as the sum of each particle species $\rho = \rho_n + \rho_p + \rho_e + \rho_\mu$, then

$$\rho_n = n_n \left(m_N + \frac{E_{\text{nuc}}}{c^2} \right), \quad (\text{B.10})$$

$$\rho_p = n_p \left(m_N + \frac{E_{\text{nuc}}}{c^2} \right), \quad (\text{B.11})$$

$$\rho_e = \frac{T_e}{c^2}, \quad (\text{B.12})$$

$$\rho_\mu = \frac{T_\mu}{c^2}. \quad (\text{B.13})$$

The generalized pressure function P for a two-fluid problem can be defined through the usual enthalpy density w as

$$\varepsilon + P = w = \sum_{j=npe\mu} \mu_j n_j. \quad (\text{B.14})$$

This gives the differential form

$$dP = \sum_{j=\text{npe}\mu} n_j d\mu_j - \alpha dv_r^2. \quad (\text{B.15})$$

It is convenient to define the specific chemical potential

$$d\tilde{\mu}_j = \frac{d\mu_j}{m_j}, \quad (\text{B.16})$$

where $m_j = \rho_j/n_j$. Note that m_j is not the usual rest mass of particle j (in particular, it is a function of density). Our definition of $d\tilde{\mu}_j$ is slightly different from that used in [Andersson & Comer \(2001\)](#) and [Prix & Rieutord \(2002\)](#) who take $\rho = (n_n + n_p)m_N$ because they do not focus on g modes induced by composition gradients. Nonetheless, if we approximate $d\tilde{\mu}_n$ (which is the only specific chemical potential that explicitly enters our numerical calculations; see appendix [C.1](#)) as $d\mu_n/m_N$, it only changes our results at the few percent level.

In our analytic work, it is also convenient to introduce a chemical potential $\tilde{\mu}_c$ corresponding to the normal fluid component of the fluid and defined such that

$$\rho_c d\tilde{\mu}_c = \rho_p d\tilde{\mu}_p + \rho_e d\tilde{\mu}_e + \rho_\mu d\tilde{\mu}_\mu, \quad (\text{B.17})$$

where $\rho_c = \rho_p + \rho_e + \rho_\mu$. Note that $\tilde{\mu}_c$ is not itself an independent variable, but rather a function $\tilde{\mu}_c = \tilde{\mu}_c(\tilde{\mu}_p, \tilde{\mu}_e, \tilde{\mu}_\mu)$. Moreover, our calculation of the background model and the set of oscillation equations we solve numerically do not depend on $\tilde{\mu}_c$; we explicitly use $\tilde{\mu}_c$ only in Section [C.1](#) when manipulating the set of differential equations defining the linear perturbation operator \mathcal{L} .

Given the definitions above, we have

$$dP = \rho_n d\tilde{\mu}_n + \rho_c d\tilde{\mu}_c - \alpha dv^2. \quad (\text{B.18})$$

In hydrostatic and beta equilibrium, this implies

$$\frac{d\tilde{\mu}_n}{dr} + \frac{d\Phi}{dr} = 0, \quad (\text{B.19})$$

(up to small corrections due to leptonic contribution to the mass density). Note that this relation only holds in the static background and not in an oscillating fluid element.

Furthermore, if we define the deviation from beta equilibrium as

$$d\beta = d\tilde{\mu}_c - d\tilde{\mu}_n, \quad (\text{B.20})$$

then equation B.18 implies (Andersson & Comer, 2001)

$$\frac{1}{\rho} = \left(\frac{\partial \tilde{\mu}_n}{\partial P} \right)_\beta, \quad (\text{B.21})$$

$$\frac{\rho_c}{\rho} = - \left(\frac{\partial \tilde{\mu}_n}{\partial \beta} \right)_P, \quad (\text{B.22})$$

$$\rho^2 \frac{\partial}{\partial P} \left(\frac{\rho_c}{\rho} \right)_\beta = \left(\frac{\partial \rho}{\partial \beta} \right)_P. \quad (\text{B.23})$$

These relations are used in Appendix C.1 when we manipulate the oscillation equations in order to express them in a form convenient for proving the Hermiticity of \mathcal{L} .

B.2 ENTRAINMENT FUNCTION

The entrainment function α accounts for the “drag” between the superfluid neutrons and the protons when they are in relative motion (see equation B.1). Many studies have discussed the entrainment effect in the context of oscillations of superfluid NSs (see, e.g., Lindblom & Mendell 1994, Lee 1995, Andersson & Comer 2001, Prix & Rieutord 2002, Kantor & Gusakov 2014, Passamonti et al. 2016, and Dommes & Gusakov 2016). Most of the discussions originate from the study by Andreev & Bashkin (1976), who parametrize the entrainment effect in terms of the Landau

effective masses of neutrons and protons, m_n^* and m_p^* . However, different authors adopt different notational conventions; the purpose of this appendix is to provide the connection between our notation and that of other studies.

Following [Andersson & Comer \(2001\)](#) and [Prix & Rieutord \(2002\)](#), we parameterize α as

$$2\alpha = \frac{(m_N - m_p^*) \rho_c}{m_N + x_p(m_N - m_p^*)} \quad (\text{B.24})$$

and define the dimensionless entrainment functions

$$\epsilon_n = \frac{2\alpha}{\rho_n}, \quad (\text{B.25})$$

$$\epsilon_c = \frac{2\alpha}{\rho_c} = \frac{\rho_n}{\rho_c} \epsilon_n. \quad (\text{B.26})$$

Typical values of m_p^* are in the range $0.3 \leq m_p^*/m_N \leq 0.8$ ([Sjöberg, 1976](#); [Chamel, 2008](#)); the smaller the m_p^* is the greater α is and the stronger the entrainment effect is.

[Lindblom & Mendell \(1994\)](#) and [Lee \(1995\)](#) describe the entrainment effect through a mass density matrix ρ_{ij} which relates the mass current and the macroscopically averaged velocities ($\mathbf{V}_c, \mathbf{V}_n$):

$$\begin{pmatrix} \rho_c \mathbf{V}_c \\ \rho_n \mathbf{V}_n \end{pmatrix} = \begin{pmatrix} \rho_{cc} & \rho_{cn} \\ \rho_{nc} & \rho_{nn} \end{pmatrix} \begin{pmatrix} \mathbf{V}_c \\ \mathbf{V}_n \end{pmatrix}. \quad (\text{B.27})$$

Note that ($\mathbf{V}_c, \mathbf{V}_n$) are different from the microscopic velocities ($\mathbf{v}_c, \mathbf{v}_n$) we use here, which follow the definitions in [Andersson & Comer \(2001\)](#) and [Prix & Rieutord \(2002](#); see the discussion in Appendix A2 of [Andersson & Comer 2001](#)). The elements of ρ_{ij} satisfy

$$\rho_{cc} + \rho_{cn} = \rho_c, \quad (\text{B.28})$$

$$\rho_{nc} + \rho_{nn} = \rho_n, \quad (\text{B.29})$$

$$\rho_{cn} = \rho_{nc}. \quad (\text{B.30})$$

In terms of m_p^* and m_n^* ([Andreev & Bashkin, 1976](#))

$$\rho_{cc} = \rho_c \frac{m_N}{m_p^*}, \quad (\text{B.31})$$

$$\rho_{nn} = \rho_n \frac{m_N}{m_n^*}, \quad (\text{B.32})$$

$$\rho_{cn} = \rho_c \frac{m_p^* - m_N}{m_p^*} = \rho_n \frac{m_n^* - m_N}{m_n^*}. \quad (\text{B.33})$$

Two useful relations connecting our notation to ρ_{ij} are

$$2\alpha = -\frac{\rho_c \rho_n}{\det \rho} \rho_{cn}, \quad (\text{B.34})$$

$$1 - \epsilon_n - \epsilon_c = \frac{\rho_c \rho_n}{\det \rho}, \quad (\text{B.35})$$

where $\det \rho = \rho_{cc} \rho_{nn} - \rho_{cn}^2$ is the determinant of ρ_{ij} .

[Gusakov et al. \(2014\)](#), [Dommes & Gusakov \(2016\)](#), and [Passamonti et al. \(2016\)](#) take finite-temperature and general-relativistic effects into account. Nonetheless, their notations can be connected to ours in the appropriate zero-temperature, Newtonian limit. In this limit, the y parameter used in [Gusakov et al. \(2014\)](#) and [Dommes & Gusakov \(2016\)](#) is given by

$$y \simeq \frac{1}{x_n} (x_p - \epsilon_n), \quad (\text{B.36})$$

while the entrainment coefficient β_{PAH} defined in [Passamonti et al. \(2016\)](#) is given by

$$\beta_{\text{PAH}} \simeq 1 - \frac{2\alpha}{\rho_n} = 1 - \epsilon_n \quad (\text{B.37})$$

(here we include a “PAH” subscript to distinguish it from the variable β we use elsewhere and define as $d\beta = d\tilde{\mu}_c - d\tilde{\mu}_n$).

B.3 RATE OF DIRECT URCA PROCESS

We show here that the timescale for a resonantly oscillating fluid element to relax toward chemical equilibrium by the Λ -hyperon direct Urca process

$$\Lambda \rightarrow p + L + \bar{\nu}_L, \quad p + L \rightarrow \Lambda + \nu_L, \quad \text{where } L = e, \mu \quad (\text{B.38})$$

is much longer than its oscillation timescale. While the nucleonic direct Urca [equation (B.38) but with n in place of Λ] is also possible in the core (Lattimer et al., 1991), its rate is greatly suppressed because the neutrons are superfluid and the core temperature is well-below the critical temperature for neutron superfluidity (see, e.g., Yakovlev et al. 2001). Previous studies have shown that other damping mechanisms are also slow compared to the oscillation timescales we consider (Reisenegger & Goldreich, 1992, 1994; Lai, 1994). We therefore conclude that the composition of the fluid element is nearly frozen and that the modes can be treated as adiabatic to a good approximation.

Our calculation is similar to one given in Yakovlev et al. (2001; Section 3.5). We focus on the reaction with $L = e$; the reaction with $L = \mu$ occurs at a similar rate (Prakash et al., 1992). Note that while our calculation should hold for an NS with $np\Lambda e\mu$ composition, as is the case for the models we consider, for more massive NSs or NSs with different equation of state that also host other hyperon species, non-Urca weak interactions like $n + \Lambda \rightleftharpoons p + \Sigma^-$ can have a much higher reaction rate than direct Urca processes and might therefore modify the calculation (Yakovlev et al., 2001).

We first define the chemical equilibrium parameter $\beta_\Lambda = \mu_\Lambda - \mu_p - \mu_e$ and the deviation from equilibrium relative to the background temperature

$$\eta = \frac{\delta\beta_\Lambda}{kT}, \quad (\text{B.39})$$

where $\delta\beta_\Lambda = \beta_\Lambda(P, \mu_n, x_{\mu e}, x_{\Lambda e})$. Although we are interested in the disequilibrium of a perturbed fluid element, and thus the Lagrangian perturbation $\Delta\beta_\Lambda$, since the

background is in chemical equilibrium $\beta_\Lambda = 0$ and therefore to linear order $\delta\beta_\Lambda = \Delta\beta_\Lambda$.

The timescale to relax toward chemical equilibrium is

$$\tau_{\text{urca}} \approx \frac{\eta}{\dot{\eta}}. \quad (\text{B.40})$$

To proceed, we estimate τ_{urca} in an iterative manner. First, we obtain a zeroth order solution by assuming the composition is frozen and thus $\Delta x_{\Lambda e} = 0$ (and also $\Delta x_{\mu e} = 0$). We then use this solution to evaluate η and τ_{urca} . As long as the resulting reaction timescale is much longer than the oscillation timescale, our approach is self-consistent. This approach implies

$$\eta \approx \frac{1}{kT} \left(\frac{\partial \beta_\Lambda}{\partial x_{\Lambda e}} \right) \delta x_{\Lambda e} = -\frac{b_a}{kT} \left(\frac{\partial \beta_\Lambda}{\partial x_{\Lambda e}} \right) \frac{dx_{\Lambda e}}{dr} \xi_c^r, \quad (\text{B.41})$$

where b_a is the amplitude of the resonantly driven mode. The first equality follows because P and μ_n adjust to the background values on very short timescales, and $x_{\mu e}$ is nearly constant in the inner core (cf. Figure 4-1). The second equality follows because in our zeroth order solution $\Delta x_{\Lambda e} = 0$. In order to calculate ξ_c^r and b_a , we use the numerical solution for the $n_a^{(\Lambda 1.6)} = 1$ mode, which has a post-resonance amplitude $b_a \simeq 1 \times 10^{-3}$. We find that $\delta\beta_\Lambda \sim 2 \text{ MeV} \gg kT$ for the largest perturbations and therefore for a cold NS we are in the limit $\eta \gg 1$.

Due to the Urca process, the deviation from chemical equilibrium changes at a rate

$$\dot{\eta} \approx \frac{1}{kT} \left(\frac{\partial \beta_\Lambda}{\partial x_{\Lambda e}} \right) \dot{x}_{\Lambda e}, \quad (\text{B.42})$$

with

$$\dot{x}_{\Lambda e} = \frac{n_e \dot{n}_\Lambda - n_\Lambda \dot{n}_e}{n_e^2} = \frac{(1 + x_{\Lambda e})}{n_e} \dot{n}_\Lambda = -\frac{(1 + x_{\Lambda e})}{n_e} \delta\Gamma. \quad (\text{B.43})$$

The net reaction rate per unit volume

$$\begin{aligned}\delta\Gamma &= \Gamma(\Lambda \rightarrow \text{p} + \text{e}^- + \bar{\nu}_e) - \Gamma(\text{p} + \text{e}^- \rightarrow \Lambda + \nu_e) \\ &= q \frac{\epsilon}{kT} H(\eta) \eta\end{aligned}\tag{B.44}$$

[equations (144)-(147) in [Yakovlev et al. 2001](#)]. Here ϵ is the equilibrium neutrino emissivity [eq. (124) and Table 4 in [Yakovlev et al. 2001](#); we use the rest masses rather than the effective masses, which is sufficiently accurate here] and is given by

$$\epsilon = 1.6 \times 10^{26} \left(\frac{n_e}{0.16 \text{ fm}^{-3}} \right) \left(\frac{m_\Lambda}{m_N} \right) \left(\frac{T}{10^9 \text{ K}} \right)^6 \text{ erg cm}^{-3} \text{ s}^{-1}.\tag{B.45}$$

Although we calculate ϵ based on the hyperonic direct Urca process, we use the nucleon direct Urca values (assuming normal fluid nucleons) for the numerical prefactor $q = 0.158$ and for the function

$$H(\eta) = 1 + \frac{10\eta^2}{17\pi^2} + \frac{\eta^4}{17\pi^4} \simeq \frac{\eta^4}{17\pi^4}.\tag{B.46}$$

The hyperon process should yield very similar values for q and $H(\eta)$ [cf. Section 3.3 and equations (112)-(117) in [Yakovlev et al. 2001](#); the energy integral I is the same for all direct Urca processes and the angular integrals A are similar].

Since the threshold of the hyperon direct Urca process is expected to nearly coincide with the threshold for the creation of hyperons ([Prakash et al., 1992](#)), we assume that equation (B.44) applies for $r \leq R_\Lambda$. We thereby find

$$\begin{aligned}\tau_{\text{urca}}^{-1} &\approx q \left(\frac{\partial\beta_\Lambda}{\partial x_{\Lambda\text{e}}} \right) \left(\frac{1 + x_{\Lambda\text{e}}}{n_e} \right) \frac{\epsilon}{(kT)^2} H(\eta) \\ &\approx 1.5 \times 10^{-2} \left(\frac{\delta\beta_\Lambda}{1 \text{ MeV}} \right)^4 \text{ s}^{-1}.\end{aligned}\tag{B.47}$$

Although both $x_{\Lambda\text{e}}$ and $(\partial\beta_\Lambda/\partial x_{\Lambda\text{e}})$ depend on density ρ , to obtain the numerical result on the second line we treated them as constant since ρ varies slowly in the inner core. Note that τ_{urca}^{-1} is independent of temperature in the limit $\eta \gg 1$.

Since τ_{urca}^{-1} is much smaller than the oscillation frequency of the g-modes, we conclude that we can safely neglect the hyperonic direct Urca process and adopt the frozen composition approximation.

Appendix C

Superfluid oscillation equations and hermiticity of the linear operator

In this Appendix we describe the superfluid oscillation equations in further detail. In Section C.1 we present the form of the Newtonian oscillation equations that we use in our numerical calculations and in Section C.2 we describe the boundary conditions that we assume. Our mode decomposition (eq. 3.36) relies on the linear operator \mathcal{L} of the oscillation equations being Hermitian, which we prove in Appendix C.3.

C.1 OSCILLATION EQUATIONS

As we are considering a two-fluid problem, we need to consider the continuity and momentum conservation of both the charged flow and the neutron flow, which are given respectively by (Prix & Rieutord, 2002)

$$\partial_t \rho_c + \nabla \cdot (\rho_c \mathbf{v}_c) = 0, \quad (\text{C.1})$$

$$\partial_t \rho_n + \nabla \cdot (\rho_n \mathbf{v}_n) = 0, \quad (\text{C.2})$$

$$(\partial_t + \mathbf{v}_c \cdot \nabla) (\mathbf{v}_c - \epsilon_c \mathbf{v}_r) - \epsilon_c \nabla_{r,i} \nabla v_c^i = -\nabla (\tilde{\mu}_c + \Phi), \quad (\text{C.3})$$

$$(\partial_t + \mathbf{v}_n \cdot \nabla) (\mathbf{v}_n + \epsilon_n \mathbf{v}_r) + \epsilon_n \nabla_{r,i} \nabla v_n^i = -\nabla (\tilde{\mu}_n + \Phi). \quad (\text{C.4})$$

The set of equations is closed by the Poisson equation

$$\nabla^2 \Phi = 4\pi G(\rho_c + \rho_n). \quad (\text{C.5})$$

We use δ to denote Eulerian perturbations and assume all perturbed quantities have an $e^{i\sigma t}$ time dependence. The Lagrangian displacements of the charged and neutron flows are thus given by

$$\partial_t \boldsymbol{\xi}_c = i\sigma \boldsymbol{\xi}_c = \delta \mathbf{v}_c, \quad (\text{C.6})$$

$$\partial_t \boldsymbol{\xi}_n = i\sigma \boldsymbol{\xi}_n = \delta \mathbf{v}_n. \quad (\text{C.7})$$

We further simplify the equations by assuming a spherical, hydrostatic background star and separating the variables into radial and angular functions using the standard spherical harmonic decomposition [equations (3.21) and (3.22)]. The linearized equations then reduce to a set of coupled ordinary differential equations in the radial direction

$$\frac{1}{r^2} \frac{d}{dr} (r^2 \xi_c^r) + \frac{d \ln \rho_c}{dr} \xi_c^r - l(l+1) \frac{\xi_c^h}{r} + \frac{\delta \rho_c}{\rho_c} = 0, \quad (\text{C.8})$$

$$\frac{1}{r^2} \frac{d}{dr} (r^2 \xi_n^r) + \frac{d \ln \rho_n}{dr} \xi_n^r - l(l+1) \frac{\xi_n^h}{r} + \frac{\delta \rho_n}{\rho_n} = 0, \quad (\text{C.9})$$

$$\sigma^2 [\xi_c^r - \epsilon_c (\xi_c^r - \xi_n^r)] = \frac{d}{dr} (\delta \tilde{\mu}_c + \delta \Phi), \quad (\text{C.10})$$

$$\sigma^2 [\xi_n^r + \epsilon_n (\xi_c^r - \xi_n^r)] = \frac{d}{dr} (\delta \tilde{\mu}_n + \delta \Phi), \quad (\text{C.11})$$

$$\sigma^2 [\xi_c^h - \epsilon_c (\xi_c^h - \xi_n^h)] = \frac{1}{r} (\delta \tilde{\mu}_c + \delta \Phi), \quad (\text{C.12})$$

$$\sigma^2 [\xi_n^h + \epsilon_n (\xi_c^h - \xi_n^h)] = \frac{1}{r} (\delta \tilde{\mu}_n + \delta \Phi), \quad (\text{C.13})$$

$$\frac{1}{r^2} \frac{d}{dr} \left(r^2 \frac{d\delta\Phi}{dr} \right) - \frac{l(l+1)}{r^2} \delta\Phi = 4\pi G (\delta\rho_c + \delta\rho_n). \quad (\text{C.14})$$

Since we have factored out the time-dependency by assuming perturbations vary as $e^{i\sigma t}$, we can write $\partial/\partial t$ as d/dr .

For numerical reasons, it is convenient to define a ‘mass-averaged’ flow

$$\boldsymbol{\xi}_+ = \frac{1}{\rho} (\rho_c \boldsymbol{\xi}_c + \rho_n \boldsymbol{\xi}_n). \quad (\text{C.15})$$

The corresponding continuity and momentum conservation equations are then

$$\frac{d\xi_+^r}{dr} + \left(\frac{2}{r} + \frac{d \ln \rho}{dr} \right) \xi_+^r - l(l+1) \frac{\xi_+^h}{r} + \frac{\delta \rho}{\rho} = 0, \quad (\text{C.16})$$

$$\sigma^2 \xi_+^r = \frac{1}{\rho} \frac{d\delta P}{dr} + g \frac{\delta \rho}{\rho} + \frac{d\delta \Phi}{dr}, \quad (\text{C.17})$$

$$\sigma^2 \xi_+^h = \frac{1}{r} \left(\frac{\delta P}{\rho} + \delta \Phi \right), \quad (\text{C.18})$$

where by equation (B.18)

$$\delta P = \rho_n \delta \tilde{\mu}_n + \rho_c \delta \tilde{\mu}_c. \quad (\text{C.19})$$

Summarizing, the set of oscillation equations we use to find numerical solutions are equations (C.9, C.11, C.13, C.14, C.16, C.17, C.18) and our independent variables are $(\xi_n^r, \xi_n^h, \xi_+^r, \xi_+^h, \delta P, \delta \tilde{\mu}_n, \delta \Phi)$. Following Kantor & Gusakov (2014) and Passamonti et al. (2016), we use $(P, \tilde{\mu}_n, x_{\mu e})$ to parametrize the equation of state in the perturbed superfluid NS. For dependent variables $\delta \rho$ and $\delta \rho_n$ appearing in the equations, we project them onto the independent ones through the Jacobian

$$\begin{aligned} \delta \rho &= \left(\frac{\partial \rho}{\partial P} \right)_{\tilde{\mu}_n, x_{\mu e}} \delta P + \left(\frac{\partial \rho}{\partial \tilde{\mu}_n} \right)_{P, x_{\mu e}} \delta \tilde{\mu}_n + \left(\frac{\partial \rho}{\partial x_{\mu e}} \right)_{P, \tilde{\mu}_n} \delta x_{\mu e}, \\ &= \left(\frac{\partial \rho}{\partial P} \right)_{\tilde{\mu}_n, x_{\mu e}} \delta P + \left(\frac{\partial \rho}{\partial \tilde{\mu}_n} \right)_{P, x_{\mu e}} \delta \tilde{\mu}_n - \left(\frac{\partial \rho}{\partial x_{\mu e}} \right)_{P, \tilde{\mu}_n} \frac{dx_{\mu e}}{dr} \xi_c^r, \end{aligned} \quad (\text{C.20})$$

where in the second line we use the fact that the Lagrangian perturbation $\Delta x_{\mu e}$ vanishes because electrons and muons move at the same speed in the charged flow and therefore

$$\Delta x_{\mu e} = \delta x_{\mu e} + \frac{dx_{\mu e}}{dr} \xi_c^r = 0. \quad (\text{C.21})$$

We compute $\delta \rho_n$ through a similar expansion. Finally, the $\boldsymbol{\xi}_c$ terms are expressed in terms of $(\boldsymbol{\xi}_+, \boldsymbol{\xi}_n)$ via equation (C.15).

In addition to ξ_+ , in the main text we also introduce the displacement

$$\xi_- = (1 - \epsilon_n - \epsilon_c)(\xi_c - \xi_n) = \frac{\rho_c \rho_n}{\det \rho} (\xi_c - \xi_n), \quad (\text{C.22})$$

which represents the difference between the normal fluid flow and the superfluid flow. Although we do not use ξ_- when numerically solving the oscillation equations, it is useful for proving the Hermiticity of the linear perturbation operator \mathcal{L} (Appendix C.3). Using (ξ_+, ξ_-) and defining $\delta\beta = \delta\tilde{\mu}_c - \delta\tilde{\mu}_n$, we can recast the oscillation equations as (see Lindblom & Mendell 1994, Andersson & Comer 2001, and equations B.21-B.23)

$$\delta\rho + \nabla \cdot (\rho \xi_+) = 0, \quad (\text{C.23})$$

$$\begin{aligned} & \left(\frac{\partial \rho}{\partial \beta} \right)_P \left(\frac{\delta P}{\rho} \right) + \frac{\rho_n^2}{\rho} \frac{\partial}{\partial \beta} \left(\frac{\rho_c}{\rho_n} \right)_P \delta\beta \\ & + \frac{1}{\rho} \left(\frac{\partial \rho}{\partial \beta} \right)_P \xi_+ \cdot \nabla P + \nabla \cdot (\tilde{\rho} \xi_-) = 0, \end{aligned} \quad (\text{C.24})$$

$$\frac{\partial^2 \xi_+}{\partial t^2} = -\nabla \left(\frac{\delta P}{\rho} + \delta\Phi \right) + \frac{\nabla P}{\rho^2} \left(\frac{\partial \rho}{\partial \beta} \right)_P \delta\beta, \quad (\text{C.25})$$

$$\frac{\partial^2 \xi_-}{\partial t^2} = -\nabla \delta\beta, \quad (\text{C.26})$$

where

$$\tilde{\rho} = \frac{\det \rho}{\rho} = \frac{\rho_c \rho_n}{(1 - \epsilon_n - \epsilon_c)\rho}. \quad (\text{C.27})$$

Writing the oscillation equations in this form simplifies the proof of the Hermiticity of \mathcal{L} given in Appendix C.3. Note that here we choose (P, β) to be the independent variables in our parameterization of the equation of state, and we use the relation

$$\delta\rho = \left(\frac{\partial \rho}{\partial P} \right)_\beta \delta P + \left(\frac{\partial \rho}{\partial \beta} \right)_P \delta\beta. \quad (\text{C.28})$$

As we discuss in Appendix B.1, there are three independent variables when we parameterize an equation of state including muons. Indeed, $\delta\beta$ is a function of two independent variables since $\delta\beta = \delta\tilde{\mu}_c - \delta\tilde{\mu}_n$ and $\tilde{\mu}_c$ is a function of two independent variables [cf. equation (B.17); note that charge neutrality decreases the number of

degrees of freedom by one].

C.2 BOUNDARY CONDITIONS

The oscillation equations can be solved numerically when boundary conditions are specified. Here we focus on the set of equations described by the averaged flow (ξ_+) and the superfluid neutron flow (ξ_n), as they form the set of equations we solve numerically in practice. Other combination can be derived accordingly.

At the center ($r = 0$) we apply the usual regularity condition

$$\xi_+^r = \xi_{0+}^r \frac{l}{\sigma^2} r^{l-1}, \quad (\text{C.29})$$

$$\xi_+^h = \xi_{0+}^h \frac{1}{\sigma^2} r^{l-1}, \quad (\text{C.30})$$

$$\xi_n^r = \xi_{0n}^r \frac{l}{\sigma^2} r^{l-1}, \quad (\text{C.31})$$

$$\xi_n^h = \xi_{0n}^h \frac{1}{\sigma^2} r^{l-1}, \quad (\text{C.32})$$

$$\delta P = \delta P_0 r^l, \quad (\text{C.33})$$

$$\delta \tilde{\mu}_n = \delta \tilde{\mu}_{n0} r^l, \quad (\text{C.34})$$

$$\delta \Phi = \delta \Phi_0 r^l, \quad (\text{C.35})$$

where

$$\xi_{0+}^r = \xi_{0+}^h, \quad (\text{C.36})$$

$$\xi_{0n}^r = \xi_{0n}^h, \quad (\text{C.37})$$

$$\xi_{0+}^r = \frac{\delta P_0}{\rho} + \delta \Phi_0, \quad (\text{C.38})$$

$$\left[\left(1 - \epsilon_n \frac{\rho}{\rho - \rho_n} \right) \xi_{0n}^r + \epsilon_n \frac{\rho}{\rho - \rho_n} \xi_{0+}^r \right] = \delta \tilde{\mu}_n + \delta \Phi_0, \quad (\text{C.39})$$

and all the background quantities are evaluated at $r = 0$.

At the core -crust interface ($r = R_{\text{cc}}$), we assume that the fluid becomes a normal fluid whose oscillation equations are identical to those of the averaged flow [equations

C.16 - C.18], but setting $\xi_+ \rightarrow \xi_{\text{NF}}$, where ξ_{NF} denotes the Lagrangian perturbation of normal fluid in the crust. Continuity across the interface (from R_{cc}^- to R_{cc}^+) then requires

$$\xi_+^r(R_{\text{cc}}^-) = \xi_{\text{n}}^r(R_{\text{cc}}^-) = \xi_{\text{NF}}^r(R_{\text{cc}}^+), \quad (\text{C.40})$$

$$\xi_+^h(R_{\text{cc}}^-) = \xi_{\text{n}}^h(R_{\text{cc}}^-) = \xi_{\text{NF}}^h(R_{\text{cc}}^+), \quad (\text{C.41})$$

$$\delta P(R_{\text{cc}}^-) = \delta P(R_{\text{cc}}^+), \quad (\text{C.42})$$

$$\delta \Phi(R_{\text{cc}}^-) = \delta \Phi(R_{\text{cc}}^+), \quad (\text{C.43})$$

$$\frac{d}{dr} \delta \Phi(R_{\text{cc}}^-) = \frac{d}{dr} \delta \Phi(R_{\text{cc}}^+). \quad (\text{C.44})$$

Finally at the surface ($r = R$), we require the Lagrangian perturbation of the pressure ΔP to vanish and the gravitational potential to be continuous, which gives (see, e.g., [Prix & Rieutord 2002](#))

$$\Delta P = \delta P - \rho g \xi_{\text{NF}}^r = 0, \quad (\text{C.45})$$

$$\frac{d\delta \Phi}{dr} + \frac{l+1}{r} \delta \Phi + 4\pi G \rho \xi_{\text{NF}}^r = 0. \quad (\text{C.46})$$

C.3 HERMITICITY OF THE LINEAR PERTURBATION OPERATOR

In this section we prove that the linear perturbation operator \mathcal{L} is Hermitian (see also [Lindblom & Mendell 1994](#); [Andersson et al. 2004](#)). Let (ξ_+, ξ_-) and (ξ'_+, ξ'_-) denote two independent perturbations. We want to show that

$$\left\langle \begin{bmatrix} \xi_+ \\ \xi_- \end{bmatrix}, \mathcal{L} \begin{bmatrix} \xi'_+ \\ \xi'_- \end{bmatrix} \right\rangle = \left\langle \mathcal{L} \begin{bmatrix} \xi_+ \\ \xi_- \end{bmatrix}, \begin{bmatrix} \xi'_+ \\ \xi'_- \end{bmatrix} \right\rangle \quad (\text{C.47})$$

i.e., by equation (3.29),

$$\begin{aligned} & \int d^3x [\rho \boldsymbol{\xi}_+^* \cdot \mathcal{L}(\boldsymbol{\xi}'_+) + \tilde{\rho} \boldsymbol{\xi}_-^* \cdot \mathcal{L}(\boldsymbol{\xi}'_-)] \\ &= \int d^3x [\rho \{\mathcal{L}(\boldsymbol{\xi}_+)\}^* \cdot \boldsymbol{\xi}'_+ + \tilde{\rho} \{\mathcal{L}(\boldsymbol{\xi}_-)\}^* \cdot \boldsymbol{\xi}'_-] \end{aligned} \quad (\text{C.48})$$

where $\mathcal{L}(\boldsymbol{\xi}_+)$ and $\mathcal{L}(\boldsymbol{\xi}_-)$ are given by the right hand sides of equations (C.25) and (C.26), respectively. Using equations (C.23)-(C.26) and defining

$$\delta W = \frac{\delta P}{\rho} + \delta \Phi, \quad (\text{C.49})$$

we have

$$\begin{aligned} & \int d^3x \rho \boldsymbol{\xi}_+^* \cdot \mathcal{L}(\boldsymbol{\xi}'_+) \\ &= \int d^3x \rho \boldsymbol{\xi}_+^* \cdot \left[-\boldsymbol{\nabla} \delta W' + \frac{\boldsymbol{\nabla} P}{\rho^2} \left(\frac{\partial \rho}{\partial \beta} \right)_P \delta \beta' \right] \\ &= \int d^3x \left[\boldsymbol{\nabla} \cdot (\rho \boldsymbol{\xi}_+^*) \delta W' + \frac{\delta \beta'}{\rho} \left(\frac{\partial \rho}{\partial \beta} \right)_P \boldsymbol{\xi}_+^* \cdot \boldsymbol{\nabla} P \right] \\ &= \int d^3x \left[-\delta \rho^* \delta W' + \frac{\delta \beta'}{\rho} \left(\frac{\partial \rho}{\partial \beta} \right)_P \boldsymbol{\xi}_+^* \cdot \boldsymbol{\nabla} P \right], \end{aligned} \quad (\text{C.50})$$

and

$$\begin{aligned} & \int d^3x \tilde{\rho} \boldsymbol{\xi}_-^* \cdot \mathcal{L}(\boldsymbol{\xi}'_-) = - \int d^3x \tilde{\rho} \boldsymbol{\xi}_-^* \cdot \boldsymbol{\nabla} \delta \beta' \\ &= \int d^3x \boldsymbol{\nabla} \cdot (\tilde{\rho} \boldsymbol{\xi}_-^*) \delta \beta' \\ &= - \int d^3x \left[\left(\frac{\partial \rho}{\partial \beta} \right)_P \left(\frac{\delta P^*}{\rho} \right) + \frac{\rho_n^2}{\rho} \frac{\partial}{\partial \beta} \left(\frac{\rho_c}{\rho_n} \right)_P \delta \beta^* \right. \\ &\quad \left. + \frac{1}{\rho} \left(\frac{\partial \rho}{\partial \beta} \right)_P \boldsymbol{\xi}_+^* \cdot \boldsymbol{\nabla} P \right] \delta \beta', \end{aligned} \quad (\text{C.51})$$

where we have integrated by parts (the surface terms can be shown to vanish by the continuity relation at the core-crust interface and the assumption of vanishing surface

density). Adding the two equations together and using equation (C.28) we find

$$\begin{aligned}
& \int d^3x [\rho \xi_+^* \cdot \mathcal{L}(\xi'_+) + \tilde{\rho} \xi_-^* \cdot \mathcal{L}(\xi'_-)] \\
&= - \int d^3x \left[\left(\frac{\partial \rho}{\partial \beta} \right)_P \delta \beta^* + \left(\frac{\partial \rho}{\partial P} \right)_\beta \delta P^* \right] \delta W' \\
&\quad - \int d^3x \left[\left(\frac{\partial \rho}{\partial \beta} \right)_P \left(\frac{\delta P^*}{\rho} \right) + \frac{\rho_n^2}{\rho} \frac{\partial}{\partial \beta} \left(\frac{\rho_c}{\rho_n} \right)_\beta \delta \beta^* \right] \delta \beta' \\
&= - \int d^3x \left\{ \left(\frac{\partial \rho}{\partial \beta} \right)_P [\delta \beta^* \delta W' + \delta \beta' \delta W^*] + \rho \left(\frac{\partial \rho}{\partial P} \right)_\beta \delta W^* \delta W' \right. \\
&\quad \left. + \frac{\rho_n^2}{\rho} \frac{\partial}{\partial \beta} \left(\frac{\rho_c}{\rho_n} \right)_P \delta \beta^* \delta \beta' - \rho \left(\frac{\partial \rho}{\partial P} \right)_\beta \delta \Phi^* \delta \Phi' \right\} \\
&\quad + \int d^3x \delta \Phi^* \left[\left(\frac{\partial \rho}{\partial P} \right)_\beta \delta P' + \left(\frac{\partial \rho}{\partial \beta} \right)_P \delta \beta' \right]. \tag{C.52}
\end{aligned}$$

The last term can be rewritten using equations (C.28) and (C.14), which give

$$\left(\frac{\partial \rho}{\partial P} \right)_\beta \delta P' + \left(\frac{\partial \rho}{\partial \beta} \right)_P \delta \beta' = \delta \rho' = \frac{\nabla^2 \delta \Phi'}{4\pi G}, \tag{C.53}$$

and noting that

$$\int d^3x \delta \Phi^* \nabla^2 \delta \Phi' = - \int d^3x \nabla \delta \Phi^* \cdot \nabla \delta \Phi', \tag{C.54}$$

where the surface term vanishes. We thus prove that all the terms are symmetric under the exchange of $(\delta W^*, \delta \beta^*, \delta \Phi^*)$ and $(\delta W', \delta \beta', \delta \Phi')$, demonstrating that \mathcal{L} is an Hermitian operator.

C.4 NUMERICAL ACCURACY OF TIDAL COUPLING COEFFICIENT CALCULATION

The oscillatory nature of the g-modes makes the calculation of the tidal coupling coefficient Q_{alm} subject to numerical error (Reisenegger, 1994; Reisenegger & Goldreich, 1994; Weinberg et al., 2012). We validated the accuracy of our calculations by

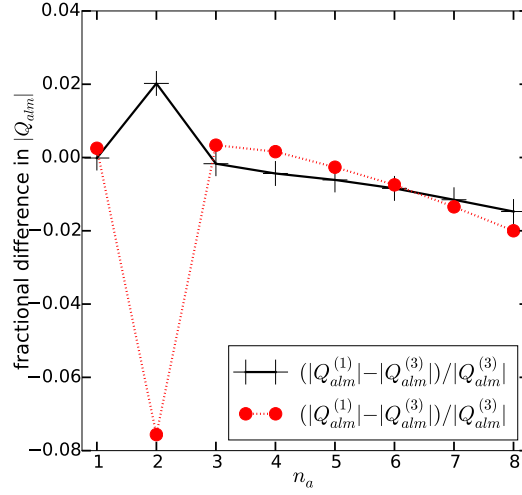


Figure C-1: Fractional difference between the three different methods of calculating $|Q_{alm}|$ (see text for details). The black solid lines are $|Q_{alm}^{(1)} - Q_{alm}^{(3)}|/|Q_{alm}^{(3)}|$ and the red dotted lines are $|Q_{alm}^{(2)} - Q_{alm}^{(3)}|/|Q_{alm}^{(3)}|$.

evaluating Q_{alm} in three different ways as given by equations (4.19) and (3.41):

$$Q_{alm}^{(1)} = \frac{1}{MR^l} \int dr l \rho r^{l+1} [\xi_{a+}^r + (l+1)\xi_{a+}^h], \quad (\text{C.55})$$

$$Q_{alm}^{(2)} = \frac{1}{MR^l} \int dr r^{l+2} \delta \rho_a, \quad (\text{C.56})$$

$$Q_{alm}^{(3)} = -\frac{2l+1}{4\pi} \frac{\delta \Phi_a(R)}{GM/R}. \quad (\text{C.57})$$

Although in the main text we give values based on $Q_{alm}^{(3)}$, we find that all three methods agree very well. For example, in Figure C-1 we show the fractional differences $|Q_{alm}^{(1)} - Q_{alm}^{(3)}|/|Q_{alm}^{(3)}|$ and $|Q_{alm}^{(2)} - Q_{alm}^{(3)}|/|Q_{alm}^{(3)}|$ for the superfluid NS model with $(M/M_\odot, m_p^*/m_N) = (1.4, 0.8)$. The differences are at the ~ 1 per cent level.

Appendix D

Phase shift

In this Appendix we derive the phase $\Psi(f)$ of the frequency-domain waveform $\tilde{h}(f) \propto \exp[i\Psi(f)]$ due to the resonant excitation of a single mode with eigenfrequency f_a . Following [Flanagan & Racine \(2007\)](#); see also [Reisenegger & Goldreich 1994](#)), the resonance induces a sudden perturbation $\delta\dot{f}$ to the rate of frequency evolution relative to the point particle model

$$\dot{f}(f) = \dot{f}_{\text{pp}}(f) + \delta\dot{f}(f). \quad (\text{D.1})$$

The time taken by the binary to evolve to some frequency f after the resonance is, to linear order in $\delta\dot{f}$,

$$t(f) = \int_0^f \frac{df}{\dot{f}} \simeq \int_0^f \frac{1}{\dot{f}_{\text{pp}}} \left(1 - \frac{\delta\dot{f}}{\dot{f}_{\text{pp}}} \right) df = t_{\text{pp}}(f) - \delta t_a, \quad (\text{D.2})$$

where $\delta t_a = -\delta\phi_a/2\pi f_a$ (see Section IV of [Flanagan & Racine 2007](#); note that their sign convention for $\delta\phi_a$ is opposite ours). Here we ignore the bandwidth of the resonance and treat the perturbation $\delta\dot{f}$ proportional to a delta function at $f = f_a$ since the duration of the resonance is much shorter than the orbital decay time scale (their ratio $\simeq 0.1 \times [(\mathcal{M}/1.2M_\odot)(f_a/500 \text{ Hz})]^{5/6}$; [Lai 1994](#)). Since $\delta\phi_a < 0$, the mode resonance speeds up the inspiral and it takes slightly less time to reach a given

post-resonance f . After the resonance, the phase

$$\frac{\phi[t(f)]}{2\pi} = \int_0^{t(f)} f(t') dt' \simeq \int_0^f \left[\frac{f'}{\dot{f}_{\text{pp}}} - \frac{f' \delta \dot{f}}{\dot{f}_{\text{pp}}^2} \right] df' = \frac{\phi_{\text{pp}}(f) + \delta \phi_a}{2\pi}. \quad (\text{D.3})$$

The phase of the frequency domain waveform post-resonance is therefore

$$\Psi(f) = 2\pi f t(f) - \phi[t(f)] - \frac{\pi}{4} = \Psi_{\text{pp}}(f) - \left(1 - \frac{f}{f_a}\right) \delta \phi_a, \quad (\text{D.4})$$

where the first equality comes from the stationary phase approximation and $\Psi_{\text{pp}} = 2\pi f t_{\text{pp}}(f) - \phi_{\text{pp}}(f) - \pi/4$ is given by equation (4.33). If we had chosen the parameters so that the perturbed and unperturbed waveforms coincide after the resonance rather than before the resonance then the $(1 - f/f_a)$ factor would have the opposite sign. For the small $\delta \phi_a$ due to g-mode resonances, we find that both choices give nearly identical rms errors $\Delta(\delta \phi_a)$ and Δf_a due to the covariance with t_c and ϕ_c .

Appendix E

More on Gaussian beams

The Gaussian beam inside a cavity is fully specified given the g-factors. Consider a simple Fabry-Perot cavity formed with an input mirror and an end mirror. If we choose the location of the waist to be at $z = 0$, then the input and end mirror's locations are respectively given by

$$z_i = -L \frac{g_e(1 - g_i)}{g_i(1 - g_e) + g_e(1 - g_i)}, \quad (\text{E.1a})$$

$$z_e = L \frac{g_i(1 - g_e)}{g_i(1 - g_e) + g_e(1 - g_i)}, \quad (\text{E.1b})$$

and the waist size w_0

$$w_0^2 = \frac{L\lambda_0}{\pi} \sqrt{\frac{g_i g_e (1 - g_i g_e)}{(g_i + g_e - 2g_i g_e)^2}}. \quad (\text{E.2})$$

Once the waist is specified, we can write the spot size at any location inside the cavity as

$$w(z) = w_0 \sqrt{1 + \left(\frac{z}{z_0}\right)^2}, \quad (\text{E.3})$$

where $z_0 = \pi w_0^2 / \lambda_0$ is the Rayleigh range. For $|z| < z_0$ it is known as the near field of the beam with the spot size $w(z) \simeq w_0$ stays approximately a constant, and for $|z| > z_0$ it corresponds to the far field where the spot size diverges as $w(z) \simeq w_0 z / z_0 = \theta_0 z$, with $\theta_0 = w_0 / z_0$ the diffraction angle. The distinction between the near and far fields can also be characterized in terms of the Gouy phase $\eta(z) = \arctan(z/z_0)$, with

$|\eta(z)| < \pi/4$ for the near field and $\pi/4 < |\eta(z)| < \pi/2$ for the far field.

Similarly the radius of curvature of the wavefront is given by

$$\text{RoC}(z) = \frac{z^2 + z_0^2}{z}. \quad (\text{E.4})$$

Note that $\text{RoC}[z_{i(e)}] = \text{RoC}_{i(e)}$.

The spatial dependence of a Gaussian beam is thus given by Hermite-Gauss function¹

$$\begin{aligned} u_m(x, z) = & \left(\frac{2}{\pi}\right)^{1/4} \left(\frac{1}{2^m m! w(z)}\right)^{1/2} H_m\left(\frac{\sqrt{2}x}{w(z)}\right) \\ & \times \exp\left[-x^2 \left(\frac{1}{w^2(z)} + \frac{i\pi}{\lambda_0 R(z)}\right) + i\left(m + \frac{1}{2}\right)\eta(z)\right], \end{aligned} \quad (\text{E.5})$$

where H_m is the Hermite polynomial; the lowest-order terms are given by $H_0(x) = 1, H_1(x) = 2x, H_2(x) = 4x^2 - 2$. Note that the spot size and radius of curvature characterize the real and imaginary parts of the wavefront, respectively.

A set of Hermite-Gaussian modes can be conveniently described in terms of the Gaussian beam parameter q , defined as

$$\frac{1}{q(z)} = \frac{1}{\text{RoC}(z)} - i \frac{\lambda_0}{\pi w^2(z)}. \quad (\text{E.6})$$

The spot size and radius of curvature can now be written in terms of q as

$$w^2(z) = \frac{\lambda_0}{\pi} \frac{|q|^2}{\text{Im}(q)}, \quad (\text{E.7a})$$

$$\text{RoC}(z) = \frac{|q|^2}{\text{Re}(q)}. \quad (\text{E.7b})$$

The propagation of the Gaussian parameter q is given by the *ABCD* formalism (Siegman, 1986). Suppose a beam initially with q_1 propagates through an optical

¹Here we included the Gouy phase term in $u_m(x, z)$. Note, however, that in Section 6.1 we typically let the mode amplitude a_m to absorb the Gouy phase.

component M , the resultant Gaussian parameter q_2 is given by

$$\frac{q_2}{n_2} = \frac{Aq_1/n_1 + B}{Cq_1/n_1 + D}, \quad (\text{E.8})$$

with $n_{1(2)}$ the refractive index at the initial (final) point. The optical component M can thus be associated with an coefficient matrix

$$M = \begin{bmatrix} A & B \\ C & D \end{bmatrix}. \quad (\text{E.9})$$

It is easy to show that the $ABCD$ formalism is associative. A beam consecutively passing through two optical components with coefficient matrices M_1 and M_2 can be equivalent modeled as it passing through a single component with coefficient M_2M_1 .

Some commonly used $ABCD$ matrices

$$M^{(\text{refl})} = \begin{bmatrix} 1 & 0 \\ -2n_1/\text{RoC} & 1 \end{bmatrix}, \text{ for reflection upon a mirror,} \quad (\text{E.10a})$$

$$M^{(\text{trans})} = \begin{bmatrix} 1 & 0 \\ (n_2 - n_1)/\text{RoC} & 1 \end{bmatrix}, \text{ for transmission through a surface,} \quad (\text{E.10b})$$

$$M^{(\text{prop})} = \begin{bmatrix} 1 & L/n \\ 0 & 1 \end{bmatrix}, \text{ for propagation in free-space.} \quad (\text{E.10c})$$

We can thus find the eigenmode of a cavity by computing the cavity $ABCD$ matrix. In the simple Fabry-Perot cavity case this is given by

$$M_{\text{cav}} = M^{(\text{prop})} M_i^{(\text{refl})} M^{(\text{prop})} M_e^{(\text{refl})} \equiv \begin{bmatrix} A_{\text{cav}} & B_{\text{cav}} \\ C_{\text{cav}} & D_{\text{cav}} \end{bmatrix} \quad (\text{E.11})$$

The Gaussian beam parameter of the cavity's eigenmode (evaluated at the point right before it hits the end mirror) is then obtained by finding q_{cav} such that

$$q_{\text{cav}} = \frac{A_{\text{cav}}q_{\text{cav}} + B_{\text{cav}}}{C_{\text{cav}}q_{\text{cav}} + D_{\text{cav}}}. \quad (\text{E.12})$$

To maximize the optical coupling, the incident beam should have a Gaussian parameter q_{in} that matches the cavity's q_{cav} . In general, the mode *mismatch* parameter K is given by

$$K = \text{i} \frac{(q_{\text{in}} - q_{\text{cav}})^*}{2\text{Im}(q_{\text{cav}})}. \quad (\text{E.13})$$

Appendix F

Supplemental materials for the LIGO-LF design

F.1 LIGO-LF SUSPENSION DESIGN

LIGO-LF adopts a 4-stage suspension system similar to that of aLIGO ([Aston et al., 2012](#)). The suspension chain consists of a top mass (TOP), an upper-intermediate mass (UIM), a penultimate mass (PUM), and a main test mass (TST), with the parameters for each stage summarized in Table [F.1](#). The blade design used for LIGO-LF vertical support is similar to that of aLIGO. Two requirements are set for the system above 5 Hz: the suspension needs to provide sufficient filtering of the residual ground motion (cf. Figure [9-2](#)), and its total thermal noise should be dominated by the pendulum mode from the TST stage.

To achieve the seismic isolation requirement, the mass ratio between the TOP and the TST stages should be similar to that of aLIGO. Decreasing the TOP mass

Table F.1: Summary of the LIGO-LF suspension parameters

Stage	mass [kg]	length [m]	Wire diameter [mm]	Material
TOP	80	0.32	1.8	C70 steel
UIM	80	0.32	1.2	C70 steel
PUM	200	0.36	1.2	Silica
TST	200	1.2	0.6 (thin); 1.8 (thick)	Silica

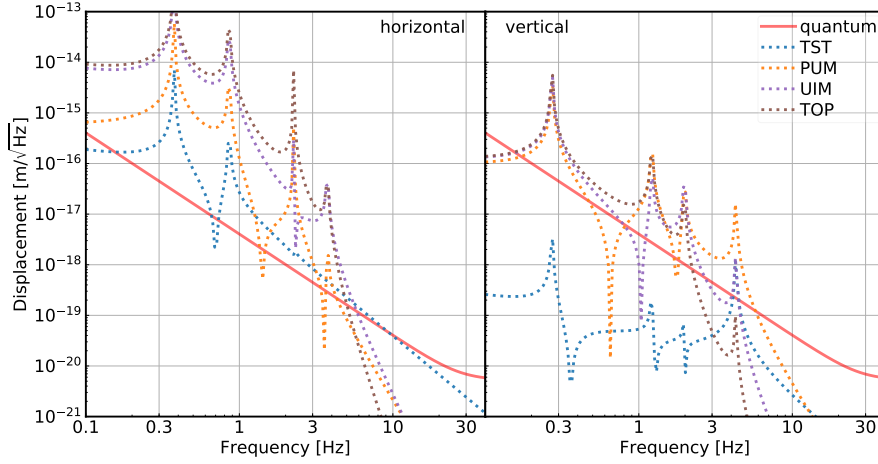


Figure F-1: LIGO-LF’s suspension thermal noise from different stages (represented by dotted lines with different colors). The quantum noise is also plotted in the red-solid line as a reference. In the left we plot the direct horizontal (along the beam line) displacement noises. The dominant contribution above 5 Hz is from the last stage and it is similar to the quantum noise in the 5 – 20 Hz band. In the right are the noises due to the vertical-to-horizontal coupling. The bounce mode is at 4.3 Hz, making the vertical contributions subdominant above 5 Hz.

shifts the highest suspension resonance to higher frequencies, making the pendulum filtering less efficient at 5 Hz. Consequently we choose $m_{\text{TOP}} = m_{\text{UIM}} = 80 \text{ kg}$, and the resultant seismic noise is shown in the dotted-brown curve of Figure 9-1.

In addition to the direct length coupling, the longitudinal ground motion can also couple to the pitch motion of the test mass. The main pitch resonance frequency can be controlled by tuning the distance between the fiber binding point and the mirror’s center of mass. Similarly, the ground rotation can couple to the yaw motion of the test mass, and the resonance frequency can be controlled as well (Rakhmanov, 2000). For LIGO-LF, the main pitch and yaw resonances are set to 0.42 Hz and 0.35 Hz, respectively, to balance the requirements for more filtering at high frequency ($> 5 \text{ Hz}$) and for less rms angular motions at low frequency ($< 1 \text{ Hz}$).

We present the suspension thermal noise for LIGO-LF in Figure F-1. In the sensitivity band above 5 Hz, the dominant contribution comes from the pendulum mode of the test mass stage. In the calculation we have assumed an effective loss

angle of 5×10^{-10} (Hammond et al., 2012) and the resultant suspension thermal noise is similar to the quantum noise from 5 to 20 Hz. In order to reduce the contamination from other stages, we replace the suspension for the PUM stage from C70 steel wire to silica fiber. Meanwhile, the wire stress in the TOP and UIM stages is increased by 30% relative to aLIGO for better dilution of the losses.

Besides the thermal motion along the beam line, the vertical vibration of the test masses also couples to the GW channel due to the Earth’s radius of curvature. A conservative estimation of the vertical-to-horizontal cross coupling is 0.1% (Cumming et al., 2012). The eigenfrequency f_v of the last stage’s vertical mode (also known as the “bounce mode”) scales as (Fritschel et al., 2002)

$$2\pi f_v \approx \sqrt{\frac{gY}{l\sigma} \frac{m_{\text{TST}} + m_{\text{PUM}}}{m_{\text{PUM}}}}, \quad (\text{F.1})$$

where g , Y , l , σ , m_{TST} , and m_{PUM} are the local gravitational acceleration, the Young’s modulus of the material, the length of the suspension, the stress inside the fiber, the mass of the test mass, and the mass of the penultimate mass, respectively. To make f_v low, we maintain the mass ratio between the PUM and the test mass to 1 as aLIGO, and double l to 1.2 m. Meanwhile, the fibers suspending the test mass have a tapered geometry: for the thick part where most of the bending energy is stored, it has a diameter of $1.8 \mu\text{m}$ to cancel the thermal-elastic noise, while the thin part has a diameter of $0.6 \mu\text{m}$ to increase the stress σ to 1.7 GPa. Consequently, the bounce mode has an eigenfrequency of $f_v = 4.3 \text{ Hz}$, which provides sufficient filtering of the vertical motion in the sensitivity band.

F.2 CALCULATION OF THE SCATTERING NOISE

For the scattering noise calculation, we introduce the effective displacement \bar{x}_{scatter} defined as

$$\bar{x}_{\text{scatter}}(t) = \frac{\lambda}{4\pi} \sin \left[\frac{4\pi}{\lambda} x_{\text{scatter}}(t) \right], \quad (\text{F.2})$$

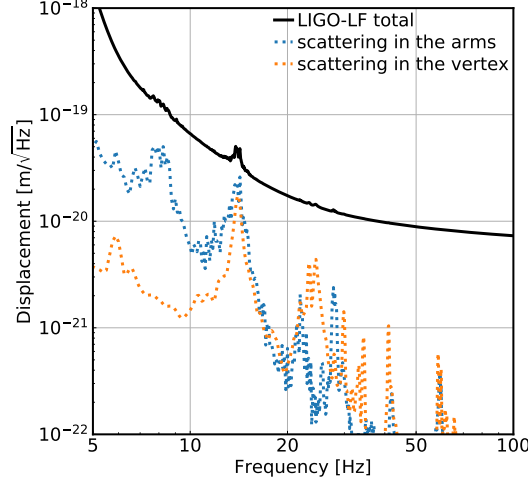


Figure F-2: The noises due to scattering in the arm tubes (dotted-blue) and in the vertex (dotted-orange). The total LIGO-LF noise is shown in the solid-black as a reference.

where $x_{\text{scatter}}(t)$ is the (physical) relative displacement between a mirror and a scattering surface at time t , and $\lambda = 1064 \text{ nm}$ the laser wavelength. The corresponding frequency-domain displacement is thus given by

$$\hat{x}_{\text{scatter}}(f) = \frac{\lambda}{4\pi} \int \sin \left[\frac{4\pi}{\lambda} x_{\text{scatter}}(t) \right] \exp(-2\pi i f t) dt. \quad (\text{F.3})$$

Notice that when $x_{\text{scatter}} \sim \lambda$, the effective displacement no more varies linearly with the physical displacement. Consequently, the large ground motion below 1 Hz can be up-converted to the sensitivity band, making scattering a significant noise source when the ground motion is severe.

The olive trace in Figure 9-1 of the main Letter is calculated including two effects: scattering in the arm tubes, and scattering in the vertex of the interferometer, with each one's contribution individually shown in Figure F-2.

For the former, the calculation follows from Ottaway et al. (2012). There are two coupling channels need to be considered. The phase quadrature of the scattered light directly enters the GW readout, with a flat transfer function from $\hat{x}_{\text{scatter}}(f)$ to the

differential arm displacement given by

$$Z_{\text{tube}}^{(\text{Im})}(f) \simeq 2.5 \times 10^{-12} \left(\frac{A_{\text{scat}}}{5.0 \times 10^{-12}} \right) \frac{\text{m}}{\text{m}}. \quad (\text{F.4})$$

In the equation above A_{scat} is the amplitude scattering coefficient that is further defined as

$$A^2 = \left(\frac{\lambda}{L_{\text{mb}}} \right) \text{BRDF}_{\text{m}}^2 \text{BRDF}_{\text{b}} \Delta\Omega_{\text{b}}, \quad (\text{F.5})$$

where L_{mb} is the distance between the mirror and baffle, $\Delta\Omega_{\text{b}}$ the solid angle subtended by the baffle, and $\text{BRDF}_{\text{m(b)}}$ the Bi-directional Reflectivity Distribution (Flanagan & Thorne, 1994) of the mirror (baffle).

Meanwhile, the amplitude quadrature of the scattered light can beat with the static optical field inside each arm to cause a differential power fluctuation, which further induces differential arm motions due to the radiation pressure force. The transfer function for this mechanism is given by

$$\begin{aligned} Z_{\text{tube}}^{(\text{Re})}(f) &\simeq 8.2 \times 10^{-12} \left(\frac{10 \text{ Hz}}{f} \right)^2 \left(\frac{A_{\text{scat}}}{5.0 \times 10^{-12}} \right) \\ &\times \left(\frac{200 \text{ kg}}{m_{\text{TST}}} \right) \left(\frac{P_{\text{a}}}{0.8 \text{ MW}} \right) \left(\frac{T_{\text{s}}}{0.25} \right) \frac{\text{m}}{\text{m}}, \end{aligned} \quad (\text{F.6})$$

where P_{a} is the power circulating in each arm and T_{s} is the power transmissivity of the signal recycling mirror. Below 20 Hz, the amplitude quadrature dominates the coupling.

The scattering in the vertex is caused by the anti-reflecting (AR) surfaces along the optical path. If not properly baffled, the stray light may hit the chamber wall and be reflected back to the optical path. The coupling coefficient per stray beam is¹

$$Z_{\text{vertex}}(f) \simeq 1.0 \times 10^{-12} \left(\frac{T_{\text{baffle}}}{0.001} \right)^{1/2} \left(\frac{R_{\text{AR}}}{250 \text{ ppm}} \right) \left(\frac{2 \text{ mm}}{w_{\text{wall}}} \right) \frac{\text{m}}{\text{m}}, \quad (\text{F.7})$$

where R_{AR} is the power reflectivity of the AR surface creating the beam, w_{wall} is the stray light's spot size on the chamber wall, and T_{baffle} is the fraction (in power)

¹<https://alog.ligo-la.caltech.edu/aLOG/index.php?callRep=29665>

of the stray light that leaks through the baffle. There are 10 AR surfaces that can contribute to this noise, 2 from the input test masses ($R_{\text{AR}} \simeq 250 \text{ ppm}$), 4 from the beam splitter ($R_{\text{AR}} \simeq 50 \text{ ppm}$), and 4 from the compensation plates ($R_{\text{AR}} \simeq 20 \text{ ppm}$). To achieve the proposed LIGO-LF sensitivity, the baffles need to reduce the power of the stray light by

$$T_{\text{baffle}}^{(\text{LIGO-LF req.})} < 0.1\%. \quad (\text{F.8})$$

Bibliography

- Aasi J., et al., 2013, [Nat. Photonics](#), 7, 613
- Aasi J., et al., 2015, [Class. Quantum Gravity](#), 32, 074001
- Abadie J., et al., 2010, [Class. Quantum Gravity](#), 27, 173001
- Abbott B. P., et al., 2016a, preprint, ([arXiv:1602.03845](#))
- Abbott B. P., et al., 2016b, [Phys. Rev. X](#), 6, 041015
- Abbott B. P., et al., 2016c, [Phys. Rev. Lett.](#), 116, 061102
- Abbott B. P., et al., 2016d, [Phys. Rev. Lett.](#), 116, 241103
- Abbott B. P., et al., 2016e, [ApJ](#), 818, L22
- Abbott B. P., et al., 2016f, [ApJ](#), 832, L21
- Abbott B. P., et al., 2017a, [Class. Quantum Gravity](#), 34, 044001
- Abbott B. P., et al., 2017b, [Phys. Rev. D](#), 96, 022001
- Abbott B. P., et al., 2017c, [Phys. Rev. Lett.](#), 119, 161101
- Abbott B. P., et al., 2017d, [ApJ](#), 848, L12
- Abbott B. P., et al., 2018a, arXiv e-prints, p. [arXiv:1811.12907](#)
- Abbott B. P., et al., 2018b, [Phys. Rev. Lett.](#), 121, 161101
- Acernese F., et al., 2015a, [Class. Quantum Gravity](#), 32, 024001
- Acernese F., et al., 2015b, [Class. Quantum Gravity](#), 32, 024001
- Adhikari R., Smith N., Brooks A., et al. 2017, LIGO Voyager Upgrade Concept. LIGO, <https://dcc.ligo.org/LIGO-T1400226>
- Adhikari R., Pele A., Kasprzack M., Frolov V., Mukund N., Quintero E., Yu H., 2018, Global Controls Length to Angle Decoupling. LIGO, <https://dcc.ligo.org/LIGO-T1800369>

- Aerts C., Christensen-Dalsgaard J., Kurtz D. W., 2010, *Asteroseismology*. Springer Science & Business Media
- Agathos M., Meidam J., Del Pozzo W., Li T. G. F., Tompitak M., Veitch J., Vitale S., Van Den Broeck C., 2015, *Phys. Rev. D*, **92**, 023012
- Ajith P., et al., 2011, *Phys. Rev. Lett.*, **106**, 241101
- Allen B., 1997, in Marck J.-A., Lasota J.-P., eds, *Relativistic Gravitation and Gravitational Radiation*. Cambridge University Press, Cambridge, UK, p. 373 ([arXiv:gr-qc/9604033](#))
- Allen B., Anderson W. G., Brady P. R., Brown D. A., Creighton J. D. E., 2012, *Phys. Rev. D*, **85**, 122006
- Ambartsumyan V. A., Saakyan G. S., 1960, *Soviet Ast.*, **4**, 187
- Andersson N., Comer G. L., 2001, *MNRAS*, **328**, 1129
- Andersson N., Ho W. C. G., 2018, *Phys. Rev. D*, **97**, 023016
- Andersson N., Comer G. L., Grosart K., 2004, *MNRAS*, **355**, 918
- Andreev A. F., Bashkin E. P., 1976, *SOv. J. Exp. Theor. Phys.*, **42**, 164
- Antoniadis J., et al., 2013, *Science*, **340**, 448
- Aston S., 2011, PhD thesis, University of Birmingham, <http://inspirehep.net/record/1444414/files/Aston11PhD.pdf>
- Aston S. M., et al., 2012, *Class. Quantum Gravity*, **29**, 235004
- Baiotti L., Rezzolla L., 2017, *Rep. Prog. Phys.*, **80**, 096901
- Balachandran P., Flanagan E. E., 2007, preprint, ([arXiv:gr-qc/0701076](#))
- Barrière N. M., et al., 2015, *ApJ*, **799**, 123
- Barsotti L., Evans M., Fritschel P., 2010, *Class. Quantum Gravity*, **27**, 084026
- Bednarek I., Haensel P., Zdunik J. L., Bejger M., Mańka R., 2012, *A&A*, **543**, A157
- Bejger M., 2017, preprint, ([arXiv:1710.06607](#))
- Berti E., Cardoso V., Casals M., 2006, *Phys. Rev. D*, **73**, 024013
- Bildsten L., 1998, in Buccheri R., van Paradijs J., Alpar A., eds, *NATO Advanced Science Institutes (ASI) Series C Vol. 515*, NATO Advanced Science Institutes (ASI) Series C. p. 419 ([arXiv:astro-ph/9709094](#))
- Bird S., Cholis I., Muñoz J. B., Ali-Haïmoud Y., Kamionkowski M., Kovetz E. D., Raccanelli A., Riess A. G., 2016, *Phys. Rev. Lett.*, **116**, 201301

- Bonila E., 2012, ISI -> SUS feedforward notes. LIGO, <https://dcc.ligo.org/LIGO-T1800301>
- Bosgra O. H., Kwakernaak H., Meinsma G., 2001, Notes for a Course of the Dutch Institute of Systems and Control, Winter term, 2002
- Boutloukos S., Miller M. C., Lamb F. K., 2010, [ApJ](#), **720**, L15
- Brooks A. F., et al., 2016, [Appl. Opt.](#), **55**, 8256
- Brown E. F., Bildsten L., 1998, [ApJ](#), **496**, 915
- Brown D. D., Freise A., 2014, Finesse, [doi:10.5281/zenodo.821363](https://doi.org/10.5281/zenodo.821363), <http://www.gwoptics.org/finesse>
- Brown D. A., Harry I., Lundgren A., Nitz A. H., 2012, [Phys. Rev. D](#), **86**, 084017
- Buonanno A., Chen Y., 2001, [Phys. Rev. D](#), **64**, 042006
- Buonanno A., Chen Y., 2002, [Phys. Rev. D](#), **65**, 042001
- Burgay M., et al., 2003, [Nature](#), **426**, 531
- Cahillane C., et al., 2017, [Phys. Rev. D](#), **96**, 102001
- Canuel B., Genin E., Vajente G., Marque J., 2013, [Opt. Express](#), **21**, 10546
- Carbone L., et al., 2012, [Class. Quantum Gravity](#), **29**, 115005
- Chabanat E., Bonche P., Haensel P., Meyer J., Schaeffer R., 1997, [Nucl. Phys. A](#), **627**, 710
- Chamel N., 2008, [MNRAS](#), **388**, 737
- Chaplin W. J., Miglio A., 2013, [ARA&A](#), **51**, 353
- Chatziioannou K., Yagi K., Klein A., Cornish N., Yunes N., 2015, [Phys. Rev. D](#), **92**, 104008
- Chen H.-Y., Holz D. E., Miller J., Evans M., Vitale S., Creighton J., 2017, preprint, ([arXiv:1709.08079](https://arxiv.org/abs/1709.08079))
- Christodoulou D., 1991, [Phys. Rev. Lett.](#), **67**, 1486
- Coughlin M., Mukund N., Harms J., Driggers J., Adhikari R., Mitra S., 2016, [Class. Quantum Gravity](#), **33**, 244001
- Creighton T., 2008, [Class. Quantum Gravity](#), **25**, 125011
- Cumming A., 2003, [ApJ](#), **595**, 1077
- Cumming A., Bildsten L., 2000, [ApJ](#), **544**, 453

- Cumming A., Macbeth J., in 't Zand J. J. M., Page D., 2006, [ApJ](#), **646**, 429
- Cumming A. V., et al., 2012, [Class. Quantum Gravity](#), **29**, 035003
- Cutler C., Flanagan É. E., 1994, [Phys. Rev. D](#), **49**, 2658
- Damour T., Nagar A., Villain L., 2012, [Phys. Rev. D](#), **85**, 123007
- Del Pozzo W., Li T. G. F., Agathos M., Van Den Broeck C., Vitale S., 2013, [Phys. Rev. Lett.](#), **111**, 071101
- Demorest P. B., Pennucci T., Ransom S. M., Roberts M. S. E., Hessels J. W. T., 2010, [Nature](#), **467**, 1081
- Dommes V. A., Gusakov M. E., 2016, [MNRAS](#), **455**, 2852
- Dooley K. L., et al., 2013, [J. Opt. Soc. Am. A](#), **30**, 2618
- Douchin, F. Haensel, P. 2001, [Astron. Astrophys.](#), **380**, 151
- Doyle J. C., Glover K., Khargonekar P. P., Francis B. A., 1989, [IEEE Trans. Automat. Contr.](#), **34**, 831
- Drever R. W. P., Hall J. L., Kowalski F. V., Hough J., Ford G. M., Munley A. J., Ward H., 1983, [Applied Physics B](#), **31**, 97
- Driggers J. C., Harms J., Adhikari R. X., 2012, [Phys. Rev. D](#), **86**, 102001
- Drischler C., Hebeler K., Schwenk A., 2016, [Phys. Rev. C](#), **93**, 054314
- Ebisuzaki T., Hanawa T., Sugimoto D., 1983, [PASJ](#), **35**, 17
- Essick R., Vitale S., Weinberg N. N., 2016, [Phys. Rev. D](#), **94**, 103012
- Farr B., Holz D. E., Farr W. M., 2018, [ApJ](#), **854**, L9
- Favata M., 2009, [ApJ](#), **696**, L159
- Flanagan É. É., Hinderer T., 2008, [Phys. Rev. D](#), **77**, 021502
- Flanagan É. É., Racine É., 2007, [Phys. Rev. D](#), **75**, 044001
- Flanagan E., Thorne K., 1994, Noise Due to Backscatter Off Baffles, the Nearby Wall, and Objects at the Fare End of the Beam Tube; and Recommended Actions. LIGO, <https://dcc.ligo.org/LIGO-T940063>
- Fricke T. T., et al., 2012, [Class. Quantum Gravity](#), **29**, 065005
- Fritschel P., 2018, A HAM-ISI for HAM1?. LIGO, <https://dcc.ligo.org/LIGO-T1800369>

- Fritschel P., Shoemaker D., Coyne D., 2002, Low-frequency Cutoff for Advanced LIGO. LIGO, <https://dcc.ligo.org/LIGO-T020034>
- Fritschel P., Evans M., Frolov V., 2014, *Opt. Express*, **22**, 4224
- Fujimoto M. Y., Hanawa T., Miyaji S., 1981, *ApJ*, **247**, 267
- Fulda P., Brown D., 2015, AS36 WFS simulations for H1. LIGO, <https://dcc.ligo.org/LIGO-G1501251>
- Galloway D. K., Keek L., 2017, preprint, ([arXiv:1712.06227](https://arxiv.org/abs/1712.06227))
- Galloway D. K., Munro M. P., Hartman J. M., Psaltis D., Chakrabarty D., 2008, *ApJS*, **179**, 360
- Galloway D. K., Yao Y., Marshall H., Misanovic Z., Weinberg N., 2010, *ApJ*, **724**, 417
- Gendreau K., Arzoumanian Z., 2017, *Nat. Astron.*, **1**, 895
- González G., 2000, *Class. Quantum Gravity*, **17**, 4409
- Graber V., Andersson N., Hogg M., 2017, *Int. J. Mod. Phys. D*, **26**, 1730015
- Graff P. B., Buonanno A., Sathyaprakash B. S., 2015, *Phys. Rev. D*, **92**, 022002
- Gras S., Yu H., Yam W., Martynov D., Evans M., 2017, *Phys. Rev. D*, **95**, 022001
- Gusakov M. E., Kantor E. M., 2013, *Phys. Rev. D*, **88**, 101302
- Gusakov M. E., Haensel P., Kantor E. M., 2014, *MNRAS*, **439**, 318
- Hall E. D., 2017, PhD thesis, California Institute of Technology, [doi:10.7907/Z9PG1PQ9](https://doi.org/10.7907/Z9PG1PQ9), <http://resolver.caltech.edu/CaltechTHESIS:01302017-113507797>
- Hammond G. D., Cumming A. V., Hough J., Kumar R., Tokmakov K., Reid S., Rowan S., 2012, *Class. Quantum Gravity*, **29**, 124009
- Hannam M., Schmidt P., Bohé A., Haegel L., Husa S., Ohme F., Pratten G., Pürrer M., 2014, *Phys. Rev. Lett.*, **113**, 151101
- Harms J., 2015, *Living Rev. Relativity*, **18**, 3
- Harms J., Chen Y., Chelkowski S., Franzen A., Vahlbruch H., Danzmann K., Schnabel R., 2003, *Phys. Rev. D*, **68**, 042001
- Harry G. M., 2010, *Class. Quantum Gravity*, **27**, 084006
- Hashimoto M.-A., Hanawa T., Sugimoto D., 1983, *PASJ*, **35**, 1

- Haster C.-J., Wang Z., Berry C. P. L., Stevenson S., Veitch J., Mandel I., 2016, [MNRAS](#), **457**, 4499
- Hefetz Y., Mavalvala N., Sigg D., 1997, [J. Opt. Soc. Am. B](#), **14**, 1597
- Hild S., Chelkowski S., Freise A., Franc J., Morgado N., Flaminio R., DeSalvo R., 2010, [Class. Quantum Gravity](#), **27**, 015003
- Hild S., et al., 2011, [Class. Quantum Gravity](#), **28**, 094013
- Hild S., et al., 2012, LIGO 3 Strawman Design, Team Red. LIGO, <https://dcc.ligo.org/LIGO-T1200046>
- Hinderer T., Lackey B. D., Lang R. N., Read J. S., 2010, [Phys. Rev. D](#), **81**, 123016
- Hinderer T., et al., 2016, [Phys. Rev. Lett.](#), **116**, 181101
- Hirose E., Kawabe K., Sigg D., Adhikari R., Saulson P. R., 2010, [Appl. Opt.](#), **49**, 3474
- Ho W. C. G., Lai D., 1999, [MNRAS](#), **308**, 153
- Hong T., Yang H., Gustafson E. K., Adhikari R. X., Chen Y., 2013, [Phys. Rev. D](#), **87**, 082001
- Hughes S. A., Thorne K. S., 1998, [Phys. Rev. D](#), **58**, 122002
- Iwai M., Dotani T., Ozaki M., Maeda Y., Mori H., Saji S., 2017, [PASJ](#), **69**, 61
- Izumi K., Sigg D., 2017, [Class. Quantum Gravity](#), **34**, 015001
- Izumi K., Sigg D., Kawabe K., 2015, Frequency Response of the aLIGO Interferometer: part3. LIGO, <https://dcc.ligo.org/LIGO-T1500559>
- Jahoda K., Markwardt C. B., Radeva Y., Rots A. H., Stark M. J., Swank J. H., Strohmayer T. E., Zhang W., 2006, [ApJS](#), **163**, 401
- Jaranowski P., Królak A., Schutz B. F., 1998, [Phys. Rev. D](#), **58**, 063001
- Joss P. C., Melia F., 1987, [ApJ](#), **312**, 700
- Kajava J. J. E., Nättilä J., Poutanen J., Cumming A., Suleimanov V., Kuulkers E., 2017, [MNRAS](#), **464**, L6
- Kantor E. M., Gusakov M. E., 2014, [MNRAS](#), **442**, L90
- Kato M., 1983, [PASJ](#), **35**, 33
- Kato M., 1986, [PASJ](#), **38**, 29
- Keek L., et al., 2018, [ApJ](#), **856**, L37

- Kimble H. J., Levin Y., Matsko A. B., Thorne K. S., Vyatchanin S. P., 2001, [Phys. Rev. D](#), 65, 022002
- Kiziltan B., Kottas A., De Yoreo M., Thorsett S. E., 2013, [ApJ](#), 778, 66
- Kokkotas K. D., Schafer G., 1995, [MNRAS](#), 275, 301
- Kovetz E. D., 2017, [Phys. Rev. Lett.](#), 119, 131301
- Kwakernaak H., 1983, in The 22nd IEEE Conf. Dec. Contr. pp 618–624, [doi:10.1109/CDC.1983.269592](#)
- Kwakernaak H., 1985, [IEEE Trans. Automat. Contr.](#), 30, 994
- Kwakernaak H., 2002, [IFAC Proceedings Volumes](#), 35, 61
- Kwee P., Miller J., Isogai T., Barsotti L., Evans M., 2014, [Phys. Rev. D](#), 90, 062006
- Lackey B. D., Wade L., 2015, [Phys. Rev. D](#), 91, 043002
- Lackey B. D., Kyutoku K., Shibata M., Brady P. R., Friedman J. L., 2012, [Phys. Rev. D](#), 85, 044061
- Lai D., 1994, [MNRAS](#), 270, 611
- Lai D., Wu Y., 2006, [Phys. Rev. D](#), 74, 024007
- Lantz B., Schofield R., Reilly B. O., Clark D. E., DeBra D., 2009, [Bull. Seismol. Soc. Am.](#), 99, 980
- Lasky P. D., Thrane E., Levin Y., Blackman J., Chen Y., 2016, [Phys. Rev. Lett.](#), 117, 061102
- Lattimer J. M., 2012, [Ann. Rev. Nucl. Part. Sci.](#), 62, 485
- Lattimer J. M., Prakash M., 2004, [Science](#), 304, 536
- Lattimer J. M., Prakash M., Pethick C. J., Haensel P., 1991, [Phys. Rev. Lett.](#), 66, 2701
- Lazzarini A., Reitze D., Berger B., Cadonati L., Gonzalez G., Cavaglia M., 2016, What Comes Next for LIGO? Planning for the post-detection era in gravitational-wave detectors and astrophysics. LIGO, <https://dcc.ligo.org/LIGO-P1600350>
- Lee U., 1995, [A&A](#), 303, 515
- Levin Y., 1998, [Phys. Rev. D](#), 57, 659
- Ligo Scientific Collaboration 2011, [Nat. Phys.](#), 7, 962
- Lindblom L., Mendell G., 1994, [ApJ](#), 421, 689

- Lombardo U., Schulze H.-J., 2001, in Blaschke D., Glendenning N. K., Sedrakian A., eds, Lecture Notes in Physics, Berlin Springer Verlag Vol. 578, Physics of Neutron Star Interiors. p. 30 ([arXiv:astro-ph/0012209](#))
- Lonardoni D., Lovato A., Gandolfi S., Pederiva F., 2015, [Phys. Rev. Lett.](#), **114**, 092301
- Mageswaran M., Black E., 2010, Optical Levers Final Design Review for test masses, recycler mirrors and HAM optical benches. LIGO, <https://dcc.ligo.org/LIGO-T1000517/public>
- Maggiore M., 2007, Gravitational Waves, Volume 1: Theory and Experiments, 1 edn. Oxford University Press, Oxford, United Kindom
- Mandel I., Brown D. A., Gair J. R., Miller M. C., 2008, [ApJ](#), **681**, 1431
- Markakis C., Read J. S., Shibata M., Uryu K., Creighton J. D. E., Friedman J. L., 2010, preprint, ([arXiv:1008.1822](#))
- Martynov D. V., 2015, PhD thesis, California Institute of Technology, [doi:10.7907/Z9Q81B1F](https://resolver.caltech.edu/CaltechTHESIS:05282015-142013480), <http://resolver.caltech.edu/CaltechTHESIS:05282015-142013480>
- Martynov D. V., et al., 2016, [Phys. Rev. D](#), **93**, 112004
- Martynov D. V., et al., 2017, [Phys. Rev. A](#), **95**, 043831
- Matichard F., Evans M., 2015, [Bull. Seismol. Soc. Am.](#), **105**, 497
- Matichard F., et al., 2015a, [Class. Quantum Gravity](#), **32**, 185003
- Matichard F., et al., 2015b, [Precis. Eng.](#), **40**, 273
- Matichard F., et al., 2015c, [Precis. Eng.](#), **40**, 287
- Matichard F., et al., 2016, [Rev. Sci. Instrum.](#), **87**, 065002
- McClelland D., Mavalvala N., Chen Y., Schnabel R., 2011, [Laser Photonics Rev.](#), **5**, 677
- Medin Z., von Steinkirch M., Calder A. C., Fontes C. J., Fryer C. L., Hungerford A. L., 2016, [ApJ](#), **832**, 102
- Miao H., 2012, Exploring Macroscopic Quantum Mechanics in Optomechanical Devices. Springer Theses, Springer Berlin Heidelberg, <https://books.google.com/books?id=Myo8jXpvx2sC>
- Miller M. C., 2013, preprint, ([arXiv:1312.0029](#))
- Miller M. C., Colbert E. J. M., 2004, [Int. J. Mod. Phys. D](#), **13**, 1
- Miller M. C., Lamb F. K., 2016, [Eur. Phys. J. A](#), **52**, 63

- Mitrofanov V. P., Tokmakov K. V., 2003, [Phys. Lett. A](#), **308**, 212
- Mizuno J., Strain K. A., Nelson P. G., Chen J. M., Schilling R., Rüdiger A., Winkler W., Danzmann K., 1993, [Phys. Rev. A](#), **175**, 273
- Mow-Lowry C. M., Martynov D., 2018, preprint, ([arXiv:1801.01468](#))
- Nättilä J., Suleimanov V. F., Kajava J. J. E., Poutanen J., 2015, [A&A](#), **581**, A83
- Ng K. K. Y., Vitale S., Zimmerman A., Chatziioannou K., Gerosa D., Haster C.-J., 2018, [Phys. Rev. D](#), **98**, 083007
- Nobili L., Turolla R., Lapidus I., 1994, [ApJ](#), **433**, 276
- Oelker E., Isogai T., Miller J., Tse M., Barsotti L., Mavalvala N., Evans M., 2016, [Physical Review Letters](#), **116**, 041102
- Oppenheimer J. R., Volkoff G. M., 1939, [Phys. Rev.](#), **55**, 374
- Ottaway D. J., Fritschel P., Waldman S. J., 2012, [Opt. Express](#), **20**, 8329
- Owocki S. P., Townsend R. H. D., Quataert E., 2017, [MNRAS](#), **472**, 3749
- Özel F., Freire P., 2016, [ARA&A](#), **54**, 401
- Özel F., Psaltis D., 2009, [Phys. Rev. D](#), **80**, 103003
- Özel F., Baym G., Güver T., 2010, [Phys. Rev. D](#), **82**, 101301
- Özel F., Psaltis D., Güver T., Baym G., Heinke C., Guillot S., 2016, [ApJ](#), **820**, 28
- Paczynski B., 1983, [ApJ](#), **267**, 315
- Paczynski B., Proszynski M., 1986, [ApJ](#), **302**, 519
- Page D., Prakash M., Lattimer J. M., Steiner A. W., 2011, [Phys. Rev. Lett.](#), **106**, 081101
- Parikh A., José J., Sala G., 2014, [AIPA](#), **4**, 041002
- Passamonti A., Haskell B., Andersson N., Jones D. I., Hawke I., 2009, [MNRAS](#), **394**, 730
- Passamonti A., Andersson N., Ho W. C. G., 2016, [MNRAS](#), **455**, 1489
- Paxton B., Bildsten L., Dotter A., Herwig F., Lesaffre P., Timmes F., 2011, [ApJS](#), **192**, 3
- Paxton B., et al., 2013, [ApJS](#), **208**, 4
- Paxton B., et al., 2015, [ApJS](#), **220**, 15

- Penner A. J., Andersson N., Samuelsson L., Hawke I., Jones D. I., 2011, [Phys. Rev. D](#), **84**, 103006
- Penrose R., 1955, [Math. Proc. Cambridge Philos. Soc.](#), **51**, 406
- Planck Collaboration 2016, [A&A](#), **594**, A13
- Poisson E., Will C. M., 1995, [Phys. Rev. D](#), **52**, 848
- Posselt B., Pavlov G. G., Suleimanov V., Kargaltsev O., 2013, [ApJ](#), **779**, 186
- Prakash M., Prakash M., Lattimer J. M., Pethick C. J., 1992, [ApJ](#), **390**, L77
- Press W. H., Teukolsky S. A., 1977, [ApJ](#), **213**, 183
- Prix R., Rieutord M., 2002, [A&A](#), **393**, 949
- Quataert E., Fernández R., Kasen D., Klion H., Paxton B., 2016, [MNRAS](#), **458**, 1214
- Quinn T., Paczynski B., 1985, [ApJ](#), **289**, 634
- Rakhmanov M., 2000, PhD thesis, CALIFORNIA INSTITUTE OF TECHNOLOGY
- Read J. S., Markakis C., Shibata M., Uryū K., Creighton J. D. E., Friedman J. L., 2009, [Phys. Rev. D](#), **79**, 124033
- Reisenegger A., 1994, [ApJ](#), **432**, 296
- Reisenegger A., Goldreich P., 1992, [ApJ](#), **395**, 240
- Reisenegger A., Goldreich P., 1994, [ApJ](#), **426**, 688
- Rikovska Stone J., Miller J. C., Koncewicz R., Stevenson P. D., Strayer M. R., 2003, [Phys. Rev. C](#), **68**, 034324
- Ro S., Matzner C. D., 2016, [ApJ](#), **821**, 109
- Rodriguez C. L., Zevin M., Pankow C., Kalogera V., Rasio F. A., 2016, [ApJ](#), **832**, L2
- Santamaría L., et al., 2010, [Phys. Rev. D](#), **82**, 064016
- Sathyaprakash B., et al., 2012, [Class. Quantum Gravity](#), **29**, 124013
- Saulson P. R., 1984, [Phys. Rev. D](#), **30**, 732
- Saulson P. R., 1990, [Phys. Rev. D](#), **42**, 2437
- Schmidt P., Ohme F., Hannam M., 2015, [Phys. Rev. D](#), **91**, 024043
- Schnupp L., 1988, Talk at a European Collaboration Meeting on Interferometric Detection of Gravitational Waves
- Schutz B. F., 2011, [Class. Quantum Gravity](#), **28**, 125023

- Sesana A., Gair J., Mandel I., Vecchio A., 2009, [ApJ](#), **698**, L129
- Shapiro B. N., Adhikari R., Driggers J., Kissel J., Lantz B., Rollins J., Youcef-Toumi K., 2015, *Class. Quantum Gravity*, **32**, 015004
- Shibata M., 1994, [Progress of Theoretical Physics](#), **91**, 871
- Shternin P. S., Yakovlev D. G., Heinke C. O., Ho W. C. G., Patnaude D. J., 2011, [MNRAS](#), **412**, L108
- Sidles J. A., Sigg D., 2006, [Physics Letters A](#), **354**, 167
- Siegman A. E., 1986, *Lasers*. University Science Books
- Sjöberg O., 1976, [Nucl. Phys. A](#), **265**, 511
- Somiya K., 2012, [Class. Quantum Gravity](#), **29**, 124007
- Steiner A. W., Lattimer J. M., Brown E. F., 2010, [ApJ](#), **722**, 33
- Steiner A. W., Lattimer J. M., Brown E. F., 2013, [ApJ](#), **765**, L5
- Steinhoff J., Hinderer T., Buonanno A., Taracchini A., 2016, [Phys. Rev. D](#), **94**, 104028
- Steinlechner J., et al., 2016, [Phys. Rev. D](#), **93**, 062005
- Strohmayer T., Bildsten L., 2003, preprint, ([arXiv:0301544](#))
- Strohmayer T., Bildsten L., 2006, *New views of thermonuclear bursts*. Cambridge University Press, pp 113–156, [doi:10.1017/CBO9780511536281.004](#)
- Suleimanov V., Poutanen J., Werner K., 2011, [A&A](#), **527**, A139
- Suleimanov V., Poutanen J., Werner K., 2012, [A&A](#), **545**
- Takatsuka T., Nishizaki S., Yamamoto Y., Tamagaki R., 2006, [Progress of Theoretical Physics](#), **115**, 355
- Tolman R. C., 1934, [PNAS](#), **20**, 169
- Tolos L., Centelles M., Ramos A., 2016, preprint, ([arXiv:1610.00919](#))
- Veitch J., et al., 2015a, [Phys. Rev. D](#), **91**, 042003
- Veitch J., Pürrer M., Mandel I., 2015b, [Phys. Rev. Lett.](#), **115**, 141101
- Venkateswara K., Hagedorn C. A., Turner M. D., Arp T., Gundlach J. H., 2014, [Rev. Sci. Instrum.](#), **85**, 015005
- Venkateswara K., et al., 2017, [Bulletin of the Seismological Society of America](#), **107**, 709

- Venumadhav T., Zimmerman A., Hirata C. M., 2014, [ApJ](#), **781**, 23
- Vitale S., Evans M., 2017, [Phys. Rev. D](#), **95**, 064052
- Vitale S., Del Pozzo W., Li T. G. F., Van Den Broeck C., Mandel I., Aylott B., Veitch J., 2012, [Phys. Rev. D](#), **85**, 064034
- Wang Y. N., Shen H., 2010, [Phys. Rev. C](#), **81**, 025801
- Weaver T. A., Zimmerman G. B., Woosley S. E., 1978, [ApJ](#), **225**, 1021
- Weinberg N. N., 2016, [ApJ](#), **819**, 109
- Weinberg N. N., Bildsten L., Schatz H., 2006, [ApJ](#), **639**, 1018
- Weinberg N. N., Arras P., Quataert E., Burkart J., 2012, [ApJ](#), **751**, 136
- Weinberg N. N., Arras P., Burkart J., 2013, [ApJ](#), **769**, 121
- Weissenborn S., Chatterjee D., Schaffner-Bielich J., 2012, [Nucl. Phys. A](#), **881**, 62
- Wen L., Chen Y., 2010, [Phys. Rev. D](#), **81**, 082001
- Winget D. E., Kepler S. O., 2008, [ARA&A](#), **46**, 157
- Woosley S. E., et al., 2004, [ApJS](#), **151**, 75
- Yakovlev D. G., Levenfish K. P., Shibano Y. A., 1999, [Phys. Usp.](#), **42**, 737
- Yakovlev D. G., Kaminker A. D., Gnedin O. Y., Haensel P., 2001, [Phys. Rep.](#), **354**, 1
- Yam W., Gras S., Evans M., 2015, [Phys. Rev. D](#), **91**, 042002
- Yamamoto H., 2017, Study of the point absorption on ITMX at LHO. LIGO, <https://dcc.ligo.org/LIGO-G1700588>
- Young W. C., Budynas R. G., 2002, Roark's formulas for stress and strain. Vol. 7, McGraw-Hill New York
- Yu H., 2017, SRC detuning induced by differential ITM thermal lens. LIGO, <https://dcc.ligo.org/LIGO-T1700246>
- Yu H., Sigg D., 2017, Alignment sensing in the signal recycling cavity using a new 118.3 MHz sideband scheme. LIGO, <https://dcc.ligo.org/LIGO-T1700215>
- Yu H., Weinberg N. N., 2017a, [MNRAS](#), **464**, 2622
- Yu H., Weinberg N. N., 2017b, [MNRAS](#), **470**, 350
- Yu H., Weinberg N. N., 2018, [ApJ](#), **863**, 53
- Yu H., et al., 2018, [Phys. Rev. Lett.](#), **120**, 141102

- Zhao W., Wen L., 2017, preprint, ([arXiv:1710.05325](#))
- in't Zand J. J. M., Weinberg N. N., 2010, [A&A](#), 520, A81
- in't Zand J. J. M., Cumming A., van der Sluys M. V., Verbunt F., Pols O. R., 2005, [A&A](#), 441, 675
- in't Zand J. J. M., Jonker P. G., Markwardt C. B., 2007, [A&A](#), 465, 953
- in't Zand J. J. M., et al., 2013, [A&A](#), 553, A83
- in't Zand J. J. M., Keek L., Cavecchi Y., 2014, [A&A](#), 568, A69
- van Paradijs J., 1979, [ApJ](#), 234, 609